The origins of olivine fabric transitions and their effects on seismic anisotropy in the upper mantle

Dissertation
Zur Erlangung des Grades eines
Doktors der Naturwissenschaften

-Dr. Rer. Nat.-

Bayreuther Graduiertenschule für Mathematik und Naturwissenschaften
der Universität Bayreuth
„Experimental Geosciences“

vorgelegt von
Sushant Shekhar
Int. M.Sc. (Exploration Geophysics)
Aus
Kharagpur (*Indien*)

May 2011

Prüfungssausschuß:

Prof. F. Langenshorst, Universität Jena (1. Gutachter)
Prof. David Rubie, Universität Bayreuth (2. Gutachter)
Prof. L. Dubrovinsky, Universität Bayreuth
Dr. Henri Samuel, Universität Bayreuth
Prof. Jurgen Senker, Universität Bayreuth

Prof. Ludwig Zöller, Universität Bayreuth
Prof. S. Peiffer, Universität Bayreuth

Table of Contents

LIST OF IMAGES

LIST OF TABLES

ACKNOWLEDGEMENTS

I feel immense pleasure in availing this opportunity for expressing my deepest sense of gratitude and regards to my supervisors - Dr. Dan Frost, Prof. Falko Langenshorst and Prof. Dave Rubie for their continuous support, invaluable suggestions and untiring effort extended during my entire doctoral research work at the Bayerisches Geoinstitut, Universität Bayreuth, Germany.

But above all, if it was not for the constant motivation provided by my acting supervisor *Dan Frost* since the inception of this project, this work may never have been completed within the given timeframe and as per the desired quality.

I am acknowledging my obligations to the Elitenetzwerk Bayern, International Graduate School program for funding my research projects and the administration of the Bayerisches Geonistitut, for providing me necessary facilities to pursue my work.

More so I am indebted to Dr. Florian Heidelbach for his substantial help and invaluable suggestions apart from his assistance in SEM and EBSD studies. I am greatly appreciative of Dr. Nobuyohi Miyajima for his help in performing TEM studies. I must acknowledge the instructions by Dr. Nicolas Walte while using Deformation-DIA and his continued support in the form of valuable inputs to this study. I also take this opportunity to express my gratitude to Prof. Hans Keppler for providing me an opportunity to work at BGI and his subsequent support in FTIR studies. Dr. Andrea Tommassi and Dr. Dave Mainprice from Geoscience Montpellier provided useful insights into interpretations of results from this study and VPSC modeling was also performed under their supervision. I also must thank Prof. Jurgen Senker for his support in conducting NMR studies.

This work would have been far from complete if it was not for the crucial support from technical staff at Bayerisches Geoinstitut.

Last but not least I thank all who have directly or indirectly sympathized with me in completing my entire dissertation.

Sincerely

Sushant Shekhar

Bayreuth, May 2011

ABSTRACT

Convecting mantle plays a central role in the thermal and geochemical evolution of the Earth. It provides the principal force responsible for major geological features such as mountains and ocean basins. Plate tectonics and its violent consequences such as earthquakes and volcanoes are all manifestations of the dynamics of the convective mantle. Shearing forces generated by mantle convection leads to lattice preferred orientation (LPO) of the major upper mantle mineral phases. LPO that develops in this way is thought to be the principal cause behind seismic anisotropy in the upper mantle, which can consequently be used to chart convective flow of the mantle.

Strong changes in seismic anisotropy occur in the top 300 km of the upper mantle where olivine is the principal mineral. In this study a solid media high pressure deformation apparatus, called the deformation-DIA or D-DIA, has been used to deform aggregates of San Carlos olivine in simple shear geometry at pressures between 3 and 8.5 GPa and temperatures from 1300-1500°C. As part of this project a high pressure and temperature solid-media cubic assembly was developed to facilitate these experiment that employed alumina pistons cut at 45° to shear the sample but minimized cold deformation of the sample by employing initially porous alumina in the sample column. Once stable high pressures and temperature were reached the cubic assembly was deformed by compressing two vertically oriented anvils of the D-DIA, while the four horizontally oriented anvils were maintained at a constant loading force. This assembly shortening led to shearing of the olivine sample. Recovered samples were analyzed for fabric development employing electron backscattered diffraction (EBSD) and microstructure was observed using transmission electron microscopy (TEM).

Experiments were performed at each pressure and temperature as a function of strain rate and H_2O content. In dry olivine deformation experiments performed at slower strain rates an A-type fabric dominated at all pressures and temperatures, implying deformation by

dislocation glide through the (010)[100] slip system. At higher strain rates evidence for the B-type fabric was observed, suggesting increased activity of the (010)[001] slip system at higher stresses. Recrystallization grains size and dislocation densities were used to estimate stresses in the samples and a good correlation was observed between strain rate and estimated flow stresses. Dry experiments from 8.5 GPa and 1500°C exhibited no LPO, which may be an indication for deformation through diffusion accommodated grain boundary sliding at these conditions. No indication was found that pressure influences the dominant slip system in olivine, in contrast to previous studies. It is considered that previously reported incidences of pressure effects can in fact be attributed to the development of higher stresses in experiments performed at higher pressures.

Fabrics in H_2O bearing olivine deformed at similar conditions revealed the overriding dominance of the C-type fabric, developed through action of the (100)[001] slip system. Variations in pressure, temperature and strain rate had little influence on this fabric development. TEM observations confirmed the presence of dislocations with slip systems consistent with the development of the macroscopic fabrics. Viscoplastic self consistent modeling was employed to understand the development of fabric in the samples and to estimate the relative contributions of variations slip systems to the developed fabrics.

These results are used to construct an olivine fabric map which is found to be consistent with some previous studies at lower pressures. It is argued that the decrease in seismic anisotropy observed in the top 300 km of the upper mantle cannot originate from a pressure induced change in the dominant olivine deformation fabric. Instead it is argued that changes in the H_2O content of olivine with depth cause a shift in the dominant fabric from A-type to C-type, with a possible excursion through the E-type fabric, dominant slip system (001)[100], which was, however, not observed in this study. Modeling is used to show that this variation in fabric with depth can cause the observed weakening the seismic anisotropy in the upper mantle if the olivine H_2O content increases from below 100 ppm at 50 km to 250 ppm at 300 km. Rather than implying an increased in the H_2O content of the mantle with depth, however, it is argued that this change in olivine H_2O content can be

caused by changes in the H_2O olivine-pyroxene partition coefficients with depth, for a fixed bulk mantle H2O content of 200 ppm.

Similar deformation experiments performed on a peridotite assemblage at 8.5 GPa and 1300°C indicate identical olivine fabrics to those observed in monomineralic experiments at the same conditions. Fabrics for diopside and enstatite were found to be similar to those found in previously performed lower pressure experiments.

Experiments on a piezoelectric single crystal of $GaPO_4$ were performed in the D-DIA and 6-ram MAVO press at high pressures in order to measure charge on the crystal developed through the application of deviatoric stresses. Electrical charges were measured through the use of an operational amplifier. Experiments performed at room temperature using a developed cubic assembly were successful in measuring quantifiable electrical charges resulting from the advancement of the deformation anvils by as little as 0.5 μm. Although the piezoelectric constant for this material is not yet calibrated at high pressures, stresses were estimated from the measured charges and measureable values were in the range 4-350 MPa.

ZUSAMMENFASSUNG

Mantelkonvektion spielt eine zentrale Rolle in der thermischen und geochemischen Entwicklung der Erde. Sie stellt die Hauptenergiequelle für die Bildung von geologischen Grossstrukturen wie Gebirgsketten und Ozeanbecken dar. Die Plattentektonik und ihre gewaltigen Folgen wie Erdbeben und Vulkanismus sind Manifestationen der Dynamik des konvektiven Erdmantels. Von der Mantelkonvektion generierte Scherkräfte bewirken eine kristallographische Vorzugsorientierung („lattice preferred orientation“, LPO) der mineralogischen Hauptphasen des oberen Erdmantels. Eine auf diese Art gebildete LPO wird als Hauptursache für die seismische Anisotropie des oberen Erdmantels angesehen, welche somit zur Kartierung der Mantelströmungen verwendet werden kann.

In den ersten 300 km des oberen Erdmantels, in dem das Mineral Olivin dominiert, verändert sich die seismische Anisotropie besonders stark. In der vorgelegten Studie wurde eine Hochdruck-Verformungspresse, der sogenannte Deformation-DIA (D-DIA), eingesetzt, um Aggregate aus San Carlos Olivin in einfacher Schergeometrie bei Drücken zwischen 3 und 8,5 GPa und Temperaturen von 1300-1500 ° C zu verformen. Zur Durchführung der Experimente wurde als Teil dieses Projektes eine kubische Hochdruck und -temperaturzelle entwickelt, in der mit einem Winkel von 45° geschnittene Al_2O_3 Stempel benutzt werden, um die Probe zu scheren. Die Kaltverformung während des Druckaufbaus wird durch den Einsatz von porösem Aluminiumoxid minimiert. Nach dem Erreichen von stabil hohen Druck- und Temperaturbedingungen während eines Experiment wurde die kubische Zelle durch Komprimierung der zwei vertikal ausgerichteten Stempel der D-DIA verformt, während die vier horizontal ausgerichteten Stempel bei konstanter Kraft gehalten wurden. Diese Verkürzung der gesamten Zelle führt zu einer Scherdeformation der Olivinprobe. Die Texturentwicklung der extrahierten Proben wurde mithilfe von rückgestrahlter Elektronenbeugung (EBSD) analysiert und die Mikrostruktur wurde mit Transmissionselektronenmikroskopie (TEM) untersucht.

Bei jedem Druck und Temperatur wurden Experimente in Abhängigkeit von Deformationsrate und Wassergehalt durchgeführt. In Verformungsexperimenten mit trockenem Olivin entwickelte sich bei niedriger Deformationsrate (niedrige Spannung) eine LPO des Typs A bei allen experimentellen Drücken und Temperaturen, was auf ein dominantes Gleitsystem (010) [100] hindeutet. Bei höherer Deformationsraten (höheren Spannungen) entwickelten sich LPOs des Typs B, was auf eine erhöhte Aktivität des (010) [001] Gleitsystems hindeutet. Die rekristallisierte Korngrösse und die Versetzungsdichten wurden dazu benutzt, die Spannungen in den Proben abzuschätzen und ergaben eine gute Korrelation mit den Deformationsraten. Experimente mit trockenen Proben bei 8.5 GPa und 1500 ° C ergaben keine LPO, was möglicherweise den Übergang zur Verformung durch Diffusions-gestütztes Korngrenzgleiten bei diesen Bedingungen anzeigt. Im Gegensatz zu früheren Studien gab es keinen Hinweis darauf, dass Druck das dominante Gleitsystem in Olivin beeinflusst. Die in diesen Arbeiten postulierte Druckabhängigkeit der Gleitsysteme im Olivin könnte daher in Wirklichkeit durch die höheren Spannungen bei den höheren experimentellen Drücken verursacht sein.

Texturen in H_2O-haltigen Olivinproben, die bei ähnlichen Bedingungen wie die trockenen Proben deformiert wurden, offenbart die Dominanz des Texturtyps C, charakterisiert durch die Einregelung des (100) [001] Gleitsystems. Änderungen von Parametern wie Druck, Temperatur und Deformationsrate hatte dabei nur sehr geringen Einfluss auf diese Texturentwicklung. TEM Beobachtungen bestätigten das Vorhandensein von Versetzungen der jeweiligen Gleitsysteme, die mit der Entwicklung der makroskopischen Texturen in Einklang stehen. Modellierungen der Texturentwicklung mithilfe eines viskoplastisch-selbskonsistenten Deformationsmodells wurden benutzt, um die Textur der Proben zu verstehen und die anteiligen Beiträge der verschiedenen Gleitsysteme zu ihrer Entwicklung abzuschätzen.

Diese Ergebnisse werden verwendet, um eine Olivintexturkarte zu erstellen, die mit den vorherigen Deformationsstudien von Olivin bei niedrigerem Druck im Einklang steht. Es

wird argumentiert, dass der Rückgang der seismischen Anisotropie, der in den obersten 300 km des oberen Mantels beobachtet wird, nicht durch eine druckinduzierte Änderung des dominanten Gleitsystems in Olivin verursacht wird. Stattdessen wird vorgeschlagen, dass Änderungen im H_2O-Gehalt des Olivins mit der Tiefe eine Verschiebung der Textur von Typ A nach Typ C bewirken, mit einem möglichen Umweg über die Textur des Typs E (charakterisiert durch das Gleitsystem (001) [100]), die in dieser Studie jedoch nicht beobachtet wurde. Modellierungen wurden durchgeführt, um zu zeigen, dass diese Änderung im dominanten Gleitsystem die Verringerung der seismischen Anisotropie mit der Tiefe im oberen Erdmantel verursachen kann. Der H_2O-Gehalt von Olivin steigt von unter 100 ppm bei 50 km Tiefe auf 250 ppm bei 300 Kilometern Tiefe an. Allerdings wird nicht argumentiert, dass der gesamte H_2O-Gehalt des Mantels mit der Tiefe ansteigt, sondern, dass diese Änderung im H_2O-Gehalt des Olivins durch die Änderung des Verteilungskoeffizienten von H_2O zwischen Olivin und Pyroxen mit der Tiefe bei einem konstanten H_2O Konzentration von 200 ppm im oberen Erdmantel verursacht werden kann.

Ähnliche Verformungsexperimente wurden mit einer Probe peridotitischer Zusammensetzung bei 8.5 GPa und 1300 ° C durchgeführt und ergaben identische Olivintexturen wie die monomineralischen Experimente. Texturen für Diopsid und Enstatit in diesen Experimenten sind ähnlich mit denen, die zuvor in Experimenten bei niedrigerem Druck produziert wurden.

Experimente mit einem piezoelektrischen Einkristall aus $GaPO_4$ wurden in der D-DIA und der 6-Stempel MAVO Presse bei hohen Drücken durchgeführt, um die elektrische Ladungen zu messen, die durch die deviatorischen Spannungen erzeugt werden. Die elektrische Ladung des Kristalls wurde mithilfe eines Operationsverstärkers gemessen. In Experimenten bei Raumtemperatur wurden unter Verwendung der kubischen Zelle erfolgreich quantifizierbare elektrische Ladungen gemessen, die bei absoluten Bewegungen der Deformationsstempel von weniger als 0,5 μm erzeugt wurden. Obwohl

die piezoelektrische Konstante für $GaPO_4$ bei hohen Drücken noch nicht kalibriert ist, konnten aus den gemessenen elektrischen Ladungen mechanische Spannungen im Bereich von 4-350 MPa abgeschätzt werden.

1 Introduction

Only rocks of the earth's outer crust are directly accessible to analysis but this surface reservoir accounts for less than 1% of Earth's total volume. Clues to the chemical and physical state of the Earth's underlying mantle can be obtained through the study of xenoliths i.e. rocks brought to Earth's surface in basalt flows or by more exotic magmas such as diamond-bearing kimberlite pipes. In addition larger sections of the oceanic lithospheric mantle can become tectonically attached to the continental crust during mountain building episodes and meteorites also provide some clues about the likely chemical composition of the bulk Earth and its metallic core. The deep interior of the Earth remains directly inaccessible, however, and it can only be studied *indirectly*, using tools provided by geophysics – such as analysis of seismic waves and the measurement of gravity, heat flow, and magnetism.

Seismology has been the most important tool for the determination of the Earth's deep structure and likely chemical composition. Seismic body wave data has been employed to produce one dimensional global model for S and P wave velocities in the Earth [*Dziewonski and Anderson,* 1981]. These one-dimensional profiles have been compared with mineral seismic velocities determined as a function of pressure, temperature and composition in the laboratory in order to determine the likely mineralogy and composition of the mantle as a function of depth [*Frost,* 2008; *Stixrude and Lithgow-Bertelloni,* 2005]. Such comparisons are generally consistent with an ultramafic upper mantle composed of olivine, ortho- and clinopyroxene and garnet to depths of approximately 410 km. The velocities for the mantle at greater depths are consistent with a bulk mantle of similar composition to the upper mantle, although undergoing phase transformations to denser mineral polymorphs with increasing depth. Seismic discontinuities at 410, 520 and 660 km, where waves are reflected and converted at sharp boundaries in mineral elastic properties, are consistent with experimental studies that show phase transformations of olivine to higher pressure

structures at pressure corresponding to these depths. Seismic observations are therefore consistent with the upper mantle being comprised dominantly of olivine, ~60 volume % (Fig 1-1), which is also in agreement with the majority of mantle xenoliths which show the upper mantle to be olivine dominated.

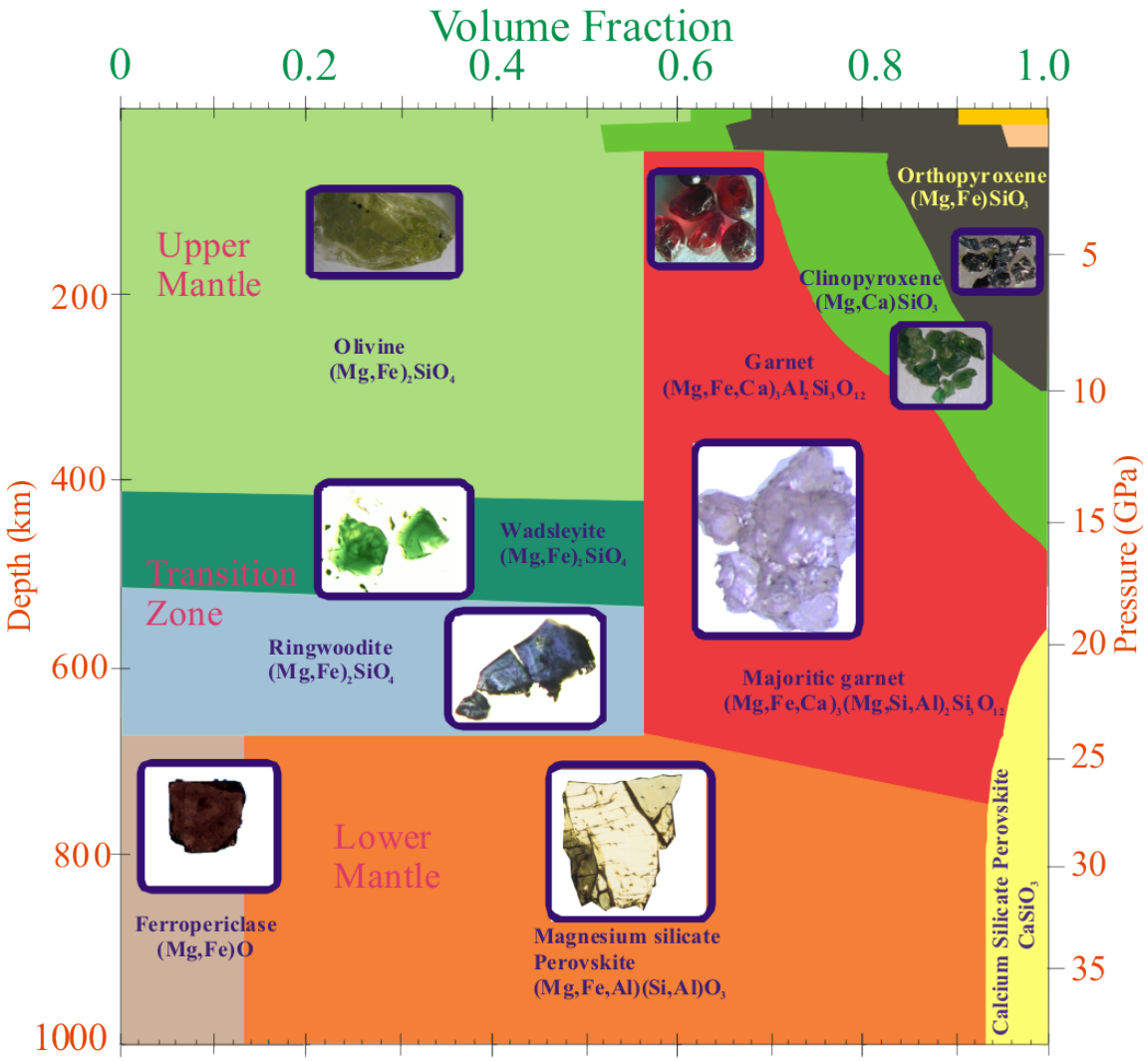

Figure 1-1: Pyrolitic mantle mineralogy as a function of mineral volume fraction and depth variation. (Figure courtesy: Dan Frost)

Velocities of seismic body waves in the Earth increase with depth as a result of both the effect of pressure on mineral elastic properties and phase transformations to denser mineral structures. While the former effect causes a gradual increase in velocity with depth the later introduces discontinuous changes in velocity. However, seismic wave velocities

also change as a function of the direction of propagation in some regions of the mantle. This anisotropic behaviour is a phenomenon of great significance because it results from the development of fabric in mantle rocks caused by convective flow driven by heat flow in the earth.

Convection in the earth's mantle has a direct bearing on the motion of tectonic plates, which in turn governs the evolution of the most prominent geological features on the earth's surface, such as mountains, oceans, volcanoes etc. The study of seismic anisotropy can therefore be used to understand the direction of mantle convection, to investigate the coupling between the lithosphere and the asthenosphere and to delineate structures in the interior such as continental roots.

1.1 Seismic anisotropy in the earth

Seismic anisotropy arises from anisotropic elastic properties of rocks and minerals and can result from two main processes in the Earth, both related to deformation. Shape preferred orientation (SPO) arises from layering, caused, for example, by mineral banding or melt channelling, while crystallographic preferred orientation (CPO) arises from the alignment of elastically anisotropic minerals. Seismic anisotropy due to SPO would infer banding of minerals into layers with strongly different elastic properties. Most mantle mineral, however, do not have sufficiently different elastic properties to cause strong seismic anisotropy through SPO [*Shearer,* 1999]. The exception would be banding involving melt layers, although these could only occur in the very top of the mantle, potentially beneath ridges, or possibly in the D'' layer. Anisotropy in the bulk of the mantle is generally attributed to CPO.

Seismic anisotropy is measured using two main techniques:

1. Azimuthal anisotropy is the variation in wave velocity, both S and P waves, with the direction of wave propagation. This was first detected from the azimuthal dependence of Pn waves (a P wave that travels along the boundary between the crust and mantle) in the oceanic lithosphere, beneath the Pacific Ocean [*Hess,* 1964]. This type of anisotropy is measured by determining the directional dependence of wave velocities through a region of the earth. For this purpose a series of different

sources (e.g. earthquakes) are required to send waves to one or more receivers so that suitable directional coverage of the region in question is obtained. The differences in velocity as a function of the direction that the wave travelled through the region of interest are then analyzed. The main drawbacks in studying azimuthal anisotropy are that many source-receiver pairs are required and heterogeneities can also cause apparent anisotropy because rays travel through different regions on their way to the region of interest. Azimuthal anisotropy can also be studied using Surface waves (Rayleigh and Love waves).

2. Polarization anisotropy is similar to birefringence in optical mineralogy and leads to shear-wave splitting in seismograms. S-wave particle motion is normal to the propagation direction and the velocity is therefore a function of the material elastic properties in directions normal to the propagating direction. In an anisotropic medium S-waves therefore become polarized with a fast S-wave direction orthogonal to a slow one. The velocity difference between the polarized S-waves causes shear wave splitting, where the two polarized waves develop a delay time. At a single receiver station the polarization direction (φ) of the fast shear wave and the time delay (δt) between the two pulses can be measured (Fig. 1-2).

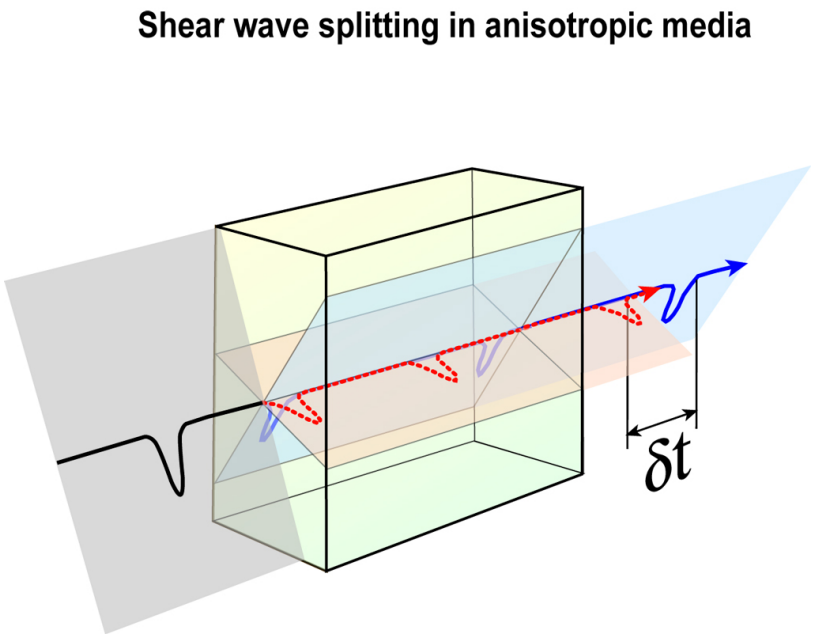

Figure 1-2: A wave travelling through a elastically anisotropic media splits into two orthogonally polarized wave. Magnitude of the shear wave splitting is given by the time delay (δt) between the fast wave and the slow wave. Figure source: - Ed Garnero - http://garnero.asu.edu/research_images

In addition to these different measurement techniques, seismologists often model anisotropy in the mantle assuming transverse isotropy, which considers an elastic medium to have a

symmetry axis normal to the propagation direction. In most instances the symmetry axis is considered to be vertical and this type of anisotropy is therefore often termed radial anisotropy. Differences in properties are implied in the horizontal and vertical directions. P waves are then resolved into PH and PV components in the horizontal and vertical directions and SH and SV are the corresponding polarized S-waves. The first reference model for seismic structure of earth, PREM (Dziewonski and Anderson, 1981), includes this kind of anisotropy in the top 220 km of the Earth (Fig 1-3). The value V_{SH}/V_{SV} or V_{SH}^2/V_{SV}^2 or inequalities such as $V_{SH}>V_{SV}$ are frequently used to quantify anisotropy in the mantle as shown in figure 1-3.

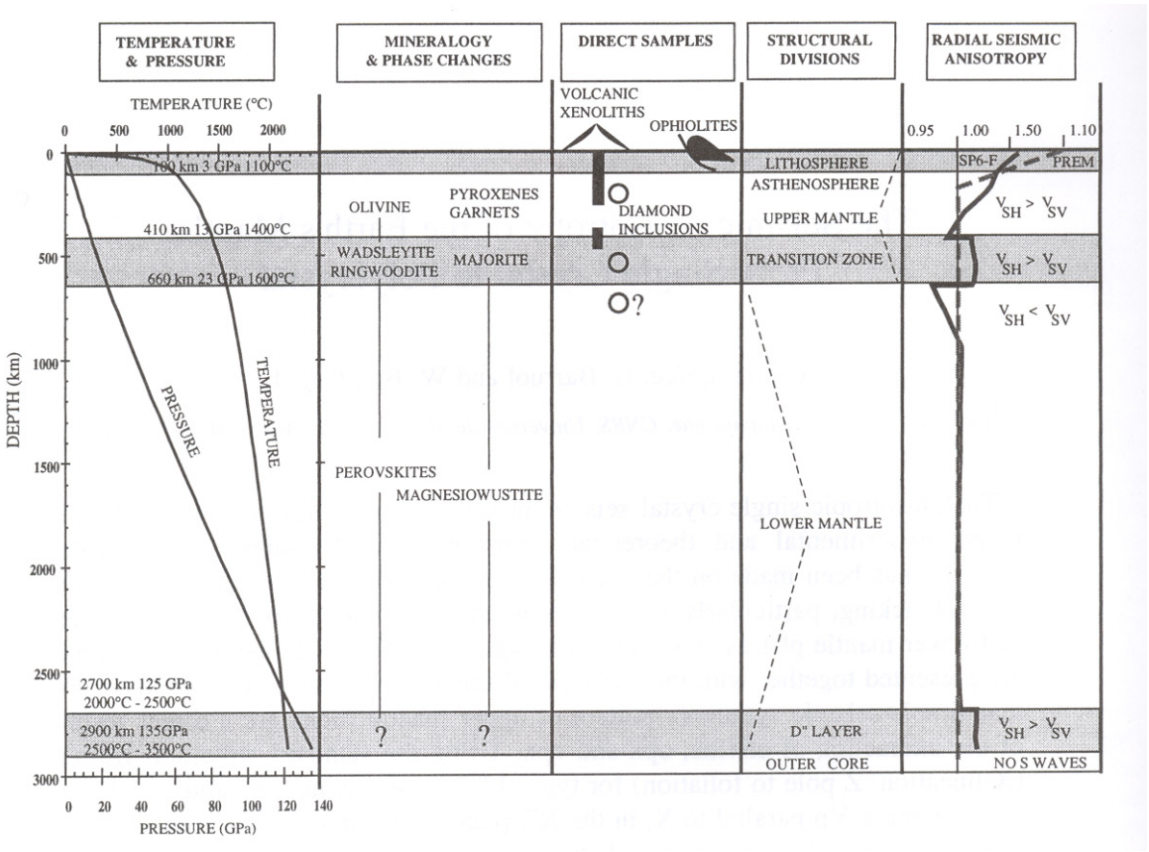

Figure 1-3: Physical and chemical structure and Radial seismic anisotropy observed in the earth. Source of significant anisotropy in the upper mantle is believed to be the crystallographic preferred orientation of mantle mineral, mainly olivine (Courtesy: D. Mainprice).

Significant seismic anisotropic is observed in the upper mantle and the D'' layer (between lower mantle and the outer core) (Fig 1-3). Major source of the seismic anisotropy in the upper mantle is the CPO of major mineral phases e.g. olivine and

pyroxene. Out of these two mineral phases, olivine has much larger contribution to the overall anisotropy in the upper mantle because of its larger intrinsic anisotropy and the volume. Anisotropy in the crustal regions is generally caused by the shaped preferred orientation and presence of melts and fluids.

1.2 CPO in Olivine

Creep within the earth's convecting mantle results in the non-random distribution of crystallographic orientations of major mantle minerals such as olivine, pyroxene and garnet because these minerals have anisotropic mechanical properties (Karato, 1989). As these minerals, particularly olivine, also have intrinsic elastic anisotropy the development of CPO makes the mantle seismically anisotropic in places. Therefore, seismic anisotropy in the mantle reflects the strain field prevailing in the past (frozen-in anisotropy) within the lithosphere or present convective processes in the asthenosphere and deeper mantle. As shown in Figure 1-3, the bulk of mantle below 200 km appears seismically isotropic, which could be interpreted as a result of diffusion creep or superplastic flow (Karato, 1995), because such diffusive processes do not lead to CPO development. CPO results from dislocation glide which acts to rotate the orientation of a crystal to match the imposed deformation regime. CPO depends on the deformation geometry and the active dislocation slip systems of the crystal. A slip system is related to the motion of the dominant dislocations active in the mineral. Natural olivine –bearing rocks show a deformation fabric dominated by alignment of the [100] axis parallel with the direction of apparent shear deformation, abbreviated as a-slip, while the (010) plane is parallel to the shear plane (Fig 1-4).

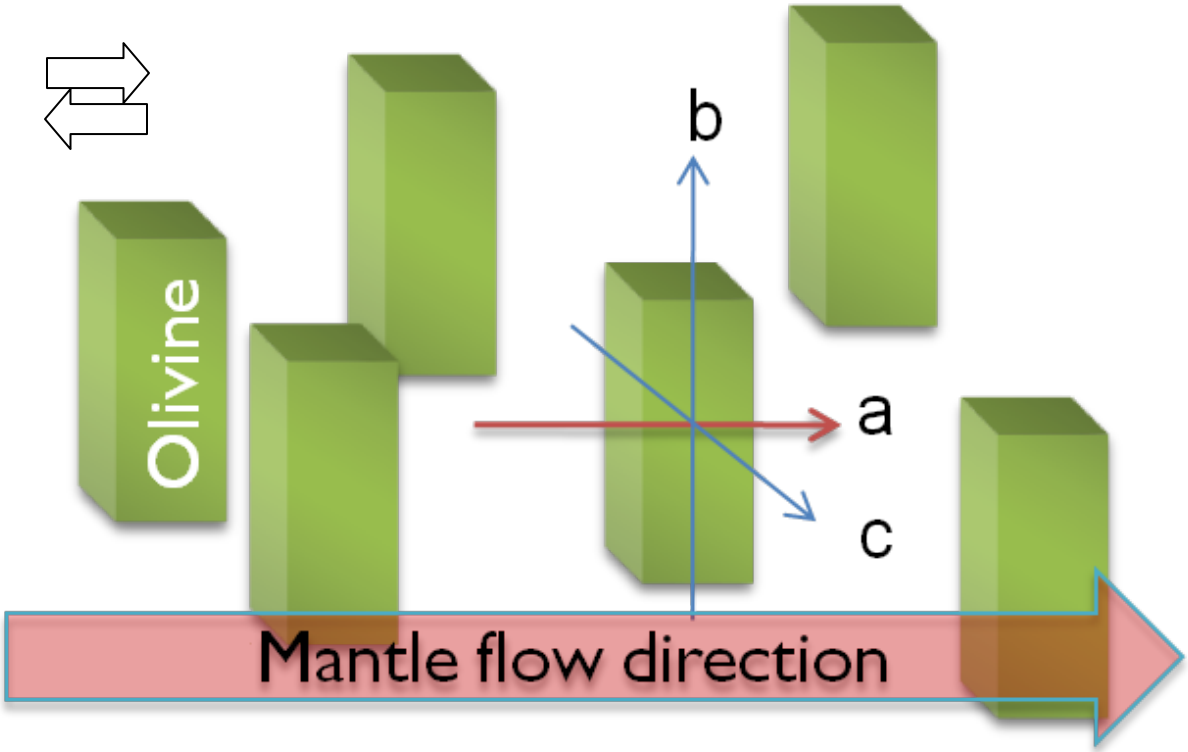

Figure 1-4: Crystallographic preferred orientation development in olivine due to shearing nature of the mantle flow. CPO of elastically anisotropic minerals is the principal cause for seismic anisotropy observed in the upper mantle.

The olivine fabric database compiled by (Ben Ismaïl and Mainprice 1998) indicates that up to 50% of naturally deformed samples possess this (010)[100] CPO olivine fabric. Apart from the most common (010)[100] slip system, other known slip systems in olivine are (001)[100], (010)[001] and (100)[001] [*Carter and Ave'lallemant,* 1970]. In the past, experimental studies have been performed on natural and synthetic samples in order to understand the effect of deformation conditions on the CPO development in olivine and other minerals (Carter and Ave'Lallemant 1970, Nicolas et al. 1973, Zhang & Karato 1995).

Initial works on experimental deformation on San Carlos olivine indicated that slip systems in olivine change with changing stress and temperature [*Carter and Ave'lallemant,* 1970; *Goetze,* 1978]. At lower stresses (or higher temperatures) (010)[100] slip system was found to be most active where as higher stresses (or lower temperatures) (010)[001] slip system was most active. Under intermediate stress and temperature conditions, {0*kl*}[100] slip system was the easiest (Fig. 1-5). Later works by Karato and co-workers

also proposed a change in slip system at from (010)[100] to (010)[001] slip system at higher stresses [*Jung and Karato,* 2001a]. Change in slip system has also been observed with change in water content of olivine [*Jung and Karato,* 2001a; *Katayama et al.,* 2004]. At moderate water content (less than 60 wt. ppm), (001)[100] slip system was found to be dominant slip system while it changed to (100)[001] slip system at higher water contents (Fig. 1-5).

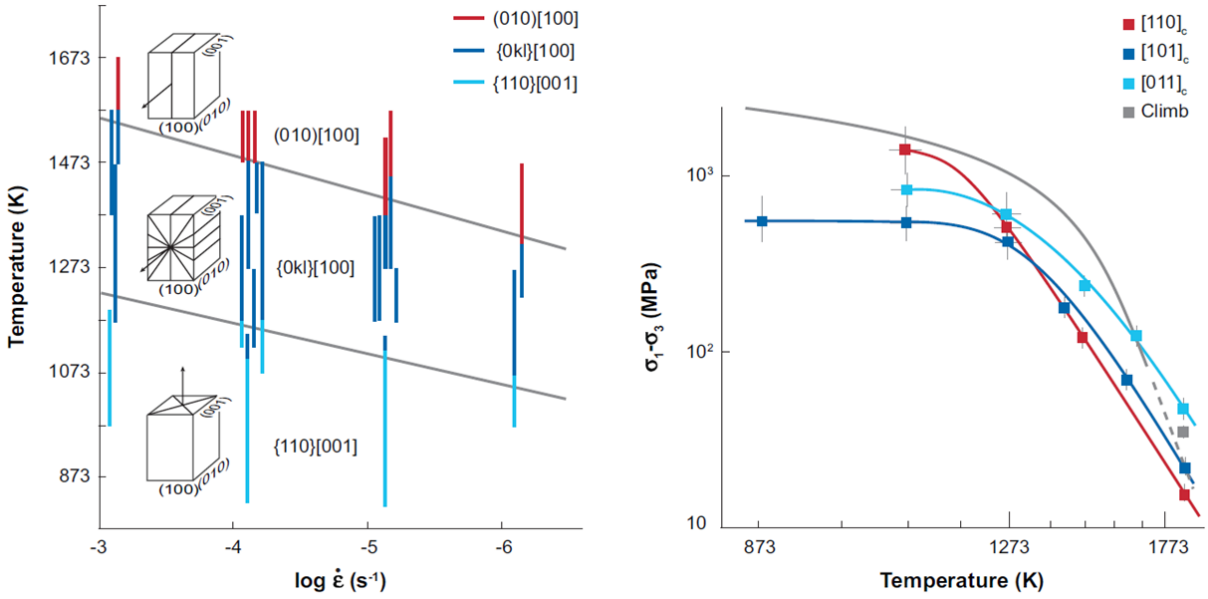

Figure 1-5: Dominant slip systems in olivine as a function of strain rate and temperature (at P = 1.5 GPa) (from Carter & Av´e Lallemant 1970). Results shown here suggest stress-induced transitions in the dominant slip systems. (*b*) A comparison of creep strength for different orientations of single crystal and polycrystal at $\dot{\varepsilon} \approx 10{-}5\ s{-}1$ (from Goetze 1978). The [110]*c* activates the [100] (010) slip system, the [101]*c* orientation, the [100] (001) and [001] (100) slip systems, and the [011]*c* and [001] (010) slip systems. Figure Source: Karato (2008)

Previous works at Bayerisches Geoinstitut [*Couvy et al.,* 2004] indicated that at higher pressures (11 GPa), the deformation was mainly caused by slip of dislocation with [001] burgers vectors, indicating that c-slip was easier under these conditions. Deformation of single crystal olivine specimens also reaffirmed this conclusion where [001]-slip over [100]-slip progressively becomes easier with increasing pressure [*Raterron et al.,* 2007]. Theoretical modelling of dislocation core structure by first principal calculations indicated that this change in slip system with pressure can be explained by change in dislocation core structure with pressure [*Durinck et al.,* 2005].

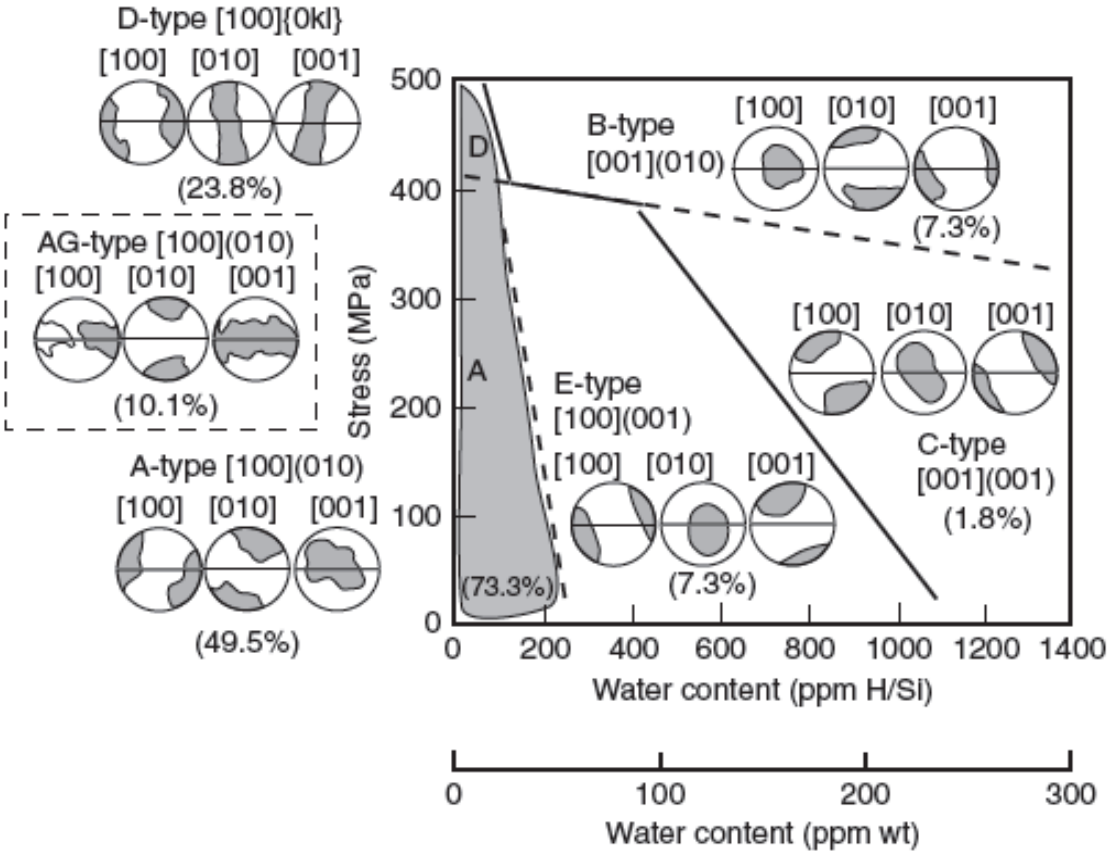

Figure 1-6: Dominant slip system in olivine as a function of stress and water content [T = 1400 to 1570K]. As evident from the plot, higher content of water promotes (100)[001] slip whereas at higher stress promotes (010)[001] slip system. Figure source: Jung & Karato (2001)

Table 1-1: Fabric type and nature of slip system (Jung and Karato, 2001)

Fabric type	A-Type	E-Type	B-Type	C-Type	D-Type
Dominant Slip system	(010)[100]	(001)[100]	(010)[001]	(100)[001]	(100){0*kl*}

However, recent results have indicated that this pressure related transition in slip system could occur at much lower pressures of approximately 3 GPa [*Jung et al.,* 2009b]. Whereas other reports on olivine deformation have put this pressure related transition point around 7.6 GPa at 1400°C [*Ohuchi et al.,* 2011]. Such conflicting reports along with the difficulty in accurate measurement of flow stresses in the sample, have put a question

mark if there is indeed a pressure related transition in slip system or is it simply the variation in stress and water content that would have lead to change in this slip system, as reported in the earlier studies [*Carter and Ave'lallemant,* 1970; *Goetze,* 1978; *Jung and Karato,* 2001a; *Jung et al.,* 2006]?

In other studies, *Holtzman et al.* [2003] have reported that presence of melt rich band affects the LPO development in olivine due to the difference in the deformation geometry between the solid and partially molten part. This implies that even if deformation regimes are similar, LPO that develops in a partially molten region is different from that in a melt free region.

1.3 CPO relationship with microstructure

TEM studies have been performed on deformed single crystals of olivine. In these studies, force on single crystals is applied along known crystallographic directions of olivine so as to preferentially activate certain slip systems (Table 1-2). Results from Bai and Kohlstedt (1992) for crystal oriented along $[110]_c$ and $[011]_c$ shows that the dislocation were generally short, curved edge or of mixed nature. For the crystal orientated along $[101]_c$, annealing had little effect on the dislocation structure, unlike for other two orientations. The density of dislocations decreased much less for these $[101]_c$ samples than for the $[110]_c$ and $[011]_c$ samples, indicating that dislocation recovery processes operated much slower for (100)[001] and (001)[100] slip system. These results appear consistent with those form Durham and Goetze (1977), where they found that stress exponent for crystals oriented along $[101]_c$ were higher than for te other two orientation. This in turn also implies that (100)[001] and (001)[100] are difficult to activate slip system because slip on these slip systems may involve breaking of tetrahedral Si-O bonds. Results from Durham and Goetze (1977) also suggest that these two harder slip systems had significant contribution (20-30%) to the overall strain from dislocation climb. straight [100] screw dislocations in the quenched samples appear to become curved due to dislocation climb and under these conditions low-angle (100) tilt boundaries develop [*Bai and Kohlstedt,* 1992; *Durham and Goetze,* 1977; *Durham et al.,* 1977].

Olivine crystals strained beyond ~50% tend to recrystallise dynamically. Evidence from such specimens also suggests the LPO development is caused by lattice rotation due to dislocation glide, and nucleation and growth of new grains. Correlation between the LPO and the strain field indicates that lattice rotation due to dislocation glide might be the more important of the two phenomenon [*Toriumi and Karato,* 1985].

Table 1-2: Summary of slip system (Durham and Goetze, 1977)

Orientation (σ1)	Primary slip system	Secondary slip system
[110]$_C$	(010)[100]	(100)[010]
[101]$_C$	(001)[100]	(100)[001]
[011]$_C$	(010)[001]	(001)[010]

Detailed TEM work by *Sharp et al.* [2004] on experimentally deformed olivine specimen has confirmed that hydrous specimens exhibiting C-type fabric (Table 1-1) with dominant slip system (100)[001], shows tilt boundaries along (100) and (001), consisting of edge dislocations with b = [100] and b = [001], respectively, suggest presence of the both (001)[100] and (100)[001] slip systems. Results from HRTEM imaging of [100] and [001] edge dislocations cores along [010] showed no dissociation for [100] dislocations, whereas the [001] dislocations were found to be dissociated into 1/2[-101] and 1/2 [101] partial dislocations. In a B-type fabric sample, presence of [100] and [001] dislocations with mixed character indicates that both (010)[001] and (010)[100] slip systems were active. HRTEM imaging of dislocations with [001] dislocations indicated that these dislocations were also dissociated in similar way as in the case of dislocations present in specimens exhibiting C-type fabric. These samples also show another kind of dissociation with burgers vector of partial dislocation being 1/2[001] and 1/2[00-1]. The A-type fabric sample contained (100) tilt boundaries and [100] edge dislocations, suggesting in the (010)[100] slip system. This sample also contained many b = [001] with predominantly screw character. However, a-dislocations in this case were found to be un-dissociated. Summary of these results is that (100)[001], (010)[001] and (010)[100] slip systems are dominant slip system in the C-, B-, and A-type fabrics, respectively.

Studies on natural olivine specimens also confirm the dissociated nature of dislocations in water containing sample. Presence of water seems to enhance the climb dissociation of [001] dislocations in planes which are not the typical slip planes for olivine [*Drury,* 1991]. C-dislocation dissociated into (001) and {021} planes with Burgers vectors approximately equal to 1/x (011), should inhibit their glide on (100) and (010) planes.

Results from these studies suggest that olivine does not exhibit only three independent slip systems (010)[100], (010)[001], (100)[001] and (001)[100] with the last two slip systems always appearing as a couplet. Absence of five independent slip system, which are necessary to satisfy Von Mises criteria for homogeneous deformation, will require processes like dislocation climb, dynamic recrystallization and other intercrystalline deformation processes to play crucial role in overall deformation of olivine polycrystal.

1.4 CPO, mantle flow and anisotropy

Spatial variation of seismic anisotropy is intricately related to the variation of CPO as a function of temperature, stress, water content and also pressure [*Karato et al.,* 2008; *Mainprice et al.,* 2005]. Model proposed by Karato (2008) discards any pressure related change in olivine fabric. In this model, A-type and/or E-type fabric are the most likely source of seismic anisotropy in most parts of the asthenosphere mantle (Fig. 1-7).

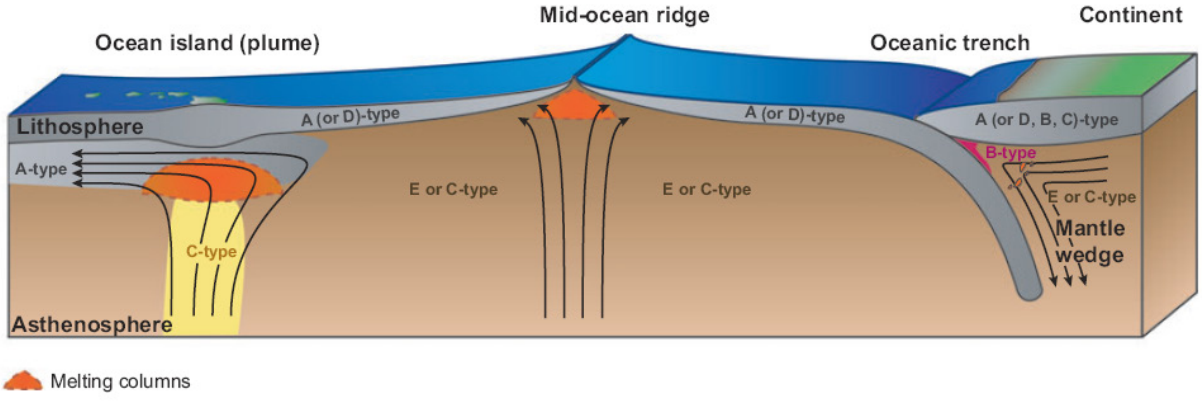

Figure 1-7: Likely distribution of olivine fabrics in the upper mantle as a response to changing stress, temperature and water content of the parts of upper mantle (Figure source: Karato 2008).

If upper mantle contains anywhere between 50 to 150 ppmw water then these part of mantle is likely to have E- or C-type fabric rather than A-type fabric. Moreover, presence of E-type fabric might be able to explain the weaker V_{SH}/V_{SV} anisotropy in asthenosphere in spite of larger straining of the rock mass in the asthenosphere [*Karato et al.,* 2008].

With the pressure induced change in slip system in the hindsight, *Mainprice et al.* (2005) have proposed weak nature of the seismic anisotropy below the 250 KM depth in the upper mantle can very well be explained by the CPO resulting from the activity of {0*kl*}[001] slip system (Table 1-3 and 1-4).

Table 1-3: Shear wave splitting (direction of the polarization of the faster, vertically traveling shear waves) (From Karato, 2008)

Fabric type	Horizontal flow	Vertical planar flow
A-type	Parallel to flow	Small splitting
B-type	Normal to flow	Parallel to the plane
C-type	Parallel to flow	Normal to the plane
D-type	Parallel to flow	Small splitting
E-type	Parallel to flow	Small splitting

This explanation does not require that diffusion creep be the dominant deformation mechanism in these lower parts of the upper mantle to generate the kind of seismic anisotropy observed there [*Karato,* 1992].

Table 1-4: V_{SH}/V_{SV} anisotropy (From Karato, 2008)

Fabric type	Horizontal flow	Vertical planar flow
A-type	$V_{SH}/V_{SV} > 1$	$V_{SH}/V_{SV} < 1$
B-type	$V_{SH}/V_{SV} > 1$	$V_{SH}/V_{SV} > 1$ (weak)
C-type	$V_{SH}/V_{SV} < 1$	$V_{SH}/V_{SV} > 1$ (weak)
D-type	$V_{SH}/V_{SV} > 1$	$V_{SH}/V_{SV} < 1$
E-type	$V_{SH}/V_{SV} > 1$ (weak)	$V_{SH}/V_{SV} < 1$

The conclusion of these studies is that the olivine [100] axes are aligned sub-parallel to the flow direction, and the olivine (010) planes become sub-parallel to the flow plane. The resultant seismic anisotropy due to this fabric is characterized by $V_{SH}/V_{SV} > 1$ for horizontal flow and $V_{SH}/V_{SV} < 1$ for vertical flow, whereas the direction of polarization of the faster shear wave becomes parallel to the flow direction. Studies performed in past 10 years have revealed that CPO development in olivine is a complex interplay between stress, temperature, water fugacity and pressure. (100)[001] slip system becomes dominant in olivine under water reach condition whereas higher stresses favour (010) [001] slip system (Figure 1-2) [Jung & Karato 2001, Katayama et al. 2004, Jung et al. 2006, Katayama & Karato 2006].

Evident from the discussion above is the fact that the relation between mantle flow and the direction of the fast axis is not as simple as was initially thought to be. The fast axis direction derived from the seismic anisotropy studies is not always parallel to the mantle flow direction. According to *Ribe* [1992], LPO development in minerals like olivine, with one dominant slip system, is a function of resultant strain ellipsoid integrated over the whole deformation path. And, hence it is not possible to infer the deformation history based upon present day seismic anisotropy data. Moreover, there is no simple and unique relation between the present day mantle flow pattern and the finite strain ellipsoid [*Mckenzie,* 1979]. Hence, barring the simpler deformation regimes like subducting slabs, beneath the lithosphere and in boundary layers, seismic anisotropy does not definitely represent the present day mantle flow (Fig. 1-7).

1.5 Mineral description - Olivine

Mg-rich olivine is a common mineral of mafic and ultramafic rocks, and is generally considered to be the major constituent of the Earth's upper mantle (40-80% in volume) with a composition close to $(Mg_{0.9}Fe_{0.1})_2SiO_4$ based on analyses of olivine in mantle xenoliths.

1.5.1 Crystal-chemistry

Olivine is an orthosilicate [*Deer et al.,* 1997], and a solid solution between the two end-members, $forsterite, (Mg)_2SiO_4$ $(Fo_{100}Fa_0)$ and $fayalite, (Fe)_2SiO_4 (Fo_0Fa_{100})$. Olivine crystal lattice has an orthorhombic symmetry (space group: *Pbnm*). The important crystallographic parameters of olivine are shown in Table 1-5. The structure consists of independent SiO_4 tetrahedra linked by divalent cations (M1 and M2) in six fold co-ordination (Fig 1-8). The oxygen anions are arranged in sheets nearly parallel to the (001) plane and closely resemble a hexagonal close-packed structure (Fig. 1-9). Each oxygen atom is bonded to one silicon cation and three divalent cations (e.g. Mg^{2+}, Fe^{2+}) with octahedral co-ordination. However, since the oxygen atoms are not perfectly close-packed, the M1 and M2 polyhedra are irregular shaped, and in such a way that the M2 site is slightly larger than the M1 site. The adjacent M1 sites share edges to form bands parallel to the [001] axis. These bands are connected to the next M1 bands in the upper layer (or lower layer) by the M2 octahedral sites. There is apparently no complete ordering in the Mg/Fe^{2+} distribution between the M1 and M2 sites, but Fe^{2+} has a preference for the M1 site. M1 and M2 may also be occupied by other cations such as Ni^{2+}, Mn^{2+}, Ca^{2+}, Cr^{3+} [*Deer et al.,* 1997] or B^{3+} [*Sykes et al.,* 1994]. In particular, olivines from Xenoliths often contain a small amount of nickel (Frey and Prinz, 1976).

Table 1-5: lattice constants and densities of Olivines (Deer et al., 1997)

	Forsterite	Mantle olivine	Fayalite
Chemical Formula	Mg_2SiO_4	$(Mg_{0.9},Fe_{0.1})_2SiO_4$	Fe_2SiO_4
a (Å)	4.754	4.755	4.8211
b Å	10.197	10.21	10.4779
c (Å)	5.9806	5.985	6.0889
Density (g/cm³)	3.222	3.4	4.392

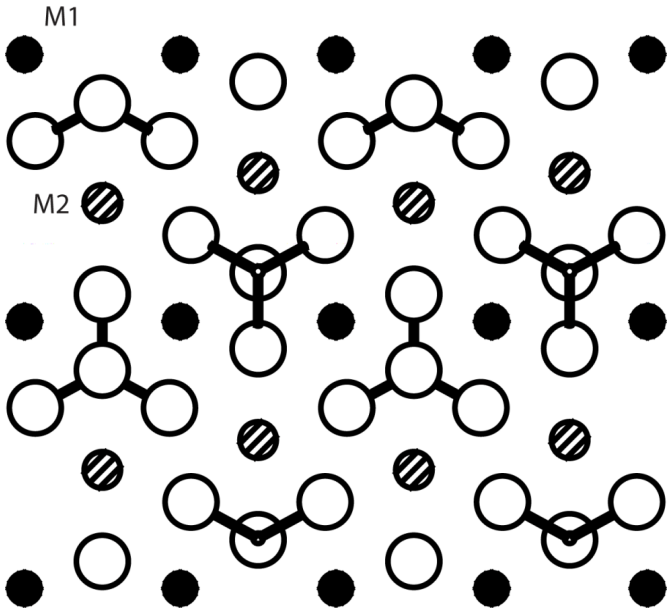

Figure 1-8: Idealized forsterite structure projected on (100) plane (Redrawn from Deer *et al.*, 1997). Si atoms are at the centre of the tetrahedrons. *Small black circle*, Si; larger *gray circle*, oxygen; *black circle*, M1; *diagonally hatched circle*, M2

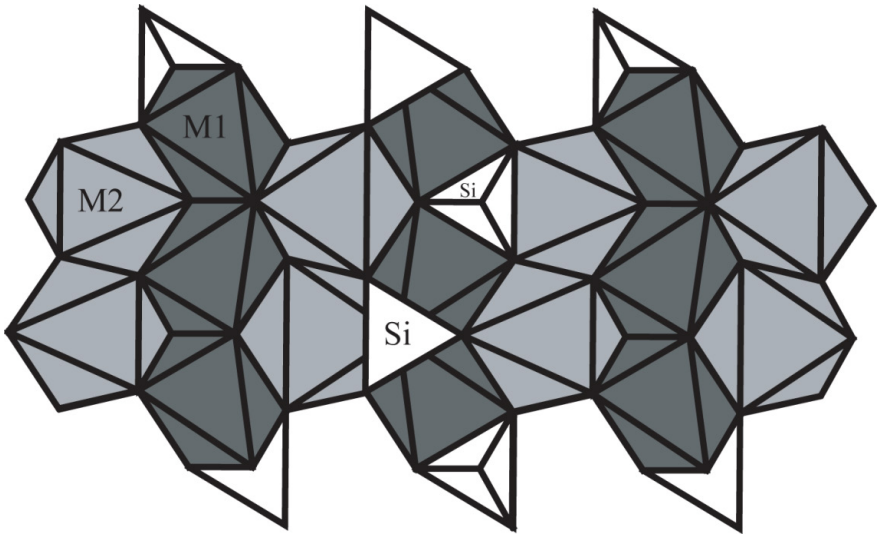

Figure 1-9: Forsterite structure perpendicular to (100) showing the approximately hexagonal close-packing structure (redrawn from Deer *et al.*, 1997)

1.6 Aim of the thesis

Principal goal of this PhD work is to determine the origin of changes in the dominant slip systems at high pressure and high temperature environment prevalent in the upper mantle. For this purpose, we plan to conduct simple shear deformation experiments on San Carlos olivine and Peridotite modal composition, using Deformation-DIA. Experiments are designed to delineate the influences of pressure, temperature, strain rate and H_2O content on slip systems in olivine.

At the initial stages of this PhD work, a new high pressure assembly will be designed which should allow us to reliable conduct deformation experiments at pressures above 8 GPa under high temperature conditions.

Deformed specimens are to be analyzed using a variety of analytical tools that includes SEM & EBSD, TEM, FTIR and NMR.

1. Effect of stress and pressure on slip systems in olivine

   A range of experiments has been conducted at various pressure and temperatures to explore the effect of stress on the slip systems in olivine. In this way, we also ascertained the role played by pressure on changes in olivine slip systems. Pressure has been varied between 3 to 8.5 GPa at temperatures between 1300 to 1500°C.

   Determination of stress in the sample, for some experiments, has been performed *Ex-Situ* using dislocation densities obtained by Transmission electron microscopy. Alternatively, stresses have also been measured using recrystallized grain size data obtained by EBSD technique and comparing them with known recrystallized grain size versus stress calibration. TEM studies were also be employed for detailed study of dislocation microstructure.

2. Effect of water on slip systems in olivine

   A similar range of experiments have been performed on “wet” olivine specimens to determine the effect of H_2O on slip systems in olivine. Water content of the hydrous specimens has been analyzed using FTIR spectroscopy. Some of these

specimens have also been studied by TEM to understand the role of water on dislocations.

3. Olivine is the most voluminous phase in the upper mantle rocks. Other important mineral phases in the upper mantle are Pyroxenes, Spinel and Garnet. Deformation studies have been performed on Peridotite modal composition, which represents the upper mantle rock composition, to understand the role of other mineral phases e.g. pyroxenes on the overall fabric development in a upper mantle.
4. Stress is the most crucial parameter in a controlled deformation experiment. Yet, it is one of the most poorly constrained. *In-situ* measurement of stress, in most cases, is either performed using externally (external to the pressure cell) placed load cell or using x-ray radiography. The former method often gives a measured value of stress that can be far off from the actual value experienced by the sample material. This difference is caused by the frictional forces active throughout the pressure cell. Other method of stress measurement using the x-ray radiography relies upon synchrotron based radiation source. This approach is not suitable for day-to-day use in a standard laboratory environment. Therefore, attempt has been made to develop a stress sensor based upon piezoelectric property of $GaPO_4$ crystal. Once this technique has fully developed, it should provide us a mean to make *in-situ* stress measurements.

2 Methodology

2.1 Deformation experiments under extreme conditions

Many types of equipment have been used to deform mineral assemblages at ambient and high pressure and temperature conditions. For many years the gas media Paterson rig and the Griggs apparatus were the main devices used to deform samples but could only be employed at conditions equivalent to the crust and very shallow mantle (see table 1). However the need to investigate rheological properties at higher pressures resulted in initial attempts using the 6-8 Kawai-type multianvil, DIA and diamond anvil cell [*Karato,* 2008a]. These devices were not designed for applying controlled deformation at high pressure but they could expose samples to high deviatoric stresses as a result of anisotropic compression. In the diamond cell this occurs quite normally when a poorly hydrostatic pressure medium is employed, while in multianvil devices deviatoric stresses can be applied by placing harder materials in the sample column direction compared to the perpendicular direction. In these devices high deviatoric stresses then develop during compression. Once high pressures are reached the application of temperature softens the pressure medium and the stresses relax.

The need to provide a better control over the sample deformation environment, however, lead to the development of new high pressure deformation devices such as the Rotational Drickamer device (Karato, 2008) and the deformation DIA apparatus. In order to study the development of Crystallographic preferred orientation (CPO) of mineral assemblages at mantle conditions, deformation experiments must be able to satisfy the criterion given below:

1. The method must provide the ability to generate and maintain extreme states of pressure (for upper mantle 1-14 GPa) and temperature (above 1000-1600°C) conditions prevalent in the earth's mantle, for time durations that allow fabrics to develop at suitable strain rates (1-48 hours).

2. Such a method should also provide *control* over strain rate (or stress) which is essential for any meaningful understanding of the fabric development.
3. The ability to *measure* strain rate and stress.
4. Provide control over chemical environment e.g. water and oxygen fugacity is also required.
5. Allow recovery of the sample for fabric and textural analysis. And,
6. Ensure that the sample does not deform during compression and decompression phase of the experiment.

2.1.1 High pressure deformation apparatus

Understanding the role of deviatoric stress (and several other physical & chemical parameters) on the development of texture in material is a prerequisite to the understanding of anisotropic behaviour of minerals. Material scientists also use such studies for establishing relations between various manufacturing processes and the mechanical performance of the product material. The immense scope of such studies has led to the development of a series of high pressures apparatuses with each having a unique set of advantages and drawbacks.

Simple dead weight loading experiments are an effective way to perform precise deformation experiments under ambient pressure condition [*Carter et al.,* 1980] whereas at the other extreme of pressure diamond-anvil cells can be used to deformed materials up to 200 GPa pressure but with poor control over strain rate and stress distribution [*Kinsland and Bassett,* 1977]. At intermediate pressures, a range of devices exist which all tend towards a compromise in terms of maximum pressure and the control over deformation and sample environment. Some salient features of various deformation apparatus are given below in the table 2-1. For experiments to address olivine fabric development pressures of between 1-15 GPa are required. Though, the 6-8 multianvil configurations can achieve these pressures, only stress relaxation experiments can be performed and no control over strain rate is possible [*Bussod et al.,* 1993; *Karato and Rubie,* 1997]. The Rotational Drickamer device (e.g. [*Yamazaki and Karato,* 2001] can provide control of strain rate over the pressures of interest, however, it is very limited in sample size and control over

pressure and temperature is limited accept when used in conjunction with in situ X-rays. Consequently the deformation-DIA appears to embody a suitable compromise between allowing control over strain rate, pressure and temperature and also achieving a range of pressure of interest to the study of olivine fabric development in the upper mantle.

Table 2-1: List of deformation devices and properties (Modified after Karato 2008)

Type of apparatus	**Max. P (GPa)**	**Max. T(K)**	***In-situ* Stress measurement**	**Comment**
Dead-weight creep apparatus	10^{-4}	2000	From applied load	Low fH_2O
Gas-medium apparatus (e.g. Paterson rig)	0.5	1600	Internal load cell	Limited fH_2O
Griggs-type apparatus	3	1600	External load cell	Limited strain
Deformation-DIA	23	1700	X-ray diffraction	Limited strain
Rotational Drickamer apparatus	18	2000	X-ray diffraction	Unlimited strain
6-8 Multianvil stress-relaxation	23	2000	X-ray diffraction	Non-steady state, relaxation experiments only
Diamond anvil	200	1000	X-ray diffraction	Non-steady state, very high stress, Study of LPO difficult due to small sample size
6- ram cubic press	25	2000	X-ray diffraction	Limited strain

Deformation-DIA

The Deformation-DIA (or D-DIA) is a modified form of DIA cubic-anvil apparatus [*Osugi et al.,* 1964]. The D-DIA incorporates two additional hydraulic actuators; here referred to as differential rams, which provide independent control of the displacement of two vertically opposing anvils [*Wang et al.,* 2003]. The original DIA consists of upper and lower guide blocks, four wedge-shaped side wedges, and six tungsten carbide anvils. The six anvils of the D-DIA define a cubic volume due to their square shaped truncation. Four out of six anvils are attached to the side wedges whereas one each of the other two anvils is mounted to the upper and lower guide blocks.

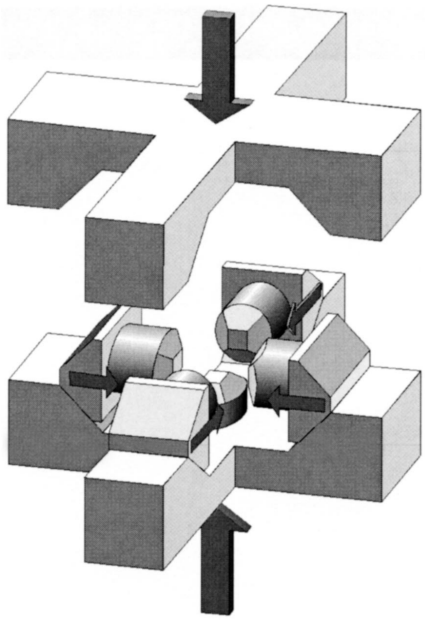

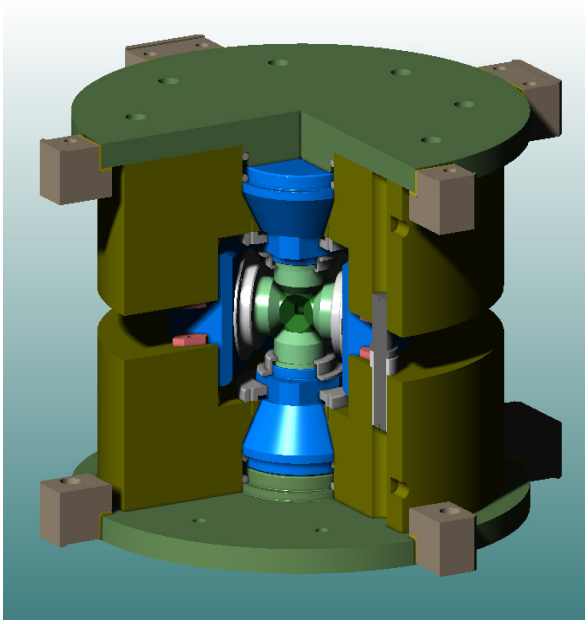

Original DIA **Deformation DIA**

Figure 2-1: Schematic diagrams of original DIA and Deformation-DIA. A) Original DIA consists of upper and lower guide blocks, four wedge shape side wedges and six tungsten carbide anvils. B) A deformation-DIA has two additional hydraulic actuators called deformation rams which provides a mean to achieve controlled deformation. (source: Y. Wang)

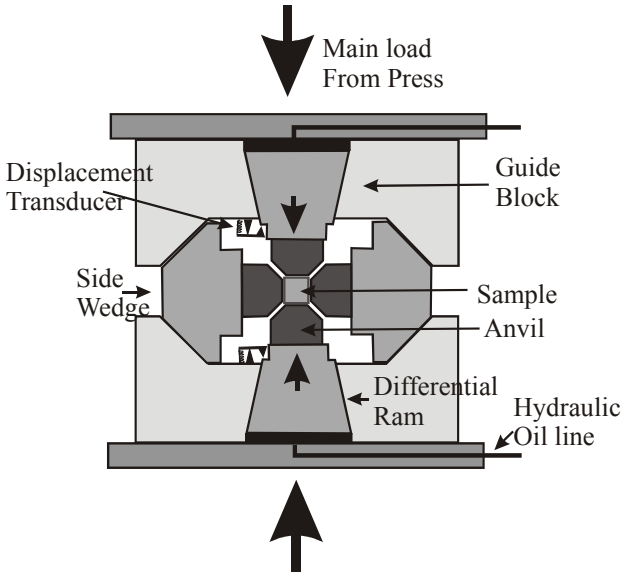

Figure 2-2: A vertical cross-section of D-DIA showing the two side wedges and the differential ram. Presence of differential rams provides controlled deformation of the cubic sample at a constant pressure.

As the main guide block of the DIA is compressed the vertically opposing anvils are advanced. The 45° surfaces of the side wedges, however, ensure that a component of the vertical displacement is converted to a horizontal displacement which advances the 4 horizontal anvils. Once high pressure has been achieved through the advancement of the main ram, the vertical differential rams can be advanced thus applying a principle stress on the cubic sample assembly.

D-DIA's unique design provides a way to advance the differential rams into the sample assembly without raising the confining pressure in the process. A typical experimental run in the D-DIA is illustrated below in Figure 2-2. One starts by hydrostatically compressing the sample assembly, with differential rams fully withdrawn to maintain the oil pressure in the main ram at a constant value. The action of the guide block transfers the vertical compressional force into horizontal compression via the side wedges. Then the sample is heated up to the requisite temperature and kept in this state for approximately 30 min, with a view to achieve thermal equilibrium. Then the differential rams are advanced so as to bring a non-cubic shape change to the assembly while simultaneously withdrawing the main ram at an appropriate rate. This ensures that total force exerted by the main ram stays constant and hence the volume of the sample assembly is also conserved (Wang et al., 2003).

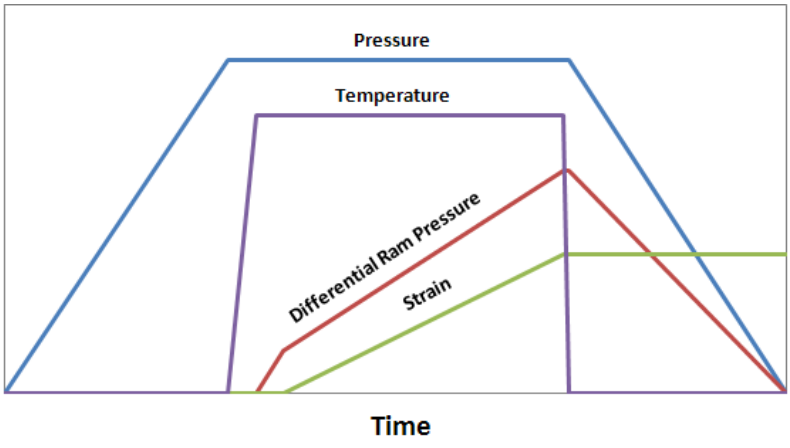

Figure 2-3: Pressure-Temperature-Strain profile of typical experimental run in D-DIA press. After compressing the pressure cell to the requisite pressure, sample is heated up to the desired temperature and it is allowed to heat for at least 30 min to release the initial stress build-up, if any present in the sample. Then, the sample is deformed at a constant strain rate. Once the target amount of strain is achieved, deformation is stopped and the sample is quenched right after that. Thereafter the pressure is released slowly.

The onset of movement of the differential rams occurs only when the differential ram pressure is sufficient enough to overcome the confining force and the friction. Hence, the higher the confining pressure, higher is the initial differential ram pressure required to move the differential rams. This imposes a limit to the maximum confining pressure at which deformation can be achieved without breaking the anvils. Using the 500 tonne Voggenreiter D-DIA press available at the Bayerisches Geoinstitut with 4 mm square truncations tungsten carbide (WC) anvils, it is possible to perform deformation experiments up to 10 GPa confining pressure, at temperatures as high as 1500°C.

The displacement of the two differential anvils is measured relative to the guide block using displacement transducers. The transducers employ a magnetic response to measure displacement to a precision of 0.2 μm.

Sample assembly design

As stated earlier, in the D-DIA a wide range of pressure and temperature conditions can be achieved (up to 10 GPa and 1700°C). In order to access higher pressures the truncation size on the tungsten carbide anvils can be reduced, however, this also reduces the sample size as the dimensions of the cubic pressure assembly must also be reduced. For the work performed in this thesis two assembly configurations were developed. The 6/8 assembly employs 6 mm edge length square faceted tungsten carbide anvil truncations with a cubic sample assembly that is 8 mm in edge length. It was used to achieve pressures up to 3.5 GPa. The 4/6 assembly, used between 3.5 and 10 GPa, employs 4 mm anvil truncations and a 6 mm edge length cube.

The experimental set-up for deformation experiments consists of a cubic pressure medium composed of fired or unfired pyrophyllite. The cube is drilled out along one axis for the insertion of a furnace separated by a thermally insulating sleeve. The resistive materials graphite and rhenium are used as furnaces, while zirconia is used as a thermally insulating sleeve around the furnace to make the experimental set-up thermally efficient. A number of attempts were made to employ lanthanum chromite as a furnace material,

however, it was found to be prone to mechanical damage and subsequent thermal instability during deformation.

Gaskets form during the experiment as material from the pressure assembly is squeezed between the anvils. For fired pyrophyllite cubes this action is less efficient due to the use of stiffer material. This may help the attainment of higher pressures however it also leads to more blow outs due to the more brittle nature of the gaskets formed. For this reason the 4/6 assembly design employs preformed gaskets of Teflon, which are attached to the anvils using glue prior to the experiment.

The sample material is sandwiched between cylindrical pistons of alumina cut at 45° (Fig 2-4). A softer crushable alumina is also required to absorb the initial shortening of the sample assembly during hydrostatic compression. During compression the entire assembly is shortened. In order that the sample is not deformed in the process, crushable alumina is added to the sample column to accommodate this compressional strain. During deformation, the majority of the sample column needs to be comprised of fully dense alumina such that the sample is the weakest material. However, the proportion of crushable and dense alumina in the sample column needs to be carefully adjusted by trial and error experiments such that minimal sample deformation occurs during compression. Determining this ratio between crushable and dense alumina in the sample column is one of the most important factors when developing a D-DIA assembly.

Alumina pistons can either be cut at 45° to the axis of the cylindrical rod or at 90° to it. The first kind of pistons are used in performing simple shear deformation experiment, whereas pistons cut at right angle to the axis of cylinder are used for plane-strain compression (pure shear) deformation experiments.

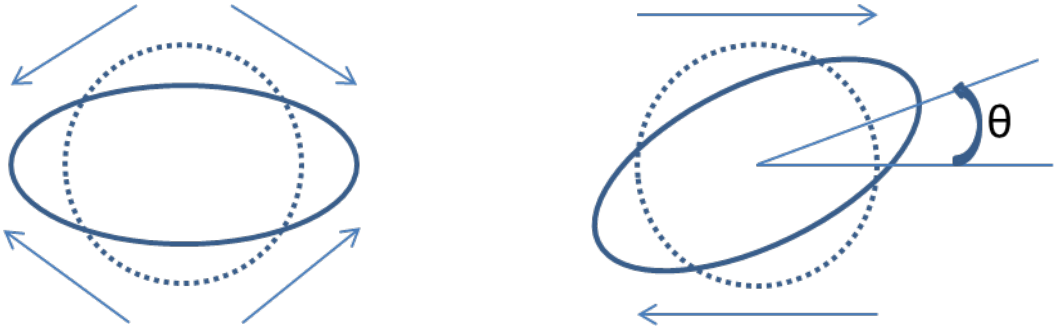

Plane-strain compression (Pure shear) Simple Shear

Figure 2-4: Cartoon comparing deformation by pure shear and simple shear

The shape of the finite strain ellipsoid may be the same at the end of deformation in the case of both, pure and simple shear but in the case of simple shear deformation; the finite strain ellipsoid is inclined at some angle to the shear. It has direct implication on the representation of CPO using pole figures. For pure shear case, one should expect an orthorhombic pole figure, whereas simple shear leads to monoclinic or triclinic pole figures. More importantly, it's easier to obtain larger strain using simple shear configuration ($\gamma > 1$), whereas strain due to pure shear is generally limited to 30-40%, in the best of cases. Apart from that, dominant deformation regimes in the upper mantle are either simple shear or plane combinations of simple and pure shear [*Tommasi et al.,* 1999]. In this thesis shear deformation experiments were performed in order to maximize strain and fabric development.

Demerits of the Deformation-DIA

The D-DIA has been an important step forward towards conducting deformation experiment at pressures in excess of 3GPa. However, as outlined below, there are some limitations to the amount of achievable strain and accurate measurement of strain rate and stress.

D-DIA allows the user to control the rate and amount of advancement of the differential rams and hence the deformation anvil. If the softest material in the assembly happens to be the sample being deformed, then it is safe to assume that deformation caused by the

advancing anvils has been absorbed by the sample. In such a scenario, it is very easy to quantify the bulk strain rate of the sample along with the strain experienced by it. However, due to the fact that some amount of the deformation is always lost in the elastic and plastic deformation of the materials surrounding the sample, the aforementioned assumption is not always valid. The way to minimize this inefficiency in transferring strain is by insuring that the parts surrounding the sample e.g. pistons, thermocouple tube, furnace and insulating materials (for instance, zirconia) have considerably higher strength than the sample. On the other hand, total strain experienced by the sample can also be characterized using a strain marker. Though, the presence of a strain marker cannot insure that externally applied strain rate, measured as the rate of deformation ram advancement, is the same as that being experienced by the sample.

The total amount of strain that can be applied to the sample is always limited by the strength of the materials surrounding the sample. In case of a non-porous sample, deformation can only be achieved if the surrounding material gives way to the sample and the piston, as the volume needs to be conserved. In case of simple shear, owing to the excessive shearing force at the tip of the wedge shaped pistons the alumina pistons fail after a certain point (shear strain = 2). It is also noteworthy that the amount of the sample that stays sandwiched between the wedge-shaped pistons decreases with increasing amount of strain. Due to the geometrical constraints imposed by the anvils which are cut at 45°, such limitations are only important for the case of simple shear deformation experiments. Referring to the orientation contrast image of the sample DD407 (Fig. 2-5), one can see the effect of large shearing stress causing the alumina pistons to fail at along the maximum shear stress direction. Evidence of necking and breaking in the assembly can also be seen.

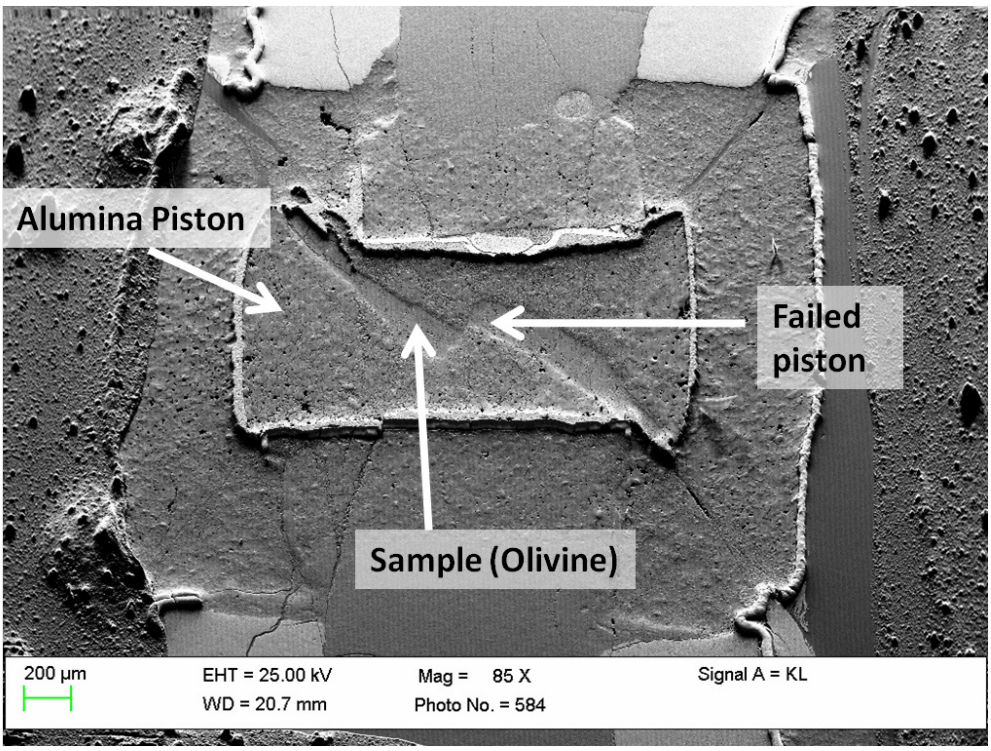

Figure 2-5: orientation contrast image of an excessively deformed sample at 8GPa (Sample No. DD407). Alumina pistons have failed, owing to the large shearing stress active on the wedge shaped alumina pistons. The applied shear strain was more than 200%.

D-DIA coupled with a synchrotron radiation source provides a direct way to measure the microscopic stresses that are active in the sample. In the absence of such a facility, user needs to apply indirect ways to estimate stress (e.g. measuring dislocation density using oxidation-coloration method and TEM). Such off-situ approaches discount the possibility of studying flow laws of materials which cannot be performed without continuous measurement of strain rate and stress.

8/6 mm Assembly description

The 8/6mm assembly consists of a cubic unfired pyrophyllite pressure cell drilled to contain a graphite furnace surrounded by a zirconia sleeve. The sample slice, along with the alumina pistons, is jacketed using Pt-foil (25 micron thick) and inserted into the furnace in an MgO sleeve (Fig. 2-6).

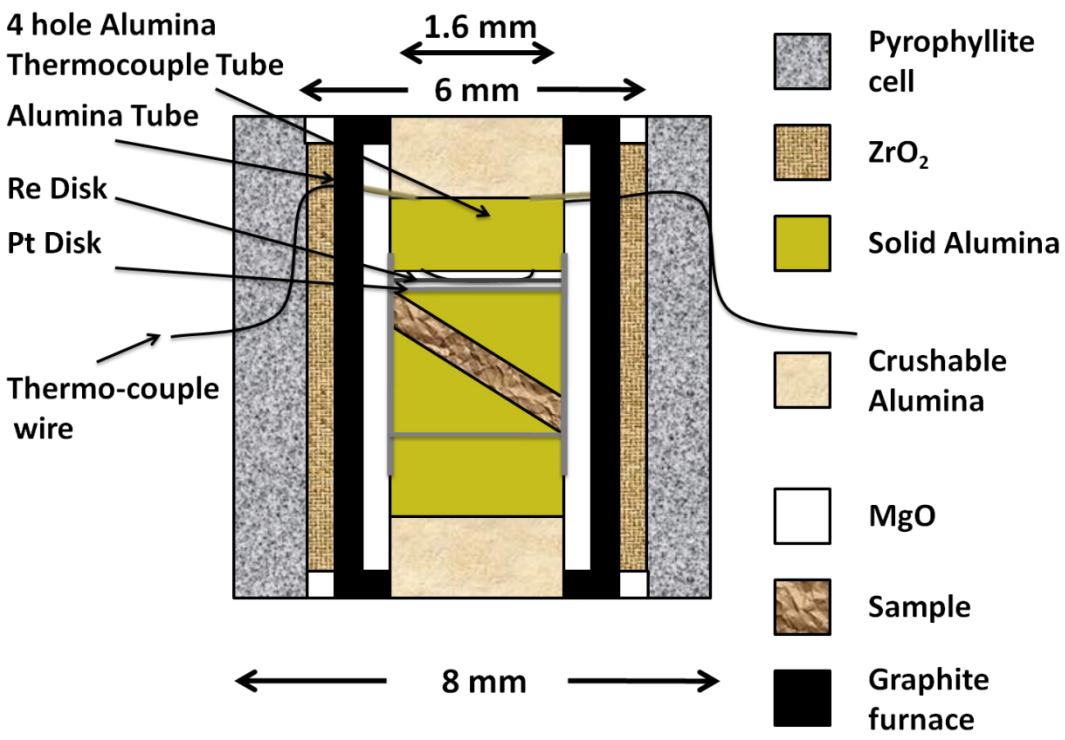

Figure 2-6: Schematic diagram of an 8/6 mm D-Dia assembly.

A suitable length of 4-hole alumina tube and crushable alumina plugs are inserted above and below the pistons to minimize the deformation during hydrostatic compression phase of experiment. Crushable and fully dense alumina is therefore distributed symmetrically about the central piston assemblage. The assembly is self-gasketing.

4/6mm Assembly description

The 4/6 assembly was developed to performed experiments in simple shear configuration up to a confining pressure of 8 GPa and 1500°C. The assembly consists of a pyrophyllite pressure cell, fired at 1000°C for 5 hours. Firing makes the assembly mechanically strong and it helps generate much higher pressure than a similar sized unfired pyrophyllite pressure cell. One important difference between the 6/8 and 4/6 assembly is the use of a rhenium metal foil furnace (25 μm thick). A foil furnace was found to be more stable than graphite at high pressure during deformation, most likely due to it being more malleable.

In the 4/6 design the sample column above and below the piston-set comprises dense and crushable alumina as shown in figure 2-7. The length ratio of crushable and dense alumina cylinders has been carefully optimized to minimize the deformation of sample during cold compression. The lengths of the dense alumina thermocouple tube and solid cylinder below the lower alumina piston are identical (in this case 0.5 mm), as are the crushable alumina cylinders above and below the pistons (1.7 mm). This ensures a symmetric configuration in the assembly, so that during deformation the sample material remains in the centre of the furnace hot-spot. Pre formed Teflon gaskets are attached to the anvils for the 4/6 assembly. 12 such gaskets, each 1.5 mm wide are glued to the 12 pairs of anvil faces.

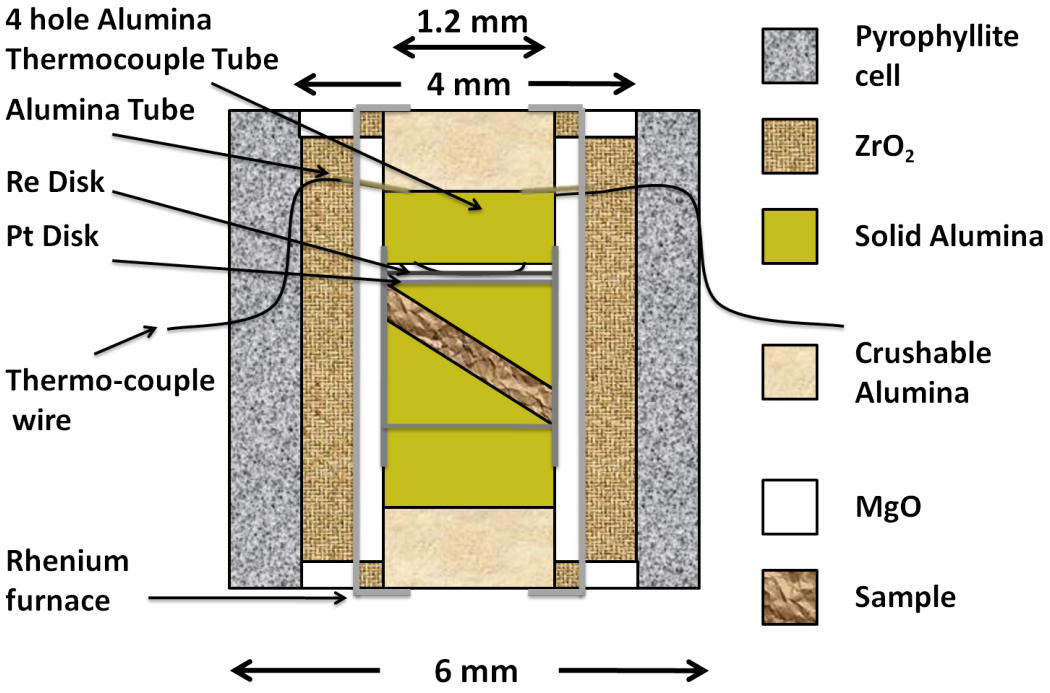

Figure 2-7 : A schematic diagram of a 4/6 mm D-DIA assembly showing its major components

Pressure and temperature calibration of the Sample assembly

Pressure calibration at room temperature

The sample pressure must be calibrated in each D-DIA assembly against the oil pressure using phase transitions that occur at well-determined pressures. Initially room temperature calibrations were employed to identify the approximate pressure range for further high temperature calibrations and to define the gradient of the pressure calibration.

Bismuth undergoes phase transitions at 2.54 GPa (Bi I-II), 2.7 GPA (Bi II-III) and 7.7 GPa (Bi III-IV) which causes a change in the resistivity of bismuth [Getting, 1998; Lloyd, 1971], whereas the resistivity of Manganin wire (Cu86/Mn12/Ni2) changes linearly with pressure. In order to calibrate the pressure achievable with the 6 mm pyrophyllite pressure cell, a thin wire of Bismuth $20\ \mu m\ x\ 0.5\ mm\ x\ 1\ mm$ was placed between two AgCl disks as shown in Fig 2-8. Thin copper foils which served the purpose of electrode, were placed at the two ends of the Bismuth wire. A constant current was supplied through the bismuth wire and the voltage across the Cu-electrodes was measured during the compression.

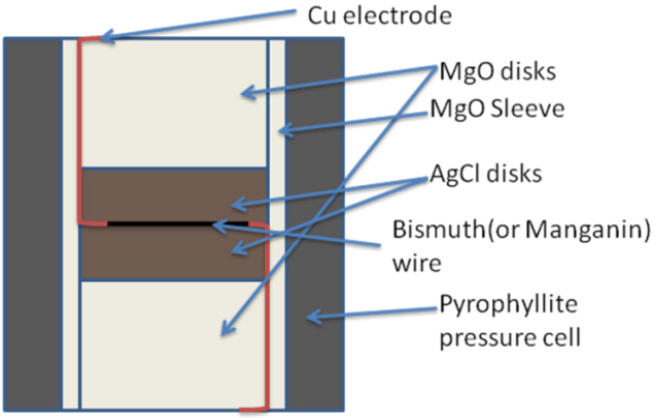

Figure 2-8: Schematic of assembly used for pressure calibration using Bismuth and Manganin

Bi I-II transition was observed at around 17 bar oil pressure. For obtaining the pressure-resistivity relationship of Manganin, the same setup was used but with Manganin wire $(10\ \mu m\ radius\ and\ 1mm\ long)$ replacing the Bismuth wire. The change in Manganin resistivity with the confining pressure can be expressed as the pressure coefficient of the resistance change given by $\left({}^{\delta R}/_{R_0}\right)\left({}^{1}/_{P}\right) = (2.322 \pm 0.008) \times 10^{-2}\ GPa^{-1}$ where δR is the change in resistance and R is the resistance at any given pressure P measured in GPa (*Robert J. Zeto and H. B. Vanfleet*). The pressure dependence of resistivity must be

calibrated using a known pressure point, for which we used the Bi I-II transition. As shown in Fig 2-8 the pressure at room temperature determined using Manganin wire reaches a plateau just over 7 GPa, consistent with the observation that we were unable to observe the Bi III-IV transition at 7.7 GPa. This plateau is typical of most multianvil assemblies and results from the gasket supporting an ever-increasing proportion of the load.

Figure 2-9 shows that data from calibration experiments at room temperature and 1000°C. The assembly is more efficient at generating pressure at 1000°C than at room temperature as shown by the Coesite/Stishovite transition, which occurs at approximately 110 bars oil pressure (78.6 tonnes of applied load).

Pressure calibration at high temperature

Phase transition in quartz to its high pressure polymorphs, coesite and stishovite, is pressure and temperature dependent. At 1000°C, quartz transforms to coesite at ~ 2.95 GPa; whereas the coesite to stishovite transition pressure at 1000°C is at ~9.25 GPa (Akaogi & Navrotsky, 1984).

A fine grained mixture of fibrous quartz was placed in the standard assembly (but in pure shear configuration). The sample assembly was brought up to the requisite pressure and then it heated at 1000°C for ~5 hours. After quenching and decompression, the end product was sectioned and polished and analyzed using Raman spectroscopy to identify the SiO_2 polymorph in the run products.

Table 2-2: List of experiments and the end products - Calibration of cell pressure at 1000°C using phase transition in Quartz

Experiment Run	Oil pressure(bars)	Observation
DD451	17.1	Quartz
DD452	19.6	Quartz and Coesite coexist
DD387	78.6	Coesite
DD400	85.7	Stishovite

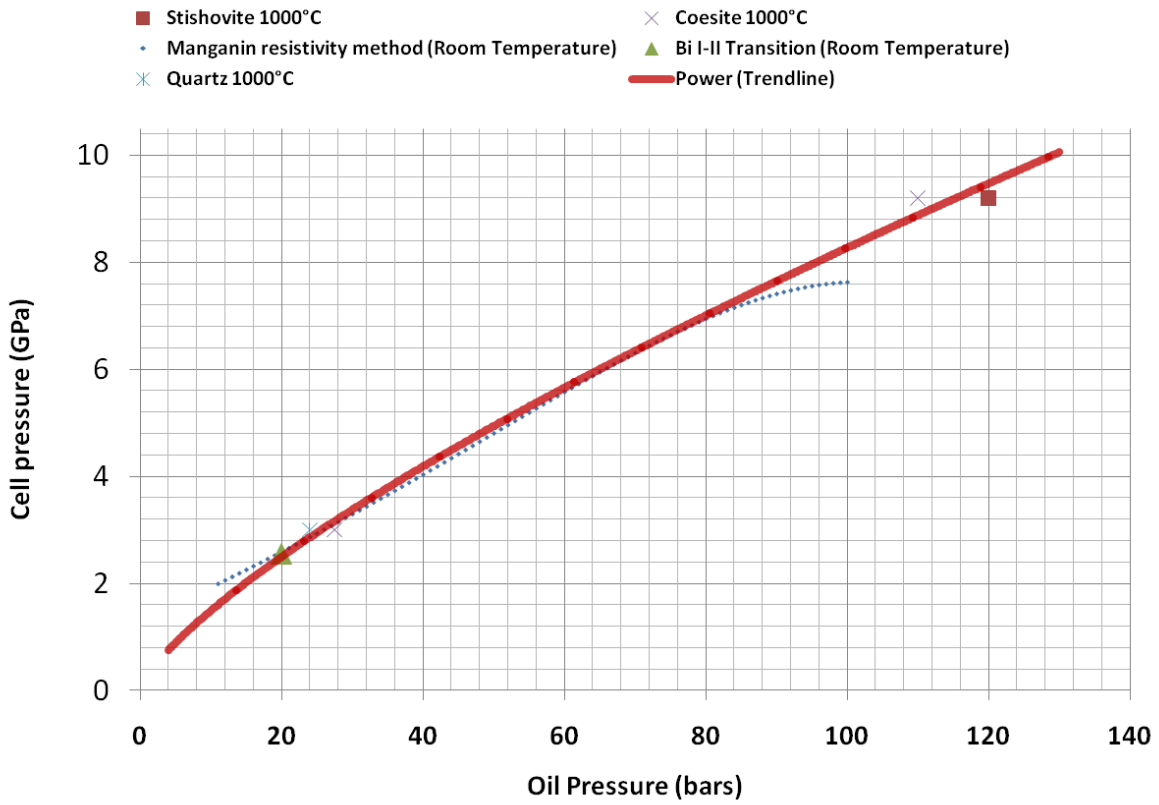

Figure 2-9: Calibrated cell pressure has been plotted as a function of oil pressure. Room temperature calibration has been done by using phase transitions in Bismuth and Manganin resistivity method. High temperature (1000°C) pressure calibration was done using phase transition in Quartz (quartz→coesite and coesite→stishovite). 700 bar oil pressure is equivalent to 500 tonne load for D-DIA press at BGI.

Temperature calibration of the sample assembly

The sample temperature distribution within the 4/6 deformation cell assembly was measured using a two-pyroxene thermometer assemblage, employing the calibration of Nickel & Brey, (1984). An equimolar powdered mixture of Al-free enstatite and diopside were placed between the alumina deformation pistons at 45° to the axial direction. 4 wt% PbO was added to the sample as a flux. The sample powder was compacted before the second deformation piston was placed on top, but the sample was not hot pressed. The experiment was heated at 1300°C (thermo-couple temperature) and 8 GPa pressure for approx. 6 hrs. No deformation was applied. Chemical compositions of fully reacted neighbouring pairs of enstatite and diopside grains were measured using a JEOL JXA – 8200 electron microprobe at BGI.

The recovered sample slice was approximately 200 μm thick in the axial direction. The calibration employs the distribution of Ca and Mg between the two-pyroxene minerals. The determined mean temperature in the central portion of the sample slice was approximately 150°C higher than the temperature measured at the thermocouple. The difference between the mean temperature at the middle of the sample and at the extreme points of the sample was found to be ~75°C (Fig 2-10). This results in a temperature gradient of 84° C/mm along the sample length. The variation in temperature likely reflects the thermal gradient along the furnace; with the centre of the sample, therefore, placed will in the hottest part of the furnace, while the thermocouple and sample extremities next to the furnace are slightly out of the hot spot.

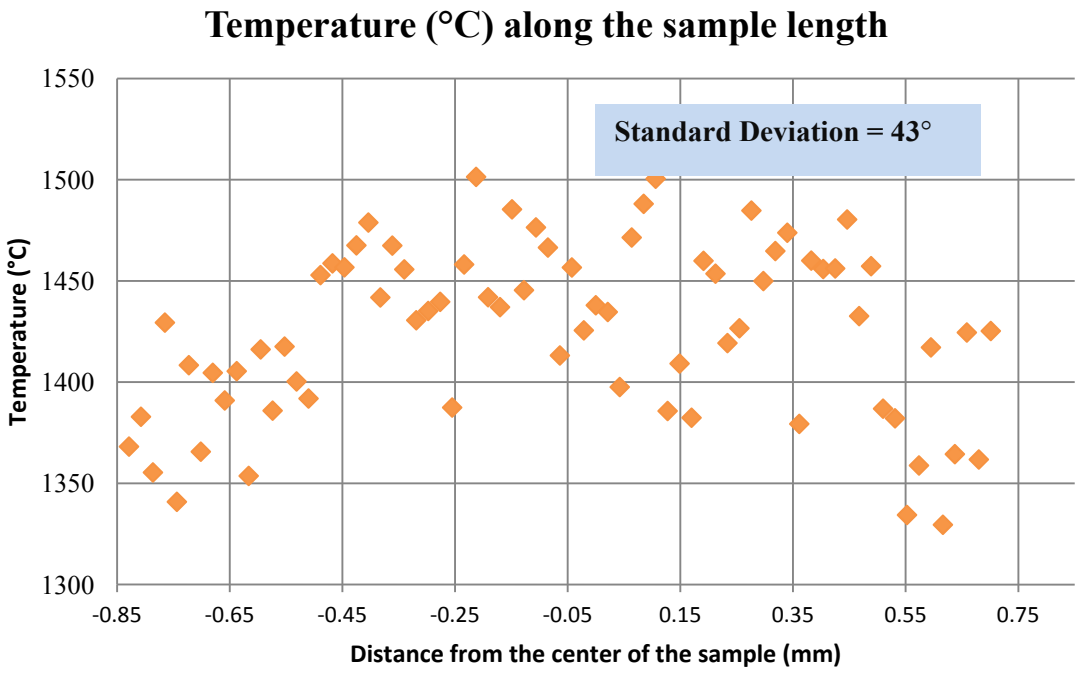

Figure 2-10: Measured temperature along the sample length. Center of the sample recorded the highest temperature with approx. 85°C/mm temperature gradient as we move towards the extremities.

Oxygen fugacity of the experiments

The oxygen fugacity is an important parameter in deformation experiments as it controls the concentration and mobility of point defects in Fe-bearing minerals [*Demouchy and Mackwell,* 2006; *Kohlstedt and Mackwell,* 1998]. The oxygen fugacity is not controlled

in D-DIA experiments but it is influenced by the type of furnace employed and by the nature of the starting material. The use of graphite or metal furnaces generally leads to more reducing conditions because the furnaces can only be oxidized during the experiment and has no mechanism to release oxygen or oxidized species. The oxygen fugacity can be measured in the experiment however particularly in the region of the Pt capsule or Pt strain markers where the proportion of Fe alloying with the Pt can be measured.

$$Fe2SiO4 = FeSiO3 + Fe + O2$$

$$Olivine \quad enstatite \quad Alloy$$

The equilibrium can be used to determine the oxygen fugacity from the thermodynamic relationship

$$\log fo_2 = \frac{-\Delta G^o}{\ln(10)RT} + \log a^{olivine}_{Fe_2SiO_4} - \log a^{orthopyroxene}_{FeSiO_3} - 2\log a^{metal}_{Fe}$$

Where, $a^{olivine}_{Fe_2SiO_4}$, a^{metal}_{Fe} and $a^{orthopyroxene}_{FeSiO3}$ are the activities of the Fe_2SiO_4 component in olivine, Fe in the Pt-Fe alloy and $FeSiO_3$ in pyroxene respectively. ΔG^0 is the free energy of the end-member equilibrium, which was taken from thermodynamic data reported by [*Stagno et al.,* 2011]Stagno and Frost (2011). In some deformation experiments where pyroxene was observed and the Fe content of Pt foil or strain marker was measured it was possible to calculate the oxygen fugacity in the experiment. For this activity composition relations for Fe in Pt alloy were required, which were taken from Mann et al. (submitted). The determined oxygen fugacity at 8 GPa and 1500°C was -0.8±0.5 log units or approximately at the fayalite-magnetite-quartz (QFM) oxygen buffer. This value is within the range found for mantle rocks, although it may be considered slightly more oxidised than many samples from the deep mantle, >100 km, which are in general closer to QFM –2 [*Frost and Mccammon,* 2008].

2.2 Sample Preparation

2.2.1 Hot pressing San Carlos olivine

A fine grained powder of $(Mg_{0.9}, Fe_{0.1})_2SiO_4$ San Carlos olivine with grain size below 10 μm was loaded into a 12 mm long and 5 mm outer Diameter cylindrical Platinum capsule. Using ¾" Talc-Pyrex glass assembly and 200t piston cylinder press at Bayerisches Geoinstitut, the assembly was cold pressed to 10kb confining pressure. Thereafter it was heated to a temperature of 1100°C and kept as such for 30 min. Then the assembly was slowly decompressed over 12 $hours$ period along with simultaneously cooling to room temperature. Slow decompression with simultaneous cooling was performed in order to avoid decompression cracks.

Hydrous olivine samples were prepared by adding an equimolar mixture of Brucite and Silica to the powdered olivine and then hotpressed in the 6-8 multianvil device. In some instance, Brucite-Silica aggregate was added to the pre-hotpressed samples while assembling process before the experiment.

2.2.2 Placing platinum Shear strain marker

After hot pressing the sintered samples were carefully removed from the high-pressure assembly and the top and bottom of the capsule removed. 1.2mm diameter cylindrical cores were prepared from these samples in the thin section laboratory by H. Schulze. Using a diamond wire saw, 200μm thick elliptical slices of hot pressed olivine sample were then cut from the core each of which were oriented at 45° to the core axis. Each olivine slice was then cut into two symmetrical halves, with the direction of cutting oriented parallel to the original cylindrical core (Fig 2-11). The exposed surfaces of this cut were then sputter coated with a ~100nm Pt layer. Putting a Pt marker in this way, on a cross-section cut parallel to the cylindrical axis minimizes the marker rotation due to axial compression of the sample.

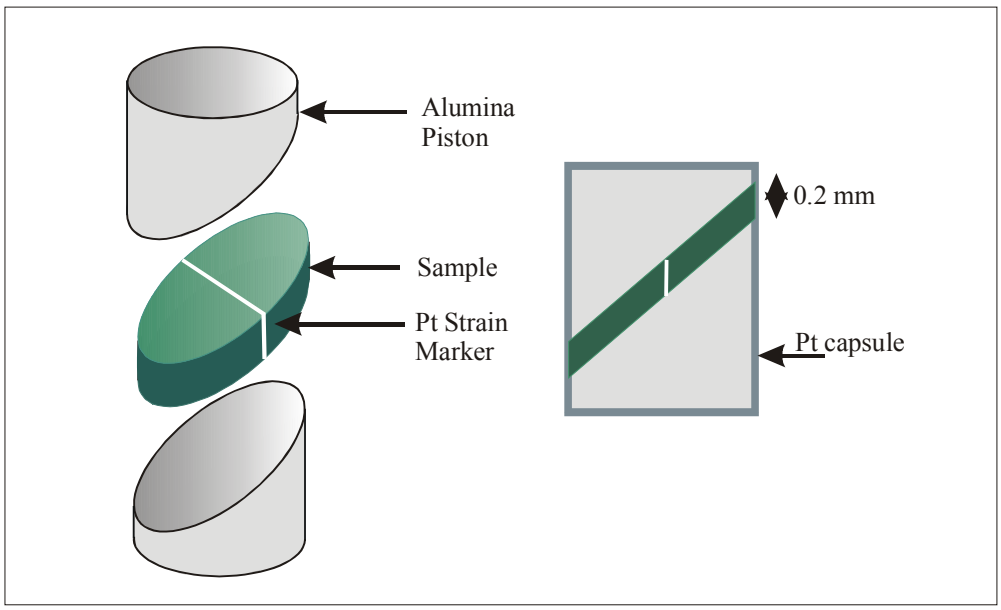

Figure 2-11: Emplacement of platinum strain marker for shear strain measurement. Approximately 100 nm thick Platinum-layer is sputter coated on the sides of the two cut halves of the hotpressed sample. Rotation of the strain marker is directly related to the shear strain

2.3 Analytical Methods

As the central theme of this thesis has been to study of the effects of physical and chemical parameters on the crystallographic preferred orientation of olivine, *electron backscatter diffractometer (EBSD)* has been the primary analysis technique. It is also crucial however to relate the determined CPO, or lack thereof, to the underlying deformation mechanism and active slip system in the crystal and for this purpose *Transmission electron microscope (TEM)* has been a vital analysis technique.

Water content in the starting sample and the recovered sample has been measured using *Fourier Transform Infrared (FTIR) spectroscopy*. A brief introduction to these three important instruments is provided in the next paragraphs.

The *Electron probe micro-analyzer (EPMA)* was used for analyzing the chemical composition of recovered samples and to examine the equilibrium distribution of Ca and Mg between enstatite and diopside aggregates employed in experiments to calibrate the temperature in the pressure cell. *Raman spectroscopy* has also been utilized for phase

identification in the run products from experiments performed to calibrate cell pressure using quartz-coesite and coesite-stishovite phase transformations.

2.3.1 Measurement of crystallographic preferred orientation using Electron backscatter diffraction technique (EBSD)

Electron backscattered diffraction (EBSD); sometimes also referred to as backscatter Kikuchi diffraction (BKD) is a technological add-on to a scanning electron microscope. It provides an SEM with a microstructural-crystallographic analysis capability. Primarily, EBSD is used to study texture or preferred orientation of any crystalline or polycrystalline material. This is achieved by indexing and identifying the crystal systems. Apart from structure and orientation information, EBSPs (Electron back scatter patterns; See figure No. 2-12 for an example of such a pattern in mineral olivine) contain additional information on crystal lattice perfection, local strain, deformation, and grain boundaries.

Traditionally these types of studies have been carried out using x-ray diffraction (XRD), neutron diffraction and/or electron diffraction in a TEM.

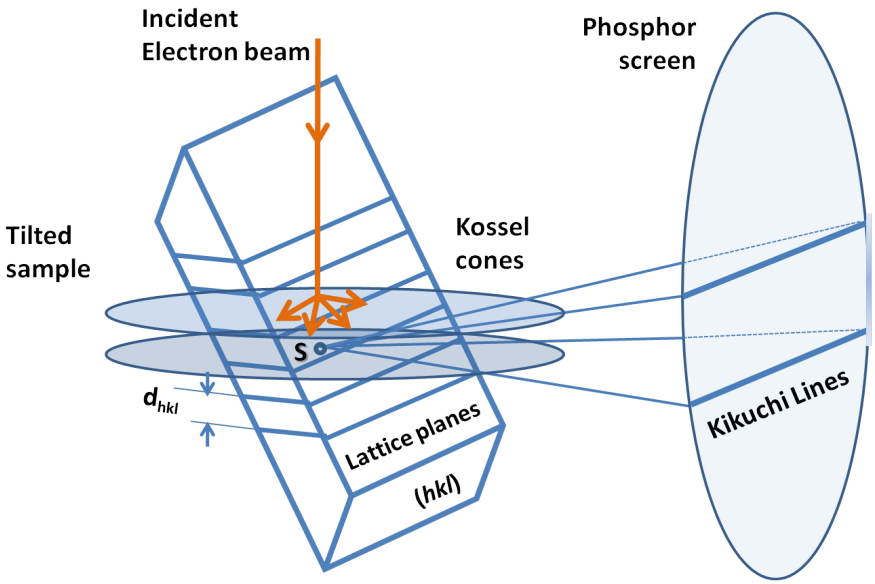

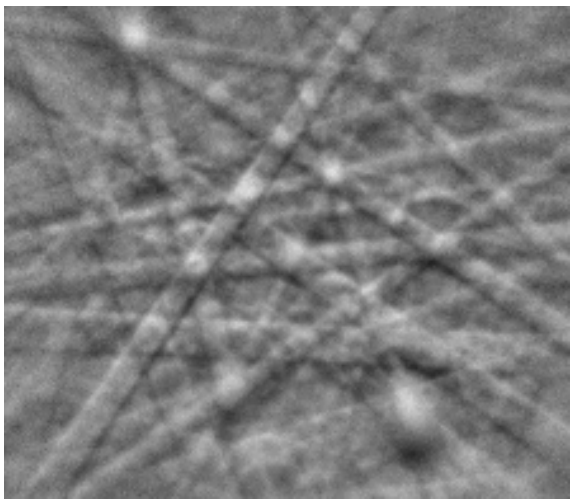

Figure 2-12: Formation of backscattered Kikuchi patterns by EBSD in the SEM. (a) Origin of Kikuchi lines from the EBSD (i.e., tilted specimen) perspective. (b) EBSD pattern from olivine (accelerating voltage 20 kV).

EBSD system consists of a phosphor screen, compact lens and low light CCD camera attached to a Scanning Electron Microscope (SEM) (Fig. 2-13). A polished sample specimen is placed into the normal position in the specimen chamber, and is tilted to ~70° from the normal position. Doing so boosts the contrast of EBSPs.

EBSPs are generated if a stationary beam interacts with the surface of a crystal [*Alam et al.,* 1954],[*Venables and Harland,* 1973]. The electrons while interacting with an atom undergo inelastic scattering. It results in a fraction of the electrons losing a small part of their energy. This process creates a divergent source of electrons close to the surface of the sample. Some of these electrons are incident on atomic planes at angles which satisfy the Bragg equation. For each given plane, these electrons emanate in diffraction cones from both the front and back surface of the plane. When these cones intersect the phosphor screen, the Kikuchi lines are formed. The Kikuchi lines appear as almost straight lines because the cones are very shallow as the Bragg angle is of the order of 1°. Small Bragg angle results from the fact that incident electrons have very high energy and hence very small wavelength ($\lambda \approx 8$ pm for a 25 KeV electron beam). Hence, Kikuchi bands are effectively the trace of the plane from which they are formed and the EBSD pattern is therefore a gnomonic projection of the crystal structure.

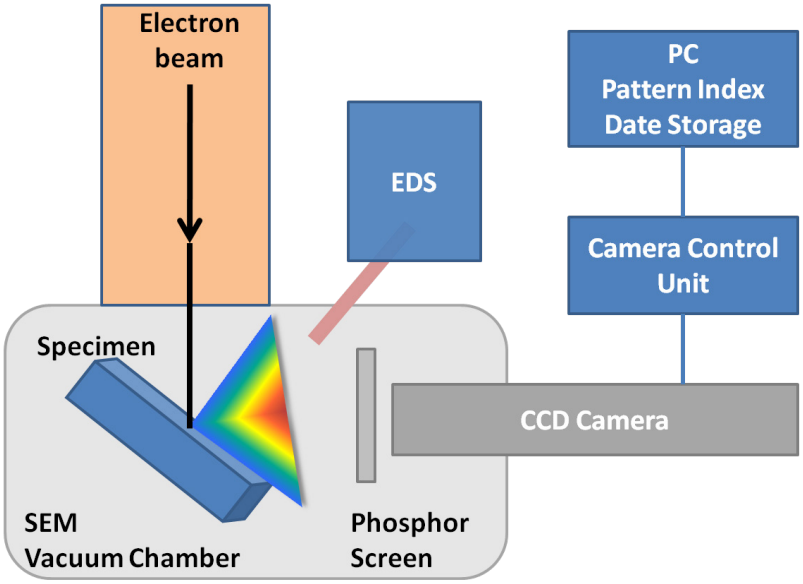

Figure 2-13: Schematic setup of an EBSD system showing its principal components

Thus, the whole Kikuchi pattern consists of pairs of parallel lines where each pair, or "band," has a distinct width and corresponds to a distinct crystallographic plane. The intersection of bands corresponds to a zone axis (pole), and major zone axes are recognized by intersection of several bands. The Kikuchi pattern therefore essentially embodies all the angular relationships in a crystal—both the - and inter-planar angles—and hence implicitly contains the crystal symmetry. Figure 2-12 shows an EBSD Kikuchi pattern from mineral San-Carlos olivine. The orientation of the pattern and hence of the volume from which it has arisen is evaluated by "indexing," that is, identifying the poles and bands in the pattern, and calculating the relationship between these and some chosen reference axes.

From Kikuchi bands to pole figure

Automated identification of a crystal orientation involves identifying the kikuchi lines in the gray scale image containing EBSPs. First step towards this process involves the pre-processing stage of edge detection. This is a non-trivial task because contrast normal to the kikuchi lines rarely change abruptly. The pattern of Kikuchi lines on the phosphor screen is electronically digitized and processed to recognize the individual Kikuchi lines. These data are used to identify the phase, to index the pattern, and to determine the orientation of the

crystal from which the pattern was generated. Individual mineral grains can be selected for identification and determination of crystal orientation, or data may be acquired on a grid over a selected area of the surface of the sample to determine the identity, orientations, and spatial relations between a large numbers of grains.

These data can be used to make statistical studies of the micro-fabric of the sample, to reveal systematic textural relations between individual grains or phases, and even to determine relative abundances of phases in a poly-phase sample.

Principles of Orientation Determination

From the information about the crystallographic indices $q^i = (q_1^i, q_2^i, q_3^i)$ with $i = 1,2 \ldots n$ (where n is the number of identified bands or poles) and the angles α_i between each band or pole i and the beam normal, the orientation of the sample normal in terms of its crystallographic indices (hkl) can be expressed as

$$\begin{pmatrix} q_1^i \\ q_2^i \\ q_3^i \end{pmatrix} \cdot \begin{pmatrix} h \\ k \\ l \end{pmatrix} = \cos \alpha_i \cdot \sqrt{(q_1^i)^2 + (q_2^i)^2 + (q_3^i)^2}$$

The root term in the equation given above normalizes the indices of the bands or axes, which are typically given as integers, for example (011) or $[110]$, to unity. Hence the resulting vector (hkl) is directly normalized to unity. It is seen that three equations are necessary to determine the vector (hkl), which means that three bands or poles have to be indexed.

Automation of Pattern Indexing and Orientation

To relate the characteristic features of an EBSD pattern – typically zone axes or bands— from the 2-D computer screen to the 3-D sample coordinate system (denoted by the superscript s in equation below), the 2-D screen coordinates (x_i^s, y_i^s) are transformed into 3-D vectors r_i by

$$r_i = \begin{pmatrix} x_i^s \\ y_i^s \\ z_i^s \end{pmatrix} = A \cdot \begin{pmatrix} x_i \\ y_i \\ z_i \end{pmatrix} = A \cdot \begin{pmatrix} x_i^* - x_{PC} \\ y_i^* - y_{PC} \\ z_{SSD} \end{pmatrix}$$

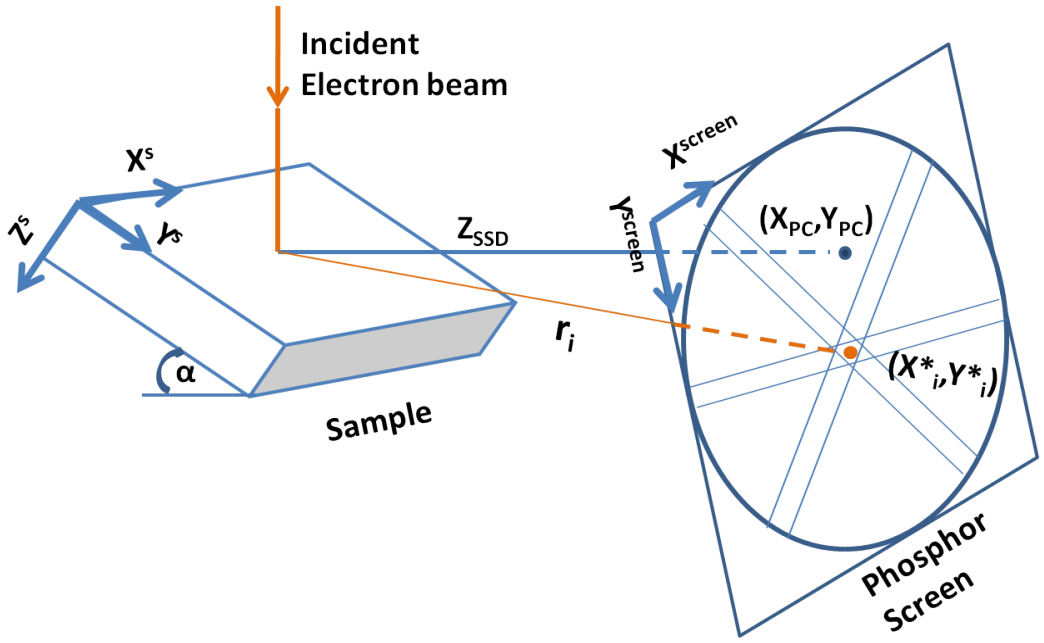

Figure 2-14: Diagram illustrating the evaluation of an EBSD pattern. Sample coordinate has been represented by superscript "s" where as screen coordinate has been represented by superscript "screen". Specimen-to-screen distance is z_{SSD} . (X^*_i,Y^*_i) are coordinates of the center of the pattern and (X_{PC},Y_{PC}) are the coordinates of the center of the screen.

With an appropriate calibration of the hardware setup, the coordinates of the pattern centre (x_{PC}, y_{PC}) and the specimen-to-screen distance z_{SSD} are known (Figure 2-14). The rotation matrix A contains all necessary geometrical corrections, most notably the tilting angle α of the sample (usually $70°$ as well as additional angles between sample and phosphor screen, which may occur in the various EBSD setups.

After indexing the pattern, the orientation of the sampled crystal volume with respect to the external specimen coordinate system can be determined (e.g. [*Schwarzer and Weiland,* 1988]; [*Dingley et al.,* 1987]. The crystallographic orientation is usually given in terms of its orientation matrix g that transforms the specimen coordinate system into the coordinate system of the crystal (indexed by the superscript c in the following equations):

$$r_i^c = g \cdot r_i^s$$

Thus, for each vector r_i (zone axis or band normal), its vector in the sample frame $r_i^s = (x_i^s, y_i^s, z_i^s)$ and, after the indexing, its crystallographic direction $r_i^c = (x_i^c, y_i^c, z_i^c)$ are known. It follows from definition of g (with $i \in 1,2,3$:

$$g = \begin{pmatrix} x_1^c & x_2^c & x_3^c \\ y_1^c & y_2^c & y_3^c \\ z_1^c & z_2^c & z_3^c \end{pmatrix} \cdot \begin{pmatrix} x_1^s & x_2^s & x_3^s \\ y_1^s & y_2^s & y_3^s \\ z_1^s & z_2^s & z_3^s \end{pmatrix}^{-1}$$

Finally, a pattern can be recalculated from the orientation matrix g and overlaid on the original pattern. If the solution is judged by the operator to be correct, the orientation matrix g is stored in a computer file for further evaluation and representation of the data.

Sample preparation for EBSD measurement

At the end of a deformation experiment the entire recovered sample assembly is cut either normal to the shear plane or parallel to it. The sample is then mounted in epoxy resin and the surface of the assembly and sample is polished to microprobe quality polished section using standard mechanical polishing methods with a finish of approximately 0.5 μm.

The electrons that generate EBSD patterns are diffracted from a depth of 10-50nm from the surface of the crystallites, and any residual surface deformation introduced during the mechanical polishing must be minimized to obtain high quality EBSD pattern. Typically standard metallography does not require such a fine surface. It should be noted that while these traditional methods can produce EBSD patterns that can be analyzed; the goal of EBSD sample preparation is to produce a flat deformation free surface that maximizes the pattern quality from the entire surface.

The next polishing stage uses a colloidal silica suspension in a mildly acidic medium. This chemical polishing removes the top surface of the sample that is mechanically damaged during standard polishing with grits. Thereafter the sample is carbon coated up to a thickness of 4-6 nm to minimize charge accumulation during the analysis.

2.3.2 Study of dislocation structure using Transmission electron microscope (TEM)

Plastic deformation of crystals occurs through the development and motion of lattice defects such as dislocations. **Transmission electron microscopy** (***TEM***) is by far the most important technique for studying such defects in great detail. TEMs are capable of imaging at a significantly higher resolution than light microscopes, owing to the small de Broglie wavelength of electrons. This enables the instrument's user to examine fine detail—even as small as a single column of atoms, which is tens of thousands times smaller than the smallest resolvable object in a light microscope.

Imaging methods in TEM utilize the information contained in the electron waves exiting from the sample to form an image. Different imaging methods attempt to modify the electron waves exiting the sample in a form that is useful to obtain information with regards to the sample, or beam itself. The observed image depends not only on the amplitude of beam, but also on the phase of the electrons, although phase effects may often be ignored at lower magnifications.

Diffraction contrast imaging is the most widely applicable way of studying dislocations, although high resolution microscopy produces more direct and spectacular images. Amplitude contrast imaging can be done by either using the direct beam or one of the diffracted beams. In the former case it is called bright field (BF) imaging, in the latter case dark field (DF) imaging. These names originate from the fact that in DF imaging, holes in the foil appear black and the picture is generally darker than for BF imaging. These two imaging techniques can be used to image strain fields within crystals. “Contrast” is the appearance of a feature in an image. Contrast in bright-field (BF) and dark-field (DF) TEM images is usually “diffraction contrast” or the variations in intensity of diffraction across the sample. Crystal defects like dislocations induce local bending of crystal planes close to the defects. This bending of crystal planes modifies the way in which the electron beam is locally diffracted. To illustrate this point further, let us consider the case of a hypothetical thin crystal flake containing an edge dislocation (Fig 2-15). The electron beam direction is now approximately at right angles to both the dislocation line (which is normal to the page) and the Burgers vector. In the immediate vicinity of the dislocation core the orientation of

the lattice planes is slightly different to that in the rest of the crystal. This means that the ways in which these lattice planes diffract electrons will be different in the distorted and undistorted parts of the crystal.

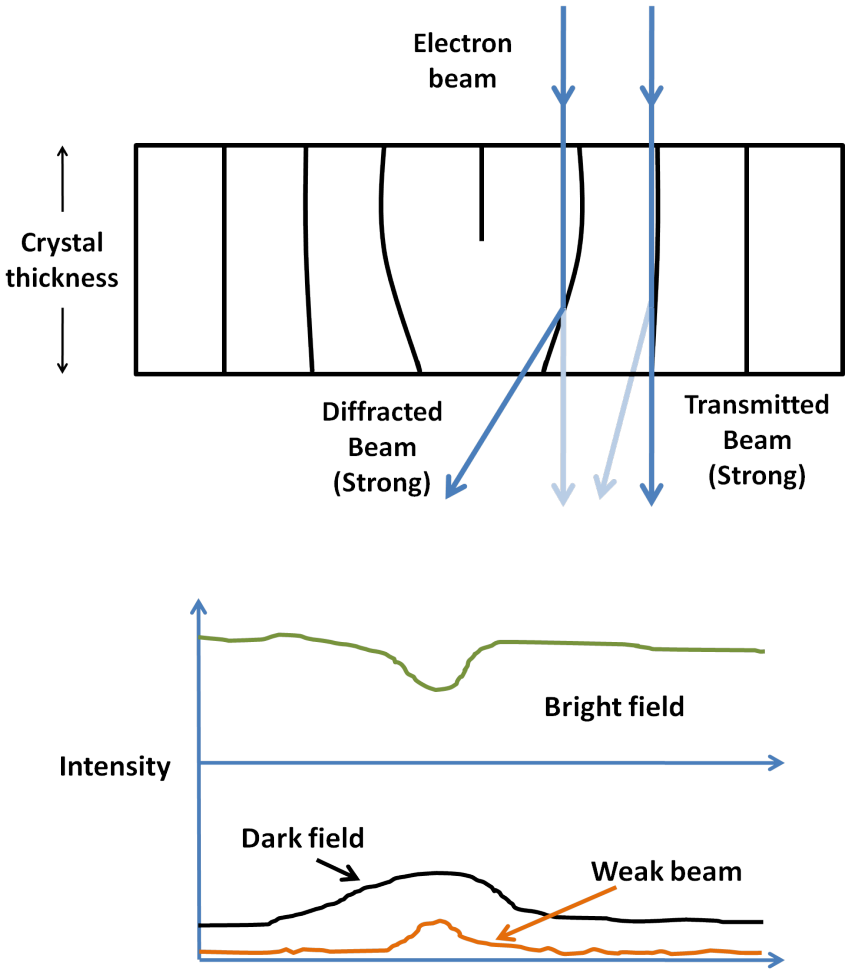

Figure 2-15 : Schematic illustration of diffraction around a dislocation core. In this case the electron beam is diffracted more strongly tiled lattice planes to one side of the dislocation core than in the undistorted parts of the crystal. The transmitted beam is depleted around the dislocation line, and in a bright-field image the dislocation line will appear darker than the rest of the crystal. On the other hand, the diffracted intensity is greater around the dislocation line and in a dark field image using the diffracted beam; the dislocation line will appear lighter than the rest of the crystal. Under Weak beam (WBDF) condition, the overall intensity of the image is reduced in comparison to a dark field image.

By slightly tilting the crystal relative to the beam it is possible to set the undistorted planes in the exact Bragg reflection (Bragg angle for short wavelength electrons is very small), in which case the planes around the dislocation core will not diffract strongly. Alternatively, a slight adjustment of the crystal will set the distorted planes into the exact

diffracting condition, while the other lattice planes will only weakly diffract. A bright field image taken in this latter position will show depleted intensity in those parts of the crystal strongly diffracting i.e. around the dislocation line. The dislocation line will appear as a dark string against a paler background. In a dark field image, using the diffracted beam, the dislocation line will appear brighter against a dark background.

Determination of the Burgers vector

As mentioned above, a dislocation bends the lattice planes near the dislocation core. This can be described by a displacement field $\vec{R}$. The displacement field generates an additional phase shift $\sim e^{2\pi i\vec{g}.\vec{R}}$ of the Bragg diffracted beam, which leads to a diffraction contrast in the image. The phase shift $e^{2\pi i\vec{g}.\vec{R}}$ only comes into effect if $\vec{g}\,.\,\vec{R} \neq 0$. This means, if $\vec{g}\,.\,\vec{b} = 0 \Rightarrow \vec{g}\,.\,\vec{R} = 0$ and the dislocation line is not visible, then the displacement field is parallel to the exploited hkl plane and does not change in phase. This relation is called $\vec{g}\,.\,\vec{b}$ criterion. If $\vec{g}\,.\,\vec{b} = 0$, the dislocation line is not visible, otherwise the dislocation is visible in the WBDF (Weak beam dark field) image. This enables the Burgers vector determination and identification of the dislocation type by taking WBDF images of the same sample area by using different $\vec{g}$ reflections.

Sample preparation

To be able to observe the sample under the TEM one needs to thin it to a thickness where it becomes transparent to electrons, which means it needs to be thinned from ~ 30 μm, the typical thickness of a thin section, to a thickness of ~100 nm. The step of sample preparation is one of most important steps in obtaining good data for a TEM study, especially when studying interfaces within materials, since these get amorphized preferentially [*Barna et al.,* 1999; *Malherbe,* 1994]. Several techniques are available for reducing the thickness of a sample, however, all of them use in one way or another beam of ionized atoms that are accelerated to an energy of several keV to tens of keV, after which they strike the sample and ablate material from the surface of the sample. In the studies presented in this thesis, Argon ion-milling technique has been used to thin a prepared thin section to electron transparency.

In an Ar ion-milling device the sample is loaded on a stage and lowered into a vacuum chamber. In this vacuum there are two argon ion guns, on opposing sides of the sample. Each gun consists of an anode inside of a cathode tube with small hole in it. The anode is connecting to an Ar supply, and since there is a several kV difference between the anode and cathode, Ar is ionized and accelerated through a hole in the cathode tube and directed at the specimen. As the accelerated Ar ions hit the surface of the specimen, they sputter the top surface layer of then specimen away, by which the specimen is thinned. Ion milling usually results in two kinds of damage to the specimen, creation of topography on a initially flat surface and secondly the creation of an amorphous layer of material on the surface (Barna et al., 1999). The first kind of damage can be reduced by rotating the sample while thinning and using a low incidence angle of the ion beam on the specimen, however due to the geometry of the holder, the lowest incidence angle that can be used for thinning in the ion milling device is 12 degrees. Rotation of the specimen reduces the creation of topography since the sputtering rate is dependent on the orientation of the incident ion beam relative to the crystal lattice of the crystallites in an aggregate [*Barna and Menyhard,* 1994]. Rotation of the specimen thus averages out (or at least reduces) the orientation dependent sputtering rate. Creation of a damaged or amorphous layer is harder to reduce. Typical operating conditions of ion miller are 2 – 5 kV, in this range ionization of the target can happen by electron exchange between the incident electron and specimen, and thus modifying the direct surface layer of the specimen (Malherbe, 1994). As the incident ions impinge on the surface, the ion will lose its energy in two different way, either through electron interactions with atoms of the specimen, or by nuclear interaction (momentum transfer) with specimen atoms before it finally becomes trapped (implanted) within the specimen. Electronic interaction results in the ionization of specimen atoms. Nuclear interaction, or collision, between the incident ion and atoms of the specimen result in a momentum or energy transfer from the impinging ion to a specimen atom. Momentum transfer sets the atoms of the specimen in motion and leads to sputtering of the specimen atoms if the atoms is freed from the surface, or otherwise may lead to a cascade of collisions inside the specimen. If the impinging ion transfers enough energy, not a single cascade of collision will occur, but a group of atoms will be set simultaneously in motion, a so-called 'spike', which may completely amorphize a portion of the lattice (Malherbe,

1994). The above mentioned processes are dependent on the incident angle, charge, mass and energy of the incident ion, and the properties of the target (Barna and Menyhard, 1994; Barna et al., 1999). The thickness of the damaged or amorphized layer thus will also vary with these variables. A higher energy of the incident ion increases penetration depth and thus the thickness of the damaged layer, whereas as higher mass of the incident ion decreases it penetration depth. A lower incident angle will decrease the thickness, though below an incident angle of 10° the dependence on incident angle becomes very weak (Barna et al., 1999). A multiply ionized incident ion will have a higher energy and thus create a thicker damage layer. Next to this, energy transfer of the incident ion to the specimen may also result in heating of the specimen, which may also damage or modify the specimen, cooling therefore is required for some specimens.

Screw and edge dislocations

Strain is defined by the displacement of an atom from its position that would be expected from the ordinary periodicity of the crystal. Causes of such a strain field can be dislocations, planar defects or other imperfections in the crystal lattice. In the case of dislocations two different types, or end types since most dislocations have a mixed character, of dislocations can be distinguished, i.e. screw and edge dislocations. Edge dislocations can be seen as the insertion of an additional lattice half plane in the otherwise regular crystal lattice. At the place where this additional half plane ends, the lattice will be distorted around the end of the edge dislocation, called the dislocation core, due to relaxation of the lattice around the core (Figure 2-16a). Screw dislocation the lattice is sheared on a plane such that part of the lattice above this plane has an offset to the lattice below the plane, the direction of the offset also lies in this plane (figure 2b). Dislocation are described by the Burgers vector **b**, the lattice vector that closes the circuit around the dislocation core (figure 2-16), and the dislocation line (direction **DL)** around which the lattice is deformed strongest. For an edge dislocation the dislocation line and the Burgers vector are perpendicular, for a screw dislocation they are parallel.

The distortion of the lattice around the dislocation core may alter the lattice is such a way that diffracted beams that are in the undistorted lattice not excited, become exited in the distorted lattice.

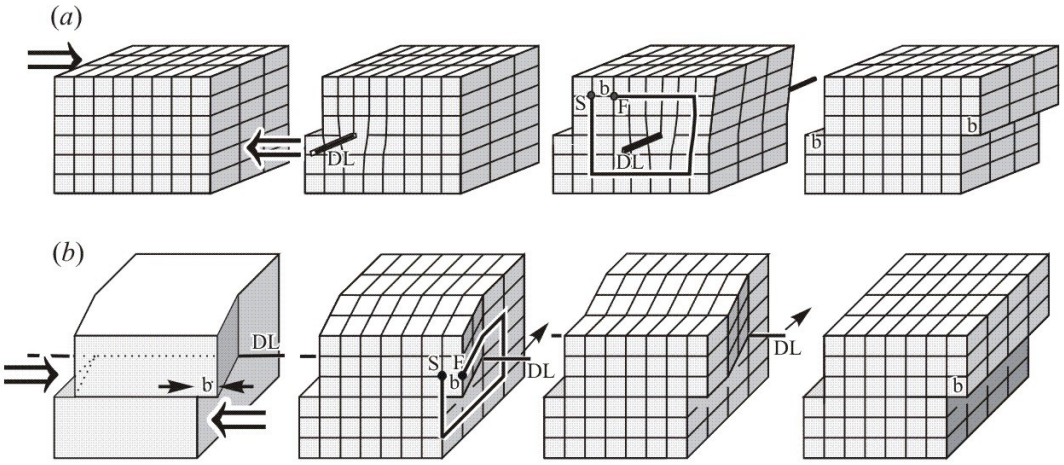

Figure 2-16: Illustration of edge and screw dislocations in a hypothetical crystal. Burgers vector "b", the lattice vector that closes the circuit around the dislocation core and dislocation line has been represented by "DL", a). In case of edge dislocation, burgers vector is normal to the dislocation line. In this case, slip plane is defined as the plane containing the dislocation line and the burgers vector, b). In case of screw dislocation, the dislocation line and burgers vector are parallel.

2.3.3 FTIR

The hydroxyl distribution within the samples were analyzed with unpolarized Fourier transform infrared (FTIR) using a Bruker™ IFS 120 HR high-resolution FTIR spectrometer with a Bruker™ IR microscope.

A schematic picture of the interferometer is shown in fig 2-17. The spectrometer is coupled with a Brucker IR microscope containing all reflecting Cassegrain optics that allows measurements of small areas with apertures down to 10 μm. Measurements in the near infrared region were carried out using tungsten light source, CaF_2 beam/splitter and high sensitivity, narrow-band MCT detector. The standard optic settings for the different frequency ranges of interest for analyzing water species are also shown in table 2-3.

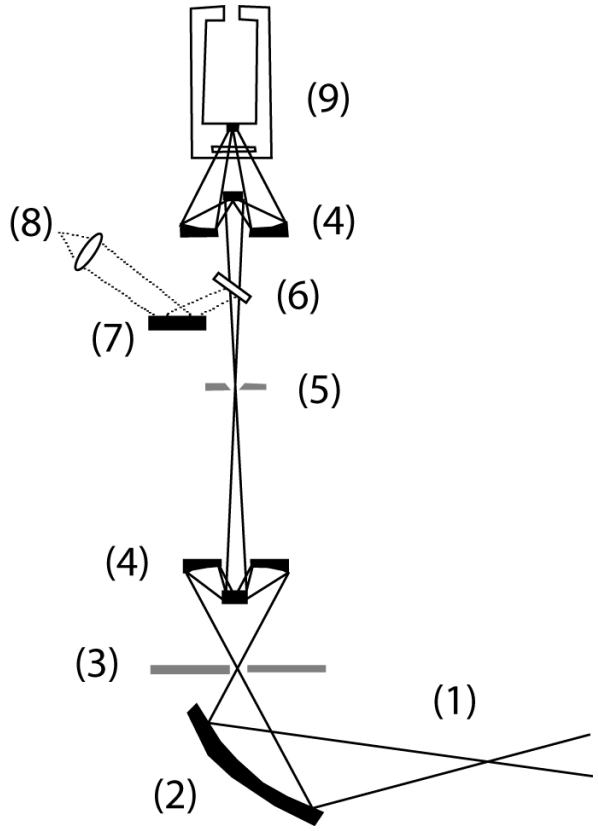

1. IR beam in transmission mode
2. Condenser mirror
3. Sample holder
4. Cassegranian objective
5. Objective
6. Aperture
7. Moving mirror
8. Ocular
9. MCT detector

Figure 2-17: Details of the FTIR microscope (Redrawn from Bolfan-Casanova, 2000)

Table 2-3 : Optics settings for different frequency ranges used to analyze water species

Optic parameter	**Near infrared**	**Mid Infrared**
Frequency Range		
Beam splitter setting	CaF2	KBr
Detector setting	MCT microscope	MCT microscope
Source setting	W lamp	Globar

Several hundred scans were accumulated for each spectrum with 1 or 4 cm^{-1} resolution. During the measurements, the optics of the spectrometer was evacuated and the microscope was purged with a stream of H_2O and CO_2—free purified air. Polarized infrared

radiation was generated using a metal-strip polarizer on a KRS-5 substrate. Background corrections of absorbance spectra were carried out by a piecewise continuous cubic fit of the baseline defined by points outside the OH-stretching region.

Calculation of the water content

The measurement of water content by IR spectroscopy is based on the Beer Lambert law:

$$A = \varepsilon \times c \times t$$

Where,

A is the absorbance,
ε is the extinction coefficient, in cm^{-1} /(mol/L),
c is the concentration of the absorber, in mol/L, and
t is the sample thickness, in cm.

Thus, to obtain quantitative data the extinction coefficients of the OH bands must be known. These are determined by the calibration of the infrared data with an independent analytical method. For most of the mantle phases, however, ε is not precisely known because its calibration is difficult for two reasons:

Analytical techniques, such as Karl Fisher titration and gas extraction manometry, are limited to high water contents and thus require a large amount of homogeneous material, which, for high pressure synthetic samples, is extremely difficult to obtain. ^{1}H MAS NMR (Magic-Angle-Spinning Nuclear magnetic resonance) spectroscopy is an intrinsically quantitative technique which has recently been used for the study of water in mantle NAMs (Kohn, 1996). The main disadvantage of this technique, however, is that the samples must be iron-free.

H_2O bound to mineral surfaces and contained in inclusions can lead to inaccurate values. Thus the water content of the sample can easily be overestimated by such bulk techniques.

In the present study, because of the absence of specific calibration for most high-pressure phases, the concentration of hydroxyl groups were determined by integrating the absorption using the calibration of extinction coefficients by Paterson (1982).

$$C = \frac{Xi}{150\xi} \int \frac{K(\bar{\nu})}{(3780 - \bar{\nu})} d\bar{\nu}$$

Where,

C is the concentration of hydroxyl (in $H/10^6$ or ppm wt H_2O),
ξ is an orientation factor, equal to $^1/_3$ for unpolarized measurement on olivine [*Mackwell and Kohlstedt,* 1990],
$K(\bar{\nu})$ is the absorption coefficient (in cm^{-1}) for a given wavenumber $\bar{\nu}$, and
X_i is a density factor. Its value is chemical composition dependent. $X_i = 4.39 \times 10^4 \ H/10^6 Si$ or 2695 wt ppm H2O for olivine (Fo90).

2.3.4 Piezoelectric measurements of stress in the Multianvil apparatus

Quantitative rheological measurements and the determination of mineral and rock flow laws rely on the ability to measure deviatoric stresses in materials under well-defined conditions. In room or low pressure devices stress measurements are achieved through the use of a load cell which must be mechanically coupled to the loaded sample but which resides outside of the sample environment or high pressure chamber. A load cell uses the strain response of a calibrated material to measure force, with strain converted into variations in electrical conductivity using a strain gauge. In the Griggs solid media deformation apparatus, which operates to pressures of approximately 3 GPa, the stress in the deformation piston is measured by means of a load cell in mechanical contact with the sample through the piston and hard alumina rods [*Holyoke and Kronenberg,* 2010]. However, at pressures higher than 3 GPa where multianvil devices are employed stress measurements are extremely challenging. *Ex-situ* measurements can be made to determine average stresses using sample specific calibrations of dislocation densities or recrystallization grain size. However, such methods can only be calibrated at lower pressures with devices that use load cells and their application at high pressure is uncertain and limited. In situ x-ray diffraction measurements to examine the distortion of diffracted Debye Scherrer rings can be used to determined lattice strain from which stresses can be determined. However, the accuracy of such measurements is currently of the order of at least 100 MPa and a rigorous internally consistent treatment of such diffraction data has yet to be demonstrated [*Durham et al.,* 2009].

A load cell that can be used internally in solid media pressure assemblies would be a significant advantage, particularly if it could preserve the accuracy in stress demonstrated by low-pressure devices. Mechanical strain gauges placed internally in a solid media devise would be extremely difficult to calibrate and to separate changes in pressure from those of deviatoric stress. The calibration of the charge developed on the surface of piezoelectric crystals as a function of force, however, may be one promising alternative.

A piezoelectric charge develops on the surface of a non-centrosymmetric crystal in response to the application of mechanical strain. Piezoelectric crystals and ceramics find

uses in an enormous range of devices such as transducers, microphones, igniters and micro-actuators. One of the most common piezoelectric crystals employed is quartz, which is used for example as a piezoelectric resonant oscillator to produce an electric signal with a precise frequency.

The charge polarization of a crystal caused by the application stress is related to the applied force through the piezoelectric charge constant, d_{ab}, where "*a*" is the direction of the polarization and *b* is the direction of the applied stress. It is convention to describe the crystallographic directions x, y, z with subscripts 1, 2, 3, with shear about one of these axes being referred to by 4, 5, 6. Piezoelectric crystals have different responses depending on the direction of stress with respect to the direction of charge polarization as shown in figure 2-18.

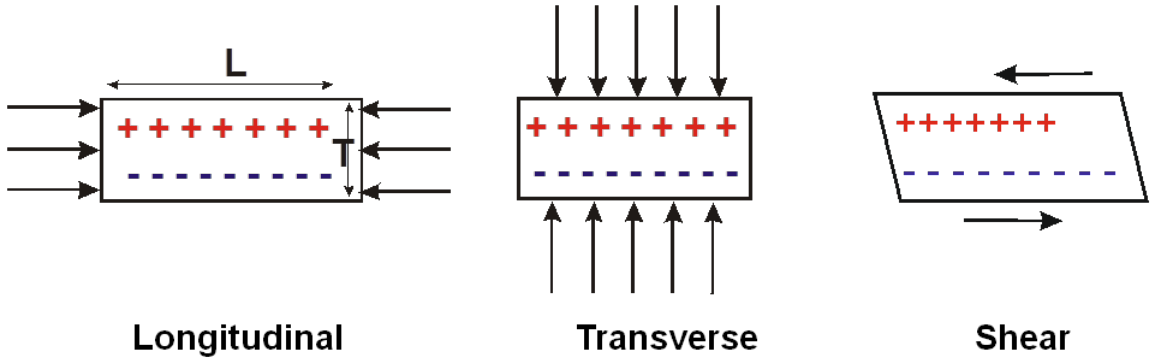

Figure 2-18: Piezoelectric crystal configurations showing different orientations of the applied force with respect to the charge polarization.

The relationship between change Q and force F varies with the configuration but only for transverse operation is it a function of crystal shape.

Longitudinal $$Q = Fd_{11}$$ 2.a

Transverse $$Q = Fd_{13}\,{}^{L}/_{T}$$ 2.b

Shear $$Q = Fd_{14}$$ 2.c

$\mathbf{d_{11}}$ for quartz, for example, is -2.3×10^{-12} C/N. The charge developed on a crystal can be determined by measuring the voltage; however, as the charge is very small the discharge time would be of the order of nano-seconds. A method of amplification is required in order to convert the charge on the crystal into a measurable voltage. This can be performed by constructing a charge amplifier or integrator amplifier. An integrator amplifier uses an operational amplifier circuit with a resistor and capacitor in series, a so called RC network. The circuit produces an output voltage, which is proportional to the integral of the input voltage as a function of time. A charge of equal magnitude to that on the piezoelectric crystal builds up on the range capacitor and the output voltage is a function of the range capacitance and the charge.

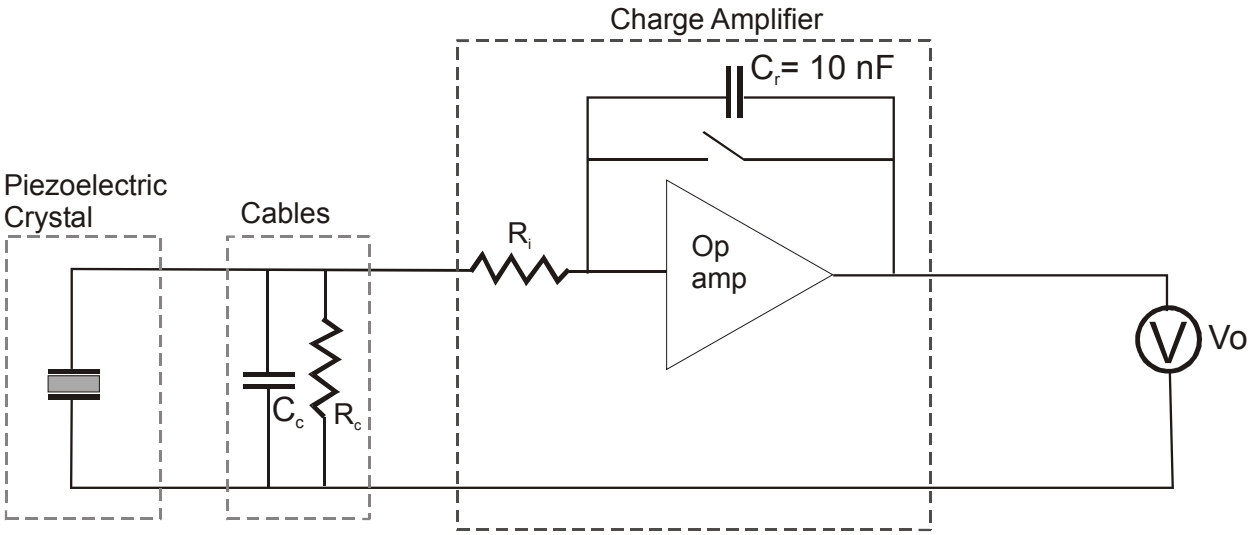

Figure 2-19: A simplified circuit diagram of the charge amplifier produced by combining an operational amplifier with an RC network.

In figure 2-19, C_r is the range capacitor, R_i is an insulating input resistance and R_c and C_c are the resistance and capacitance of the cables connecting the crystal to the charge amplifier. The output voltage Vo is

Shear $$V_0 = {}^{-Q}/_{C_r}$$ 2.d

An important aspect in the use of a charge amplifier in the measurement of small charges is the elimination of drift, which is an undesirable change in the output signal over time. Drift originates from leakage of current or charge through the cabling (C_c,R_c), the crystal itself or the operational amplifier (although modern MOSFET op amps have an extremely high gain that eliminates drift). If a piezoelectric charge is to be measured from within a high pressure multianvil assembly, then the cabling within the cell assembly needs to have a very high Rc. As many ceramics can contain H_2O or C extreme caution has to be taken to ensure the resistance across the cables remains extremely high in order to eliminate drift.

Choice of Piezoelectric crystal

For high pressure and potentially high temperature measurements in a multianvil assembly a piezoelectric crystal needs to be selected with a suitable thermodynamic stability. Although quartz is stable to at least 15 GPa at room temperature, at 573°C it transforms to β-quartz and the piezoelectric effect is lost. GaPO4 is isomorphic with quartz but has a piezoelectric coefficient ($d11 = -4.5x10 - 12\ C/N$) that is twice as large [*Krempl et al.,* 1997]; [*Damjanovic,* 1998]. The comparable β-quartz high temperature phase transition occurs at 930°C at room pressure, enabling GaPO4 to be used as a piezoelectric material to much higher temperatures than quartz. High pressure studies have indicated that at room temperature GaPO4 is stable in the quartz structure to at least 9 GPa [*Sowa,* 1994]; [*Badro et al.,* 1998] Two x-plates of $GaPO_4$ single crystal (a plate with the thickness in x-direction to measure d_{11} in the longitudinal configuration) were kindly donated by *Piezocryst GmBH*. The plates were 0.4 and 1 mm thick and could be cored to any diameter.

High pressure sample assembly for piezoelectric measurements

The main consideration in the development of a high pressure cell assembly for piezoelectric measurements is eliminating or minimizing drift by ensuring that no current can leak across the piezoelectric crystal through the assembly material. Drift causes the output voltage to rise steadily and often rapidly with time. Once the saturation voltage of 10 V is reached C_r is fully charged and is discharged automatically by the closing of the switch across C_r. Many different assembly and cable configurations were tested in order to

minimize the drift. In early attempts an unfired pyrophyllite cubic assembly was used which resulted in high drift due to conductivity through the pyrophyllite. Similarly the use of MgO around the crystal also caused drift. Unshielded cable configurations and connections also led to drift. In many instances it was difficult to identify the origin of drift, however, in many experiments drift worsened on the addition of pressure and electrical conductivity through the assembly was the most likely cause.

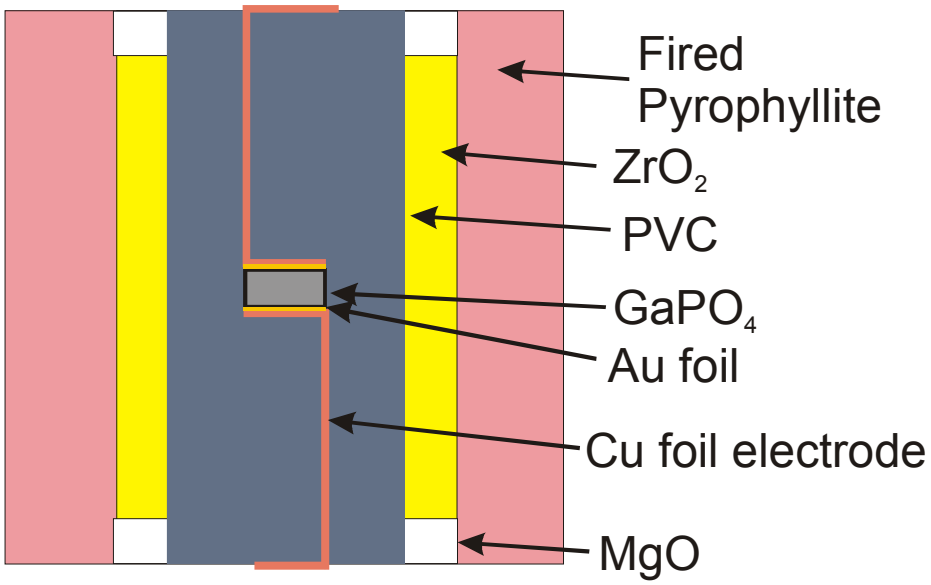

Figure 2-20: Final assembly design for piezoelectric effect measurements at high pressure in the D-DIA and 6-axis multianvil presses. Cube is 8 mm in edge length and is compressed using 6 mm edge length truncations. The crystal is 1.2 mm in diameter and 0.4 mm thick and is coated with Au using vapour deposition.

Figure 2-20 shows a successful assembly design. An 8mm pyrophyllite cube is employed which has been fired to 1000°C for 1 hour to ensure dehydration. The $GaPO_4$ single crystal of 1.2mm diameter and 0.4mm thick is within a PVC cylinder with a 1.2 mm diameter hole which is also filled with PVC rods. PVC has an extremely high resistivity and provides a relatively soft pressure medium. Gold layers of a few nm thick were vapour deposited onto each face of the crystal, with care taken to mask off the cylindrical surface. Au foil discs 25 μm thick were placed on each phase and copper foil electrodes 15 μm thick connected the crystal faces with the upper surface of the cube. The opposing cube faces

were in contact with anvils of the D-DIA or 6-axis Mavo press. The anvils in contact with the cube were connected to the charge amplifier using shielded coaxial cables.

3 Results

3.1 Deformation experiments on San-Carlos olivine using the D-DIA

3.1.1 Simple shear deformation experiments on dry San Carlos olivine

Deformation experiments on hot pressed dry olivine in simple shear configuration were performed at the conditions given in Table 3-1. All experiments employed the D-DIA apparatus with slices of polycrystalline San Carlos olivine approximately 200 microns thick cut at 45° from previously hot pressed cylinders. Olivine slices were deformed in simple shear configuration between alumina pistons because of the advancement of independent deformation anvils once the experimental pressure and temperature had been reached. Samples were first compressed over a period of approximately 10 hours then heated to target temperature over a period of 30 mins. After annealing at target temperature for approximately 2-3 hours, in order to remove microstructure potentially developed during compression, the samples were deformed at a strain rate governed by the advancement rate of the independent deformation anvils. Recovered samples were analyzed with the SEM and TEM in order to determine the sample strain, grain size evolution, lattice preferred orientation and deformation microstructure. The results of these analyses are reported in this section along with a description of the methods used to estimate sample stresses from grain size and microstructure observations. Strain rates were then determined from the total strain measured within the recovered sample from the rotation of strain marker assuming that strain was proportioned constantly over the deformation period of the experiment. When the total strain imparted on the cubic D-DIA assembly is compared with the sample strain measured after the experiments it is clear that

approximately 25% of the assembly strain is not transferred to the sample, although this loss is highly variable and ranges between 5-30%.

Table 3-1: Experimental conditions and results of dry San Carlos olivine experiments

Run ID	Starting material	P(GPa)	T(°C)	Strain rate ($x10^{-5}$ s^{-1})	Shear Strain	Strain measurement	Stress (MPa)
DD344	Hot-pressed(1 GPa)	3	1300	2.5	1.5	Pt strain marker	242
DD319	Powder	3	1300	50	1.2	Piston displacement	280
DD474	Hot-pressed (1 GPa)	5	1300	2.5	1.1	Pt strain marker	248
DD350	Powder	5	1300	40	0.7	Piston Displacement	286
DD403	Hot-pressed (1 GPa)	5	1400	4	1.4	Pt strain marker	177
DD404	Hot-pressed (1 GPa)	5	1400	50	1.5	Piston Displacement	196
DD455	Hot-pressed (1 GPa)	8.5	1300	2.5	1.4	Pt strain marker	250
DD335	Powder	8.5	1300	50	1.2	Piston Displacement	318
DD405	Hot-pressed (1 GPa)	8.5	1500	10	0.6	Piston Displacement	153
DD402	Hot-pressed (1 GPa)	8.5	1500	50	0.7	Pt strain marker	180

3.2 Characterization of the starting material

Deformation experiments are particularly sensitive to the grain size of the starting material because smaller grain sizes tend to promote diffusion creep at the expense of the dislocation creep [*Karato et al.,* 1986; *Karato et al.,* 1993; *Mei and Kohlstedt,* 2000]. It is equally important to know beforehand the fabric of the hot-pressed starting material, with

respect to crystallographic preferred orientation. Knowledge of the CPO in the starting material is necessary if we want to interpret meaningfully the CPO observed in the deformed sample. In addition it is important to determine the OH^- content of the starting material.

After hot pressing of the San Carlos olivine powder, cylindrical cores of the requisite diameter were drilled out from the recovered specimens. These cylinders were then cut at an angle of 45° to the vertical axis into thin elliptical slices of 200 μm thickness using a diamond wire saw. A slice of the remaining core was polished and prepared for EBSD analysis. Poles figures of two such specimens are shown below.

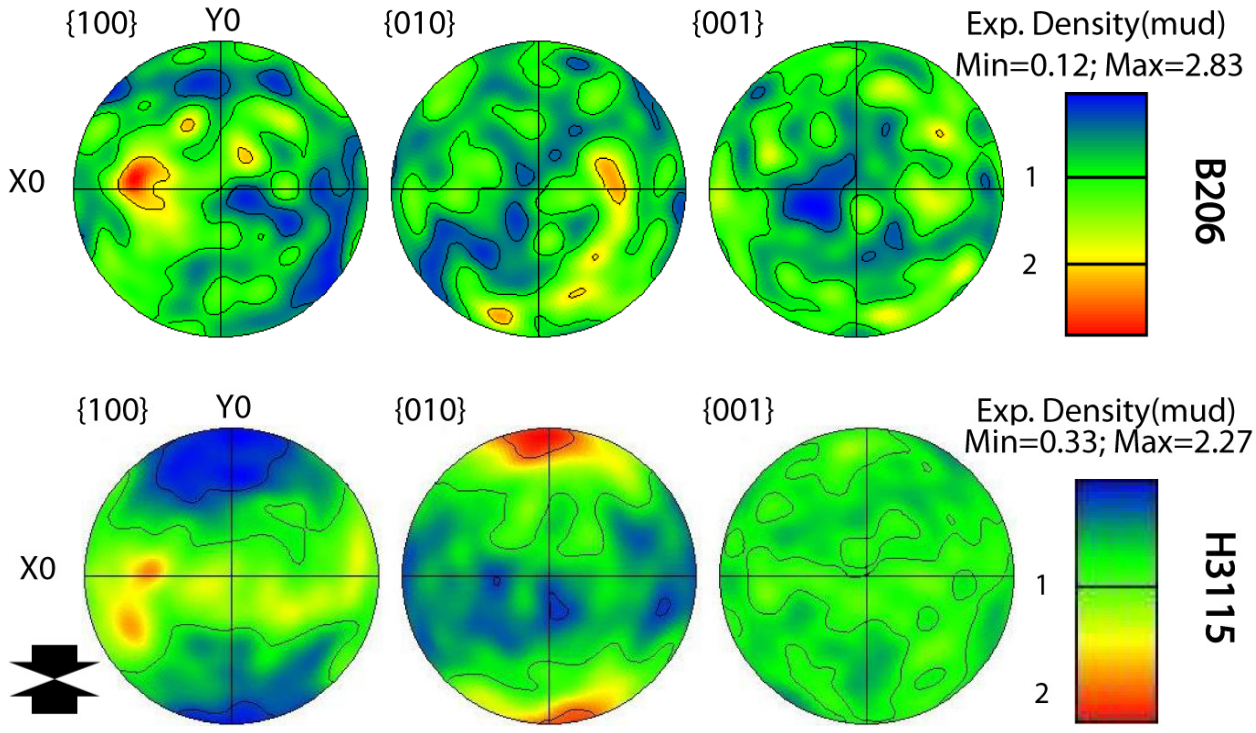

Figure 3-1: ***Top*****: Specimen ID B206 – Pole figure for polycrystalline olivine sample hot-pressed at 1** GPa **and 1200°C using piston cylinder press (Talc-Pyrex assembly). We found no LPO in this specimen.** ***Bottom*****: Specimen ID H3115 – Pole figure for olivine sample hot pressed at 8.5** GPa **and 1200°C using an 8-6 Multi-anvil apparatus. This hot pressed specimen exhibits a weak LPO resulting from the activity of the** $(010)[100]$ **slip system.**

No appreciable fabric could be observed in specimens that had been hot pressed at 1 GPa (Specimen ID B206; Figure 3-1: Top) in the piston cylinder press using a Talc-Pyrex assembly. Mean grain size of the hotpressed sample was found to be approximately 31 μm.

FTIR spectra of this hot pressed specimen revealed that no detectable amount of water was present. EBSD results of hot pressing experiments performed at higher pressure (8.5 GPa) show that some of the samples have weak LPO present. Figure 3-1: Bottom shows the pole figure for one such specimen (ID H3315). The presence of LPO in this sample results from the deviation from truly hydrostatic conditions during hot pressing in the 6-8 multianvil assembly. During compression anisotropy in the ceramic multianvil assembly materials results in shortening of the sample as pressure increases and dislocations are introduced in the olivine specimen. Once the assembly is heated to high temperature, dislocation recovery processes start. This leads to a minor amount of straining of the sample and a fabric develops that resembles fabrics formed under pure shear strain. Such hot pressed samples prepared in the multianvil have been avoided as starting materials for deformation experiments. Nevertheless, this pole figure provides crucial information about the easiest slip system present in olivine at 8.5 GPa pressure. The pole figure is consistent with slip in the a-direction on the (010) plane, which is counter to arguments that c-slip is activated at high pressures (Couvy et al. 2004). In the discussion chapter, this observation will be employed to further understand the effect of pressure on the dominant olivine slip system.

3.3 Measurement of sample strain

The strength of LPO development is directly related to the amount of strain experienced by the sample. In natural olivine samples the strength of the LPO does not generally reflect shear strains significantly over a value of 300%, because once this level of strain is approached dynamic recrystallization slows the further strengthening of the fabric [*Bystricky et al.,* 2000; *Tommasi et al.,* 2000]. In experimental studies starting with olivine samples without initial fabric shear stains as low as 30% is sufficient to generate recognizable LPO [*Couvy et al.,* 2004]. Although, a clear relation between LPO and the sense of shear is not observed for strains less than 70% [*Karato et al.,* 1998]. Moreover, starting material with redeveloped LPO may require shear strains as high as 150% before they start to reflect the new deformation conditions [*Warren et al.,* 2008].

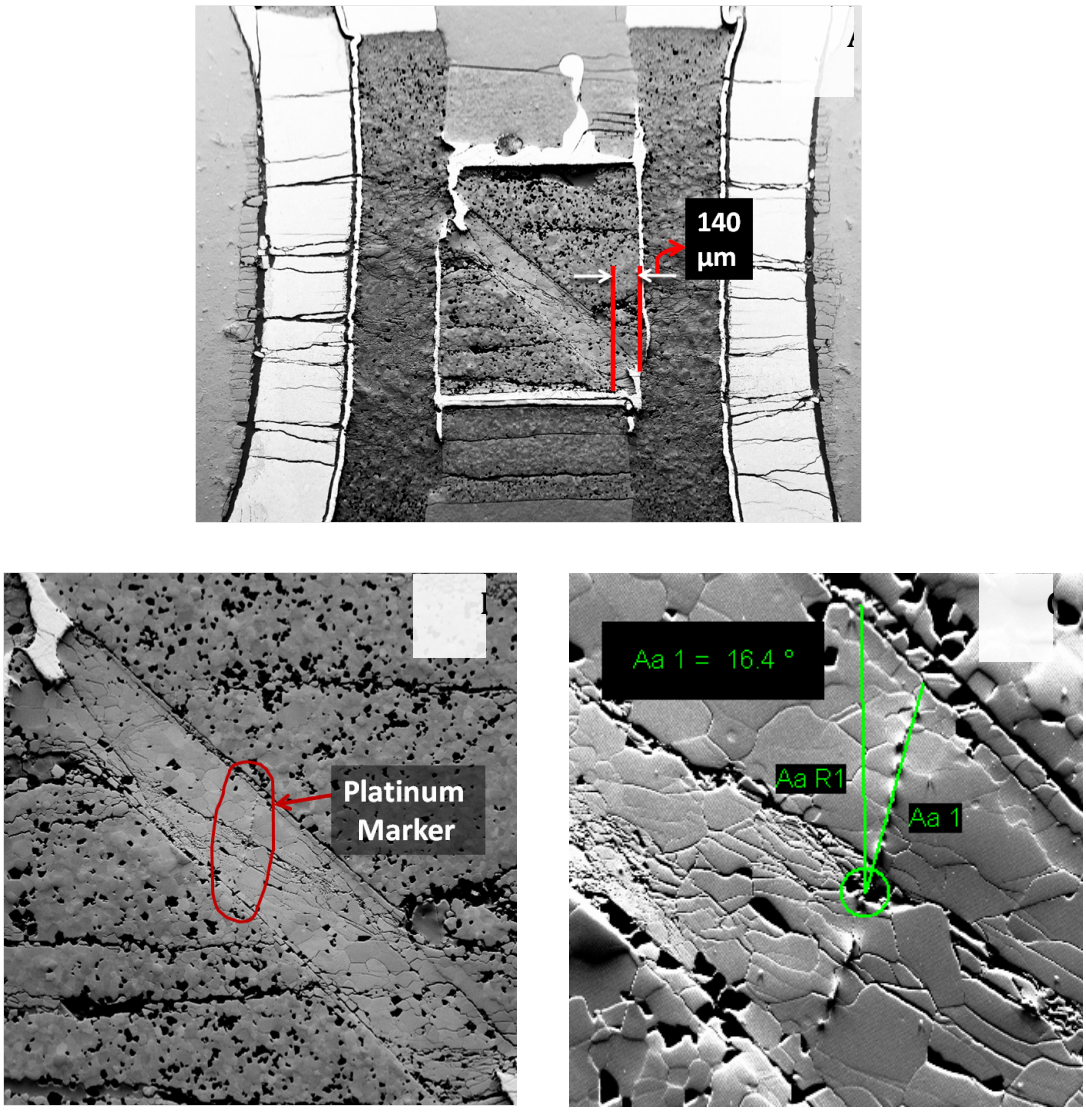

Figure 3-2: Platinum shear marker in the sample DD402 is shown. A). Sidewise displacement (140 µm) of the alumina pistons can be seen. B) Faintly visible platinum marker is shown for the same assembly. C). A close-up look at the platinum and its average rotation due to sample shear (16.4°); Note that the rotation of the marker is more pronounced near the piston.

Strain in the simple shear configuration is measured using a platinum strain marker vapour deposited onto two cut halves of the olivine sample slice (Figure 3-2A). Initially the strain markers are parallel to the direction of principal stress. Specimens recovered after annealing under pressure showed no measureable rotation of the strain marker. Shear strain γ is related to the strain marker rotation angle θ (Figure 3-1) as follows:

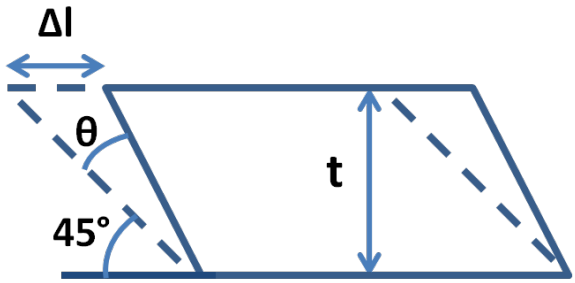

Figure 3-3: Rotation of platinum strain marker θ and amount of shear Δl for a strain marker initially oriented at 45° to the base of the specimen. Dotted parallelogram depicts the initial orientation of a hypothetical planar element of thickness "t" that undergoes shearing due to the sidewise movement of the alumina pistons. Solid lines indicate the new rotated position of the same element after the shear strain of γ.

$Case\ I: if\ \theta\ \leq 45°$

$$\gamma = \left(\frac{\Delta l}{t}\right) = 1 - \tan\left(45° - \theta\right) \qquad 3.a.$$

$Case\ II: if\ \theta > 45°$

$$\gamma = \left(\frac{\Delta l}{t}\right) = 1 + \tan\left(\theta - 45°\right) \qquad 3.b.$$

$Hence, in\ general, shear\ strain$

$$\gamma = \left(\frac{\Delta l}{t}\right) = 1 - \tan(|45° - \theta|) \qquad 3.c.$$

$where\ |x|\ is\ modulus\ of\ x.$

In a reference frame attached to the alumina piston, rotational component of the strain matrix is absent. Hence, the equivalent strain matrix can be represented as:

$$[\epsilon_{ij}] = \begin{bmatrix} 0 & \varepsilon_{12} & 0 \\ \varepsilon_{21} & 0 & 0 \\ 0 & 0 & 0 \end{bmatrix} \qquad 3.d.$$

$where\ \varepsilon_{12} = -\varepsilon_{21} = \gamma/2$

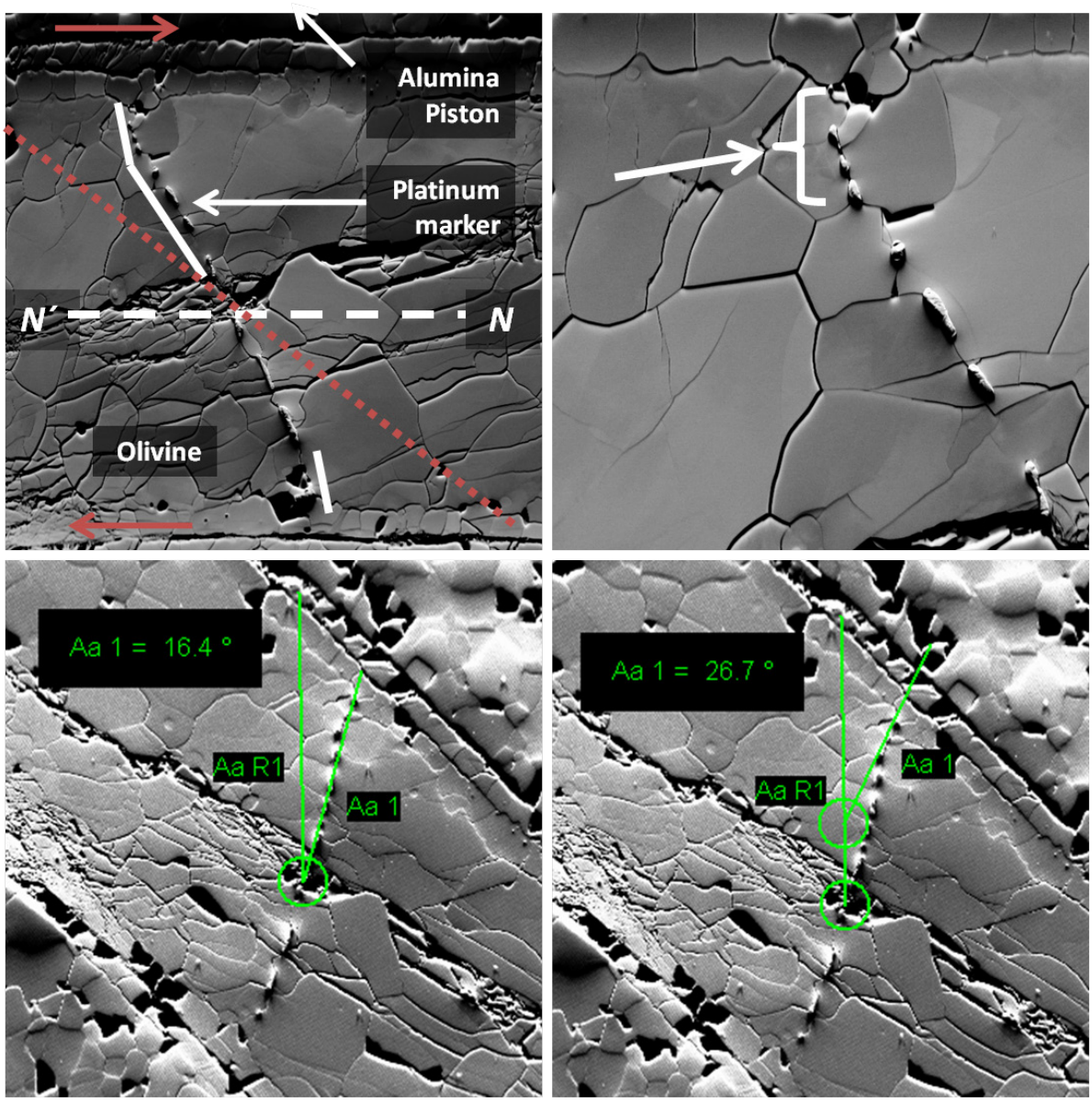

Figure 3-4: Variation in strain experienced by the sample DD402 along its thickness. *Top-Left:* The parts closer to the alumina piston are strained more than those are close to the neutral line *N´N*. Local orientation of the Pt strain marker is shown using a solid white line whereas original orientation of Pt-marker is shown using a dotted red line. Sense of shear is as indicated by the two red arrows on the top and bottom. *Top-Right:* Local increase in the shear strain in the sample near alumina piston has been marked by a curly bracket. *Bottom (Left and Right):* These images show the difference in the rotation angle as we move away from the neutral line towards the alumina piston.

The platinum strain marker also preserves evidence that in most instances the sample experiences non-uniform strain along its thickness. The shear strain close to the alumina piston is generally slightly larger than the strain near the centre or neutral line of the

sample, N´N in Figure 3-4. This occurs because the polycrystalline specimen, unlike a single crystal, does not behave as a perfect rigid body. Transference of shear force between two adjacent flow layers occurs via the interlayer friction, similar to a fluid column. This variation in shear strain should be more marked when grains are polygonal shaped and have straight edges. In this case, grains can easily slip past each other with lesser effect of inter-granular friction than in the case of irregular shaped grains (as is the case with hydrous olivine sample).

Employing the Pt strain marker and equation 3.c the shear strain determined for the edge of the sample is calculated from,

$$\gamma_{max} = 1 - \tan(45° - 26.7°) = 0.67$$

However in the centre of the sample the angle of the strain marker is only 16.4° and the determined shear strain is 0.44. Inhomogeneities in shear strain of the order of 30% occur through most samples and the shear strain reported is the maximum value recorded.

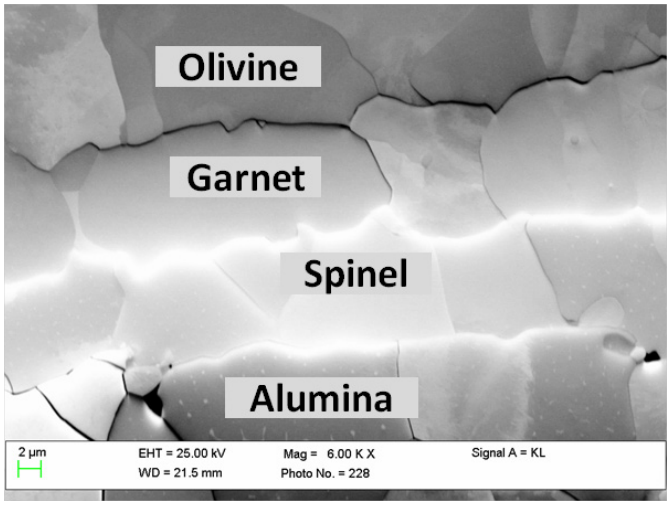

Figure 3-5: Reaction of olivine with alumina forms a layer of spinel and garnet at their interface. This may enhance the coupling between the piston and the specimen material (olivine)

It is also possible to estimate shear strain from the sidewise displacement of the alumina pistons. This assumes that the pistons are mechanically coupled to the sample because slip at the sample pistons interface would result in erroneously large maximum strain estimates. The maximum shear strain experienced by sample DD402 can be calculated from the piston displacement from:

$$\gamma_{max} = \frac{Displacement\ of\ the\ anvil}{Sample\ thickness} \cong \frac{140\ \mu m}{200\ \mu m} = 0.7$$

This is in excellent agreement with the strain marker estimate and implies good mechanical coupling between the sample and pistons.

The shear strain imparted to the sample decreases as the distance from the piston increases even though there is no appreciable sliding between the alumina piston and the sample material, unlike in other studies ([*Zhang et al.,* 2000]) where loss of strain has been observed quite frequently. We have made no special attempts at enhancing the coupling between the piston and the specimen material. All alumina pistons were cut using diamond wire saw.

In our case, the better coupling could be result of higher confining pressures (3 to 8.5 GPa) which should ensure a much better frictional contact by localized deformation of the alumina pistons and the olivine sample along their interface. Reaction between olivine and alumina leading to the formation of layer of spinel and garnet at the olivine-alumina interface could be another factor that might be responsible for a better coupling (Figure 3-5).In some instances it was not possible to place a Pt strain marker in the sample due to the sample being too fragile. In these cases it was also possible, to estimate the shear strain by measuring the lateral displacement of the top and bottom alumina pistons (Figure 3-2B).

3.4 SEM and EBSD characterization

Recovered samples were cut and polished for SEM observations to determine the grain size distribution and lattice-preferred orientation. 5° cluster size and 15° Gaussian smoothing has been applied for generating the pole figures from EBSD data, unless otherwise specified.

3.4.1 LPO determinations of dry San Carlos olivine samples

3 GPa pressure and 1300°C

Strain-rate: 2.5x10-5; No. Of grains: 1835; Shear strain ≈ 1.5

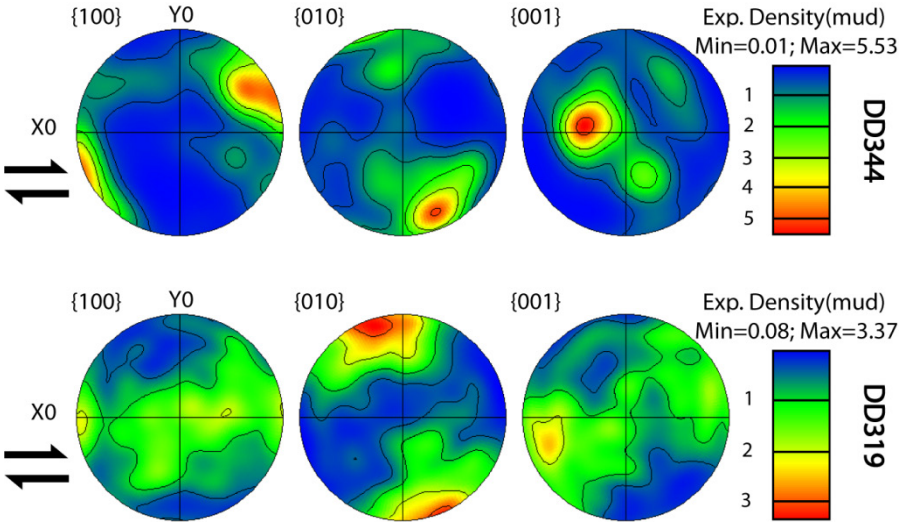

Figure 3-6: Dry samples deformed at 3 GPa and 1300°C. Sample deformed at lower strain rate (Top) shows dominant slip system to be (010)[100]. Olivine a-axes are preferentially aligned sub-parallel to the shear direction whereas b-axes are aligned subnormal to the slip plane. (Bottom) Sample deformed under higher strain rate also show the presence of (010)[100] slip system along with (010)[001] slip system.

EBSD patterns from samples recovered from experiments performed at 3 GPa and 1300°C are shown in Figure 3-4 for fast and slow strain rates. The experimental shear direction is indicated horizontal to the page. The sample deformed at a slower strain rate of $2.5x10^{-5}$ s^{-1} exhibits alignment of olivine a-axes sub-parallel to the shear direction whereas the olivine (010) is aligned sub-parallel to the shear plane, as evident from the alignment of olivine [010] axes normal to the shear direction. The specimen deformed at a higher strain rate of $50x10^{-5}$ s^{-1} also shows a strong fabric originating from the (010)[100] slip system.

However, there is also an evidence for a weaker texture originating from slip on (010)[001] slip system as indicated by the partial alignment of [001] axes sub parallel to the shear direction. Observation of (010)[001] along with (010)[100] is in line with the observation of Jung and Karato (2001) where they found (010)[001] slip system to be dominant at higher stresses.

5 GPa pressure and 1300°C

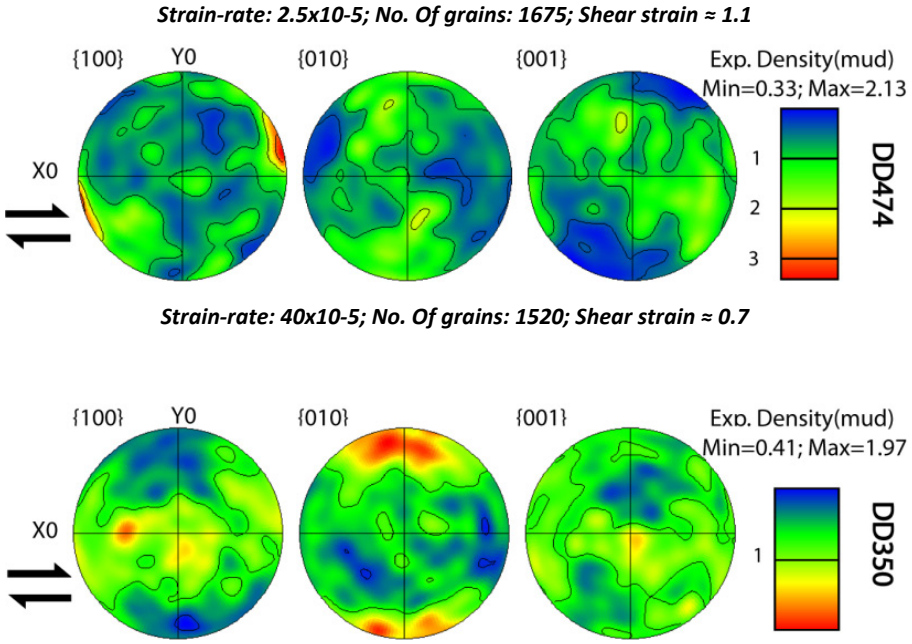

Figure 3-7 : Dry samples deformed at 5 GPa and 1300°C. Sample deformed at lower strain rate (Top) shows dominant slip system to be $(010)[100]$. Olivine a-axes are preferentially aligned sub-parallel to the shear direction whereas b-axes are aligned subnormal to the slip plane. (Bottom) Sample deformed under higher strain rate also has both $(010)[100]$ slip and $(010)[001]$ slip system active. 20° Gaussian smoothing was applied to the pole figure of specimen DD350.

The sample deformed at 5 GPa and 1300°C at a strain rate of $2.5x10^{-5}$ has (010)[100] as the dominant slip system, similar to experiments at 3 GPa. Whereas the sample deformed under similar condition but with a faster strain rate of $50x10^{-5}$ appears to have the (010)[001] slip system also making an important contribution to the overall deformation. In this case, the overall LPO in the sample becomes weaker. This weakness may result from the competing actions of more than one slip system.

5 GPa pressure and 1400°C

Samples deformed at 5 GPa, but at a slightly higher temperature of 1400°C show a similar mix of the two slip systems as found at lower temperatures. While at the slower strain rate both (010)[100] and (010)[001] slip systems are sub equally active, at the higher strain rate of $50x10^{-5,}$ the (010)[001] slip system appears to dominant deformation. Interestingly, the LPOs at this temperature appear to be stronger than at 1300°C. This may be a result of slightly higher strains in these samples.

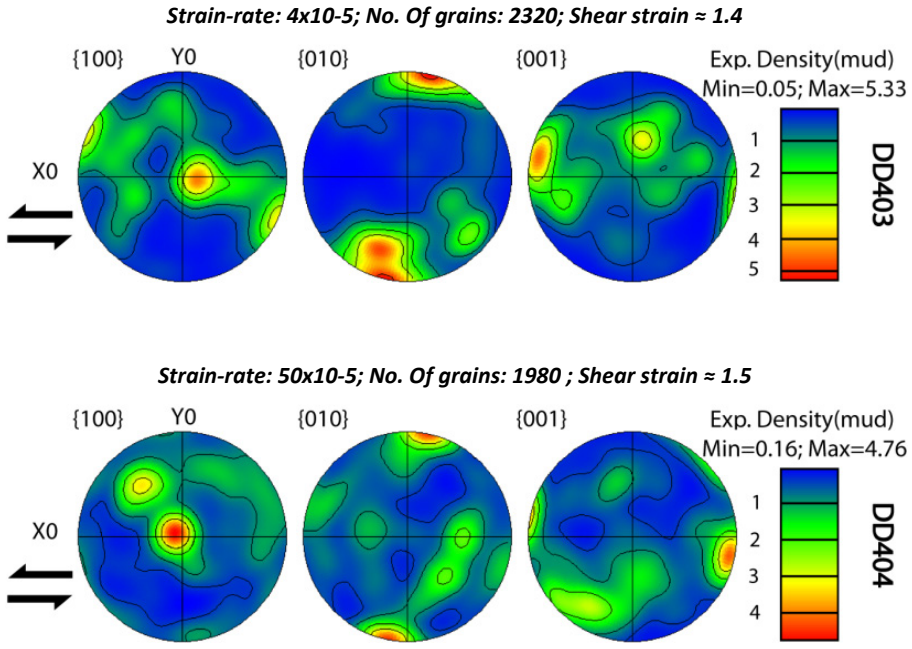

Figure 3-8: Dry samples deformed at 5 GPa and 1400°C. Sample deformed at lower strain rate (Top) shows has an LPO resultant of significant strain contribution from both $(010)[100]$ and $(010)[001]$ slip system. (Bottom) Sample deformed under higher strain rate has $(010)[001]$ slip system dominant.

8.5 GPa pressure and 1300°C

The LPO for the sample deformed at 8.5 GPa, 1300°C and a strain rate of $2.5x10^{-5}$ shows evidence for contribution from (010)[100], (010)[001] and (100)[001] slip system. Presence of (010)[100] and (010)[001] slip system is consistent with deformation under moderately high stress (285 MPa). Presence of (100)[001] may be result of the activation of harder slip system as per the Von Mises criteria.

Specimen DD335, which was also deformed at 8.5 GPa and 1300°C but at a higher strain rate ($50x10^{-5}$) indicates that the (010)[001] slip system was predominately active. This observation is also consistent with the reports of (010)[001] being easy slip system under higher stresses (395 MPa).

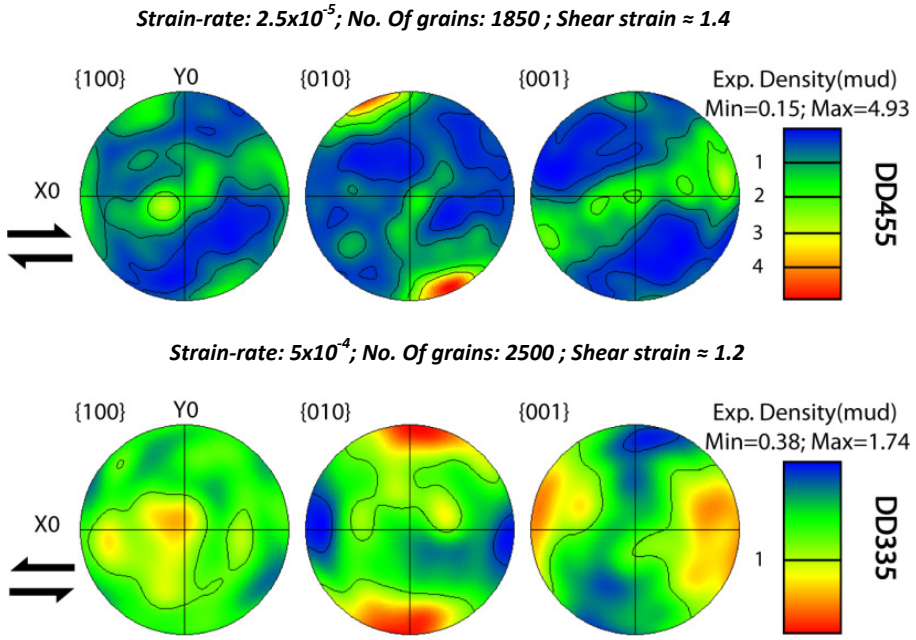

Figure 3-9: Dry samples deformed at 8.5 GPa and 1300°C. Sample deformed at slower strain rate (Bottom) shows dominant slip system to be $(010)[100]$ and $(010)[001]$. Olivine a-axes and c-axes are preferentially aligned sub-parallel to the shear direction whereas b-axes are aligned subnormal to the slip plane. (Bottom) Sample deformed under higher strain rate show the presence of $(010)[001]$ slip system. 20° Gaussian smoothing was applied to the pole figure of DD335.

Specimen DD455 and active slip systems

HKL Channel™ 5 program which has been used for EBSD data analysis allows for selection of subsets of a few data points. A new data file is created by using an elliptical subset selection tool shows by red-dotted like in figure 3-10-A. Such a subset can be created in a way to include grains with a particular orientation. Figure 3-10-A shows selection where only the grains with their [010]-axes oriented sub-parallel to the specimen Y0 axis. The selected data points marked by red-dotted ellipse are used for drawing a new EBSD pole-figure as shown in figure 3-10-B. The purpose of analyzing such subsets is to establish the simultaneous activity of more than one slip system.

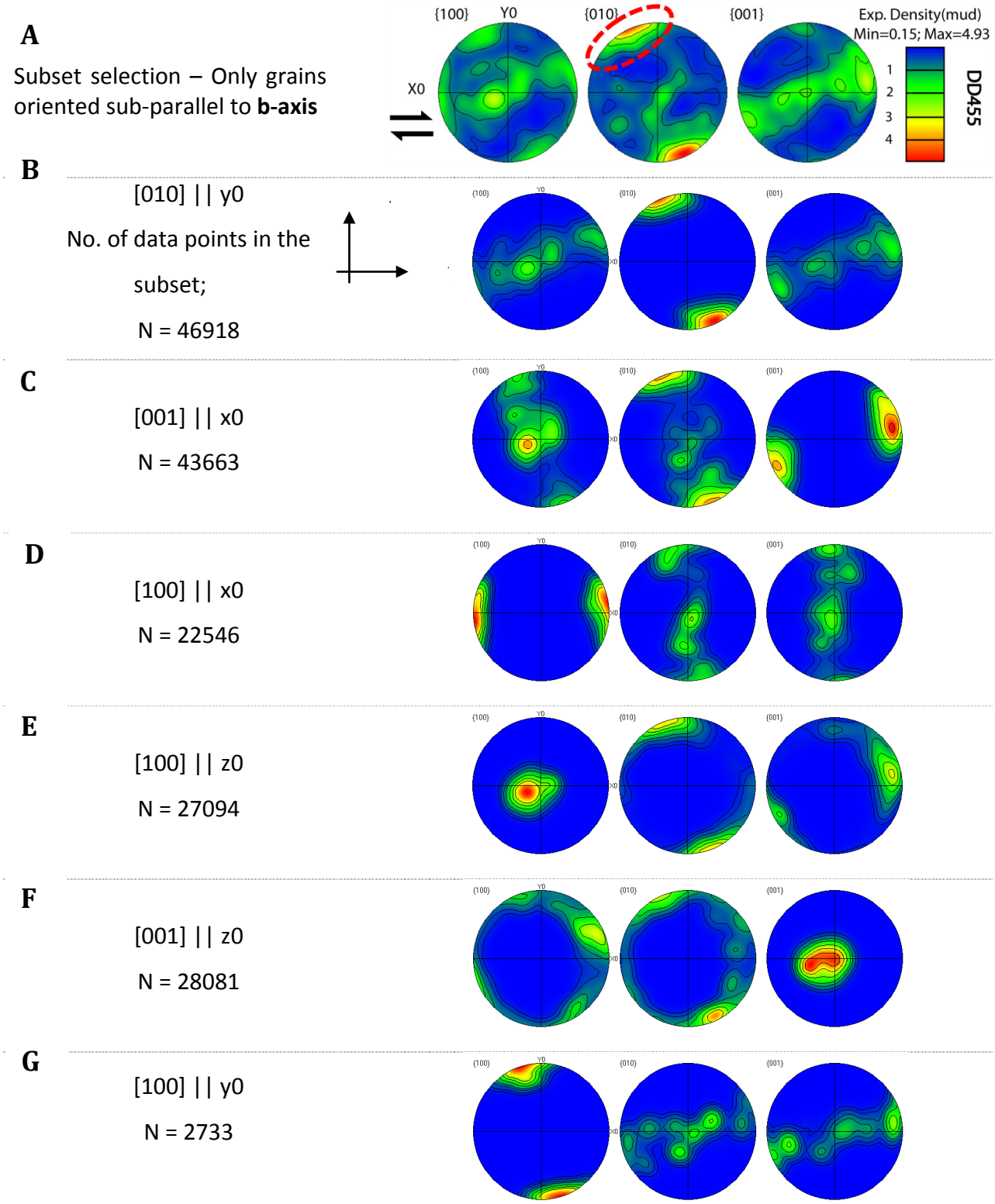

Figure 3-10: Subsets of pole figures indicated a particular crystallographic axis parallel to a selected specimen axis. [100] || x0 implies that the subset contains only the data points such that olivine [100] axes are aligned parallel (or sub-parallel) to x-axis of the specimen.

Taking the example of DD455, the [010] || y0 subset i.e. a subset consisting of grains with their b-axes aligned (sub-)parallel to the y0 specimen axes, we observe that some of these grains have their a-axes aligned sub-parallel to x0 –specimen direction or shear direction. This particular subset also includes grains with their c-axes aligned sub-parallel to shear direction. This observation can be construed to be indicative of comparative activity of the two slip systems – (010)[100] and (010)[001]. A more refined understanding of slip system activity can be obtained by analyzing several such subsets and counting the number of grains (or data points) present in those subsets. Figure 3-10-E shows mostly the grains with dominant slip system being (010)[001]. We can make such an assumption because all such grains with their a-axes aligned parallel to z0-axis of the specimen also have their b-axis aligned sub-normal to the shear direction and c-axis aligned sub-parallel to the shear direction. Such a configuration develops due to the dominant activity of (010)[001] slip systems with number of data points being 27094. On the other, figure 3-10-B shows the pole figure for those grains who are neither deformed preferably either in (010)[100] slip system or (010)[001] slip system and the number of data points in this case is 46918. Hence, the number of data points indicative of (010)[100] slip system is (46918 – 27094) = 19824. Hence, we can say that the relative activity of (010)[100] to (010)[010] is 19824/27094 = 0.73:1. Similarly, from figure 3-10-D the relative activity of (001)[100] to (010)[100] is (22546 – 19824)/19824 = 0.137:1. From figure 3-10-G, we can derive the relativity activity of (100)[001] slip system with respect to (010)[100] which is equal to (2733 / 19824) = 0.138:1. Hence, the activity of 4 major slip systems is as follows:

Slip system	(010)[100]	(010)[001]	(100)[001]	(001)[100]
Activity	1	1.37	0.138	0.137

8.5 GPa pressure and 1500°C

Specimens deformed at 8.5 GPa but at much higher temperature (1500°C) display no recognizable LPO. Mean grain sizes in these specimens are much higher than samples deformed at 1300°C and 1400°C (See figure 3-11). The maximum shear strain in these specimens was no more than 60%. Due to the shorter life of the assembly at 1500°C, it was not possible to continue deforming the sample for longer duration of time because of failure of the furnace.

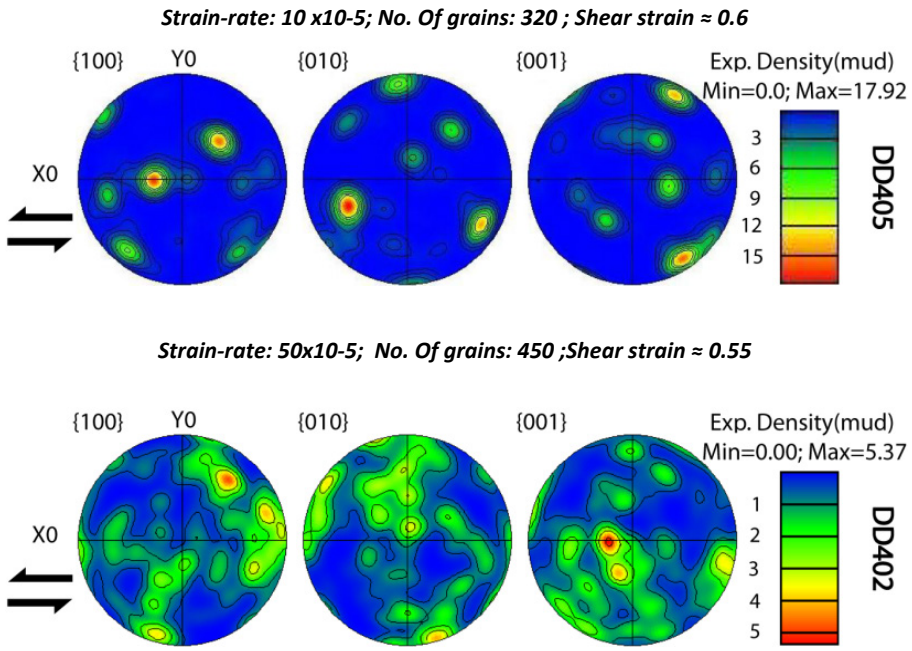

Figure 3-11: Dry samples deformed at 8GPa and 1500°C. No recognisable LPO is present in these samples.

3.4.2 Estimation of the mean grain size

Before grain size and distribution can be determined from EBSD sample maps non-indexed data points need to be assigned a crystallographic orientation. This can be performed using the grain-area determination module of the *HKL Channel 5* software suite. Non-indexed data points are assigning the same orientation as nearest neighbour point, under the condition that all of these neighbours have the same orientation. The number of neighbours requiring the same orientation can be varied but in this study a value of 4 was employed. This is essentially a noise reduction procedure that filters out un-indexed data points by assigning them to the most likely orientation. This process is repeated until almost all the non-indexed points have been assigned an orientation. This algorithm performs optimally (with an accuracy better than 10%) when the data collection step size is lower than one-fifth of the grain size [*Humphreys,* 2001]. Figure 3-10: top shows the raw data with several non-indexed points (Grey colour) whereas the bottom figure shows the same orientation map with reconstructed grains using the nearest neighbour noise-reduction algorithm in the *HKL Channel 5* software-suites.

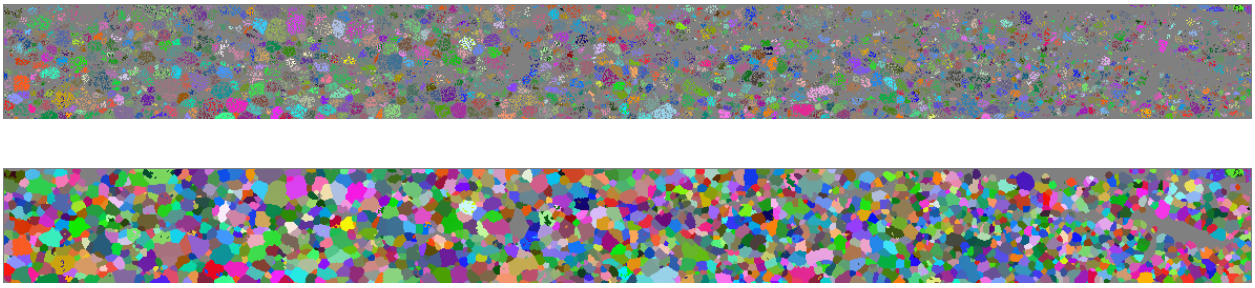

Figure 3-12 : Top: EBSD map for specimen DD350 with non-indexed data points; grains have been assigned colour according to their Euler angles 1 to 3; Bottom: EBSD map after grain reconstruction using the nearest neighbour noise-reduction method.

Recrystallized grain size and fraction of recrystallization

Estimation of the mean value of recrystallized grains size and fraction of recrystallization can be performed after grains have been reconstructed according to the procedure described in the last section (Figure 3-10). The programme *Tango* which is a part of the *HKL Channel 5* software suite, initiate the following procedure to differentiate between deformed, substructured and recrystallized grain fractions:

1. *Tango* initially performs a grain reconstruction using the user-defined parameters in the grain-area determination window, e.g. critical misorientation angle, $\theta_c = 10°$ for olivine. Individual grains are defined to be separated by this difference in orientation angle.
2. In the next step, the programme measures the internal average misorientation angle within each grain.
3. If the average angle in a grain exceeds the user-defined minimum angle to define a subgrain, (θ_c), the grain is classified as being "deformed", which simply implies that the sub-grain structure is as yet poorly developed.
4. Some grains consist of subgrains whose internal misorientation is under θ_c but the misorientation from subgrain to subgrain is above $\theta_{sub} = 2°$. In that case, the grain is classed as "substructured" i.e. composed of subgrains.
5. All the remaining grains are classified as "recrystallized".
6. A geometric correction factor of 1.5 [*Gifkins,* 1970] has been used to account for 3-D nature of the grains.

Dynamic recrystallization plays an important role in the deformation of olivine. It often leads to grain size reduction due to nucleation of smaller strain free grains from the strained ones. Reduction in grain size may change the dominant deformation mechanism from grain-size-insensitive (GSI) dislocation creep to grain-size-sensitive (GSS) diffusion creep, leading to weakening and strain localization [*Drury,* 2005; *Karato and Wu,* 1993; *Michibayashi et al.,* 2006; *Schmid,* 1982]. It has been suggested that weakening effect related to dynamic recrystallization could be minor and the transition from GSI to GSI may not happen if grain growth is an active phenomena [*De Bresser et al.,* 2001]. Rather, a switch from GSI power law dislocation creep to GSS power law creep (instead of GSS linear diffusion creep) is more likely to occur in the case of olivine [*Drury,* 2005; *Montesi and Hirth,* 2003].

Table 3-2: Measurement of stress using recrystallized grain size

Run ID	P (GPa)	T (°C)	Strain rate ($x10^{-5}$ s^{-1})	Shear Strain	Grain size (µm)		Stress (MPa)
					All	Recrystallized	
DD344	3	1300	2.5	1.5	15.4	7.1	242
DD319	3	1300	50	1.2	14.5	5.5	280
DD474	5	1300	2.5	1.1	8.1	6.8	248
DD350	5	1300	40	0.7	7.8	5.3	286
DD403	5	1400	4	1.4	17.4	12.4	177
DD404	5	1400	50	1.5	23	10.3	196
DD455	8.5	1300	2.5	1.4	8.7	6.7	250
DD335	8.5	1300	50	1.2	9.5	4.4	318
DD405	8.5	1500	10	0.6	24.5	16	153
DD402	8.5	1500	50	0.55	24.3	12	180

Comparison of results from simple shear deformation experiments and VPSC modelling of LPO development suggests that dynamic recrystallization results in further reorientation of the LPO [*Tommasi et al.,* 2000]. Significant presence of dynamic recrystallization eliminates the need for strain contributions from hard slip systems and in such a scenario, only the easiest slip system may control the fabric development and flow behaviour of olivine [*Zhang et al.,* 2000]. Furthermore, in the presence of dynamic recrystallization, developed texture in olivine has been found to be symmetric in nature. In the absence of significant contribution from dynamic recrystallization, the developed texture has asymmetry (for example, one can see the rotation of [100] direction away from the shear direction in Figure 3-6) [*Wenk and Tome,* 1999; *Zhang et al.,* 2000].

Recrystallized grain size in the dislocation creep regime is strongly stress dependent [*Jung and Karato,* 2001b; *Karato et al.,* 1980; *Nicolas,* 1978; *Ross et al.,* 1980; *Twiss,* 1977; *Van Der Wal et al.,* 1993] and as such presents a potential method for stress determination as discussed earlier. Theoretical models for recrystallized grain size also propose temperature dependence [*De Bresser et al.,* 2001; *Derby and Ashby,* 1987]. Furthermore, recrystallized grain size in olivine is also affected by the presence of water [*Jung and Karato,* 2001b].

In general, recrystallized grain size D can be expressed as:

$$D = K\sigma^{-c} \exp(\Delta Q/RT) \qquad 3.e.$$

$where\ K\ and\ c\ are\ constants$

$\sigma = flow\ stress$

$\Delta Q = activation\ enthalpy\ for\ dynamic\ recrystallization\ and$

$T = temperature$

In the case of olivine, value of ΔQ has been found to be $\approx 30\ kJ/mol$ for dry specimen and $\Delta Q \approx -30\ kJ/mol$ for wet specimen with low water content [*Drury,* 2005]. Hence, the temperature dependence of recrystallized grain size for olivine can most likely be ignored because of small activation enthalpy. This implies that recrystallization grain size can be a useful indicator for stress provided that H_2O contents are also considered.

3.4.3 TEM characterization

TEM observations have been made on several of the recovered samples in order to correlate the developed CPO with the action of specific dislocations (Figure 3-11). Sample DD384 deformed at 8.5 GPa and 1300°C shows straight edge dislocations with b = [001]. Absence of screw segments indicates that screw segments were more mobile than the edge segment. Top-right figure shows that no dislocation with b = [100] are present in this grain. Most of the c-dislocations are short and straight. In the samples deformed at 8.5 GPa and 1500°C (Figure 3-11: Bottom), both a-dislocation and c-dislocations are present in almost equal density. Low-angle grain boundaries (tilt walls) are also visible in the bottom-left image. Unlike c-dislocations which appear to be very straight, a-dislocations appear wavy. Most of the c-dislocations in this case are short and straight edge segments. Abundance of low angle tilt walls in this sample points to the presence of numerous small subgrains.

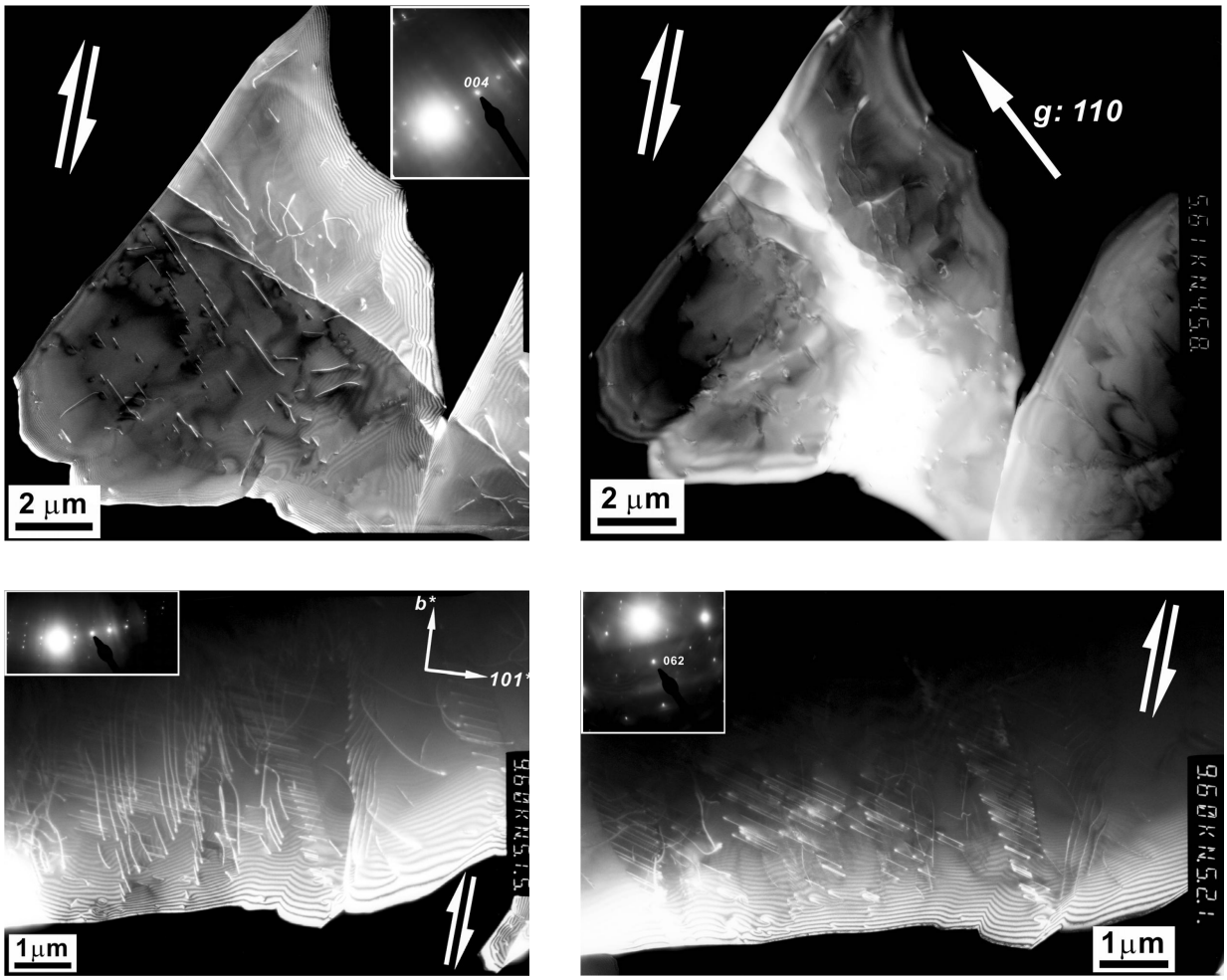

Figure 3-13: *Top* -TEM micrograph for specimen D384 that was deformed at 8.5 GPa and 1300°C. C-dislocations (only edge segments are visible) are visible in the top-left image ($\vec{g} = [004]$). No a-dislocation could be seen from $\vec{g} = [110]$ imaging direction, which implies that c-slip was the dominant slip system. *Bottom* – TEM micrographs for specimen DD391 deformed at 8.5 GPa and 1500°C. Both a- and c-dislocations can be seen in the left image. Right image shows only the c-dislocation for the same specimen. White double-arrows in the picture indicate that sense of shear for the bulk sample.

TEM micrograph for the specimen DD455, which was deformed at a slower rate at 8.5 GPa and 1300°C, shows that active slip systems in this case are (010)[100], (100)[001] and (010)[001] (Fig 3-12-left). Dislocation with b = [001] are short and straight and appear to be of mainly edge nature. The image on the right (Fig 3-12) shows high density of dislocation with b = [100]. These dislocation appear wavy unlike most of the b = [001] dislocations in previous images. This indicates that Peierls barrier to the movement of c-dislocations is generally higher than those for a-dislocations.

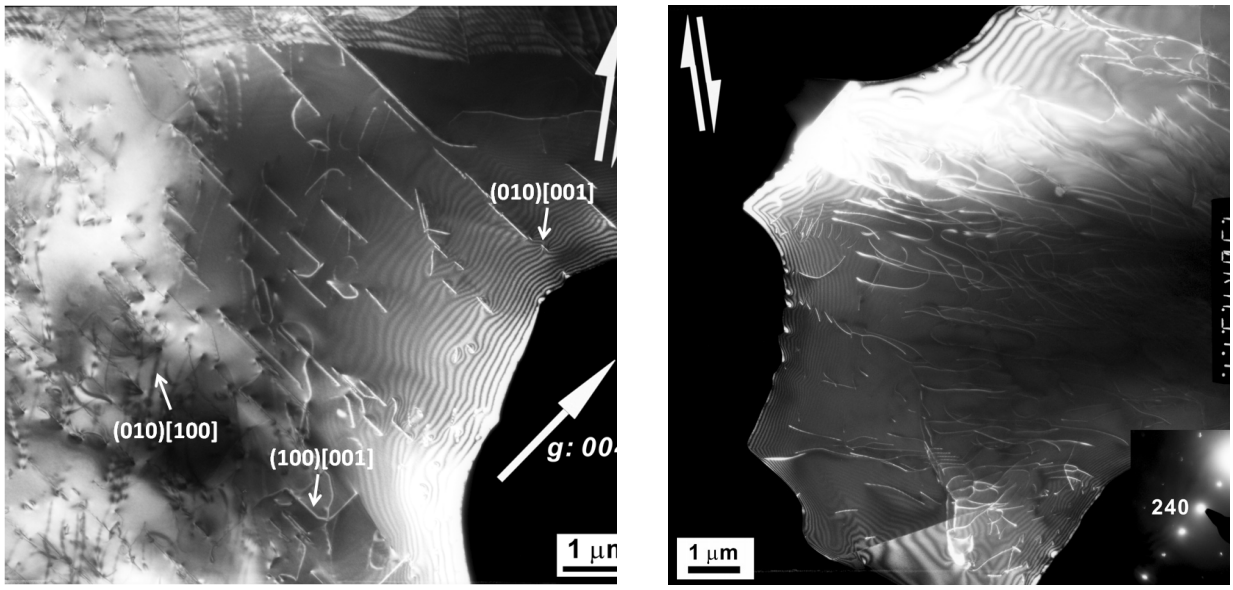

Figure 3-14: TEM micrographs for the dry sample DD455 deformed slowly at 1300°C. Active slip systems are (010)[100], (100)[001] and (010)[001]. Figure on the left side shows large number of b = [100] dislocations present in one grain. White double-arrows in the picture indicate that sense of shear for the bulk sample.

3.4.4 Measurement of sample stress

Dislocation density method

In this work, we have taken two different approaches for measuring flow stress in the sample. The first approach is based upon the relationship between dislocation density and flow stress, whereas the second approach relies upon the fact that the recrystallized grain size in materials that have deformed plastically, is a function of stress as has been discussed in the last section.

Wherever, TEM micrographs are available, stress has been estimated using the Taylor's equation (Eq. 3.f), which relates flow stress to the dislocation density in the specimen [*Kohlstedt et al.,* 1976b].

$$\sigma_1 - \sigma_3 = \alpha b \mu \rho^{1/2} \qquad 3.f.$$

Where; $\alpha \approx 3$

$b = burger's\ vector$

$\mu = shear\ modulus$

$\rho = dislocation\ density$

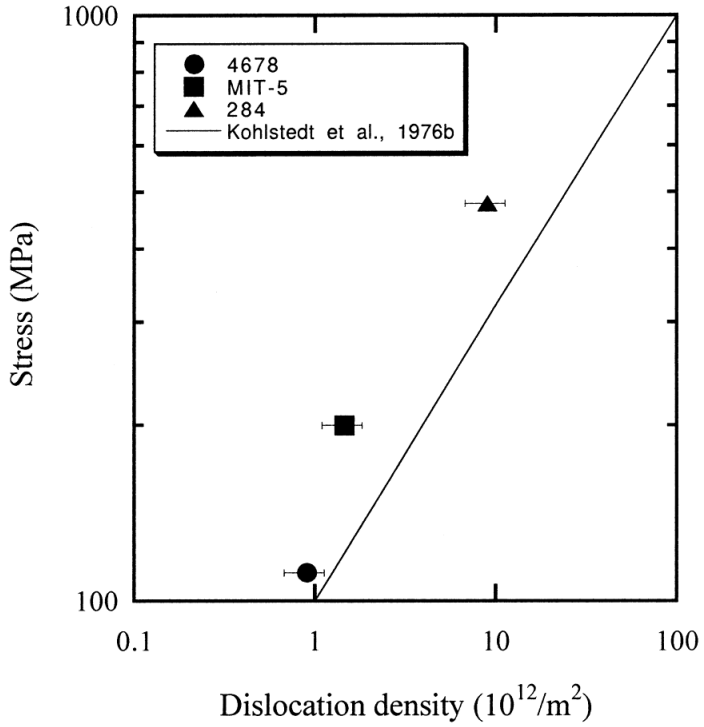

Figure 3-15: Dislocation density versus stress relationship [*Jung and Karato,* 2001a]. The solid line is the stress versus dislocation density relationship for a single crystal with the Schmidt factor = 0.5 [*Kohlstedt et al.,* 1976b].

The critical step in adopting this procedure is the estimation of dislocation density, ρ, which in turn is defined as the total length of dislocation in a unit volume of the specimen. Several methods have been proposed for the measurement of total length of dislocation which involve manual processing of the micrographs [*Bailey and Hirsch,* 1960; *Ham,* 1961]. It is also noteworthy that the dislocation density in polycrystalline aggregate may differ from a single crystal because of heterogeneous deformation near grain-boundaries [*De Bresser*, 1996] and grain boundary migration [*Jung and Karato,* 2001b]. Jung and Karato 2001) have proposed a new calibration curve for the relationship between dislocation densities and stress (Fig 3-16).

Measurement of the sample thickness: As described in the last chapter, our TEM specimens have been thinned using Argon milling process. This process results in a wedge shaped grain with a plateau top as shown in Figure 3-15 for the specimen DD384 deformed

at 8.5 GPa and 1300°C. Wedge shaped region can be identified easily by the presence of thickness fringes at the edge of the grain.

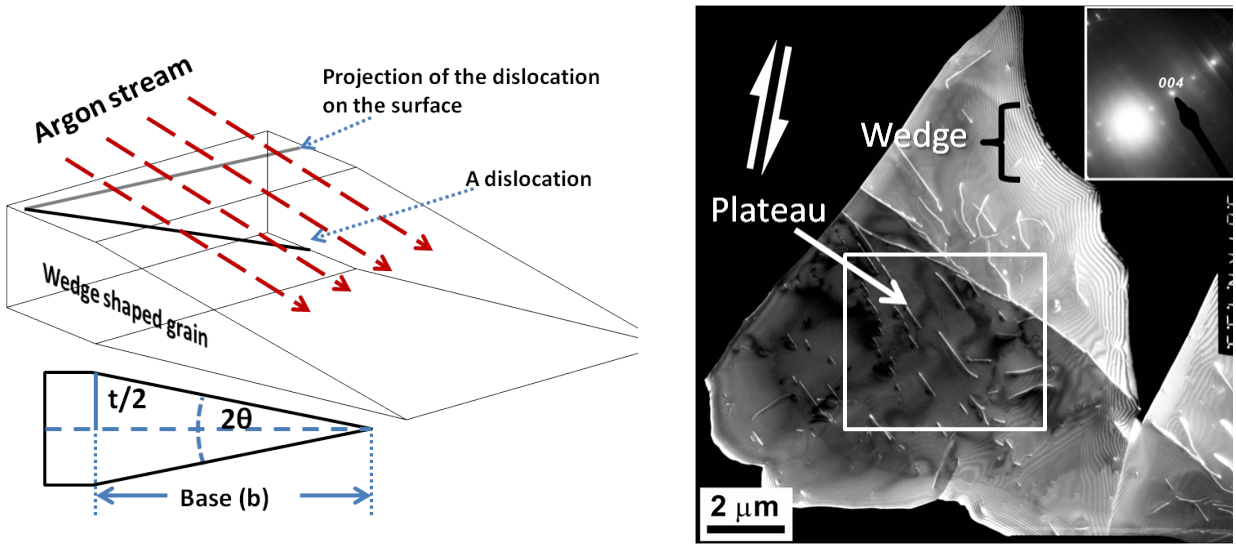

Figure 3-16: *Left*-During argon milling process, argon stream bombards the sample from top and bottom (only top stream is shown in the figure). This gives the milled grain shape of a wedge (marked by the presence of thickness fringes) with half-angle being equal to the angle of incidence of argon stream (~5°). Approximate thickness of the plateau of the grain can be calculated from this simple model. *Right*-Wedge shaped part and plateau top (region enclosed by white rectangle) of argon-milled olivine grain for specimen DD384 is shown here. This sample was deformed at 8.5 GPa and 1300°CNote than base (b) of the wedge part is approximately *2 μm*.

Argon milling has been done at varying voltage with an angle of incidence of Argon stream being ~5°.

From figure 3-14, we have:

$$Thickness\ of\ the\ plateau, t = 2b \tan\theta$$

$$For\ b \cong 2\mu m\ and\ \theta = 5°; sample\ thickness \approx 350\ nm$$

Total length of dislocations: Projected length of dislocation in the area of interest (white rectangular region marked in Figure 3.14-right) can be estimated manually or using an image processing program. Assuming that dislocations are a straight line and are inclined to the surface of the micrograph (Figure 3.14-left), the true length of a

dislocation, $l = \sqrt{(l_p)^2 + (t)^2}$ where l_p is the projected length of a dislocation and t is the thickness of the grain. Total length in this case, as measured from the 2-D micrograph, turns out to be $\sim 17.34\ \mu m$.

Dislocation Density: Now the dislocation density in the volume corresponding to the white rectangular area in the Figure 3.14 is $l/(area \times thickness) = \frac{17.34\ \mu m}{12.92\ \mu m^2 \times 0.35\ \mu m} = 3.84\ \mu m^{-2} = 3.84 \times 10^{12}\ m^{-2}$

$$Hence, from\ Eq.3.f;\ \ \boldsymbol{Flow\ stress}, \sigma_1 - \sigma_2 = \mathbf{272\ MPa}\ at\ 8.5\ GPa\ and\ 1300°C.$$

Measurement of stress using recrystallized grain size piezometer

As has been discussed in the previous sections, mean recrystallized grain size in a deformed specimen varies with flow stress.

Figure 3-15 shows this relationship for dry and wet specimens [*Jung and Karato,* 2001b]. Figure 3-17: Stress versus recrystallized grain-size relationship from Jung and Karato 2001. Stress magnitudes in the samples from this study were estimated from dislocation densities. The solid lines indicate the results of the least square fit for the 'dry' and 'wet' condition. The size of recrystallized olivine deformed under 'wet' conditions is significantly larger than that under 'dry' conditions at the same stress.

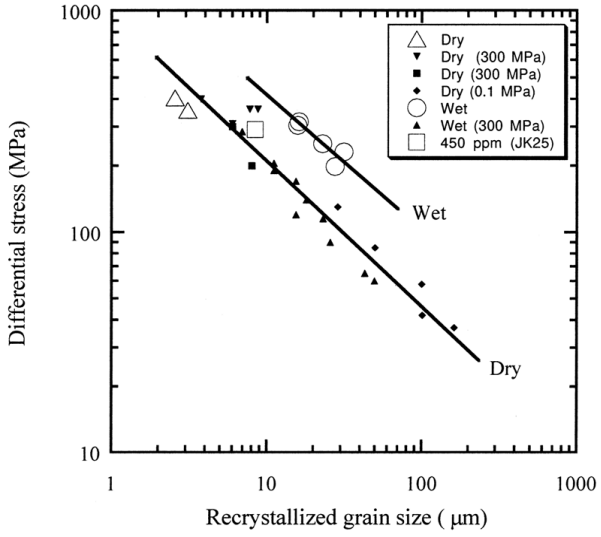

Referring back to the same sample DD384 (See figure 3-14 for a TEM micrograph of the same sample), recrystallized grain size in this sample has been found to be $\sim 7.6\ \mu m$. The stress corresponding to this value of recrystallized grain size is $\sim 230\ MPa$. This value is 40 MPa lower than the calculated value from the dislocation density method in the last section. The source of this discrepancy in the flow stress value could be the error in estimating grain sizes from EBSD measurement or due to the error in the thickness measurement of the grain from TEM micrograph. In this case, a step size of 4 μm has been used for data collection whereas the mean grain size is 7.6 μm.

3.5 Experiments under wet condition

Deformation experiments on wet olivine samples were performed at 3, 5 and 8.5 GPa pressures with the maximum value of the pressure corresponding to ~250 KM of depth in the upper mantle (Table 3-2). At least two experiments were performed at each pressure-temperature condition with the strain rate differing by an order of magnitude. For each of the three pressure points, experiments were carried out at 1300°C. Additionally, experiments were also performed at 1400°C at 5GPa and 1500°C at 8.5GPa.

The starting material for each deformation experiment consisted of polycrystalline San Carlos olivine powder mixed with equimolar mixture of brucite and silica as the source of water (Table 3-3). After achieving the desired pressure, the assembly was heated up and left to anneal for 2-3 hours at 1150°C, a temperature value less than the target temperature, to avoid excessive grain growth during annealing. This period also provides sufficient time for hydration of the olivine sample because of the breakdown of brucite during heating. Thereafter, the temperature was raised to the final target level for that experiment and deformation commenced through the advancement of the deformation anvils.

Table 3-3: List of experiments and experimental conditions under wet condition

Run ID	Pressure (GPa)	Temperature (°C)	Strain rate ($x10^{-5}$ s^{-1})	Shear[1] Strain	Water Content[2] (wt. ppm)	Stress[3] (MPa)
DD430	3	1300	3.2	1.2	90	250
DD477	3	1300	55	1.3	74	340
DD463	5	1300	4	1.1	279	210
DD461	5	1300	50	0.9	214	325
DD462	5	1400	5	2.4	168	310
DD466	5	1400	50	1.0	189	365
DD457	8.5	1300	2.5	1.1	419	310
DD456	8.5	1300	50	1.2	461	370
DD473	8.5	1500	15	1.1	401	300
DD460	8.5	1500	60	1.3	340	325

[1] Shear strain has been determined using sidewise displacement of the pistons.
[2] Estimation of water content is based upon calibration by Paterson (1982).
[3] Stress has been determined using recrystallized grain size versus stress relation except for DD456 which has been calculated using the dislocation-density obtained from TEM micrograph.

The shear strain for each experiment was calculated from the sideward displacement of the top and bottom alumina shear-pistons from post-mortem observation of the deformed assembly. This method had to be employed because hot pressed H_2O-bearing olivine aggregates proved to be far too fragile to cut into slices or added Pt strain markers. The totally strain applied to the cubic assembly, measured using the transducers attached to the independent deformation anvils, was always greater than that determined from the sideward displacement of the alumina shear pistons. This implies that the strain rate initially applied to the cubic assembly was actually moderately faster than those experiences by the sample. This difference results from the minor deformation of assembly parts other than the sample material. Hence, the nominal target strain on the cubic assembly was accordingly replaced by the determined sample strain and then the true strain rate experienced by the sample was calculated and given in Table 3-1. The corrections in strain between those measured on the entire cubic assembly and those actually experienced by the sample where generally within 10% of each other. This is in better agreement with what was observed for the dry samples and likely results from significant softening of the samples in the presence of H_2O.

Table 3-4: Starting material for deformation experiments on hydrous olivine

Sample ID	Starting material
DD477	Hotpressed San Carlos olivine (1 GPa) + 0.1 wt % Brucite+SiO_2 equimolar mixture
DD466	Hotpressed San Carlos olivine (1 GPa) + 0.5 wt % Brucite+SiO_2 equimolar mixture
Others	Polycrystalline olivine aggregate + 0.5 wt % Brucite+SiO_2 equimolar mixture

3.5.1 Measurement of water content using FTIR

The water content of each deformed specimen has been analyzed using FTIR spectroscopy. Two hundred scans are collected for each spectrum at a resolution of 1 cm^{-1}. Background correction has been made using a baseline obtained by piecewise cubic interpolation method (Fig. 3-16). Absorbance values for each specimen are normalized for hypothetical specimen of 1 cm thickness. Integration has been performed between wavenumbers 2950 to 3780 cm^{-1}. The calibration proposed by Paterson (1982), instead of the relatively newer one proposed by Bell et a. (2003), has been employed to relate the total integrated absorbance with wavenumber to the water content. This choice of calibration makes it possible to compare our water content data with results from Kohlstedt et al. (1996) and also directly compare with results from previous deformation studies (Jung et al. 2001; Karato et al., 2008) which have routinely employed the Paterson calibration.

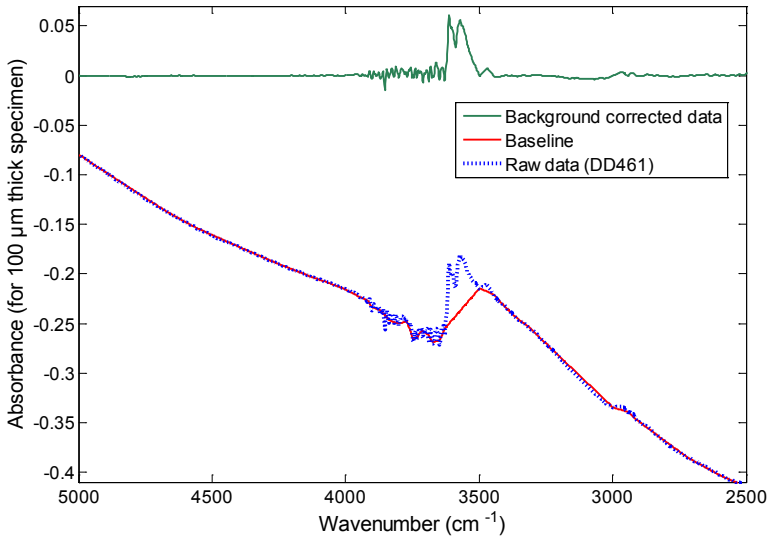

Figure 3-18: Background correction of the raw FTIR data. A baseline was created using piecewise cubic interpolation method. Water solubility values are sensitive to the choice of the baseline and range of wavenumber used for integration (2950 to 3780 cm^{-1} in our case).

The Bell et al. (2003) calibration most likely provides a better estimate of the H_2O content of olivine because it was performed specifically on olivine. The Bell calibration would imply H_2O contents that are approximately 3 times higher in comparison to that

measured by the Paterson calibration for H_20 content. However, rather than correcting data previous studies using an arbitrary correction parameter the H_2O contents are simply reported using the older calibration. Ultimately, the absolute H_2O contents are less important than the degree of saturation, which can be determined from comparison with the study of Kohlstedt et al. (1996), which also used the older calibration. Measurement of water content by either of the above-mentioned approaches, results in solubility values that are sensitive to both the choice of baseline and the range of wavenumber selected for the integration.

As shown in the figure 3-17, strong IR absorbance peaks can be observed at wavenumbers (in cm^{-1}) 3612, 3599, 3579, 3568 and 3568 for 8.5 GPa experiments (DD456, DD457 and DD460). Minor peaks at 3504, 3475 and 3450 cm^{-1} can also be seen. In the 5 GPa run products (DD461, DD463 and DD462), peaks at 3579 cm^{-1} and 3568 cm^{-1} are not so well resolved. IR spectra for neither of the samples exhibit any recognizable presence of *group II* bands that has been reported to occur below 3450 cm^{-1} [*Bai and Kohlstedt,* 1993; *Matveev et al.,* 2001].

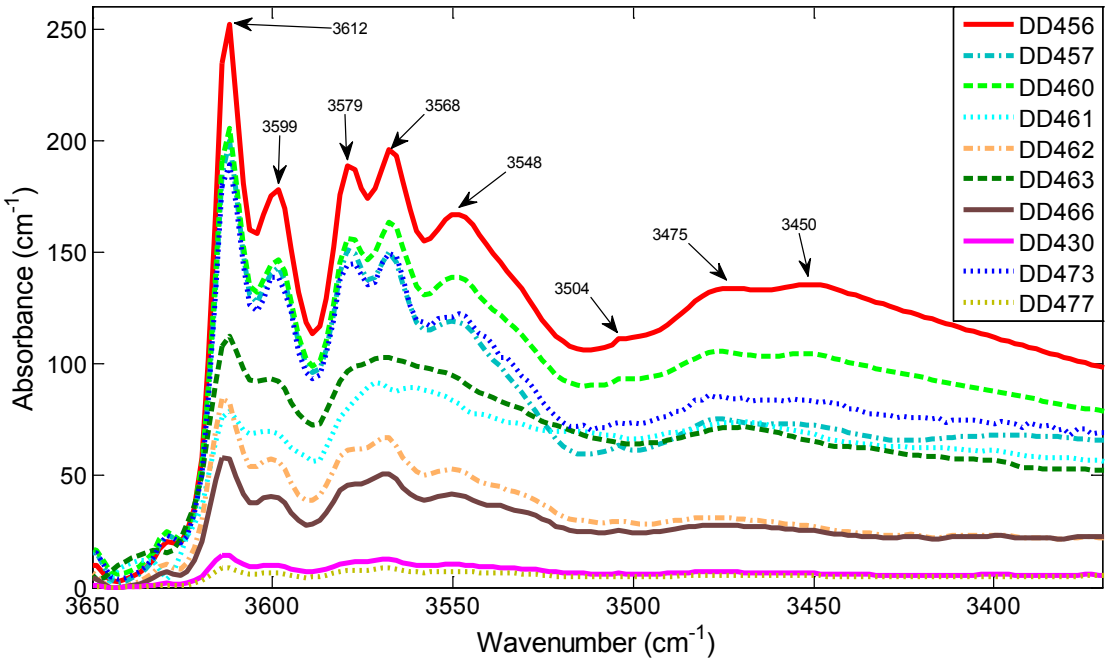

Figure 3-19: FTIR spectra of hydrous olivine specimen after the experiments. Absorbance of the spectra was normalized for 1 cm thick specimen.

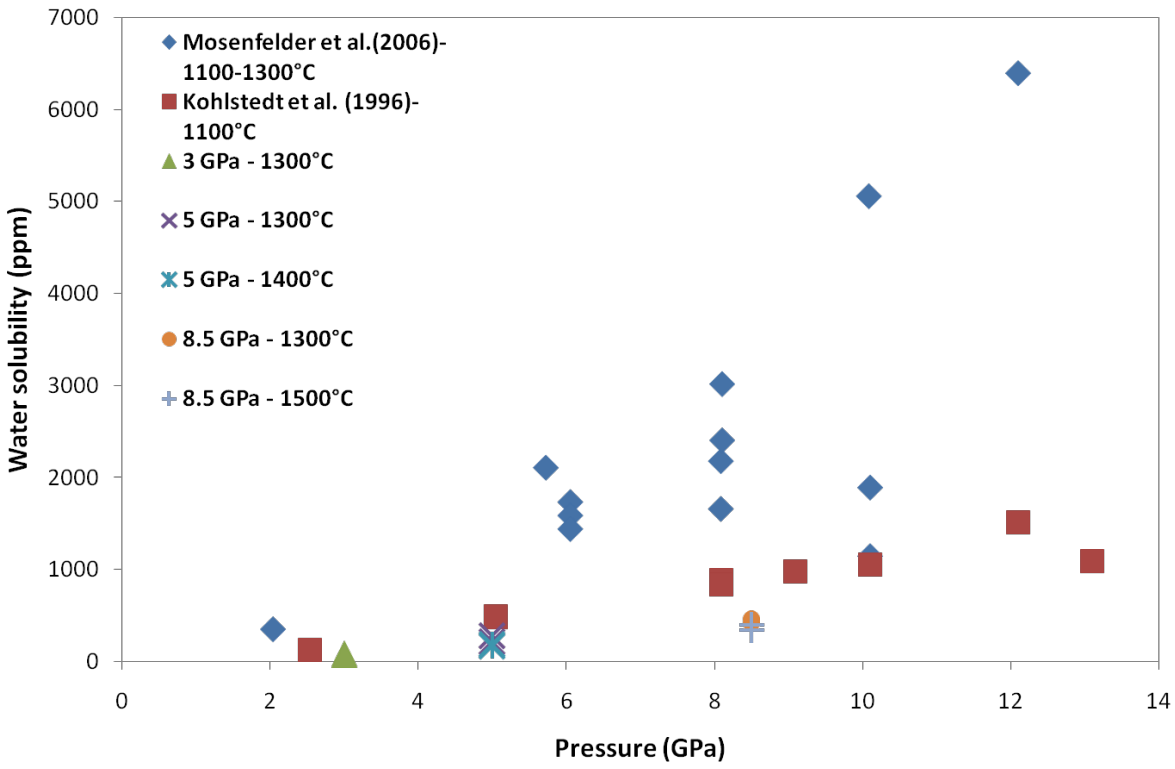

Figure 3-20: Water solubility in San Carlos olivine (modified after Keppler and Bolfan-Casanova [2006]). Our results are shown along with the experimental data from Mosenfelder et al. (2006; blue diamond) and Kohlstedt et al. (1996; red squares). The H_2O contents from this study employ the Paterson calibration so as to compare them directly with the work of Kohlstedt et al., 1996 where olivine was saturated with excess H_2O.This comparison indicates that the olivine from this study had H2O contents less than the saturation level (25-35%). The Study of Mosenfelder et al (2006) reported higher H_2O contents mainly because of using the newer Bell et al calibration.

Comparison of our water solubility results with previous works indicates that solubility values observed in our samples are lower than the saturation level reported by Kohlstedt et al. (1996) from 1100°C (Fig. 3-18). The water content in olivines recovered from this study varies between 25 and 35 % of the saturation level. Saturated H_2O olivine contents are expected to rise slightly with temperature but then drop at higher temperatures due to the presence of silicate melting. Some idea of how temperature may influence H_2O saturation levels can be gained by examining experiments performed by Smyth et al. (2006) on forsterite. The H_2O saturation limit in pure forsterite at 1250°C is almost double the value at 1100°C but it drops to almost half of the 1100°C value by 1500°C. The H_2O contents reported for San Carlos olivine in this study from 1500°C are lower than the saturated values reported by Kohlstedt et al. (1996) at 1100°C but may still be close to the

saturation limit, which may be lower at this higher temperature. Data from Mosenfelder et al. (2006) yield saturated H_2O contents for temperatures between 1100-1300°C are 2-4 times higher than the water contents from Kohlstedt et al. (1996), but most of this increase can be attributed to the use of the newer FTIR H_2O calibration proposed by Bell et al. (2003).

3.5.2 NMR spectroscopy on hydrous Forsterite

Positions of the resonance peaks obtained from ^1H MAS (magic angle spinning) NMR are extremely sensitive to the minute differences in the chemical environment around a nucleus. Differences in the position of the resonance peaks are referred as chemical shift, which is measured in ppm. A known weight of powdered sample material is loaded in a ceramic rotor of length 1.2 cm and inner diameter 1.5 mm. After being placed in the NMR probe, such that the angle between the direction of the external magnetic field and rotor axis is 54.7° (the magic angle), the rotor is spun at very high speed (30 KHz). This choice of angle coupled with high rotation speed, minimizes the broadening of resonance peaks.

In nominally anhydrous minerals, H should be strongly bonded to the adjacent oxygen [*Kohn,* 2006]. Results from hydroxyl containing minerals and other materials indicate that a strong correlation exists between not only between chemical shift (δ) and $O-H$ distance (r_{OH}) [*Brunner and Sternberg,* 1998] but also between δ and $O-H..O$ distance ($r_{O..O}$) [*Eckert et al.,* 1988]. Moreover, the area under an NMR resonance curve is directly proportional to the number of resonating nuclei. Hence, position of the resonance peaks, expressed as chemical shift with respect to the resonance peak of reference material Tetramethylsilane ($(CH_3)_4Si$, usually referred to as TMS), gives us information regarding the chemical environment of the hydrogen. On the other hand, calculating the area under the resonance curve and comparing it with NMR spectra of a standard material with known water content (e.g. Gypsum), we can find out the absolute number of the H nuclei present in the sample. This approach of measuring water content using ^1H MAS NMR has a detection limit as small as 1 ppm of H_2O by weight [*Kohn,* 2006].

Hydrous forsterite samples were prepared at 11 GPa and 1150°C using 6-8 type multi-anvil apparatus. In case of sample Z771, 2 wt% of equimolar mixture of brucite and silica

was added to the synthetic forsterite powder whereas 0.5 wt% of brucite-silica mixture was added to the sample in case of the specimen Z769. Annealing time for both the samples was approx. 4 hours.

Table 3-5: Description of the starting material and water content from ^{1}H MAS NMR and FTIR measurements

Sample ID	Starting material	Weight – sample material (gms)	Resonance peak area (x10^{6} units)	Water content (1H MAS NMR) (wt %)	Water content (FTIR) (wt ppm)
Gypsum (Standard)	Powdered Gypsum	0.0152	2.0738	20.93	
Z771	Synthetic Forsterite (11 GPa, 1150°C) With 0.5 wt% rucite-SiO_2 equimolar mixture	0.0224	0.2725	1.87	
Z769	Synthetic Forsterite (11 GPa, 1150°C) With 2.0 wt% Brucite-SiO_2 equimolar mixture	0.0209	1.0292	7.55	559

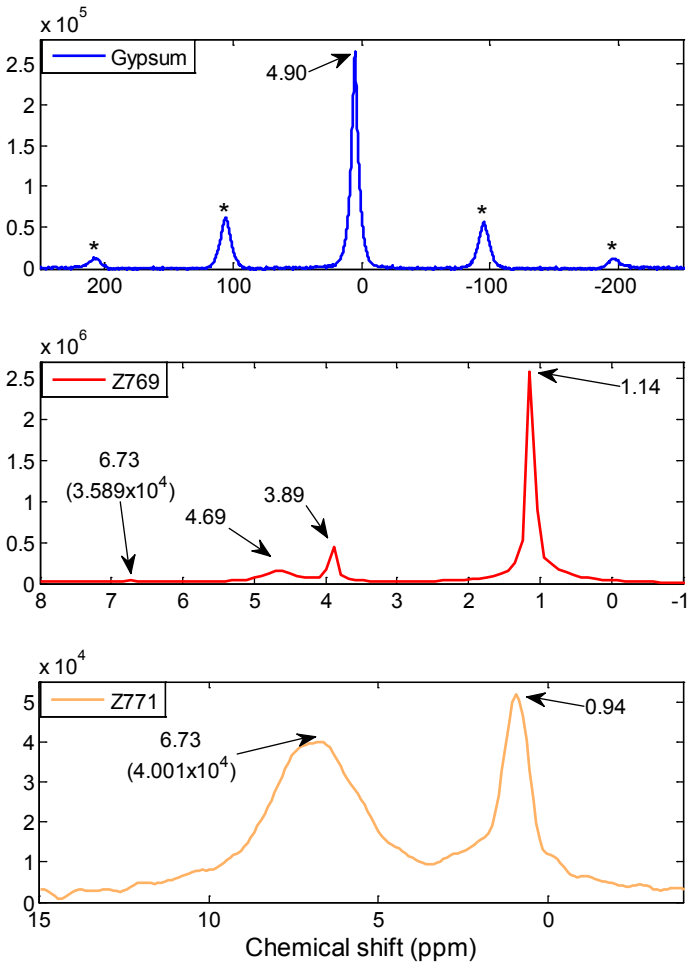

Figure 3-21: NMR spectra for gypsum and synthetic forsterite sample. Gypsum with its known water content has been used as the standard. Synthetic forsterite was synthesized by adding small amount of equimolar mixture of Brucite and Silica with forsterite (see Table 3-2) at 11 GPa and 1150°C using 8-6 type MA apparatus. Sample Z769 was added with 4 times more brucite-silica mixture than Z771. Chemical sift for peaks are marked by the arrow. The value in the parenthesis for δ 6.73 is the corresponding value of the ordinate.

Figure 3-21 shows the NMR spectra for the standard material, gypsum and two synthetic hydrous forsterite samples. Gypsum shows resonance peaks at chemical shifts δ *at* 4.90 *ppm.*

Hydrous forsterite *Z769* specimen with higher amount of added water (as brucite) to start with, shows peaks at δ 1.14, 3.89, 4.69 *and* 6.73 *ppm*. Specimen *Z771*, with four times lower water added water in the beginning, shows peaks at δ 0.94 *and* 6.73. In the case of specimen Z769, relative contribution of peak at δ 6.73 *ppm* is far lower than that in specimen *Z771*. Interestingly, the absolute contribution of this δ 6.73 *ppm* for both cases has stayed the same, around $4x10^4$ units (Z769 -> $3.59x10^4$ and Z771 -> $4.01x10^4$) and minor difference in the value could be related to slight difference in the probe conditions during measurements of the two specimens.

Table 3-6: *O – H...O* distance for different stretching frequencies present in the FTIR spectra of the hydrous Forsterite (Z769) and olivine sample using relation correlation proposed by Libowitzky (1999). Chemical shift values observed using ^{1}H MAS NMR and corresponding *O – H...O* distance in the hydrous forsterite sample (Eckert,1988) has been shown in the bottom two rows.

Wavenumber (cm^{-1}) Z769	3612		3579		3566		3541	3533		3477			3396	3232	3066	2927
Wavenumber (cm^{-1}) Olivine	3612	3599	3579	3568		3548			3504		3475	3450				
$r_{O..O}$ (Å)	3.22	3.10	3.02	2.99	2.98	2.95	2.93	2.92	2.88	2.86	2.85	2.83	2.80	2.72	2.68	2.65
δ (ppm) Z771		1.14				3.89		4.69			6.73					
δ (ppm) Z769		0.94														

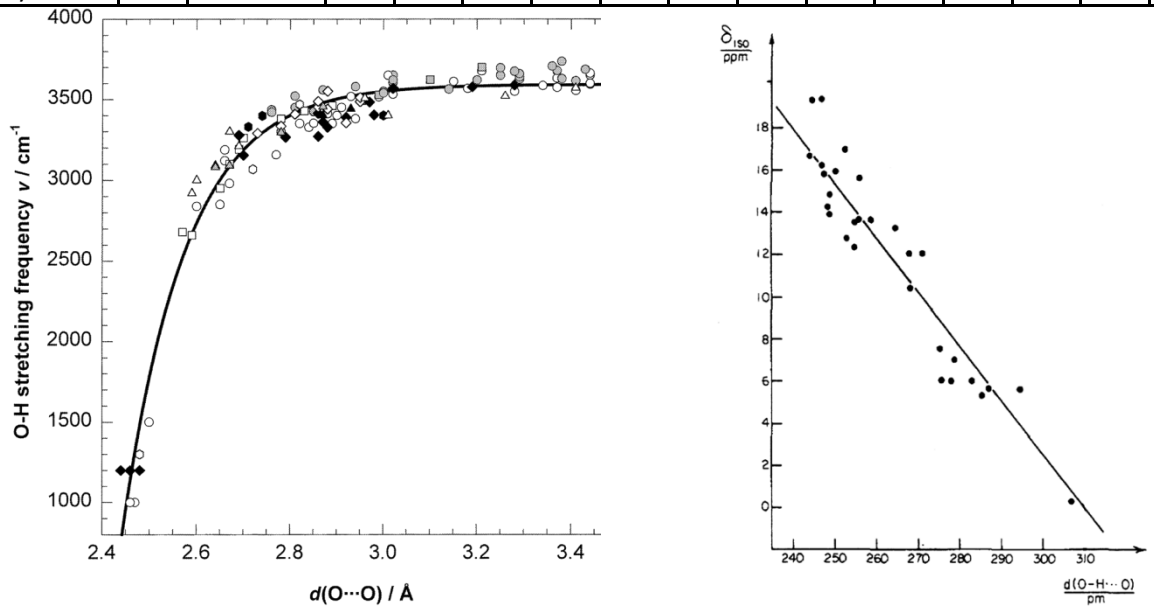

Figure 3-22: Left: relation between O-H stretching frequency and d (O...O) [*Libowitzky,* 1999]. open symbols represent straight H bonds, shaded symbols mark bent H bonds, and filled ones denote copper compounds; circles - silicates, squares - (oxy)hydroxides, hexagons - carbonates, diamonds - sulfates, triangles - phosphates and arsenates. Right: isotropic chemical shifts versus O – H...O distance for various crystalline compounds (Eckert et al. 1988)

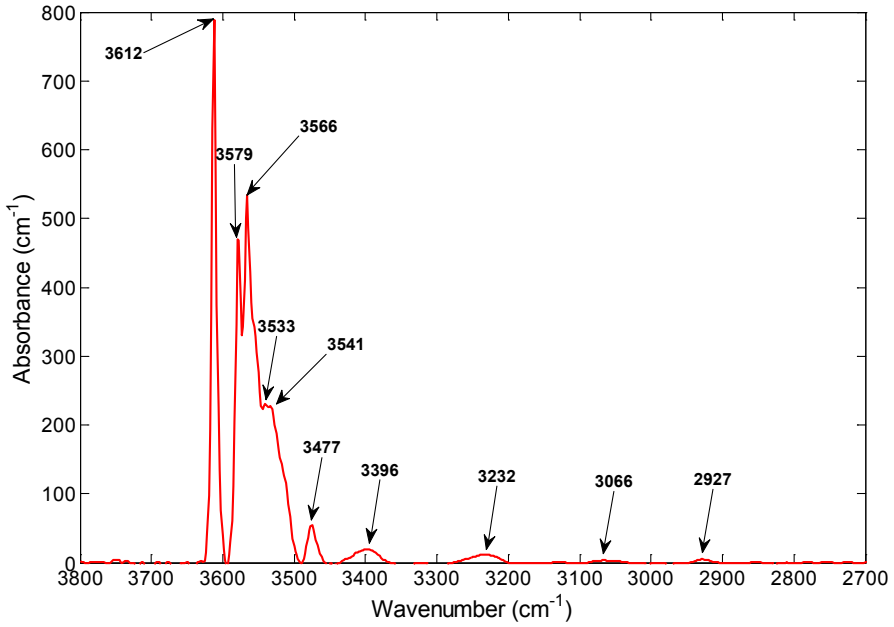

Figure 3-23: FTIR spectra of the specimen Z769 containing Fe-free synthetic forsterite with two wt. percentage brucite-SiO2 equimolar mixture. Water content in this sample was measured using FTIR is 559 wt. ppm using calibration by Paterson (1982)

As has been mentioned above, chemical shift δ and $O-H..O$ distance ($r_{O..O}$) have a correlation [*Eckert et al.,* 1988] (Fig 3-22) and it can be expressed using the following relation.

$$r_{O..O}(\text{Å}) = (79.05 - \delta)/25.5 \qquad \text{3.g.}$$

where; δ is the chemical shift in ppm

Alternatively, one can use estimate $O-H..O$ distance ($r_{O..O}$) from O-H stretching frequencies (from infrared spectroscopy) using the relation proposed by Libowitzky (1999) for silicates (Fig 3-22), expressed as:

$$r_{O..O}(\text{Å}) = -0.1346 \times \ln\frac{(3622 - \nu)}{2.38 \times 10^{11}} \qquad \text{3.h.}$$

where; ν is the wavenumber in cm^{-1}

Table 3-6 shows the likely $r_{O..O}$ values for the stretching peaks observed in the FTIR spectra of the specimen Z769 and other olivine samples and the corresponding relation

with the chemical shift from two specimens Z771 and Z769 are shows in the table 3-6 in the last two rows.

3.5.3 General microstructures

In general, the average grain sizes for the wet specimens are smaller in comparison to their dry counterparts deformed under similar P, T and strain rate conditions. Grains are rarely polygonal shaped and they have serrated boundaries (e.g. Fig 3-8:DD462). The degree of recrystallization is much higher for wet specimens (Table 4-3), on average more than 50%, whereas for dry specimens recrystallization was limited to 20% for most of the samples. Moreover, a clear foliation is visible in all the specimens with the long axes of the grains parallel to the plane of foliation (e.g. Fig 3-8:DD462).

As has been discussed before, the strain partitioned into the wet specimens was in general larger than that in the dry specimens for the same amount of deformation anvil displacement. For the dry samples, a larger proportion of the strain was accommodated by deformation of other assembly components. This apparent weakening of hydrous olivine is correlated with higher degrees of dynamic recrystallization in these samples. If this is the case weakening due to H_2O is unlikely to be because of so-called hydrolytic weakening as observed in quartz for examples where Si-O-Si bonds are broken through hydrolysis. In olivine, it is more likely that H_2O is enhancing dynamic recrystallization, which is pushing the specimen into the GSS diffusion creep regime, leading to weakening and strain localization.

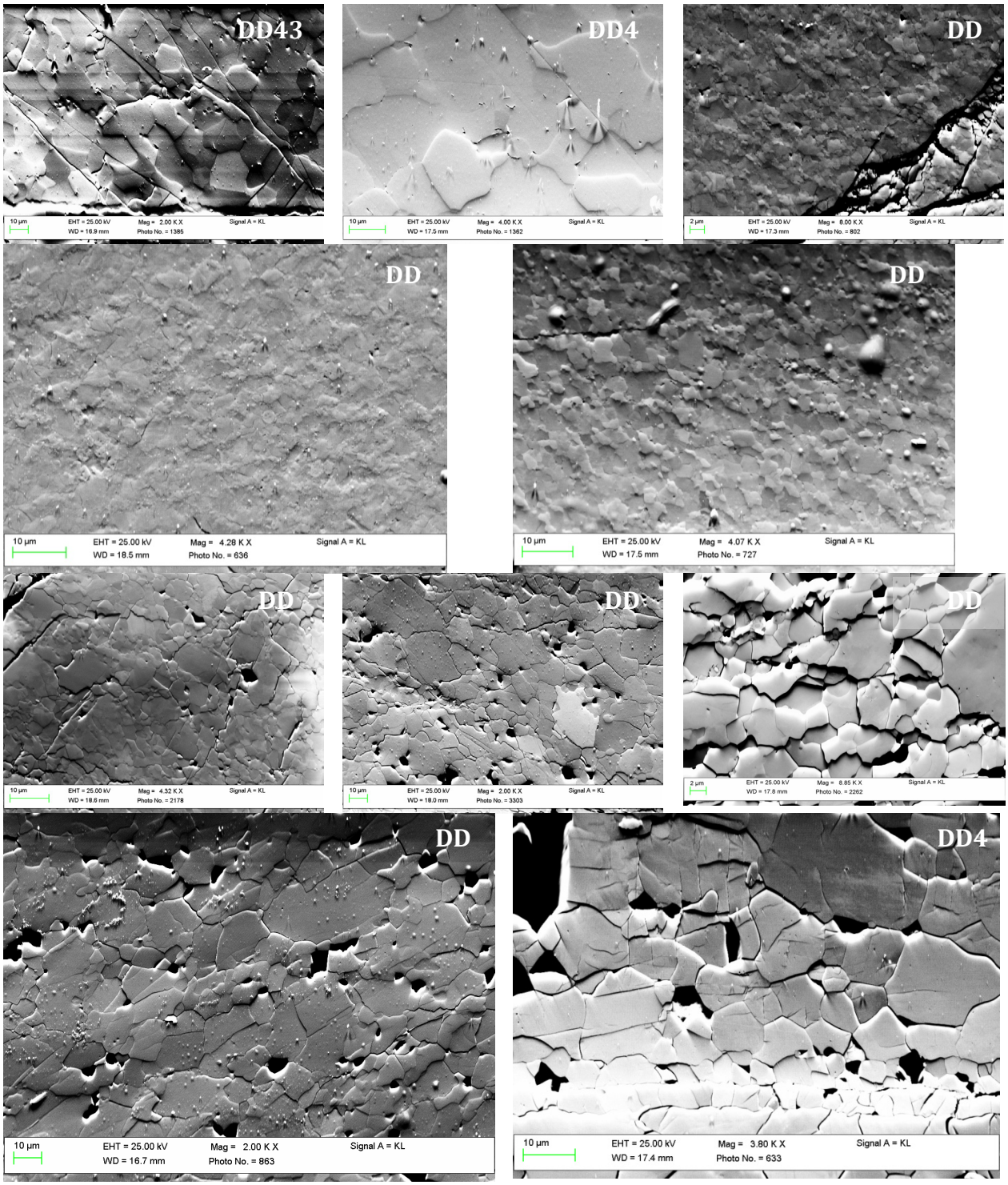

Figure 3-24: SEM orientation contrast images of the specimens deformed under wet condition. In general, the average grain sizes in the hydrous specimens are smaller in comparison to their dry counterparts in terms of P-T conditions. Grains in wet specimens have serrated boundaries.

Table 3-7: Degree of recrystallization and recrystallized grain size for wet specimens

Run ID	Press-ure (GPa)	Temperature (°C)	Strain rate ($x10^{-5}$ s^{-1})	Shear Strain	Water Content (wt. ppm)	Stress (MPa)	Fraction of grains recrystallized (%)	Recrystallized grain size (μm)
DD430	3	1300	3.2	1.2	90	250	62.8	10.70
DD477	3	1300	55	1.3	74	340	55.3	6.92
DD463	5	1300	4	1.1	279	210	51.3	12.32
DD461	5	1300	50	0.9	214	325	32	7.2
DD462	5	1400	5	2.4	168	310	65.8	6.84
DD466	5	1400	50	1.0	189	365	55.7	4.8
DD457	8.5	1300	2.5	1.1	419	310	35.9	7.35
DD456	8.5	1300	50	1.2	461	370	52.5	4.65
DD473	8.5	1500	15	1.1	401	300	43.6	7.65
DD460	8.5	1500	60	1.3	340	325	54.8	7.2

3.5.4 SEM and EBSD characterization

3 GPa pressure and 1300°C

In the wet sample deformed at 3GPa and at a slower strain rate of $3.2x10^{-5}$ evidence can be seen for relatively equal activity of both the (010)[100] and (100)[001] slip systems (Fig.3-23: Top). Interestingly poles to the (100) plane of the (100)[001] slip system are sub horizontal and rotated anticlockwise with respect to the Y_0 axis. This rotation is anomalous, as the shear sense should cause anticlockwise rotation only until the maxima are aligned with the Y_0 axis. The most likely explanation for this is as a result of additional compressive strain experienced by the powdered starting material. The direction of the compressive strain is at 45° to the shear direction.

In the dry experiments, reported in section 3.3.2, (010)[100] was found as the most common slip system. This is also observed to be the most common slip system in natural samples and in previous experiments performed at relatively lower stresses under dry conditions [*Carter and Ave'lallemant,* 1970; *Nicolas et al.,* 1973; *Phakey et al.,* 1971; *Zhang and Karato,* 1995; *Zhang et al.,* 2000]. The (100)[001] slip system on the other hand is common in experimentally deformed specimens that contain more than approximately 40 wt. ppm water [*Karato,* 1995; *Karato et al.,* 2008; *Katayama and Karato,* 2008], which is therefore quite consistent with this result.

The pole figure for the specimen (DD477) deformed under similar pressure-temperature-water conditions but performed at a higher strain rate ($5.5x10^{-4}$ s^{-1}) (Fig. 3-23: Bottom) exhibits a fabric developed only through the activity of the (100)[001] slip system. This experiment is therefore also consistent with previous experiments performed at these H_2O concentrations at pressures below 2.2 GPa [*Karato,* 1995; *Karato et al.,* 2008; *Katayama and Karato,* 2008].

Strain-rate: 3.2×10^{-5}; Water content: 90 wt. ppm; No. Of grains: 3320; Shear strain ≈ 1.2

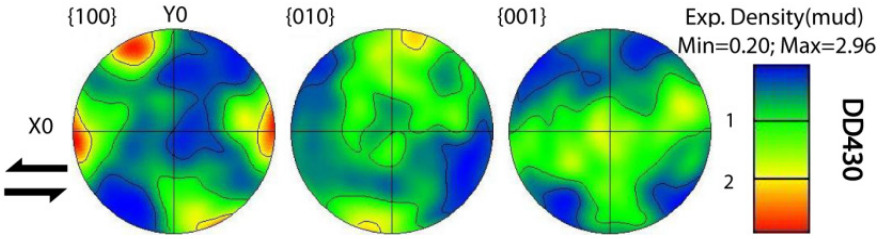

Strain-rate: 5.5×10^{-4}; Water content: 74 wt. ppm; No. Of grains: 3500; Shear strain ≈ 1.3

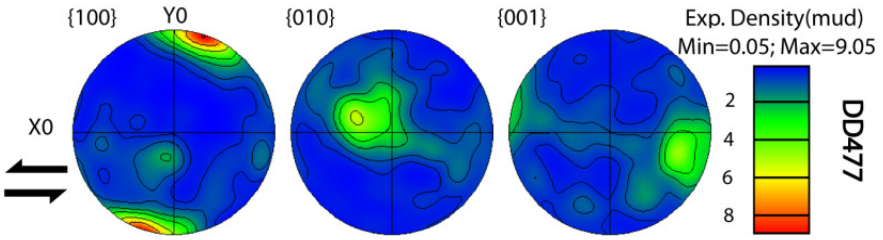

Figure 3-25: Wet samples deformed at 3 GPa and 1300°C. Sample deformed at lower strain rate (Top) shows two active slip systems – (010)[100] and (100)[001]. (Bottom) Sample deformed under higher strain shows only (100)[001] slip system to be active.

5 GPa pressure and 1300°C

Strain-rate: 4×10^{-5}; Water content: 279 wt. ppm; No. of grains: 4010; Shear strain ≈ 1.1

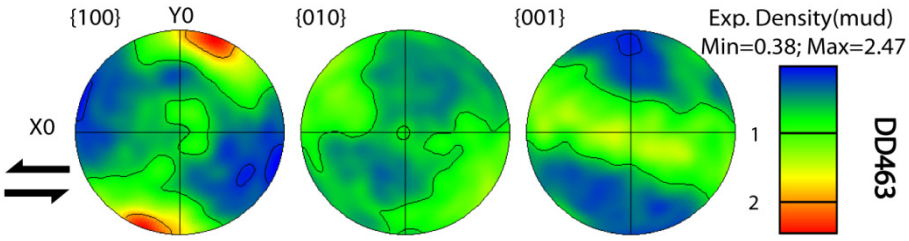

Strain-rate: 5×10^{-4}; Water content: 214 wt. ppm; No. of grains: 3800; **Shear strain ≈ 0.9**

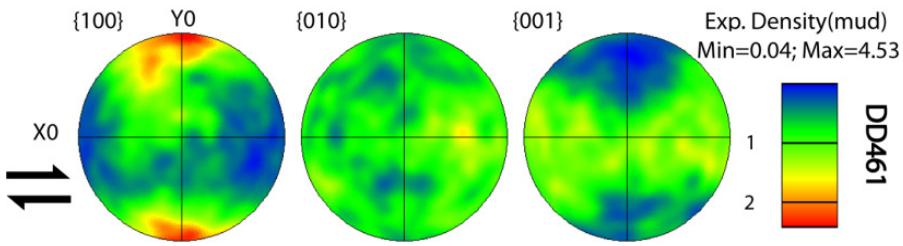

Figure 3-26: Wet samples deformed at 5 GPa and 1300°C. Both the high strain rate and low strain rate sample exhibit only one active slip system – (100)[001].

5 GPa pressure and 1400°C

Strain-rate: $5x10^{-5}$; Water content: 168 wt. ppm; No. Of grains: 4670; Shear strain ≈ 2.4

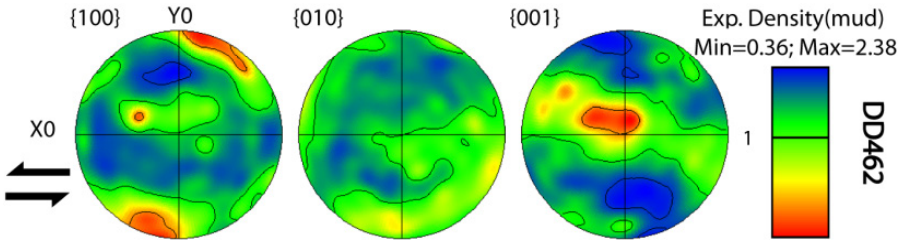

Strain-rate: $5x10^{-4}$; Water content: 189 wt. ppm; No. Of grains: 3920; Shear strain ≈ 1.0

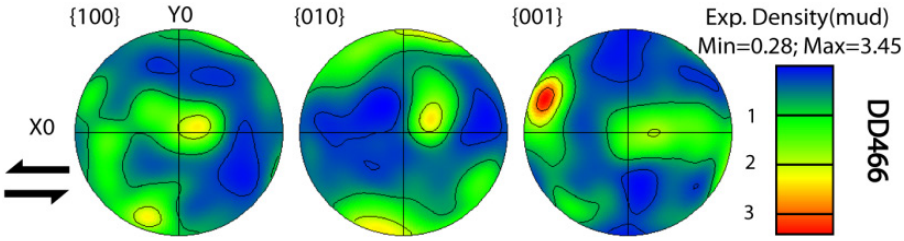

Figure 3-27: Wet samples deformed at 5 GPa and 1400°C. Sample deformed at lower strain rate (Top) shows mainly one active slip systems – (100)[001]. Whereas, (Bottom) Sample deformed under higher strain has two (010)[001] and (100)[001] slip systems active.

The (100)[001] slip system is the only active slip system observed in the specimens deformed at 5 GPa and 1300°C irrespective of the strain rate at which they were deformed (Fig 3-24). In this case the [001] axis poles appear in a girdle pattern which likely results from a component of compressive strain of the powdered aggregate sample. Compression causes alignment in the [001] direction but as there is no unique shear direction a girdle develops. Deformation experiments on powdered aggregates often result in a non-zero contribution from compressive strain to the overall deformation during compaction of the sample material.

At 5 GPa and slightly higher temperature of 1400°C the slower strain rate experiment exhibits the same fabric as that observed at lower temperature i.e. (100)[001]. At the same conditions but at higher strain rate the fabric of the recovered sample is again dominated by the (100)[001] slip system (Fig 3-25). In addition, however, a weaker fabric resulting from activity of the (010)[001] slip system is also present. While the (100)[001] slip

system has been previously observed to be active at high H2O content, the (010)[001] slip system has been previously documented under higher stress conditions irrespective of the H2O content. (Karato 1995; Karato et al. 2008; Katayama et al. 2008) report the (010)[001] slip system as dominant over a range of H2O contents at stresses over 300 MPa, from experiments performed at pressures <2.2 GPa. This would again be consistent with the experiments performed at these conditions where evidence for the (010)[001] slip system appears in the experiment performed with a faster strain rate and therefore under higher stresses.

8.5 GPa pressure and 1300°C

Strain-rate: $2.5x10^{-5}$; Water content: 419 wt. ppm; No. Of grains: 3850; Shear strain ≈ 2.4

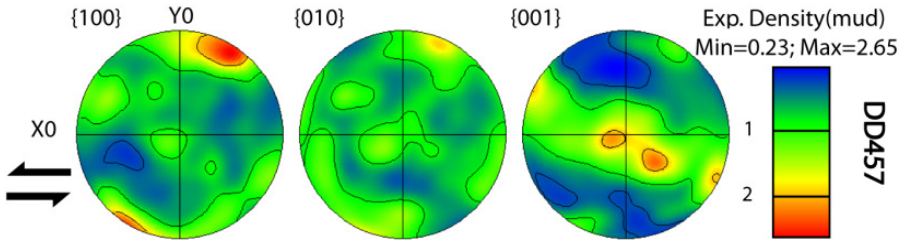

Strain-rate: $5x10^{-4}$; Water content: 461 wt. ppm; No. Of grains: 4350; Shear strain ≈ 1.0

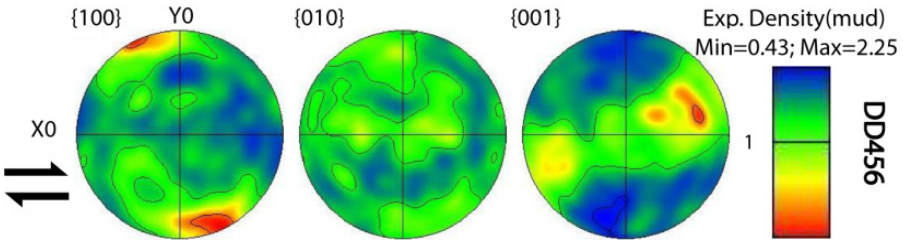

Figure 3-28: Wet samples deformed at 8.5 GPa and 1300°C. Irrespective of the strain rate, both the specimens deformed at 8.5 GPa and 1300°C show two active slip systems –(010)[100] and (100)[001]. This observation is consistent with activity of (010)[001] slip system at relatively higher stresses and (100)[001] slip system under hydrous condition.

Fabrics developed in samples deformed at 8.5 GPa and 1300°C (Fig 3-26) are in general very similar to those found in the wet samples at 3 and 5 GPa. The sample at low strain rate shows evidence for the dominant slip system being (100)[001], however either (010)[100] or (010)[001] or both may also be active, albeit with much lower activity than the (100)[001] slip system.

Sample DD456, which was deformed at the same pressure and temperature conditions but at a higher strain rate, has also developed a fabric dominated by the (100)[001] slip system but again a weak contribution from the (010)[001] slip system also seems to be present. This two-slip system combination appears consistent with dislocation activity under higher stresses and hydrous condition as also proposed in previous studies [*Karato,* 1995; *Karato et al.,* 2008; *Katayama and Karato,* 2008]. TEM observation on the sample DD456 confirms the presence of these two slip systems (See section 3.1.2).

8.5 GPa pressure and 1500°C

Unlike the pole figures for dry experiments deformed at 8.5 GPa and 1500°C, where no appreciable LPO was detected, most likely as a result of deformation occurring in the diffusion creep regime and likely assisted by grain boundary sliding, wet experiments have developed strong fabrics under both slow and fast strain rates.

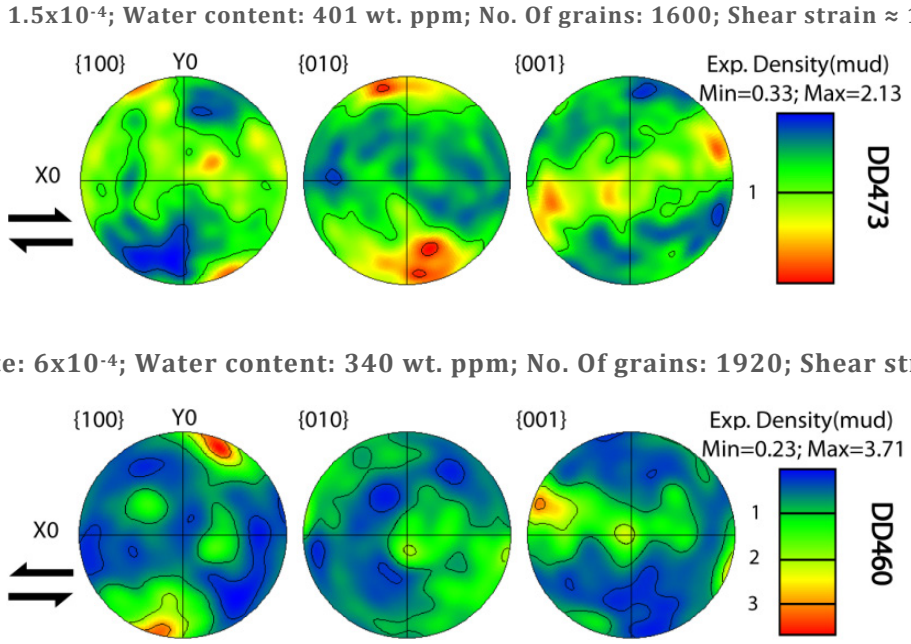

Figure 3-29: Wet samples deformed at 5 GPa and 1500°C. Sample deformed at lower strain rate (Top) shows two active slip systems – (010)[100] and (100)[001]. (Bottom) Sample deformed under higher strain shows only (100)[001] slip system to be active.

At the relatively slower strain rate of $1.5x10^{-4}$ the (010)[001] slip system appears to have led to a slightly stronger fabric than the sub equally present (100)[001] slip system. At the faster strain rate of $6x10^{-4}$, however, the (100)[001] slip system dominates with only a faint indication that (010)[001] slip may also be present.

3.5.5 TEM characterization

In order to relate the observed fabric with the dislocation microstructure a TEM investigation was carried out on sample DD456, which was deformed under a higher strain-rate of 5x10-4 at 8.5 GPa and 1300°C and contained a water content of 958 wt. ppm. It was considered unnecessary to examine multiple wet samples from various conditions using the TEM as EBSD measurements show all wet samples to have essentially similar LPO fabric and therefore should all show evidence for dislocations with [001] Burgers vectors slipping on either the (010) or (100) planes. The LPO for sample DD456 is typical of this wet fabric, which is dominated by the (100)[001] slip system but with evidence for weaker activity of the (010)[001] slip system.

TEM micrographs of DD456 show evidence for c-dislocations with slip planes being (010) and (100). Edge segments for the (010)[001] dislocations are more mobile whereas for the (100)[001] slip system dislocations, screw segments are more mobile. Cross-slip is an active process as marked by the pointer 1 in the top image (Fig 3-28) and some of the edge (100)[001] dislocations are kinked (pointer 2 in Fig 3-28). Evidence of cross-slip can also be seen in the bottom-left image as indicated by the white arrows. The bottom-right image shows long and straight screw dislocations from (010)[001] slip system. There is fewer sub grain boundaries observed in comparison to samples deformed under dry conditions. Presence of long and straight screw segments could also indicate resistance to the glide of dislocation.

Although potentially also showing the tops of dislocation loops, the structures in the HRTEM image shown in Fig 3-29 seem to be more consistent with being the cores of a weakly dissociated c-dislocations. The Fast Fourier transformed image (Fig 3-29: lower right) of the dissociated c-edge dislocation when viewed along the {110} zone axis, shows a

variation in contrast. The image contrast in the dislocation core regions is different from that in the surrounding bulk, indicating the core is expanded.

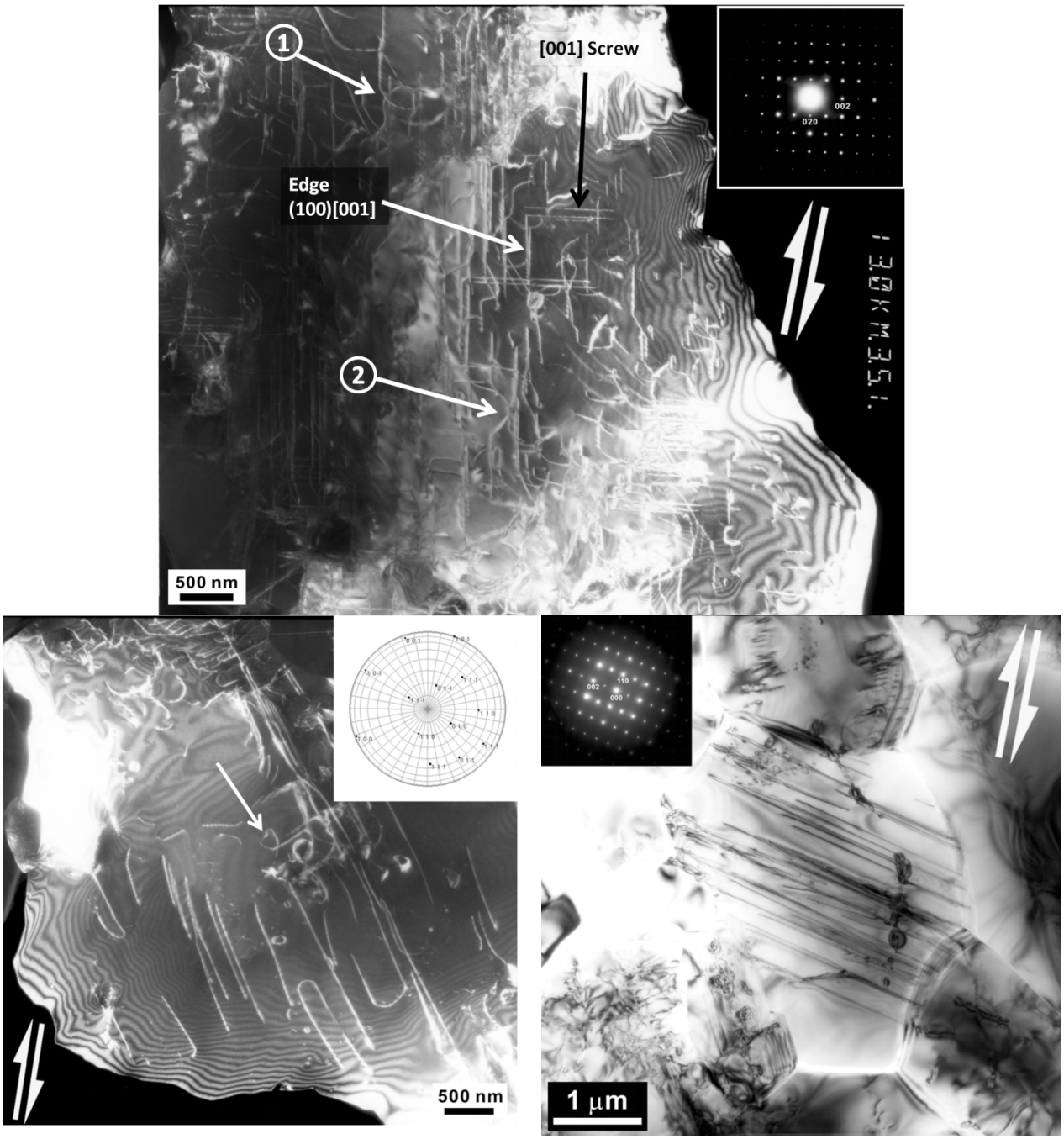

Figure 3-30: TEM micrographs for the wet specimen DD456. Deformation experiment was carried out at 8.5 GPa and 1300°C with a strain rate of $5x10^{-4}$. Top figure shows the presence of c-dislocations. (100)[001] dislocations are mostly of edge nature where as the [001] screw dislocations are most likely from (010)[001] dislocation. Evidence of cross-slip can be also seen as indicated by marker 1 in top image and white arrow in the bottom-left image. Bottom-right figure also shows straight c-screw dislocation from (010)[001] slip system.

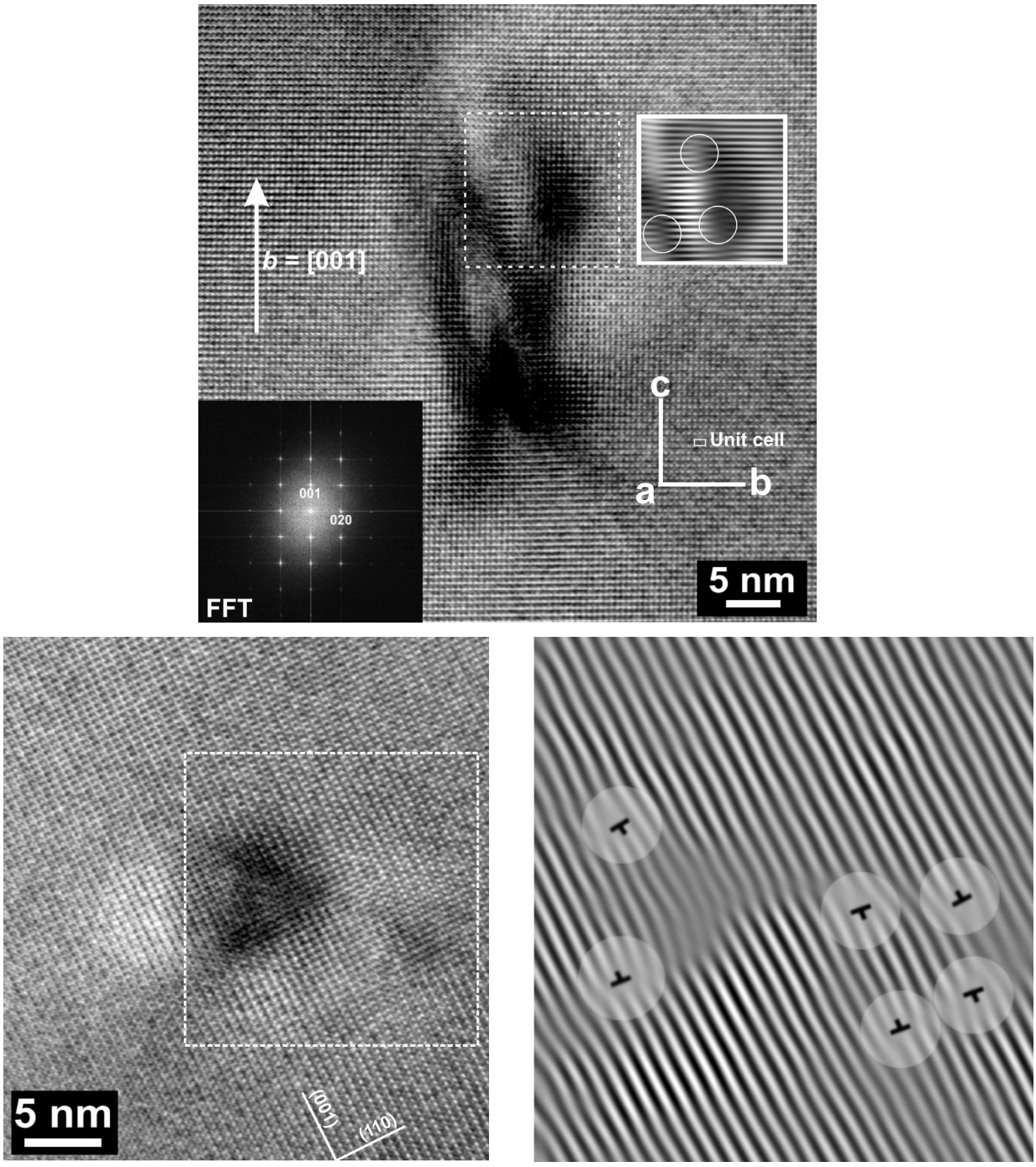

Figure 3-31: A typical HRTEM image (upper and lower right) and the Fast Fourier transformed image (lower right) of the dissociated c-edge dislocation viewing along the {110} zone axis of a deformed hydrous olivine. The image contrast in the dislocation core regions is different from that in the surrounding bulk, which indicates that the core is expanded.

3.6 Deformation experiment on Peridotite modal composition

Deformation experiments performed were performed on a peridotite assemblage at 8.5 GPa and 1300°C. In the low strain rate sample, the likely active slip systems are (010)[100] and (010)[001] whereas the dominant slip system in olivine in the high strain rate sample is (010)[001]. In case of pyroxene assemblage (100)[001] slip system is the only likely active slip system in both high and low strain rate sample (Table 3-8).

Table 3-8: Experimental conditions for Peridotite deformation experiments and likely active slip systems

Run ID	Pressure (GPa)	Temperature (°C)	Strain rate ($x10^{-5}$ s^{-1})	Stress (MPa)	Likely Active slip systems
DD495	8.5	1300	5	230	Olivine: (010)[100] and (010)[001] Pyroxene : (100)[001]
DD483	8.5	1300	40	325	Olivine: (010)[001] Pyroxene : (100)[001]

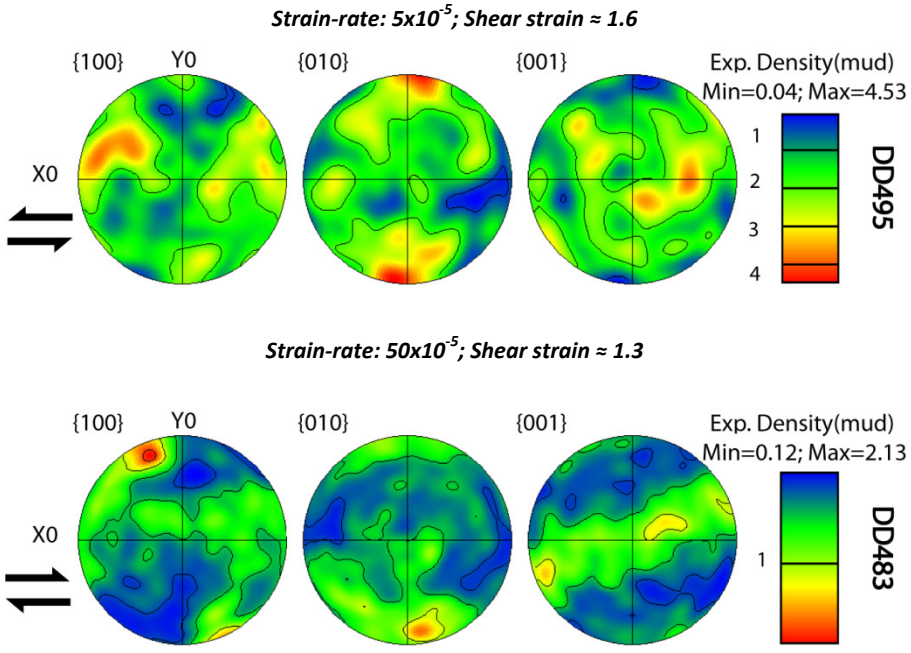

Figure 3-32: Peridotite samples deformed at 8.5GPa and 1300°C. Olivine in the slowly deformed aggregate likely has both (010)[100] and (010)[001] slip systems active whereas in the experiment conducted at higher strain rate the slip system is (010)[001]. Pyroxene in both the cases show (100)[001] slip system

These results indicate an identical olivine fabrics to those observed in monomineralic experiments at the same conditions. Fabrics for diopside and enstatite were found to be similar to those found in previously performed lower pressure experiments.

In-situ measurement of stress using piezoelectric sensor

Piezoelectric stress measurements were made using $GaPO_4$ single crystals within a 8/6 multianvil assembly. Many test experiments were made in the D-DIA however the most successful runs, where drift was minimal, were performed using the 6-axis MAVO press. The success of the MAVO press in these experiments most likely originates from the highly resistive electrical insulation of each individual anvil. In the D-DIA press the top and bottom guide blocks are electrically connected via the oil lines to the deformation rams.

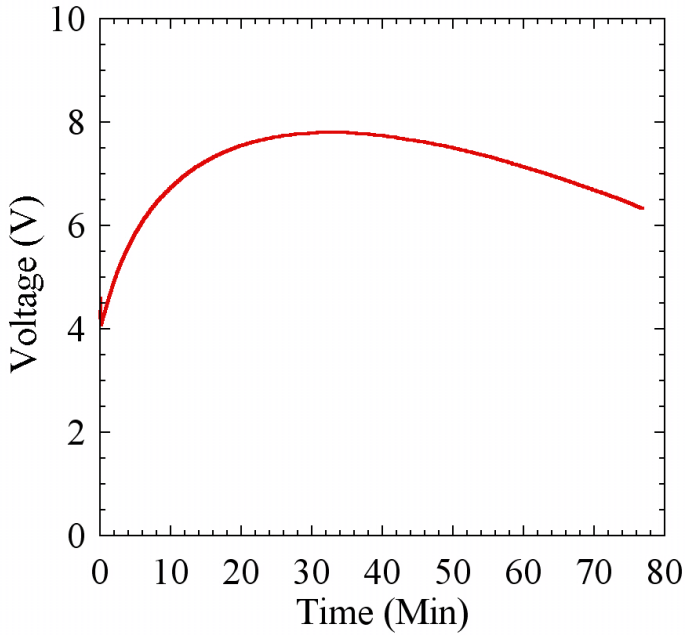

Figure 3-33: Output voltage from the charge amplifier as a function of time for an experiment where a $GaPO_4$ crystal was compressed to 2 GPa and then held at constant static pressure for 80 min.

The anvils therefore cannot be used as part of the circuit and crystals must, therefore, be connected via separate cables that pass through the gasket. The use of the cables that have to pass through the gaskets that form as the cubic assembly is compressed probably results in current leakage.

Figure 3-33 shows the output voltage from the charge amplifier for an experiment compressed to 2 GPa, which remained under static conditions for 80 min. This voltage change would correspond to changes in stress of the order of 5 GPa over this time period and more likely results from drift. The origin of this drift is unclear. Drift is positive for the first 30 min but eventually goes through a maximum and decreases. However, the slope of

the drift is relatively linear over periods of a few minutes such that drift can be eliminated from the data through fitting of a linear background over short periods.

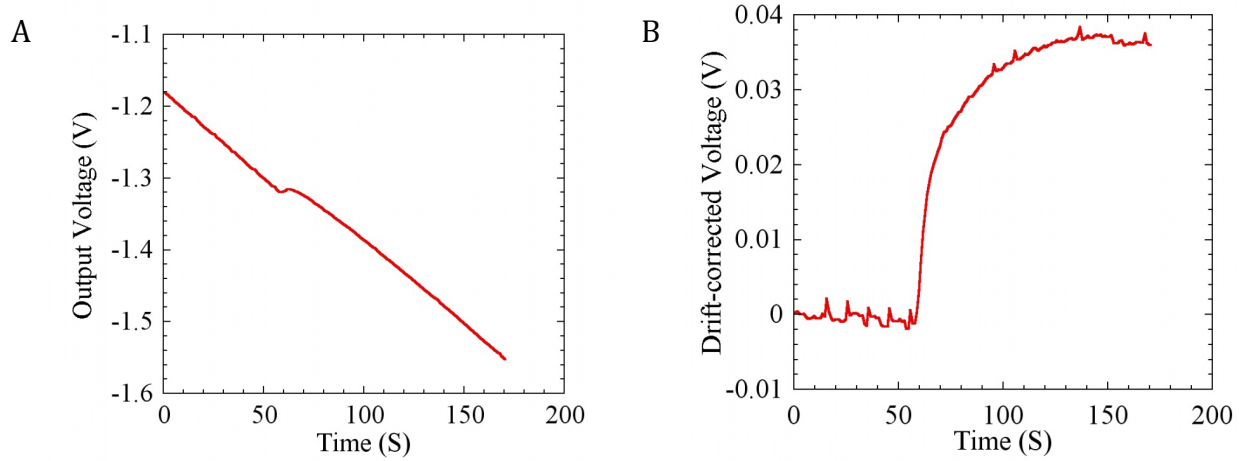

Figure 3-34: Output voltage as a function of time for an experiment held statically at 2 GPa and then deformed by driving out the anvils in the horizontal direction simultaneously after approximately 60 s by 20 microns. The drift before 60 s is linear and is removed by subtracting a linear background as shown in B.

Figure 3-34 shows the output voltage as a function of time in seconds for an experiment at 2 GPa were the cubic assembly has been deformed by 40 μm at approximately 60s after the start of data recording. The assembly is deformed by driving the 4 horizontally aligned anvils in the decompression direction by 20 μm. As the pressure on the vertical anvils remains constant this results in a concurrent compression of the vertical anvils by approximately the same distance. As deformation of the assembly occurs, a break in slope of the output voltage is observed. In figure 3-32A the background drift has been subtracted from the voltage measurements by fitting a linear background to the data recorded just before deformation. This drift corrected voltage shows a clear and sharp signal generated by the piezoelectric crystal as a result of the deformation.

The charge Q on the crystal, developed as a result of deformation, can be calculated from $Q = Vo.Cr$ where $Cr = 10x10^{-9}F$ and Vo is the drift corrected voltage. The force on the crystal can then be calculated using equation 2.a. The stress on the crystal is determined by diving the force by the surface area of the crystal which is 1.2 mm in diameter.

Four examples of assembly deformation are shown in Figure 3-33 where the stresses determined from the piezoelectric crystal can be compared with the corresponding anvil

displacement. Figure 3-35A shows the stress determined from the same deformation event as shown in Figure 3-34. The vertical anvils were each compressed by 20 μm and the corresponding stress reached approximately 80 MPa.

The timescale for the increase in stress is longer than the deformation event as the anvils displace in a matter of a few seconds. Figure 3-35B shows the piezoelectric stress developed as a result of retracting the horizontal anvils, which lead to advancement of the vertical anvils, by 0.5 μm each. Although the signal is noisy an increase in stress of the order of 2-3 MPa can be observed indicating that the technique is extremely sensitive.

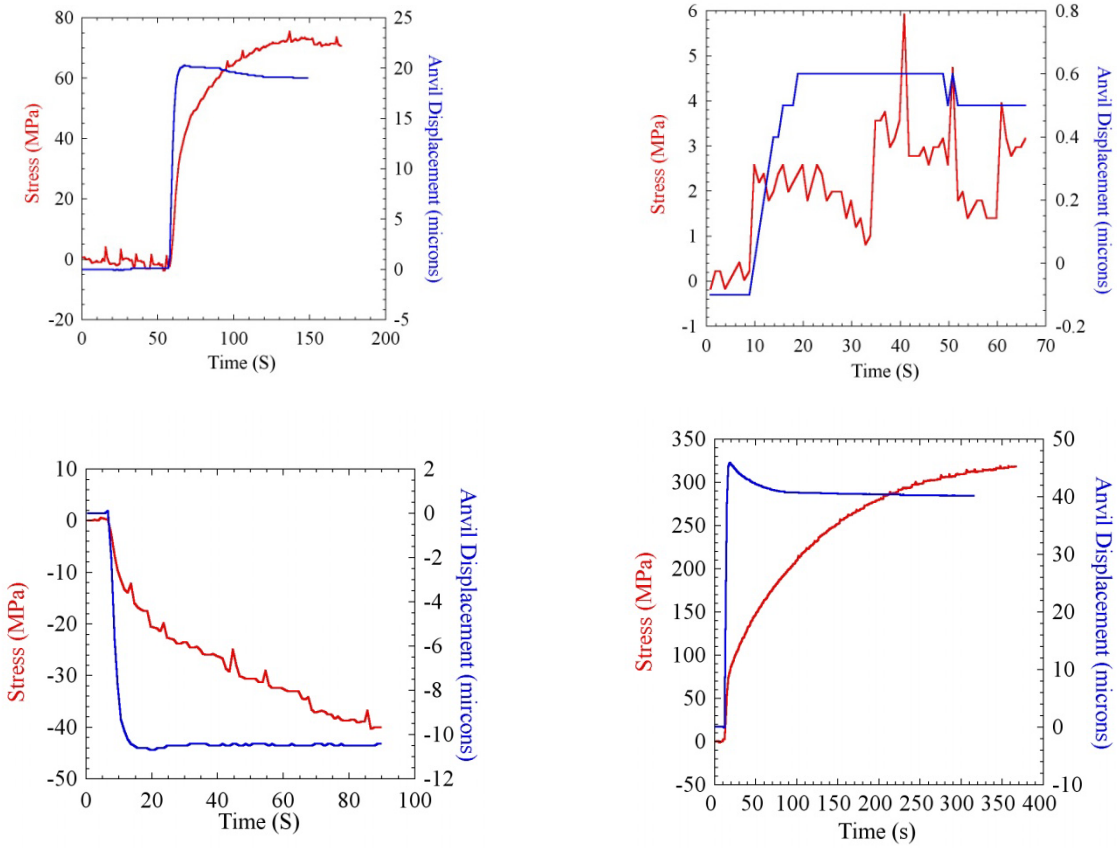

Figure 3-3-35: Stress and anvil displacement versus time for 4 deformation events performed at 2 GPa.

Figure 3-35C shows a test where the horizontal anvils were advanced rather than compresses leading to a retraction of the anvils in the vertical direction. This release of the anvils in the vertical direction caused a negative stress pulse, demonstrating that the effect is sensitive to the direction of the applied stress. In Figure 3-35D an advancement of the vertical anvils by approximately 50 μm, i.e. a combined deformation of 100 μm, has caused a large stress to develop of the order of 300 MPa. Therefore the determined piezoelectric stress is not only sensitive to direction of the stress but is also seemingly proportional to the strain of the assembly.

4 Discussion

Randomly oriented grains deforming plastically develop crystallographic preferred orientation or CPO as a result of anisotropic mechanical properties. The primary reason for the preferred alignment of the crystals is the mismatch between the rotational component of the crystal and the macroscopic strain [*Karato et al.,* 2008]. Although phenomena such as dynamic recrystallization also play an important role in the overall deformation of a polycrystalline aggregate, dislocation glide is often the primary agent of deformation.

The total intercrystalline deformation in a polycrystalline aggregate generally results from slip on more than one slip system. For an individual crystal to deform in a homogeneous manner, a minimum of five independent slip systems are required. This condition is called 'Von Mises criteria'. If this condition is satisfied then a crystal can take any arbitrary shape in response to the external force field. Olivine does not possess five independent slip systems (Durham et al. 1977), in addition the three available slip systems that olivine has, are of varying strength. Onset of deformation occurs when the shearing force acting on a given slip system exceeds a critical value called the "Critical resolved shear stress" or CRSS. The requirement for homogeneous deformation drives olivine crystals to deform also on the harder slip planes. Sometimes, harder slip planes are activated first because they are oriented most favorably with respect to the external stress field (Lister *et al.* 1978). The need for slip on harder slip systems, on the other hand, can be minimized if additional deformation processes are also active. Dislocation, climb which is another intercrystalline deformation process, is one such process. In fact the results of Durham et al. (1977) suggest a significant contribution from climb processes during deformation for olivine grains oriented along $[101]_c$. This orientation activates two harder slip systems – (001)[100] and (100)[001]. Other intercrystalline deformation processes such as, grain boundary migration and grain boundary sliding can also accommodate some amount of strain, thereby reducing the need for slip on harder slip system (Lister *et al.* 1978; Paterson 1969).

Based upon the observation that a significant portion of the strain can be generated by diffusive processes (e.g. dislocation climb and grain boundary sliding), the need for 5 independent slip systems can be relaxed. For this reason Karato has argued that dislocation glide on only the easiest slip system can in many cases accommodate sufficient strain such that a simple relationship exists between the LPO and this easiest slip system [*Karato,* 1986; 1998; *Karato et al.,* 2008]. However, the results obtained in this thesis imply that this is likely to be an over simplification. With the aid of VPSC (Visco-plastic self consistent) modeling, the results of which will be discussed in section 4.4, it can be shown that many of the LPOs observed in this study require sufficient strain on more than one slip system to explain their development. Although, some of these specimens display LPO resultant from high stress deformation, stresses which are unrealistic for the upper mantle, the complex LPO development is, never the less, apparently due to significant strain on more than one slip system. The activation of multiple slip systems is likely also to occur in the mantle, particularly in regimes which are transitional between dominant slip systems, such as resulting from changes in the H_2O content of the mantle rocks. It has also been shown that the activity of three independent slip systems may be sufficient to accommodate enough strain by dislocation glide if modest strain heterogeneity is allowed. Results from Paterson (1969) suggest that in the case of olivine, strain accommodated by the fourth and fifth hardest slip systems was around 15% and 1% respectively.

As this study is focused on changes in the olivine fabric resulting from changes in various physical-chemical conditions (stress, temperature, water and pressure), it is important to understand how these changes in the relative activity of slip systems translates in to changes in the LPO. A crucial aspect in studying LPO transitions is to understand if changes are gradual or abrupt. Based upon a Taylor-Bishop-Hill model Lister and coworkers have simulated the possible LPOs with a given set of active slip systems [*Lister and Hobbs,* 1980; *Lister and Paterson,* 1979; *Lister et al.,* 1978]. They found that a range of smoothly varying CRSS values can produce very similar LPOs, but there are critical CRSS ratios where abrupt changes in the LPO may occur. This model allows for a complex kind of LPOs with abrupt changes in it as the (relative) CRSS values change with changing state of stress, water and other parameters. Moreover, merely the relative ease (or

difficulty) of slip activity does not necessarily guarantee that a set of slip systems should be active together. Geometric constraints on deformation by dislocation glide, imposed by the need for homogeneous strain, may prevent a set of slip systems being active together even if their CRSS values permit their activity. For example, for olivine the (001)[100] LPO pattern should not develop when the (010)[001] slip system is active, even when (001)[100] is an easy slip system [*Tommasi et al.,* 2000], unless significant contribution to strain is made by phenomena such as dynamic recrystallization, grain boundary sliding etc.

In the following section the results of high pressure and temperature deformation experiments on olivine will be summarized and the main findings discussed. The main observation is that changes in pressure have a minor influence on olivine LPO development compared to changes in olivine H_2O content and flow stresses. Explanations for these effects will be examined.

4.1 Effects of stress and pressure on the slip systems in olivine: Evidence from deformation experiments on "dry" olivine

As has been discussed previously, stress, water and pressure can have all be reported to have strong effects on the slip systems in olivine. Results from previous studies suggest that higher stresses tend to promote the (010)[001] slip system whereas (100)[001] slip systems are more active under water rich conditions [*Jung et al.,* 2006; *Karato et al.,* 2008]. Reports also indicate that the (001)[100] slip system can also be the dominant slip system under moderately hydrous conditions [*Katayama et al.,* 2004]. It has also been proposed based upon experimental results and computer modeling that c-slip becomes easier at higher pressures [*Couvy et al.,* 2004; *Durinck et al.,* 2005; *Jung et al.,* 2009a; *Raterron et al.,* 2007]. Although doubts have been raised about the validity of the last conclusion, mainly due to uncertainties related to stress and water content under which these experiments were performed [*Karato et al.,* 2008]. The results obtained in this thesis, however, apparently indicate that pressures up to 11 GPa may not actually cause any change in the major slip system (Fig 4-1 and 4-2), as discussed below.

Figure 4-1 shows a summary of the active slip systems in various specimens deformed under wet and dry conditions in this study. Each slip system has been assigned a separate color for clarity. As shown on the top-right part of the image, the four rectangular boxes show the data from four experiments that were performed at same pressure-temperature conditions. Two rectangles on the bottom show results from the experiments performed under dry conditions whereas the top two rectangles show data from wet experiments. Two rectangles on the left side show the samples deformed at relatively slower strain rates (lower stresses) whereas the other two rectangles on the right show the fabric observed in experiments conducted at higher strain rates (higher stresses). Evidence for four slip systems was observed in the experiments and the width of the colour bars is proportional to the number of grains in each sample that show evidence for activity of that particular slip system.. At 1300°C and 3 GPa, for example, the first rectangle at the bottom-left is colored in only green, implying that the fabric in this specimen is of the A-type which results from the dominant activity of the (010)[100] slip system. The top-right rectangle at 3GPa and 1300°C contains green and blue coloured rectangles of equal width, which implies that approximately half of the data points display an A-type fabric (green colored), indicative of (010)[100] slip system activity, while the other half , (blue), indicate activity of (100)[001] i.e. producing a C-type fabric (Table 4-1). The presence of both of these fabrics in this specimen indicates that physical and chemical conditions are suitable for the activity of both (010)[100] and (100)[001] slip systems.

Table 4-1: Fabric type and nature of slip systems (Jung and Karato, 2001)

Fabric type	A-type	E-type	B-type	C-type	D-type
Dominant Slip system	(010)[100]	(001)[100]	(010)[001]	(100)[001]	(100){0*kl*}

Based upon the summary of fabrics shows in the image below, it is clear that under dry conditions, mainly two kinds of slip systems dominate the deformation by dislocation glide in olivine, (010)[100] and (010)[001]. Every specimen deformed under similar P-T condition but at a different strain rate has a different proportion of data points indicating A-type and B-type fabrics. In addition, every specimen which was deformed at a higher

strain rate (and hence higher flow stress) has a larger proportion of data points indicating the B-type fabric.

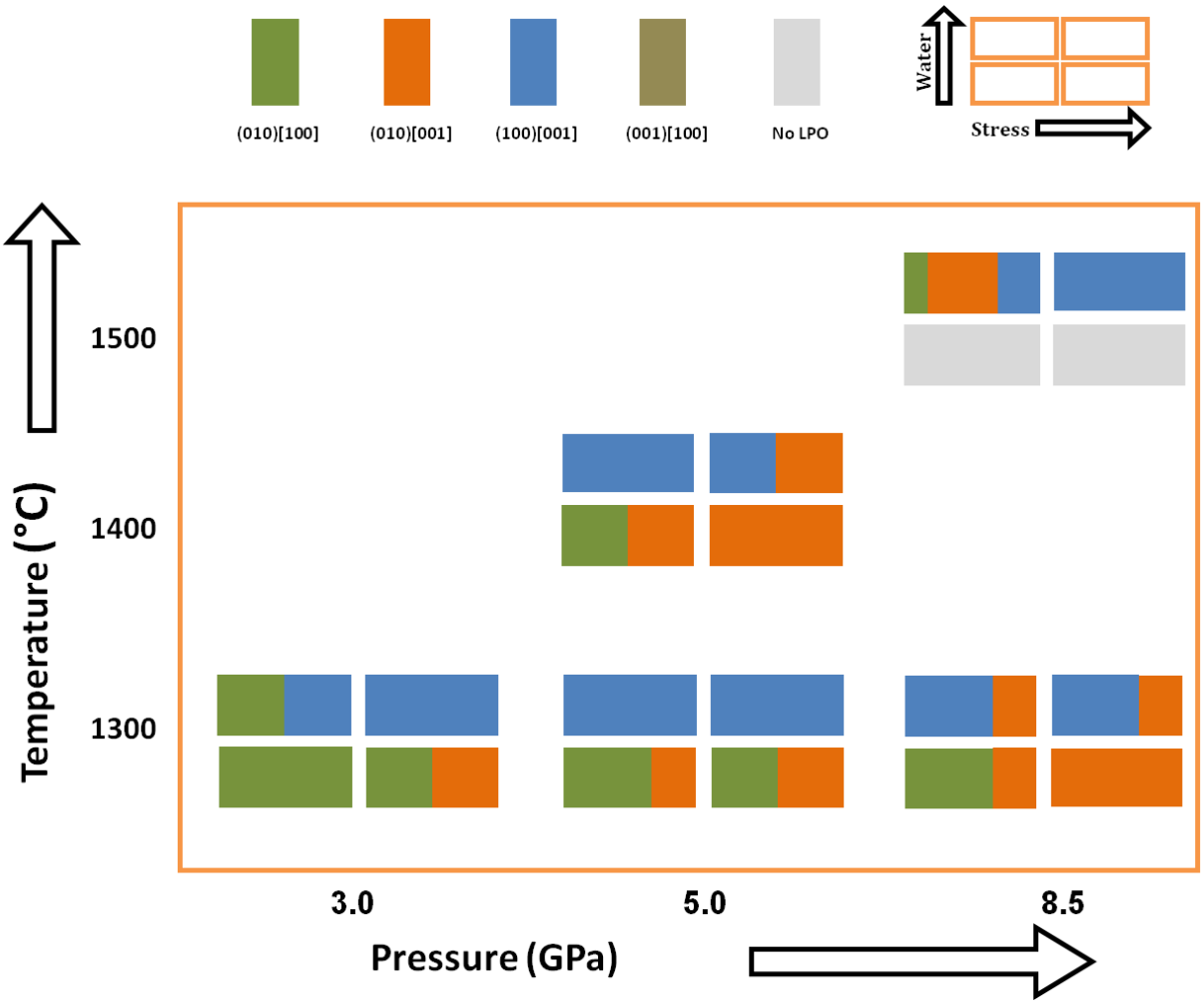

Figure 4-1: Summary of fabrics observed in San-carlos olivine deformed under dry and wet condition at different strain rates. Experiments were performed between 3 to 8.5 GPa and 1300°C to 1500°C. Width of each colour bar is proportional to the approximate number of grains that were present in the subset containing data points for that slip system. Refer to section 3.4.14 for more details. As shown in the table at top-right corner of the page, the lower row in the 2x2 matrix contains results from dry experiments while upper row contains results from wet experiments. The left column in 2x2 matrices has results from slowly deformed samples whereas samples deformed at relatively higher strain rate have their fabrics shown in the right column.

Hence, it can be concluded that under high stress deformation conditions the B-type fabric dominates i.e. the (010)[001] slip system contributes to most of the strain. Although,

the proportion of data points with the B-type fabric increases at 5 GPa and 1400°C with respect to 5GPa and 1300°C , this is actually in line with a slightly higher strain rate and hence higher flow stresses in specimens deformed at 1400°C.

Equally important is the observation that at 8.5 GPa and 1300°C, the specimen deformed at a slower strain rate shows a larger proportion of data points with the A-type fabric. There have been reports that at higher pressures c-slip, slip with a Burgers vector [001], becomes easier than a-slip. The approximate transition pressure between a-slip and c-slip apparently varies between studies with Jung et al. (2009) reporting this transition at approximately 3.6 GPa whereas Raterron et al. (2007) place the transition at approximately 7.6 GPa. If there was indeed a pressure related easing of the b = [001] slip then it would be hard to reconcile this with the results in Fig. 4-1, which show dominant (010)[100] slip system activity at slower strain rates at 8.5 GPa. These results are rather more in line with the observation that a change from a-slip (b = [100] slip) to c-slip (b = [001] slip) can occur at higher stresses [*Jung et al.,* 2006]. Another piece of strong evidence that a-slip continues to be the dominant slip mechanism at high pressures, comes from analysis of specimens that were hot-pressed in the 6-8 multianvil under pseudo-hydrostatic conditions i.e. without the inclusion of alumina hard parts in the multianvil assembly that can lead to strong deformation (Fig 4-2). In two such hot-pressing experiments, dry olivine powder was hotpressed at 1400°C at pressures of 8.5 GPa and 11 GPa. During cold compression of the multianvil assembly, some dislocations are introduced in the olivine sample. Once, the sample is heated up to high temperatures, dislocation recovery processes start, leading to deformation of the sample and development of a weak LPO. As seen in the pole figures on the next page, the A-type fabric are clearly present both of these specimens.

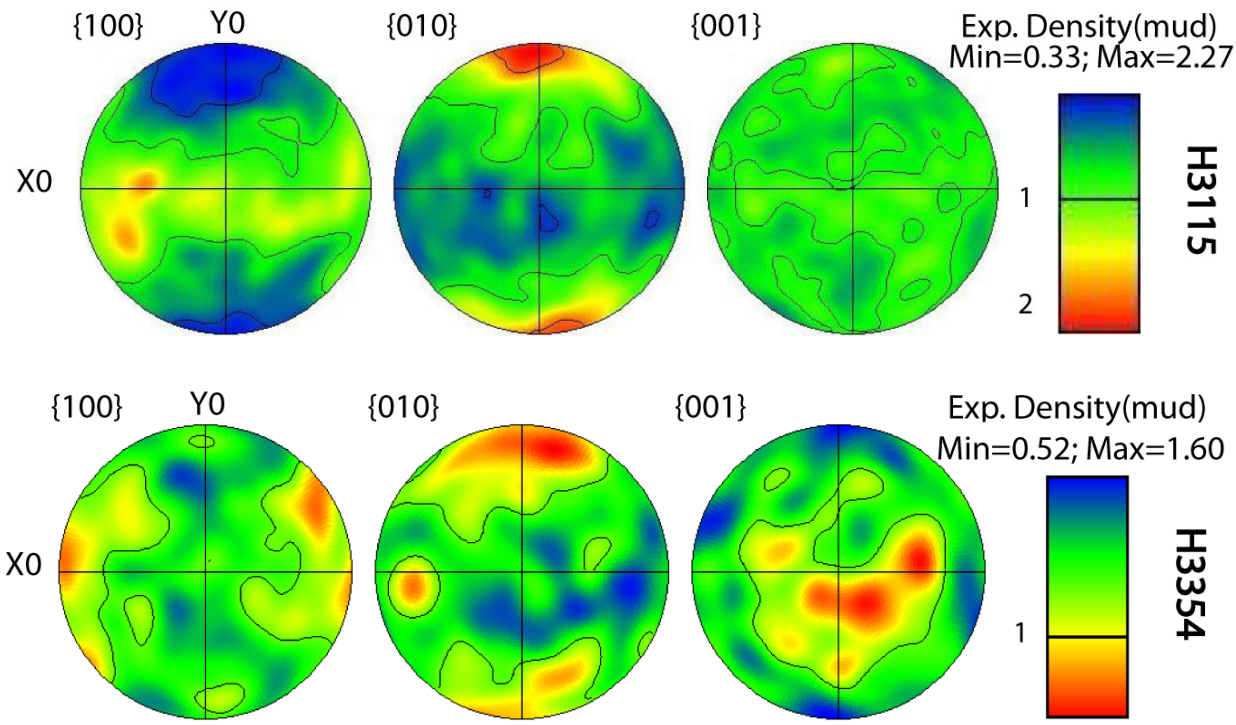

Figure 4-2: Pole figures for two polycrystalline olivine specimen hotpressed at 8.5 GPa (H3115) and 11 GPa (H3354). Specimens were annealed at 1400°C. Both pole figures resemble A-type fabric which is often observed under low stress and dry deformation environment. Presence of A-type fabric in these hotpressed specimen is indicative of (010)[100] slip system activity.

The LPO fabrics observed in Fig 4-2 could have only developed in these samples if a-slip was dominant. Interestingly, the first report of a pressure induced transition in olivine LPO was by Couvy et al. (2004) from deformation experiments performed at BGI using a similar multi-anvil apparatus. The assembly setup was in simple shear configuration, however, unlike that reported here where no deliberate attempt was made to deform the olivine sample during hot-pressing. The peak stress that would have developed during the initial stages of annealing must be lower than in the experiments of Couvy et al. (2004). Hence, the hot-pressing fabric in specimens H3115 and H3354 must result from deformation under low stresses and thus it can be concluded that a-slip continues to be the easiest slip mechanism even up to 11 GPa pressure under low stress deformation conditions.

The observations in previous studies where a transition of a-slip to c-slip has been attributed to increasing pressure are more likely to result from higher stresses which may inevitably increase in experiments at higher pressures.. Pole figures shown by Jung et al. (2008) do not show strong LPOs despite large amounts of strain that their samples

experienced. Results from *Raterron et al.* [2007] where they observed a pressure related transition in the slip system, are based upon experiments performed at stresses varying between 300 MPa to 1800 MPa. Similarly in the study of *Ohuchi et al.* [2011] most specimens exhibiting the presence of c-slip have estimated stresses in excess of 350 MPa. Only in one specimen are stresses reported to have been less than 300 MPa but this sample actually indicates dominant activity of the (100)[001] slip-system under dry conditions. Additionally the observation that various studies have placed the pressure of the transition at widely varying values can also be explained if this transition in fact results from increasing flow stresses.

Figure 4-3 shows the fabrics observed in this study compared with those reported in previous studies. Larger symbols with black boundaries are data points from this study. The results are in very good agreement with variations in fabric reported by *Karato et al.* [2008]. At higher stresses, under dry condition the B-type fabric was observed, whereas under lower stresses and dry conditions deformation resulted in the dominance of A-type fabric. Hydrous specimens exhibit C-type fabric which also agrees with previous reports from lower pressure deformation studies. None of the specimens characterized in this study showed evidence of E-type or D-type fabric because experimental conditions in were never entered these regions of stress-water content space. Broken grey lines in the image are the likely transition boundaries between two different fabric types.

The main conclusion of the results obtained from deformation experiments under dry condition is that pressure apparently plays no direct role in the slip system transition in olivine. (010)[001] slip system contributes most to the overall strain at higher stresses and the B-type fabric should be observed under such environment. A-type fabric should be the most dominant type fabric that we would expect to see in the lithospheric mantle because stresses are expected to be too low (<10 MPa) to generate B-type fabric. However, in the mantle wedge near subducting slabs it is possible that regions exist where B-type fabric could occur as these regions are most likely deforming at relatively high stresses.

[115]

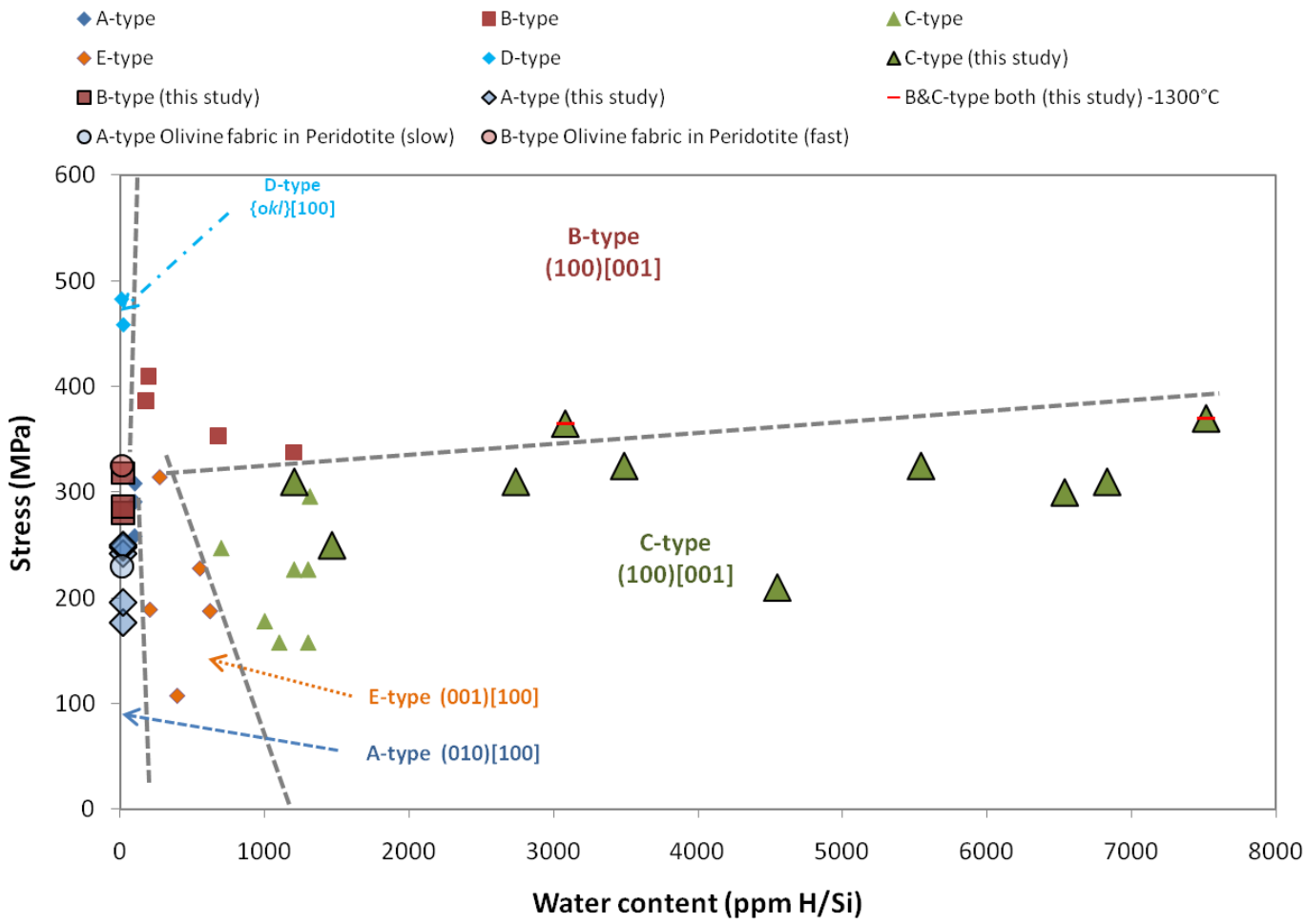

Figure 4-3: Deformation data from this study and other studies are shown as a function of stress and water contents (T ~ 1470–1670 K). Larger symbols with black boundaries represent data from this study whereas rest of data are from Katayama et al. 2004. Except, one of the data for D-type fabric is from Bystricky et al. (2001). Water content was estimated using the Paterson (1982) calibration. Broken gray lines indicate the likely transition line between two different fabric types (Modified after Karato *et al.*, 2008)

Lack of LPO in the dry samples deformed at high temperature at 1500°C and 8.5 GPa has likely resulted from diffusion accommodated grain boundary sliding. High grain growth, as evident from grain size measurements made in recovered experiments, points to the dominance of diffusion creep. The presence of straight grain boundaries indicate that conditions were suitable for grain boundary sliding. There were many four-grain junctions present in these samples and these junctions were slightly diamond shaped which is additional evidence that grain boundary sliding may have been the active deformation process. It is well known that diffusion creep does not result in LPO development. Moreover, grain boundary sliding (GBS) also does not favour LPO development because in the presence of GBS, intracrystalline deformation is only weakly dependent on the orientation of grains [*Drury and Humphreys,* 1988; *Karato et al.,* 1986; *Zhang et al.,* 1994].

Fabric types observed in the olivine deformed as a part of the peridotite modal composition are identical to those observed in monomineralic experiments at the same conditions. The dominant slip system in the pyroxene component of this aggregate had most likely (100)[001] slip system active.

4.2 Fabric types under water rich conditions

The hydrous specimens in this study all contain water contents in excess of 50 ppmw. From figure 4-3, it can be seen that the C-type fabric is the most commonly observed fabric in these specimens. However, some of the high stress water-rich samples also indicate the presence of the B-type fabric e.g. DD456. A TEM study on one of the wet samples (DD456) indicates the dominant presence of b = [001] dislocations. The active slip systems in this specimen were observed through TEM to be (100)[001] and (010)[001]. The activity of the (010)[001] slip system in this sample is similar to activity observed in the dry specimens deformed under higher stresses. The (100)[001] slip system is an unusual slip system because glide on the (100) plane most likely involves breaking of SiO_4-tetrahedra, unlike glide on (010) where no SiO_4 tetrahedra are encountered during glide. Dislocation microstructures in the wet sample (DD456) observed using the TEM show that dislocation loops on the (010) glide plane have longer screw segments than their edge components. There are long edge segments of c-dislocations visible and most of them are part of c-

dislocations on the (100) glide plane. Where only screw segments of c-dislocations are visible it is unclear whether glide is also occurring on the (100) plane because determination of the glide plane is not possible when only screw segments are visible. The abundant number of c-dislocation on the (010) slide plane with a screw nature is in clear contrast to the c-dislocations observed in the dry specimens which were mostly of edge nature under similar P-T-stress conditions. Another pertinent observation in the wet sample is the evidence of climb of edge dislocations and cross-slip of screw dislocations. A few prismatic loops lying in the (010) plane can also be observed, which have been associated with the presence of H_2O in olivine.

A further interesting observation is that the transition line between C-type and B-type fabrics appears to have a positive slope with respect to the olivine H_2O content. This is in contrast to the previous study of Katayama *et al.* 2004 where a negative slope was proposed. In accordance with Fig 4-3 it would require increasingly higher stresses to push olivine from the C-type fabric regime into the B-type regime with increasing water content of olivine. It would also imply that water favours slip on the (100) plane over the (010) plane.

4.3 Physical basis for slip system changes in olivine

In the following section an attempt is made to identify a physical basis for changes in slip systems as a function of stress and water content. As mentioned previously, under high stress deformation conditions deformation by b = [001] slip becomes dominant and the slip system changes from (010)[100] to (010)[001]. Slip with b = [001] also becomes dominant in the presence of water. In this case, the dominant glide plane becomes (100) which are not known to be an easy glide plane because of way the SiO4 tetrahedra are arranged in olivine. Based upon the rheological and microstructural data available from previous studies along with results from this study, an attempt is made here to explain the dominance of the (010)[001] slip system under higher stresses and the cause of C-type fabric development in wet specimens due to the likely action of the (100)[001] slip system.

4.3.1 Dominance of (010)[001] slip system at higher stresses

Studies on rheology of olivine single crystals point towards a temperature related transition in the olivine slip system (Fig 4-4).

Measurements of the critical resolved shear stresses for (010)[100] and (010)[001] slip systems indicates that CRSS for the (010)[001] slip system is lower than the CRSS for the (010)[100] slip system at lower temperature. Whereas, the reverse is observed at higher temperatures where the (010)[100] slip system is initiated at much lower stresses. This transition between CRSS values of the two slip systems occurs at around 1200°C at a corresponding value of 400 MPa CRSS.

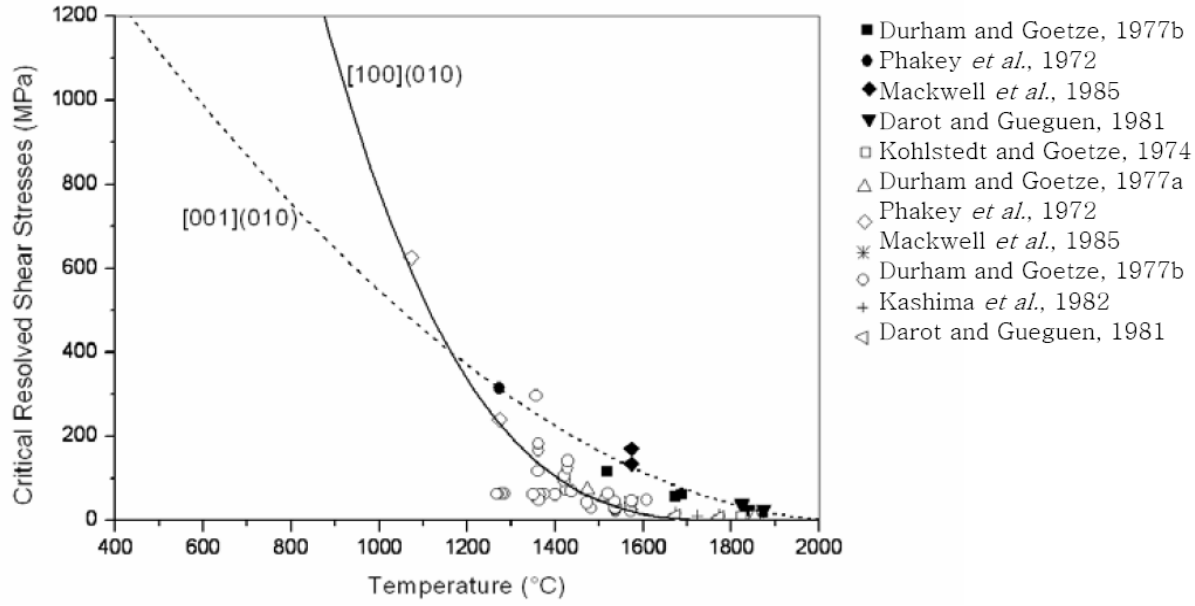

Figure 4-4: Critical resolved shear stresses (CRSS) of the (010)[100] and (010)[001] slip systems as a function of temperature. Data (corresponding to a strain rate of 10^{-5} s^{-1}) from experiments performed on single crystals oriented along [011]c (black-filled symbols) to promote [001](010) glide and along [110]c (open symbols) to promote [100](010) glide. (Source- PhD thesis – Helen Couvy, 2005)

Interestingly, in this study the fabric transition from A-type to B-type, which is related to the transition between the dominant slip systems (010)[100] and (010)[001], was also observed at around 300 MPa, which given the uncertainty in both determinations puts it in close proximity to the cross-over in the CRSS for the two slip systems shown in Fig 5-4. In the following section, it is argued that the stress related transition in the fabrics is a logical

consequence of changes in the CRSS of the two slip systems with temperature. Before this argument is pursued, however, it is worthwhile to review why CRSS changes with stress.

The temperature dependence of CRSS has been observed in metals and various ionic and covalent compounds [*Castaing et al.,* 1981]. Also, different slip planes can have different temperature dependency of CRSS as is shown for α-Al_2O_3 in Fig 4-5.

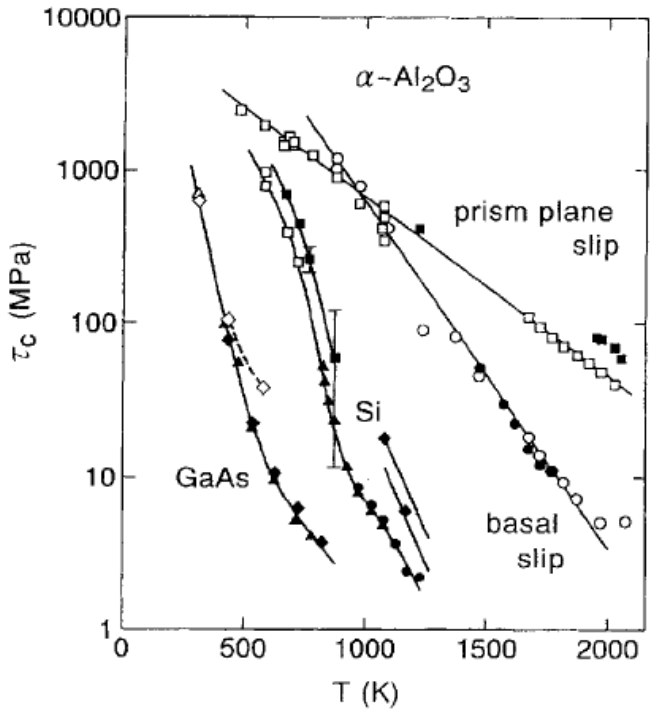

Figure 4-5: Temperature dependence of the critical shear stress τc(T) of covalent crystals measured under high or atmospheric pressure. The data are taken from the references: Lagerlof et al. (1994) for α-Al_2O_3, Castaing et al. (1981b) for Si and Boivin et al. (1990) for GaAs of intrinsic and p-type. (Figure source: Koizumi *et al.,* 1994)

This temperature dependence of the CRSS value is generally explained on the basis of intrinsic resistance to dislocation motion by the process known as the "Peierls process". It has been suggested that the Peierls process becomes important for the rheology of olivine at higher stresses. Power law creep provides a good description for olivine flow only at lower stresses, whereas at higher stresses the olivine flow law becomes exponential [*Goetze,* 1978; *Katayama and Karato,* 2006]. An exponential flow law can be predicted based upon dislocation motion by the Peierls mechanism via nucleation of double kinks. Dislocation motion by the Peierls mechanism may be more important for b = [001] because

dislocation lines tend to be straighter for c-dislocations [*Karato et al.,* 2008; *Phakey et al.,* 1971]. Although, the value of critical stress at which the Peierls process starts to dominate the flow behaviour is not yet clear.

Peierls mechanism of deformation by double kink nucleation

At finite temperatures, dislocations do not move all at once in a plane strain manner but motion occurs through the generation and nucleation of kink-pairs. In this regime, nucleation of kink-pairs is the rate determining step for slip. Once a kink grows above a critical size, further straining takes place by migration of these kinks.

A kink on a dislocation line can be envisaged as a dislocation on a dislocation line (Fig 4-6). According to the Peierls mechanism, a straight dislocation line has its lowest energy when it lies in a potential valley parallel to lines of closest packing of atoms on the slip plane. During the motion of a straight dislocation from one valley towards the next, the atoms in the vicinity of the core of the dislocation change their positions and bond angles, causing the energy of the dislocations to increase. Midway between two adjacent valleys, the dislocation energy reaches a maximum value and any additional displacement will cause the dislocation to fall down the energy maxima into the next valley. The maximum shear stress necessary to promote such forward motion of the dislocation is known as the Peierls stress τ_p.

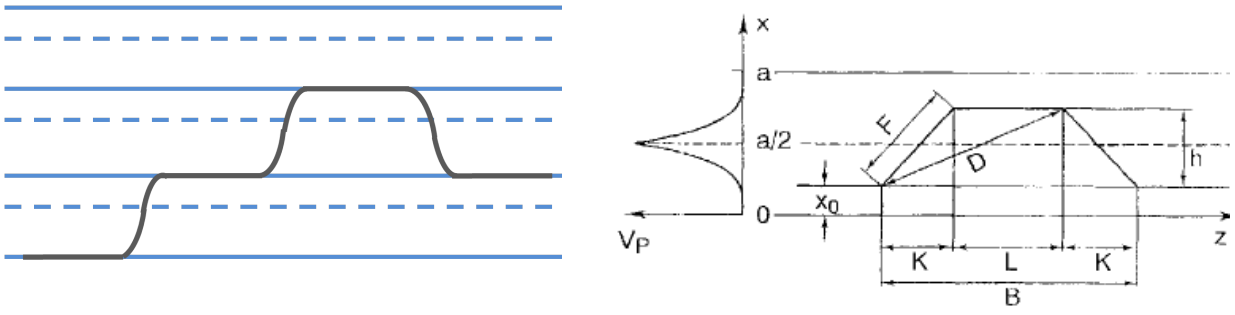

Figure 4-6: Left image shows a kink (dark line) lying across a potential valley. Broken lines indicate the potential maxima with minima represented by the solid lines. *Right*: A kink in the presence of external stress has its equilibrium position displaced away from the unstressed position. Size of the kink is represented by kink height h and width 2K+L in case of a trapezoidal kink model. (Source: Suzuki *et al.* 1995)

At a fixed strain rate, the number of kinks forming per second is a constant because kinks act as the basic unit of deformation. In such a scenario, total power imparted to the kink must be held constant to maintain their nucleation frequency. If the temperature is dropped while holding the strain rate constant, flow stress will increase to maintain the nucleation rate and vice versa (Fig 4-7). Nucleation of a kink takes place with the help from thermal agitation and energy supplied by the external stress. If the energy supplied by these two means is not sufficient then a double kink may form momentarily and then collapse to annihilate each other. Hence, there is a defining set of stresses and temperatures at which dislocations can move by kink nucleation. The locus of this (σ,T) pair is the CRSS versus temperature curve.

Any (σ,T) combination that lies towards the origin-side of the CRSS-T curve will not be able to initiate slip on a given slip system whereas (σ,T) combinations lying on the far side of the curve will lead to high activity of that slip system.

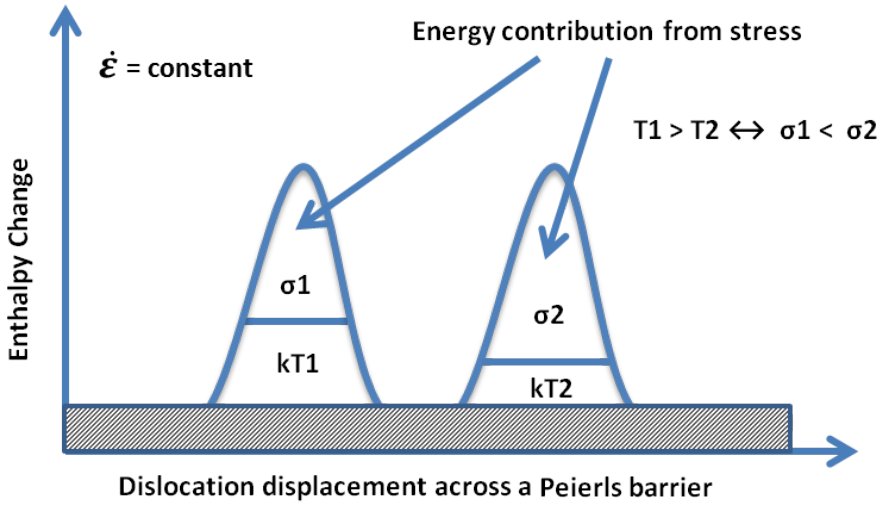

Figure 4-7: Enthalpy change associate with the contribution from thermal perturbation at temperature T and mechanical work done by stress σ.

The enthalpy change associated with the displacement of kinks from one barrier to another can be expressed as

$$\Delta H = \Delta P + \Delta E - \Delta W \qquad 4.a$$

$where;\ \Delta P\ is\ energy\ change\ due\ to\ the\ Peierls\ potential$

$\Delta E\ is\ the\ elastic\ self\ energy\ change\ of\ bowed\ out\ dislocation;\ and$

$\Delta W = \tau \times b \times (kink\ area)\ \ i.e.\ the\ work\ done\ by\ the\ external\ stress$

In general, enthalpy change associated with the formation of a critical kink size,ΔH^* can be expressed as a function of stress for a material of shear modulus G as *Koizumi et al.* [1994]

$$\Delta H^*(\tau) = 2U_k^* - AGb^3\left(\tau/\tau_p\right)^{1/2} \qquad 4.b$$

$$where;$$

$$U_k^* = Energy\ of\ an\ isolated\ kink, \qquad A = constant,$$

$$b = Burgers\ vector\ and\ \tau_p = Peierls\ stress$$

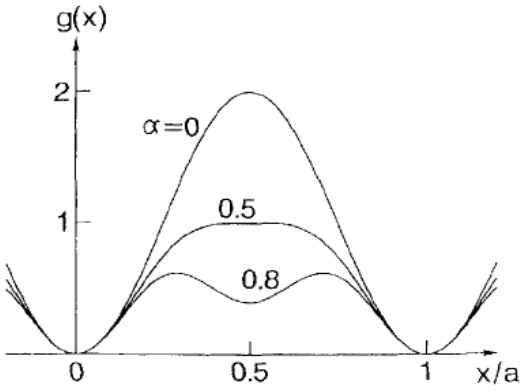

Parameter "A" is dependent upon the shape of the Peierls barrier. Calculations performed here indicate that value of A for a-slip should be close to 0.274, whereas it should be 0.72 for c-slip. Koizumi *et al.* 1994 have suggested a shape dependent formalism for this periodic Peierls potential by introducing a constant α (Fig 4-8).

Figure 4-8: The function g(x) giving the shape of the Peierls potential. It is sinusoidal for a = 0, dam-like with a Roof top for a=0.5, and camel-hump shaped, with an intermediate minimum for a = 0.8. (Source: Koizumi 1994)

Calculations made using the sinusoidal potential of [*Hirth and Lothe,* 1992] (see Appendix II for details); fail to predict the slope of the CRSS versus Temperature curve. This calculation would correspond to a $\alpha = 0$ curve from Koizumi *et al.* (1994). At this stage it is not clear if a simple symmetric Peierls potential is even suitable for a description of olivine, however, a relation of the form presented below (Eq. 4.c) seems to describe well

the CRSS-temperature curve for the two slip systems in olivine (Fig 4-9) with values of different parameters show in the table below (Table 4-2). Normalized kink energies are derived for an abrupt kink using a sinusoidal potential.

$$\Delta H^*(\tau) = Gb^3\left(2U_n^* - A\left(\tau/\tau_p\right)^{1/2}\right) \qquad 4.c$$

$$where\ U_n^*\ is\ the\ normalized\ energy\ of\ an\ isolated\ kink$$

To relate the enthalpy calculated using double kink nucleation method to the flow temperature a relation of the form $\Delta H^*(\tau) = \beta k_B T$ is used. β is a dimensionless constant whose value ranges from 30-35 for metals and alloys and it is weakly dependent upon the strain rate [*Suzuki et al.,* 1995]. In olivine higher values of β, 68 for a-slip and 155 for c-slip are required for a strain rate of $10^{-5}s^{-1}$.

Table 4-2: Value of constants that describe well the CRSS-Temperature relation for the two slip systems in olivine

Slip systems	**A**	**β**	U_n^*	τ_p**(MPa)**[1]	**b (Å)**
(010)[100]	0.274	68	0.6437	9100	4.76
(010)[001]	0.72	155	0.6708	15600	5.99

1. Value of Peierls stress for a-slip -9100 MPa is sourced from Evans and Goetze, 1979. Peierls stress of c-slip is from Raterron *et al.* 2007

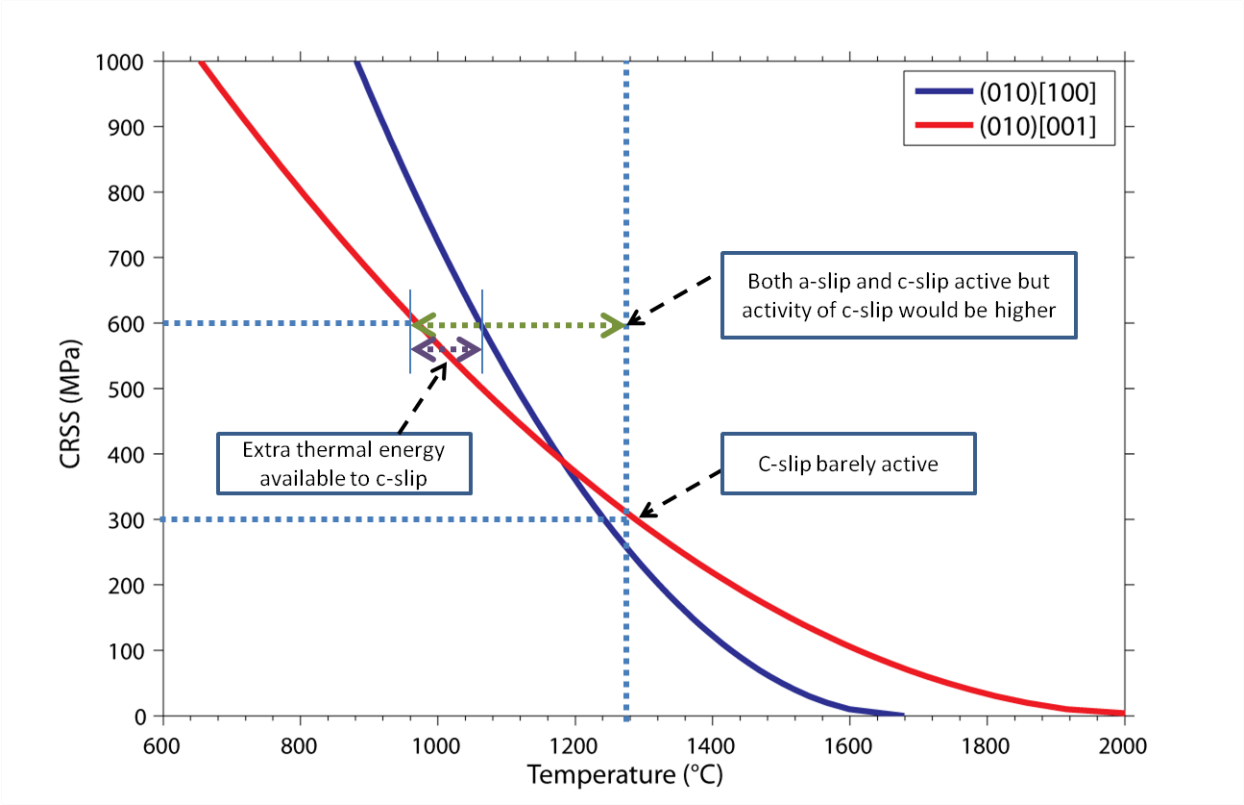

Figure 4-9: Predicted CRSS values for a-slip and c-slip using double kink nucleation theory. At around 1300°C, 300 MPa stress would barely activate c-slip whereas at around 600 MPa, both c-slip and a-slip are active. In this case, activity of (010)[001] slip system would be higher because this slip system has extra thermal energy available at its disposal.

Higher activity of c-slip at higher stresses

Natural consequence of the CRSS versus Temperature relation observed in olivine for two slip systems (010)[100] and (010)[001] is that c-slip in (010)[001] slip system should have higher activity at higher stresses. This can be understood by looking at the image presented above (Fig. 4-9). If we consider a constant temperature line at around 1300°C in Stress-Temperature space then at a stress of 300 MPa, c-slip would be barely active because the minimum values of stress-temperature pairs required to nucleate kink for C-dislocations are barely met. On the other hand a-slip would be active under these conditions because 300MPa-1300°C lies on the far side of CRSS-Temperature curve. But if we consider the case of higher stress on the same temperature line, for example at 600 MPa-1300°C by raising the strain rate, then both a-slip and c-slip should be active under these conditions because the energy available is higher than the energy required for kinks

to grow beyond their critical size. Moreover, this spare energy is available to c-slip is higher than for a-slip and hence the activity of c-slip should be higher. The CRSS-temperature curves should slightly shift away from the origin if the strain rate is increased because the parameter β is weakly dependent on strain rate. However ignoring this minor change should have no bearing on the conclusion presented here. Hence, we see that the different behaviour of the two slip systems in the terms of the variation of their CRSS with temperature will lead to a higher activity of (010)[001] slip system at higher stresses.

4.3.2 Higher (100)[001] activity at higher water content

As discussed previously, in comparison to dry olivine specimens deformed at lower stresses where the (010)[100] slip system is more dominant, in the presence of water the dominant slip system changes to the (100)[001] slip system. There are two puzzling aspects to this slip system change,

1. Why does the mobility of b = [001] dislocations increase in wet samples?
2. Why does dislocation motion switch to the (100) glide plane, which would appear to require breaking of covalent Si-O bonds in the SiO_4 tetrahedra?

The mechanisms that allow these processes to occur favourably under wet conditions are unclear, but in the following sections some possible explanations are discussed.

Higher mobility of b = [001] dislocations at higher water content

Hydrogen diffusivities in olivine are anisotropic. Diffusion along the [001] crystallographic direction is known to be fastest at higher water content while at lower water contents diffusion is fastest along the [100] axis [*Demouchy and Mackwell,* 2006; *Mackwell and Kohlstedt,* 1990]. At lower temperatures (<900°C), water incorporation in olivine can occur by exchange of protons with polarons, electron holes localized on iron atoms occupying octahedrally coordinated metal cation cites [*Kohlstedt and Mackwell,* 1998; *Mackwell and Kohlstedt,* 1990]. Water incorporation by this mechanism is limited by the concentration of polarons in olivine and this mechanism is not known to incorporate much water. Proton diffusion during this process is highly anisotropic and diffusivity along the [100] direction is fastest at $\sim 10^{-10}\, m^2 s^{-1}$. At higher temperatures, additional

hydrogen incorporation can occur at metal vacancy sites [*Kohlstedt and Mackwell,* 1998; *Mackwell and Kohlstedt,* 1990]. Hydrogen diffusivities resulting from this "proton-vacancy process" is also highly anisotropic with diffusion parallel to [001] being the fastest at around $10^{-12}\ m^2 s^{-1}$ at 1000°C. This rate is two orders of magnitude slower than what is possible by "redox-exchange" process where H diffuses through redox interaction with iron. Much more water can be associated with "proton-vacancy" process and in hydrous samples with large amount of water it can be expected that diffusion of hydrogen along [001] should be much faster than in [100] or [010] directions.

Bearing in mind the anisotropic diffusion rate of hydrogen and associated vacancies in olivine, two possible explanations arise for the increase in b = [001] dislocation mobility. The first is that anisotropic diffusion leads to a corresponding anisotropic reduction in the Peierls barrier [*Heggie and Jones,* 1986] favouring b = [001] dislocation motion. The fact that most of the dislocations in hydrous specimens are very straight screw segments also supports a Peierls-stress-controlled model of creep in these samples [*Karato,* 2008b]. However, quantifying this possibility would be very difficult. The second possible explanation arises if the creep process in hydrous specimens is controlled by dislocation climb, as has been proposed for dry specimens [*Kohlstedt,* 2006]. An increase in jog density due to reduction in the dislocation self energy should be also anisotropic with the increase being more prominent for b = [001] dislocations [*Karato et al.,* 2008]. This second possibility seems a less likely explanation for c-slip enhancement, however, because dislocation climb in olivine occurs under jog-saturated conditions, even in dry specimens [*Kohlstedt,* 2006]. Thus, the addition of water can not affect the concentration of jogs any further. Hence, enhanced mobility of c-dislocations is more likely to result from the first possibility i.e. anisotropic reduction in the Peierls barrier for the two kinds of dislocation.

The fact that the presence of water will considerably enhance (by more than three order of magnitude) the concentration of Si vacancies due to an increase in self-diffusivity of the silicon ion [*Chakraborty and Costa,* 2004; *Dohmen et al.,* 2002], implies that dislocation climb will become much more significant in wet samples. This can explain why most of the c-dislocations in hydrous specimens are actually screw segments and not edge

segments unlike in dry specimens. It is a known fact that motion of screw dislocation is conservative and it generally does not involve diffusion [*Nabarro,* 1967].

Glide on (100) plane in hydrous specimens

As mentioned earlier (100) plane is not an easily explicable glide for dislocations in olivine because it would appear to involve breaking of Si-O bonds present in the SiO_4 tetrahedra (Fig 4-10). There are models of glide on the (100) plane which involve significant contribution from dislocation climb. After observing frequent occurrence of (100)[001] slip system in natural olivine *Olsen and Birkelan.T* [1973] proposed that such a glide may be possible by periodic occurrence of jogs on the dislocation line shown as the broken line in the figure 4-10.

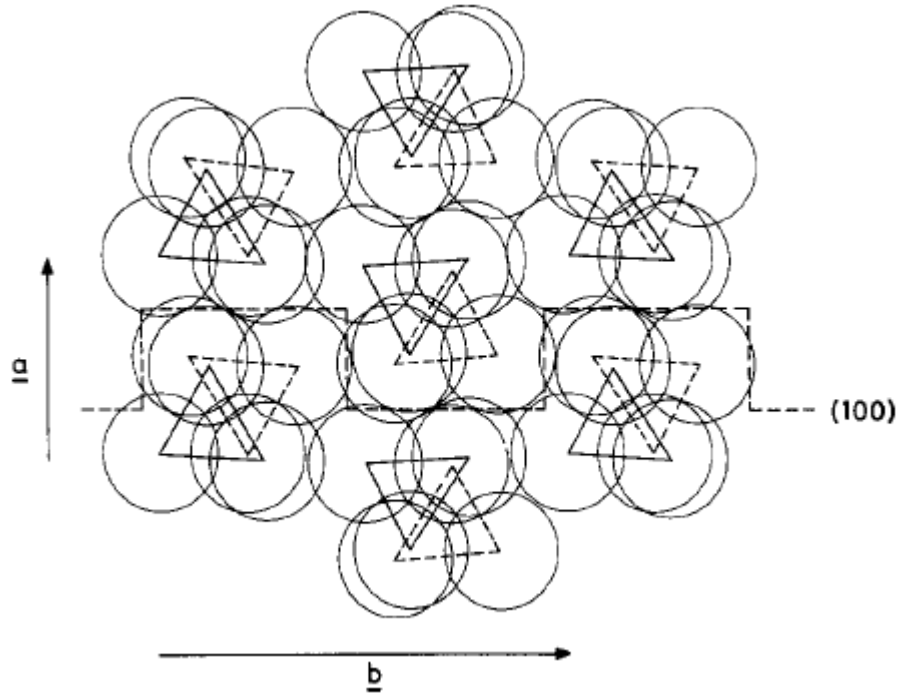

Figure 4-10: (001) projection of the olivine structure. Only the oxygen ions are shown, but the positions of the silicon ions are indicated by the Si 04 tetrahedra. Periodic jogs in a (100) plane are indicated by the broken line. The atom positions are those of the paper by Hanke (1965). (Figure source: Olsen and Birkeland, 1973)

Figure 4-10 shows olivine (001) plane parallel to the plane of paper. It is clear that (010) is easier because dislocation line gliding on this plane will experience no obstruction from SiO_4 tetrahedron whereas glide on (100) plane would be extremely difficult. However,

model proposed by *Olsen and Birkelan.T* [1973] cannot explain development of CPO in olivine. According to their model ratio of strain by glide to strain by climb $l_g/l_c < 1$ because for every glide step by a segment of dislocation, it needs to climb by minimum of one climb step, hence the maximum l_g/l_c ratio in this case would the $b[100]/b[001] = 4.76/5.99 \approx 0.80$. This implies that a significant part of the strain would be accommodated by dislocation climb alone. This observation becomes even more pertinent because dynamic recrystallization and grain growth are very active in wet specimens and the former is known to randomize the CPO. So, in order to produce a perceptible CPO, the ratio l_g/l_c should be considerably higher than 1. This can happen only if dislocation segments are actually able to slice through the SiO_4 tetrahedra. Another relevant observation in this regard is the deformation studies on olivine single crystal by *Durham and Goetze* [1977] where they have reported only 20-30% strain by dislocation climb.

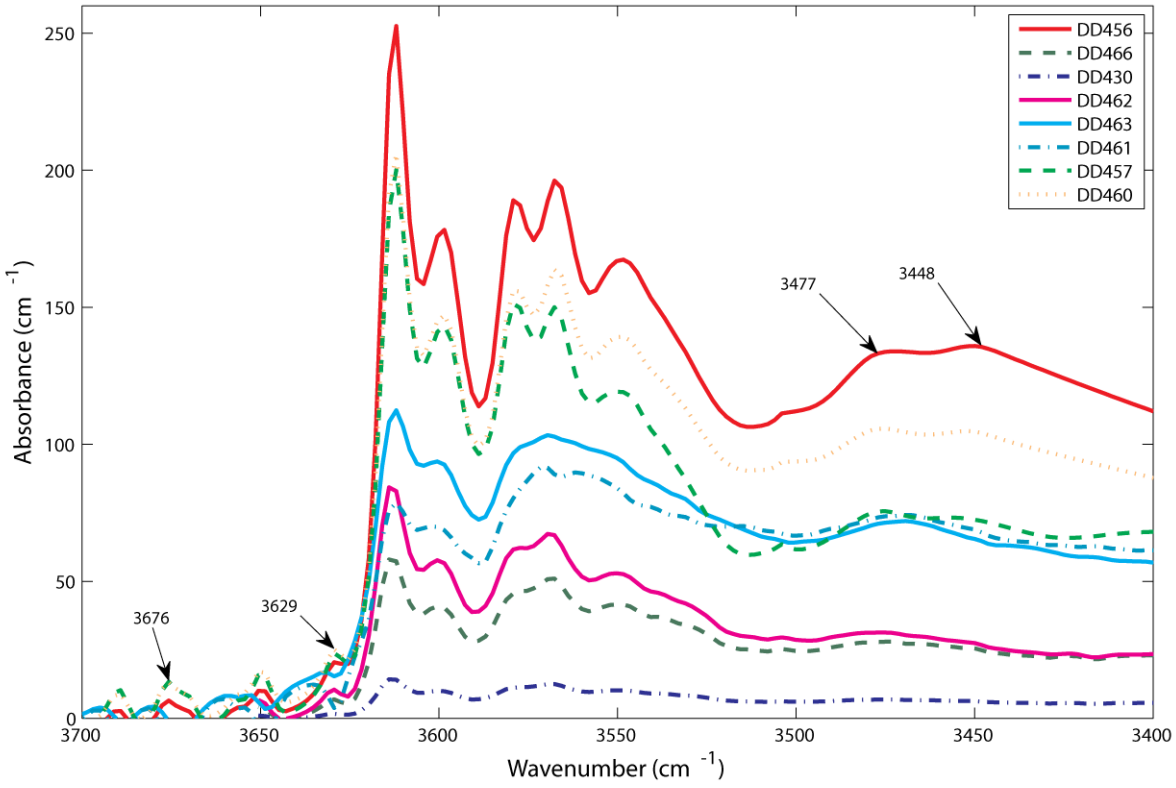

Figure 4-11: FTIR spectra for hydrous samples show peaks at 3477, 3448, 3629 and 3676 cm^{-1}. These peaks could be arising from hydrogen associated with vacant Silicon sites.

As breaking of Si-O covalent bonds is energetically unfavourable, the only reasonable way to achieve this glide may be to replace some of the Si-O bonds by weak hydrogen bonds. Although most of the water in hydrous olivine is known to be associated with divalent metal vacancies, it has been argued that some OH^- is accommodated by charge balancing through the creation of vacancies at Si sites [*Braithwaite et al.,* 2003; *Brodholt and Refson,* 2000]. Theoretical modelling on forsterite has shown that the hydrogarnet defect, $4H_{Si}^{X}$ should produce IR peaks around 3425, 3448, and 3478cm^{-1} [*Braithwaite et al.,* 2003]. Whereas IR peaks at 3674 and 3624 cm^{-1} could also be band doublets related to Si vacancies [*Libowitzky and Beran,* 1995]. Broad peaks at 3448 and 3478cm^{-1} present in the hydrous specimens studied here might result from hydrogarnet substitution and peaks at 3676 and 3629 cm^{-1} are also present in these specimens (Fig. 4-11). If these peaks indeed result from OH bonds associated with silicon vacancy sites and thus a small of water is dissolved at the silicon site, then such sites could act as preferred locations for dislocation nucleation in (100)[001] slip system. Also, in such a scenario glide on the (100) plane would become the preferred glide plane because it is in fact the densest close packed plane of the olivine oxygen anion sub-lattice. This explanation is also in line with the observation that with increasing water content, glide on (010) plane becomes increasing difficult as evident from the positive slope of the transition boundary between C-type and B-type fabric (Fig. 4-3).

4.4 Viscoplastic self consistent modelling of fabric development in olivine

Viscoplastic self consistent modelling is a useful tool for modelling fabric development in mineral phases and has been used particularly to model olivine fabrics [*Tommasi et al.,* 2000]. Input parameters in the model are relative slip system CRSS values for the mineral phase concerned, their elastic constants and stress exponent "n". Based upon these input parameters, the modelling programme can predict the CPO development in various deformation geometries. Other useful information obtainable from this modelling tool is the nature of interaction between different slip systems and their relative contribution to the total strain in the sample. Furthermore, the fabric data obtained from these models can be employed for predicting seismic anisotropy resulting from activity of the chosen slip systems.

The crucial aspect of this kind of modelling is the choice of relative CRSS values. The information about CRSS values can be estimated from the observation of CPO and the nature of dislocations in naturally or experimentally obtained specimens by using various tools such as EBSD and TEM.

To perform this kind of modelling initial guesses are made for the relative CRSS values for different slip systems and then these choices can be improved further based upon the predicted activity of different slip systems by the program. Similarity of the visual appearance and strength of the predicted pole figure with the experimentally determined pole figures provides one way to constrain the correct choices for the relative CRSS value. This kind of modelling also provides information on geometrical constraints in the activity of the probable slip systems. In certain cases an easy slip system may be prevented from making significant contribution to the overall strain because of geometrical constraints imposed by the choice of active slip systems. For example, activity of (001)[100] slip system is suppressed in the presence of (010)[001] slip system [*Tommasi et al.,* 2000].

However, it must be borne in mind that this kind of modelling does not take into account the effect of deformation processes other than dislocation glide. Dynamic recrystallization and other diffusive processes may stabilize the activity of some slip systems at levels which are either higher or lower than those predicted by the programme.

4.4.1 Modelling the pole fabric for dry specimen DD455

Specimen DD455 was deformed under dry condition at 8.5 GPa, 1300°C at slow strain rate of 2.5×10^{-5} s^{-1}. Active slip systems as observed under TEM are (010)[100], (010)[001] and (100)[001]. Pole figure for the specimens shows the presence of A-type and B-type fabric. A minor component of C-type could also be seen.

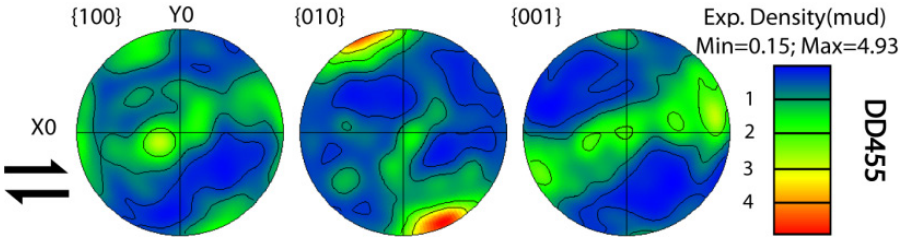

Figure 4-12: Dry samples deformed at 8.5 GPa and 1300°C. Sample deformed at slower strain rate shows dominant slip system to be (010)[100] and (010)[001].

Table 4-3: Choice of relative CRSS values used for various models in order to synthetically generate the pole figure for specimen DD455

Models	(010)[100]	(010)[001]	(100)[001]	(001)[100]
Model 1	1	1	1	1
Model 2	1	1	1	5
Model 3	1	1	5	1
Model 4	1	3	1	4
Model 5	1	3	1.5	5
Model 6	1	3	1	3

In order to synthetically generate a pole figure similar to what is observed in the specimen DD455 (Fig 4-12); a number of models were chosen. Starting by assigning all the slip systems an equal value of CRSS, the relative CRSS values are then iterated until a fair similarity is achieved between the observed pole figure in the specimen and the synthetic pole figure.

The first model, which assumes all the slip systems to have similar CRSS value, clearly fails to recreate the pole figure for the specimen DD455. By suppressing the slip system (001)[100] with a choice of higher CRSS in model 2, because the relevant fabric generated

by this slip system shows very weak contribution in the original pole figure for DD455, a closer similarity in the visual appearance of the simulated and measured pole figures is achieved. Model 3 is again very different from the original pole figure. On the other hand, models 4, 5 and 6 which assume (010)[100] and (010)[001] to have very similar CRSS with later being slightly more difficult than the former, produces a much better match in the visual appearance and relative concentration of different crystallographic directions. The last 3 models also assume that (100)[001] and (001)[100] slip systems are at least three times more difficult than the slip systems with (010) glide plane.

When the best fit models are examined they all identify the (010)[100] slip system as the easiest slip system at 8.5 GPa and 1300°C under dry conditions. Two of the successful models also identify the (100)[001] slip system as being of comparable strength to (010)[100],however, any model that impose this slip system to be weaker than (010)[100] results in a poor match with the experimental pole figure. This observation is in line with our other observations that there is no appreciable hardening of a-slip with pressure up to 11 GPa.

Figure 4-14 shows that activity of various slip systems may vary with changes in strain to maintain the strain homogeneity in the aggregate without the need for grain boundary migration or other secondary strain generating processes. In this sense, models 4 and 5 are very stable and this is additional evidence that relative CRSS choices representing models 4 and 5 are representative of the slip systems active in specimen DD455.

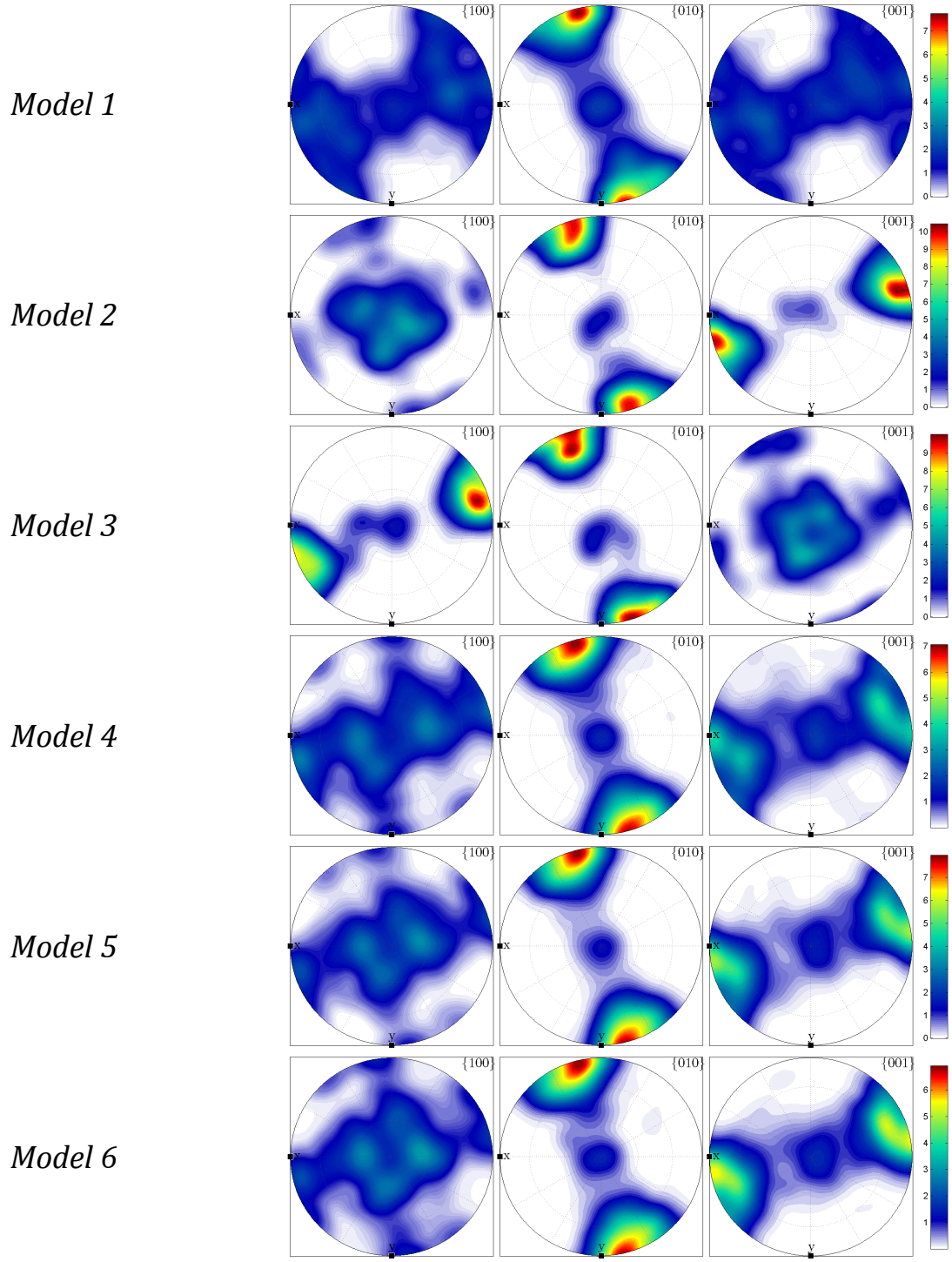

Figure 4-13: Pole figures for models described in the table 5-3. Models which assume very similar CRSS value for (010)[100] and (010)[001] and at least three times higher CRSS value for other two slip systems can mimic the experimental pole figure.

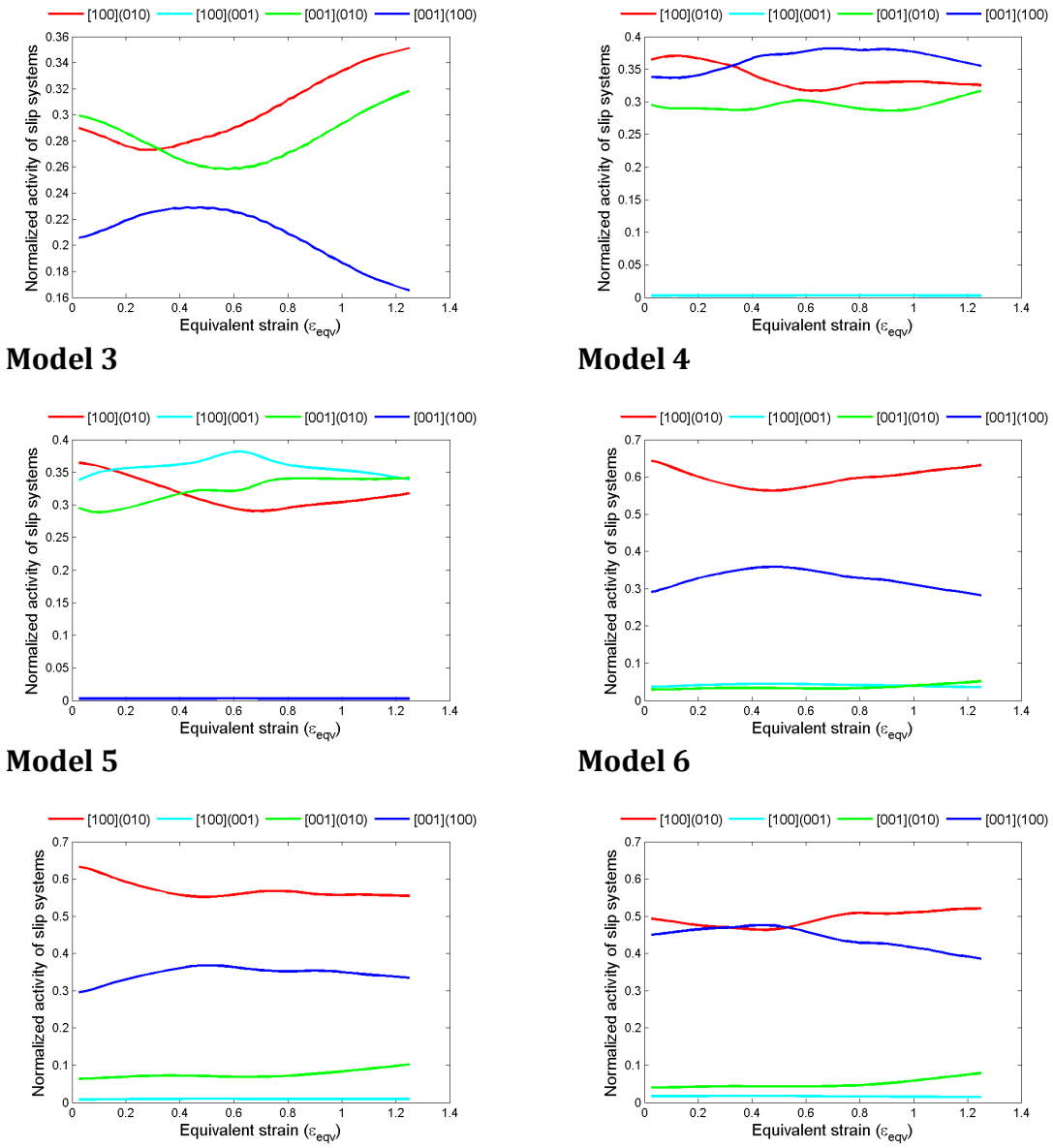

Figure 4-14: Normalized activity versus equivalent strain plot for various model. Model 1 to 6 is shown here. Activity of slip systems can change with increasing strain because of geometrical constraints. In this sense, model 4 and 5 appear very stable

4.4.2 Modelling the pole fabric for dry specimen DD456

Specimen DD456 was deformed under wet condition at 8.5 GPa, 1300°C at a relatively fast strain rate of 5×10^{-5} s^{-1}. Active slip systems as observed under TEM are (010)[001] and (100)[001]. The pole figure for the specimens shows the presence of C-type and B-type fabric.

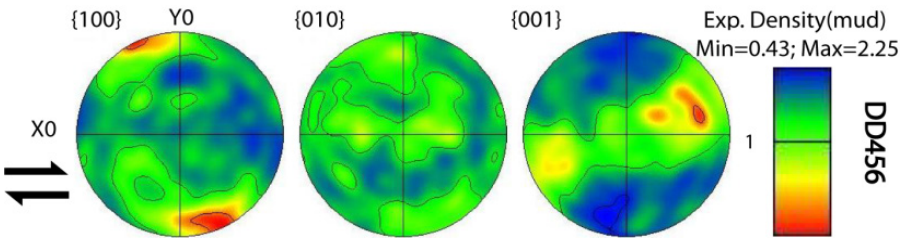

Figure 4-15: Wet samples deformed at 8.5 GPa and 1300°C. The specimens shows two likely active slip systems – (010)[100] and (100)[001] which has also been confirmed by TEM study on this sample.

Table 4-4: Choice of relative CRSS values used for various models in order to synthetically generate the pole figure for specimen DD456

Models	(010)[100]	(010)[001]	(100)[001]	(001)[100]
Model 1	10	1	1	10
Model 2	10	2	1	10

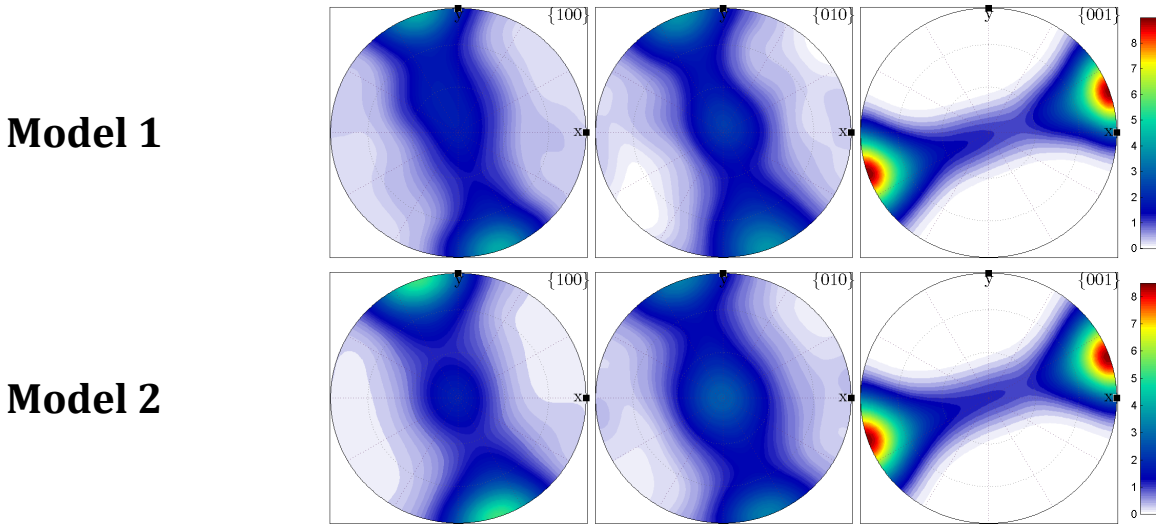

Figure 4-16: Pole figures for models described in the table 5-4. Models which assume (100)[001] to be the easiest and (010)[100] as slightly higher than the former along with very high value of CRSS for (010)[100] and (001)[100] i.e. for a-slip can reproduce well the pole figure for the specimen DD456.

Models (table 4-4) that assume the (010)[001] system to be the easiest with (010)[001] being slightly harder can recreate the pole figure for DD456 (Fig 4-16). These models also require that the other two slip systems involving a-slip i.e. (010)[100] and (001)[100] should be considerably hard to prevent the alignment of olivine [100] axes along the shear direction.

Seismic anisotropy in the upper mantle – Implications from this study

Crystallographic preferred orientation of major mantle mineral phases e.g. olivine, pyroxene and garnet is believed to be the major cause of seismic anisotropy in the upper mantle. Seismic anisotropy by CPO development is the result of intrinsic seismic anisotropy of these crystals.

Compositionally, mantle peridotite consists of up to 60% olivine, of orthopyroxene, clinopyroxene, ~ 0%– 20% of garnet, and spinel depending on the depth (e.g., *Ringwood* [1975]. Olivine, being the compositionally dominant and mechanically weakest phase in the peridotite, dictates the overall anisotropy of the aggregate and contribution of pyroxenes results in slight dilution of the overall P-wave and S-wave anisotropy [*Blackman et al.,* 2002; *Mainprice et al.,* 2000; *Mainprice et al.,* 2005]. Whereas, garnet is known to develop only weak LPO in the presence of other weaker phases e.g. olivine and pyroxenes [*Mainprice et al.,* 2004].

The general characteristic of Seismic anisotropy resulting from LPO of olivine, as seen in the natural samples, is that the fastest S-wave polarization direction lies (sub-)parallel to the foliation plane. The maximum shear wave splitting is observed normal to the lineation direction in the foliation plane. P-wave velocity is the fastest along the olivine a-axis. Symmetry of S-wave anisotropy is influenced by both [100] and [001] axis and P-wave anisotropy is mainly dependent upon [100] axis. Overall magnitude of the seismic anisotropy is dependent upon the orientations of all three olivine axis [*Ben Ismail and Mainprice,* 1998]. Magnitude of Seismic anisotropy increases the fabric strength but does not increase beyond 20% for P-waves and 15% for S-waves [*Ben Ismail and Mainprice,* 1998]. P-wave propagation direction is also fastest parallel to its [100] axis like in olivine. However, unlike in olivine where the maximum splitting directions occurs at an angle of $15 - 20°$ from the *c*-axis direction, polarization direction of the fastest s-wave in enstatite lies at ~25° from the *b*-axis [*Blackman et al.,* 2002].

In case of olivine, the ratio V_{SH}/V_{SV} varies from fabric to fabric. In general, A-type fabrics are known to produce stronger V_{SH}/V_{SV} ratio than E-type fabric with ratio being

greater than 1 for horizontal flow pattern. V_{SH}/V_{SV} ratio should be less than 1 for aggregate dominated by C-type fabric in olivine. Fabric resulting from the activity of [001](hk0) type of slip system should produce weaker anisotropy [*Karato et al.,* 2008; *Mainprice et al.,* 2005]. The V_{SH}/V_{SV} ratio for shear wave anisotropy resulting from olivine would definitely change with change in flow direction in the mantle (Table 4-5).

Table 4-5: V_{SH}/V_{SV} anisotropy for various olivine fabrics as a function of mantle flow direction (From Karato, 2008)

Fabric type	Horizontal flow	Vertical planar flow
A-type	$V_{SH}/V_{SV} > 1$	$V_{SH}/V_{SV} < 1$
B-type	$V_{SH}/V_{SV} > 1$	$V_{SH}/V_{SV} > 1$ (weak)
C-type	$V_{SH}/V_{SV} < 1$	$V_{SH}/V_{SV} > 1$ (weak)
D-type	$V_{SH}/V_{SV} > 1$	$V_{SH}/V_{SV} < 1$
E-type	$V_{SH}/V_{SV} > 1$ (weak)	$V_{SH}/V_{SV} < 1$

Seismic anisotropy in the upper mantle

Seismic anisotropy in the upper mantle has a general trend of decrease in its strength with increasing depth. This observation holds true for both P-wave and S-waves. Horizontally propagating P-waves travel faster than the vertically travelling ones and velocity ratio slowly decreases and becomes close to one at around 350 km depth [*Montagner and Kennett,* 1996]. This observation is true for most of the 1-D representation of seismic structure of earth e.g. PREM, IASP, AK135 and AK303 [*Mainprice et al.,* 2005]. The S-wave seismic anisotropy expressed in terms of V_{SH}/V_{SV} also shows a trend of decreasing ratio up to a depth of 250 km. This ratio becomes less than 1 and does not decrease a lot below this depth (Fig 4-17).

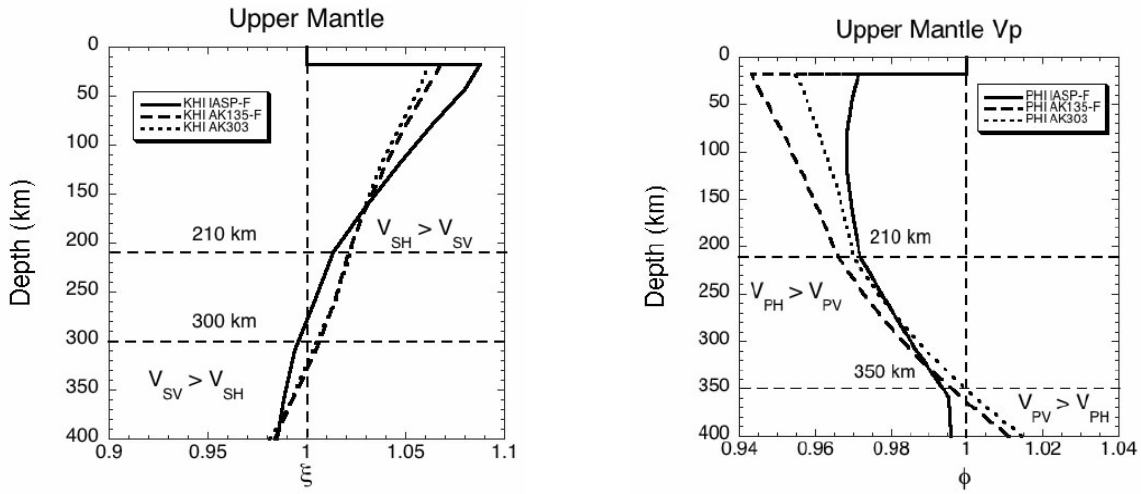

Figure 4-17: Left: Shear wave anisotropy in the upper mantle as a function of depth. Right: P-wave anisotropy as a function of depth (Source: PhD Thesis – Helen Couvy, 2005).

Olivine LPO transitions and changes in seismic anisotropy with depth

Several explanations have been proposed for the origin of the decrease in the strength of P-wave and S-wave seismic anisotropy in the upper. PREM [*Dziewonski and Anderson,* 1981] predicts a strongly anisotropic upper part of the upper mantle but close to seismically isotropic behaviour in the upper mantle below 250 km depth. Anisotropy in the upper reaches of the upper mantle is well explained by the existence of the A-type fabric in olivine [*Cara and Leveque,* 1988; *Montagner,* 1985; *Nishimura and Forsyth,* 1989; *Revenaugh and Jordan,* 1991]. Observation of negligible seismic anisotropy below 250 km could very well be explained by assuming that the deformation within this part of the mantle is minimal and hence no seismic anisotropy should develop in lower parts of the upper mantle. A transition in deformation mechanism from dislocation creep to diffusion creep below 250 km depth could also be one way to reconcile the seismically isotropic state of the upper mantle below this depth [*Karato,* 1992]. However, these models cannot explain the detailed seismic anisotropic structure of the lower parts of the upper mantle e.g. the inversion of the V_{SH}/V_{SV} ratio, as has been reported by more recent 1-D models of upper mantle seismic anisotropy (IASP, AK135 and AK303). Following the reports of pressure related slip system changes in olivine (e.g. [*Couvy et al.,* 2004; *Raterron et al.,* 2007], [*Mainprice et al.,* 2005] proposed an alternate explanation for the patterns of upper mantle seismic anisotropy. If c-slip dominates the deformation mechanism of olivine at pressures above 5-7 GPa then the seismic anisotropy resulting from the activity of the

(*hk*0)[001] slip system can explain the weak shear wave splitting and the inversion of theV_{SH}/V_{SV} ratio in the lower parts of the upper mantle.

However, in light of the new results presented in this study, that there is no pressure related change in slip system up to pressures of 11 GPa corresponding to an approximate depth of 330 km in earth, the behaviour of upper mantle seismic anisotropy is again an open question. Based upon the results from this study, however, the original argument of Mainprice *et al.* (2005), that the dominant olivine slip system becomes (*hk*0)[001] at high pressure, can still be retained if the change in slip system is not attributed to increasing pressure but to increasing H_2O content of olivine. Increasing olivine H_2O content with depth would cause a change in slip system ultimately to (100)[001] which in horizontally flowing mantle would produce weaker anisotropy. Rather than the water content of the mantle as a whole increasing with depth, however, a more plausible explanation is that changes in the partition coefficient of H_2O between olivine and other peridotite minerals leads to an increase in the olivine H_2O content with depth [*Hirschmann,* 2006]. In Fig. 4-18 H_2O contents of mineral phases in a peridotite bulk composition have been calculated as a function of depth by assuming fixed bulk H_2O content in the solid mineral phases of 200 ppm. To perform this calculation mineral melt partition coefficients were used for olivine, clinopyroxene, orthopyroxene and garnet taken from the study of [*Hirschmann,* 2006]. Although these partition coefficient are not well known at pressures above 3 GPa, particularly for garnet, good approximations of the behaviour can be made based on low pressure data and data from simple chemical systems [*Hirschmann,* 2006]. The presence of a melt phase is assumed with an H_2O content that is refined in order to obtain the correct bulk H_2O content in the solid phases using suitable partition coefficients. For a bulk rock H_2O content of 200 ppm, however, the assemblage would be sub solidus at conditions above 3 GPa along a mantle adiabat and the melt phase is simply assumed in order to use available mineral melt partition coefficients, rather than the less well known mineral-mineral partition coefficients. At low pressures most of the H_2O in the rock is dissolved in ortho- and clino-pyroxenes, which have mineral melt partition coefficients of the order of 0.01 at 3 GPa, however, these partition coefficients are strongly dependent on the Al content of both phases and with increasing pressure the Al contents decrease due to an

increase in the modal abundance of garnet. The modal abundance of orthopyroxene decreases with depth, which coupled with an increase in the mineral melt partition coefficient for olivine (= $X_{H_2O}^{olivine} / X_{H_2O}^{Melt}$) from ≈0.002 at 3 GPa to ≈0.01 at 6 GPa results in an increase in the olivine H_2O content. Effectively H_2O is partitioning out of pyroxenes and into olivine with increasing depth, increasing the olivine H_2O content even though the bulk H_2O content in the solid assemblage is constant. The main uncertainty is the garnet H_2O partition coefficient, which is not well known at pressure above 3 GPa and has been fixed at this level. However, even if the garnet H_2O partition coefficient is significantly larger than assumed here, olivine H_2O contents would still rise with depth due to decreasing abundance and Al content of pyroxenes. For olivine H_2O contents to then exceed 200 ppm by 300 km would simply require a larger H_2O content in the bulk rock.

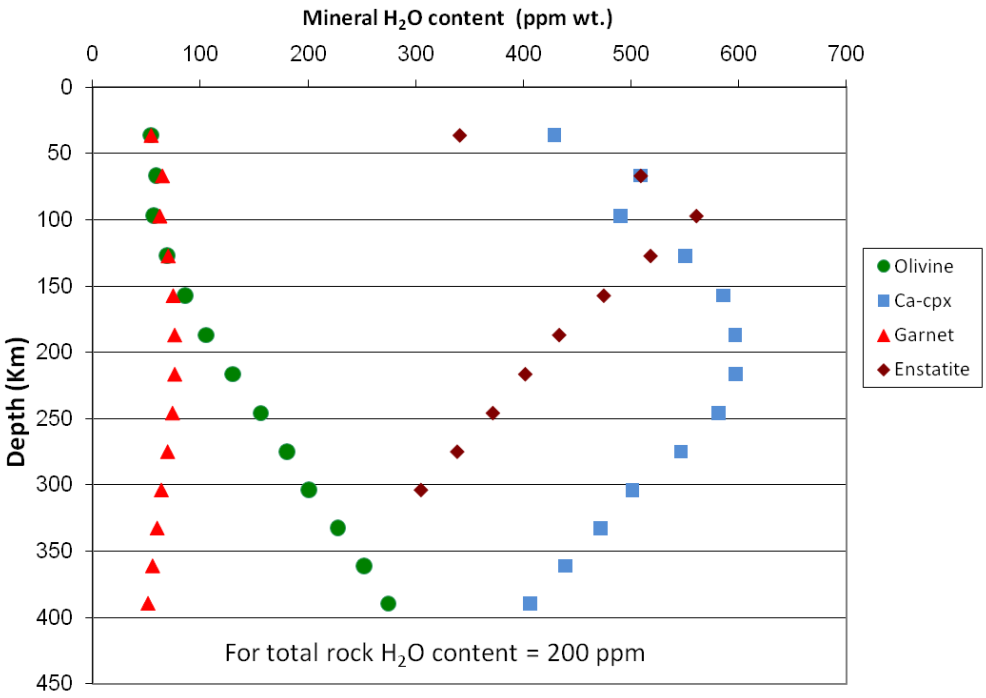

Figure 4-18: Variation of water content of major mineral phases in the upper mantle. Changes in the water content are result of variation in the portioning coefficient of water for various phases with depth.

Variation in the water content of olivine with depth will result in changes in fabric exhibited by olivine. Above 200 km depth in the upper mantle, if olivine contains no more

than 100 ppm wt. water then A-type or E-type fabric should be dominant in olivine (e.g. *Jung et al.* [2006]. Olivine exhibiting this kind fabric of fabric will have V_{SH}/V_{SV} ratio greater than 1 for horizontally flowing mantle. Seismic anisotropy would gradually decrease if rising water content of olivine results in increasing presence of the E-type fabric in the upper parts of the upper mantle. Once water content in olivine has gone up high enough (above 100 ppm wt. - [*Jung et al.,* 2006]) then the dominant fabric would become C-type (Fig. 4-19). Such a change in fabric should translate into the reversal of V_{SH}/V_{SV} to less than 1 which we observer in most of the 1-D radial anisotropy models of earth below 250 km depth. Olivine fabric dominated by C-type can also explain overall weaker anisotropy as has been argued by Mainprice *et al.* 2005.

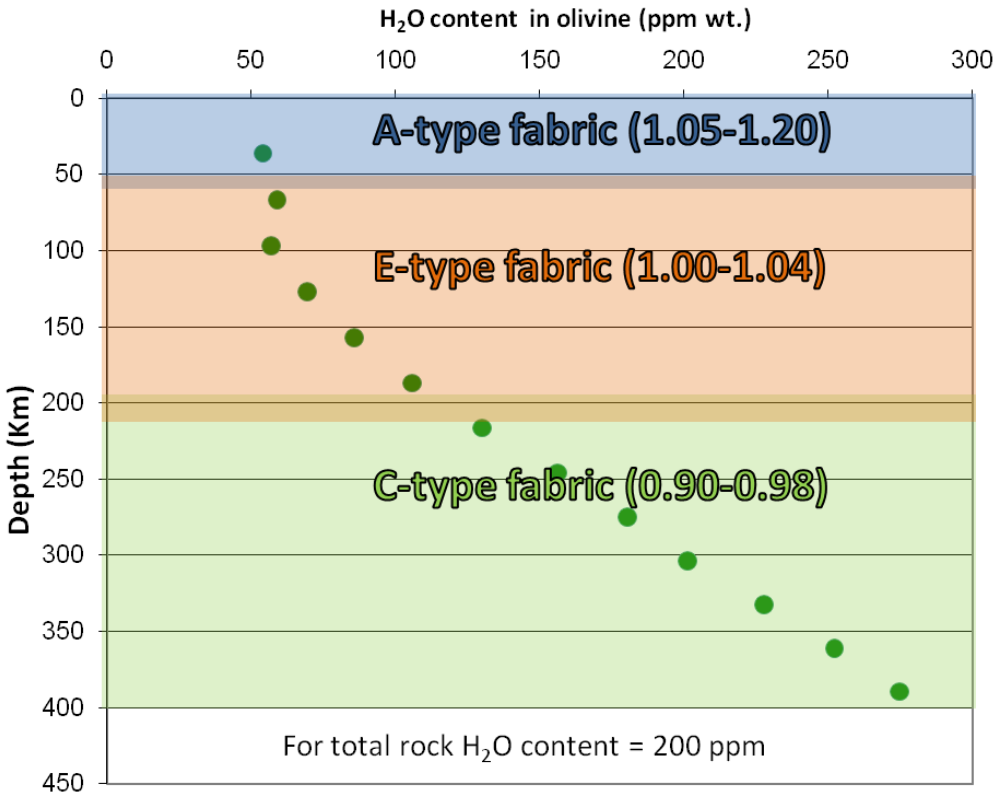

Figure 4-19: Variation in olivine fabric with changes in water content as a function of depth. Presence of C-type fabric can explain the nature of the seismic anisotropy in the lower parts of the upper mantle. Numbers in the parenthesis are the V_{SH}/V_{SV} ratios (from Karato et al., 2008) that are observed in natural olivine specimens exhibiting corresponding fabric types.

However, the exact depth of such a transition from A (or E)-type dominated fabric in olivine to that dominated by C-type fabric, cannot be well constrained at this stage the

transition line between E-type to C-type fabric is not well defined. Nevertheless, changes in olivine fabric with increasing water content, due to an increase in the partition coefficient of H_2O between olivine and other minerals with depth, can certainly explain the decrease in the seismic anisotropy within the top part of the upper mantle.

5 Conclusion

Major theme of this study has been to unravel the cause of upper mantle seismic anisotropy. Detailed deformation studies on San Carlos olivine has been conducted to determine the role played by various physical and chemical parameters i.e. stress, water, pressure and temperature on the fabric development in olivine. LPO of olivine undergoes remarkable changes with changes in the state of stress and water under which olivine deforms. Olivine present in the lithospheric part of the mantle should exhibit dominantly A-type fabric because of very low stresses present there. However, the fabric displayed by olivine should show a wide variety in the asthenosphere. It can be A-type to E-type in weakly hydrous condition (< 100 ppm wt.) to C-type or B-type fabric in moderately hydrous condition (> 100 ppm wt.) depending upon stresses. One major highlight of the results from this study is the negligible role of pressure on slip systems in olivine. Unlike many of the previous studies, where it has been shown that rising pressure changes the slip system in olivine from slip with b = [100] to slip with b = [001], we have established that those changes must have been simply as a result of poor characterization of flow stress in those studies. Thus highlights of this study are as follows:

1. It has been established that Deformation-DIA lives up to its promise of being a tool for conducting controlled deformation experiment. It is possible to control stresses during experimentation by exercising control over strain rate. The newly designed high pressure assembly should allow one to reliably conduct controlled deformation experiments on materials up to a pressure of 8.5 GPa and 1500°C.
2. Slip system in olivine changes to (010)[001] slip system at higher stresses and this effect is directly related to the observed lower CRSS value for this slip system at lower temperatures.

   However, a simple sinusoidal Peierls potential fails to predict the CRSS-Temperature relation in olivine. Computer modeling of dislocation motion by double-kink nucleation should help resolve this issue. Alternatively, TEM study of kink

structure in olivine can also provide valuable information regarding nature of the Peierls process in olivine.

3. Presence of C-type fabric in olivine necessitates a significant amount of glide on (100) plane. At this stage, there is no reliable model available which can explain sufficient glide on this plane without resorting to cutting Si-O bonds in the SiO_4 tetrahedra. However, water associated with Silicon vacancies in olivine structure can allow glide on this plane. Amount of water that can be dissolved at Silicon vacancy sites is still contentious issue. Moreover, it is not clear how much water need to be associated at Si sites to cause appreciable glide on (100) plane. Though, studies on hydrolysis of quartz indicate that it need not be a lot. Further studies on the role of Silicon vacancies and associated volume of water dissolved on this site should resolve this issue.

   Another related issue with (100)[001] slip system is the apparent hardening of (010)[001] slip system. Widely dissociated dislocation core of dislocation in this slip system may produce such an effect. The difficulty with this study is that imaging of dislocation cores of screw dislocation is not straightforward and most of the dislocations in hydrous specimens are screw segments.
4. Piezoelectric stress sensor based on Gallium phosphate has shown a great promise. This kind of sensor should allow us to overcome the biggest challenge in conducting the deformation experiments at high pressure i.e. in-situ measurement of stress.

References

Alam, M. N., M. Blackman, and D. W. Pashley (1954), High-Angle Kikuchi Patterns, *Proceedings of the Royal Society of London. Series A. Mathematical and Physical Sciences*, *221*(1145), 224-242, doi:10.1098/rspa.1954.0017.

Badro, J., J. P. Itie, and A. Polian (1998), On the high-pressure phase transition in GaPO4, *European Physical Journal B*, *1*(3), 265-268.

Bai, Q., and D. L. Kohlstedt (1992), High-temperature creep of olivine single crystals, 2. dislocation structures, *Tectonophysics*, *206*(1-2), 1-29.

Bai, Q., and D. L. Kohlstedt (1993), EFFECTS OF CHEMICAL ENVIRONMENT ON THE SOLUBILITY AND INCORPORATION MECHANISM FOR HYDROGEN IN OLIVINE, *Physics and Chemistry of Minerals*, *19*(7), 460-471.

Bailey, J. E., and P. B. Hirsch (1960), The dislocation distribution, flow stress, and stored energy in cold-worked polycrystalline silver, *Philosophical Magazine*, *5*(53), 485 - 497.

Barna, A., and M. Menyhard (1994), Auger Depth Profile Analysis of Deeply Buried Interfaces, *physica status solidi (a)*, *145*(2), 263-274, doi:10.1002/pssa.2211450206.

Barna, A., B. Pecz, and M. Menyhard (1999), TEM sample preparation by ion milling amorphization, *Micron*, *30*(3), 267-276.

Ben Ismail, W., and D. Mainprice (1998), An olivine fabric database: an overview of upper mantle fabrics and seismic anisotropy, *Tectonophysics*, *296*(1-2), 145-157.

Blackman, D. K., H. R. Wenk, and J. M. Kendall (2002), Seismic anisotropy of the upper mantle 1. Factors that affect mineral texture and effective elastic properties, *Geochemistry Geophysics Geosystems*, *3*, doi:10.1029/2001gc000248.

Braithwaite, J. S., K. Wright, and C. R. A. Catlow (2003), A theoretical study of the energetics and IR frequencies of hydroxyl defects in forsterite, *J. Geophys. Res.-Solid Earth*, *108*(B6), doi:10.1029/2002jb002126.

Brodholt, J. P., and K. Refson (2000), An ab initio study of hydrogen in forsterite and a possible mechanism for hydrolytic weakening, *J. Geophys. Res.-Solid Earth*, *105*(B8), 18977-18982.

Brunner, E., and U. Sternberg (1998), Solid-state NMR investigations on the nature of hydrogen bonds, *Prog. Nucl. Magn. Reson. Spectrosc.*, *32*, 21-57.

Bussod, G. Y., T. Katsura, and D. C. Rubie (1993), The large volume multi-anvil press as a high<i>P-T</i> deformation apparatus, *Pure and Applied Geophysics*, *141*(2), 579-599, doi:10.1007/bf00998346.

Bystricky, M., K. Kunze, L. Burlini, and J.-P. Burg (2000), High Shear Strain of Olivine Aggregates: Rheological and Seismic Consequences, *Science*, *290*(5496), 1564-1567, doi:10.1126/science.290.5496.1564.

Cara, M., and J. L. Leveque (1988), Anisotropy of the asthenosphere: The higher mode data of the Pacific revisited, *Geophys. Res. Lett.*, *15*, 205-208.

Carter, J. C. H., C. A. Stone, R. F. Davis, and D. R. Schaub (1980), High-temperature, multi-atmosphere, constant stress compression creep apparatus, *Review of Scientific Instruments*, *51*(10), 1352-1357.

CARTER, N. L., and H. G. AVE'LALLEMANT (1970), High Temperature Flow of Dunite and Peridotite, *Geological Society of America Bulletin*, *81*(8), 2181-2202, doi:10.1130/0016-7606(1970)81[2181:htfoda]2.0.co;2.

Castaing, J., J. Cadoz, and S. H. Kirby (1981), PRISMATIC SLIP OF AL2O3 SINGLE-CRYSTALS BELOW 1000-DEGREES-C IN COMPRESSION UNDER HYDROSTATIC-PRESSURE, *J. Am. Ceram. Soc.*, *64*(9), 504-511.

Chakraborty, S., and F. Costa (2004), Fast diffusion of Si and O in San Carlos olivine under hydrous conditions, *Geochimica Et Cosmochimica Acta*, *68*(11), A275-A275.

Couvy, H., D. J. Frost, F. Heidelbach, K. Nyilas, T. Ungar, S. Mackwell, and P. Cordier (2004), Shear deformation experiments of forsterite at 11GPa-1400 degrees C in the multianvil apparatus, *Eur. J. Mineral.*, *16*(6), 877-889, doi:10.1127/0935-1221/2004/0016-0877.

Damjanovic, D. (1998), Materials for high temperature piezoelectric transducers, *Current Opinion in Solid State & Materials Science*, *3*(5), 469-473.

De Bresser, J. H. P. (1996), Steady state dislocation densities in experimentally deformed calcite materials: Single crystals versus polycrystals, *J. Geophys. Res.*, *101*(B10), 22189-22201, doi:10.1029/96jb01759.

De Bresser, J. H. P., J. H. Ter Heege, and C. J. Spiers (2001), Grain size reduction by dynamic recrystallization: can it result in major theological weakening?, *Int. J. Earth Sci.*, *90*(1), 28-45.

Deer, W. A., R. A. Howie, and J. Zussman (1997), Rock-Forming Minerals, Vol. 2B, Double-Chain Silicates, edited.

Demouchy, S., and S. Mackwell (2006), Mechanisms of hydrogen incorporation and diffusion in iron-bearing olivine, *Physics and Chemistry of Minerals*, *33*(5), 347-355, doi:10.1007/s00269-006-0081-2.

Derby, B., and M. F. Ashby (1987), ON DYNAMIC RECRYSTALLIZATION, *Scripta Metallurgica*, *21*(6), 879-884.

Dingley, D. J., M. Longden, J. Weinbren, and J. Alderman (1987), ONLINE ANALYSIS OF ELECTRON BACK SCATTER DIFFRACTION PATTERNS .1. TEXTURE ANALYSIS OF ZONE REFINED POLYSILICON, *Scanning Microscopy*, *1*(2), 451-456.

Dohmen, R., S. Chakraborty, and H. W. Becker (2002), Si and O diffusion in olivine and implications for characterizing plastic flow in the mantle, *Geophys. Res. Lett.*, *29*(21), 4, doi:2030
10.1029/2002gl015480.

Drury, M. R. (1991), Hydration-induced climb dissociation of dislocations in naturally deformed mantle olivine, *Physics and Chemistry of Minerals*, *18*(2), 106-116, doi:10.1007/bf00216603.

Drury, M. R. (2005), Dynamic recrystallization and strain softening of olivine aggregates in the laboratory and the lithosphere, *Geological Society, London, Special Publications*, *243*(1), 143-158, doi:10.1144/gsl.sp.2005.243.01.11.

Drury, M. R., and F. J. Humphreys (1988), MICROSTRUCTURAL SHEAR CRITERIA ASSOCIATED WITH GRAIN-BOUNDARY SLIDING DURING DUCTILE DEFORMATION, *Journal of Structural Geology*, *10*(1), 83-89.

Durham, W. B., and C. Goetze (1977), PLASTIC FLOW OF ORIENTED SINGLE CRYSTALS OF OLIVINE 1. MECHANICAL DATA, *J. Geophys. Res.*, *82*(36), 5737-5753, doi:10.1029/JB082i036p05737.

Durham, W. B., C. Goetze, and B. Blake (1977), PLASTIC FLOW OF ORIENTED SINGLE CRYSTALS OF OLIVINE 2. OBSERVATIONS AND INTERPRETATIONS OF THE DISLOCATION STRUCTURES, *J. Geophys. Res.*, *82*(36), 5755-5770, doi:10.1029/JB082i036p05755.

Durham, W. B., S. Mei, D. L. Kohlstedt, L. Wang, and N. A. Dixon (2009), New measurements of activation volume in olivine under anhydrous conditions, *Physics of the Earth and Planetary Interiors*, *172*(1-2), 67-73.

Durinck, J., A. Legris, and P. Cordier (2005), Pressure sensitivity of olivine slip systems: first-principle calculations of generalised stacking faults, *Physics and Chemistry of Minerals*, *32*(8), 646-654, doi:10.1007/s00269-005-0041-2.

Dziewonski, A. M., and D. L. Anderson (1981), PRELIMINARY REFERENCE EARTH MODEL, *Physics of the Earth and Planetary Interiors*, *25*(4), 297-356.

Eckert, H., J. P. Yesinowski, L. A. Silver, and E. M. Stolper (1988), WATER IN SILICATE-GLASSES - QUANTITATION AND STRUCTURAL STUDIES BY H-1 SOLID ECHO AND MAS-NMR METHODS, *J. Phys. Chem.*, *92*(7), 2055-2064.

Frost, D. J. (2008), The Upper Mantle and Transition Zone, *Elements*, *4*(3), 171-176, doi:10.2113/gselements.4.3.171.
Frost, D. J., and C. A. McCammon (2008), The redox state of Earth's mantle, *Annu. Rev. Earth Planet. Sci.*, *36*, 389-420, doi:10.1146/annurev.earth.36.031207.124322.
Gifkins, R. C. (1970), TRANSITIONS IN CREEP BEHAVIOUR, *Journal of Materials Science*, *5*(2), 156-&.
Goetze, C. (1978), Mechanisms of Creep in Olivine, *Philosophical Transactions of the Royal Society of London Series a-Mathematical Physical and Engineering Sciences*, *288*(1350), 99-119.
Ham, R. K. (1961), THE DETERMINATION OF DISLOCATION DENSITIES IN THIN FILMS, *Philosophical Magazine*, *6*(69), 1183-1184.
Heggie, M., and R. Jones (1986), MODELS OF HYDROLYTIC WEAKENING IN QUARTZ, *Philos. Mag. A-Phys. Condens. Matter Struct. Defect Mech. Prop.*, *53*(5), L65-L70.
Hess, H. H. (1964), SEISMIC ANISOTROPY OF UPPERMOST MANTLE UNDER OCEANS, *Nature*, *203*(494), 629-&.
Hirschmann, M. M. (2006), WATER, MELTING, AND THE DEEP EARTH H2O CYCLE, *Annu. Rev. Earth Planet. Sci.*, *34*(1), 629-653, doi:doi:10.1146/annurev.earth.34.031405.125211.
Hirth, J. P., and J. Lothe (1992), Theory of Dislocations, edited.
Holtzman, B. K., D. L. Kohlstedt, M. E. Zimmerman, F. Heidelbach, T. Hiraga, and J. Hustoft (2003), Melt segregation and strain partitioning: Implications for seismic anisotropy and mantle flow, *Science*, *301*(5637), 1227-1230.
Holyoke, C. W., and A. K. Kronenberg (2010), Accurate differential stress measurement using the molten salt cell and solid salt assemblies in the Griggs apparatus with applications to strength, piezometers and rheology, *Tectonophysics*, *494*(1-2), 17-31, doi:10.1016/j.tecto.2010.08.001.
Humphreys, F. J. (2001), Review Grain and subgrain characterisation by electron backscatter diffraction, *Journal of Materials Science*, *36*(16), 3833-3854, doi:10.1023/a:1017973432592.
Jung, H., and S. Karato (2001a), Water-induced fabric transitions in olivine, *Science*, *293*(5534), 1460-1463.
Jung, H., and S. I. Karato (2001b), Effects of water on dynamically recrystallized grain-size of olivine, *Journal of Structural Geology*, *23*(9), 1337-1344.
Jung, H., I. Katayama, Z. Jiang, T. Hiraga, and S. Karato (2006), Effect of water and stress on the lattice-preferred orientation of olivine, *Tectonophysics*, *421*(1-2), 1-22.
Jung, H., W. Mo, and H. W. Green (2009a), Upper mantle seismic anisotropy resulting from pressure-induced slip transition in olivine, *Nat. Geosci.*, *2*(1), 73-77, doi:10.1038/ngeo389.
Jung, H., W. Mo, and H. W. Green (2009b), Upper mantle seismic anisotropy resulting from pressure-induced slip transition in olivine, *Nature Geosci*, *2*(1), 73-77.
Karato, S.-I., M. S. Paterson, and J. D. Fitzgerald (1986), Rheology of Synthetic Olivine Aggregates: Influence of Grain Size and Water, *J. Geophys. Res.*, *91*(B8), 8151-8176, doi:10.1029/JB091iB08p08151.
Karato, S. (1986), Does partial melting reduce the creep strength of the upper mantle?, *Nature*, *319*(6051), 309-310.
Karato, S. (1992), ON THE LEHMANN DISCONTINUITY, *Geophys. Res. Lett.*, *19*(22), 2255-2258.
Karato, S. (1995), EFFECTS OF WATER ON SEISMIC-WAVE VELOCITIES IN THE UPPER-MANTLE, *Proc. Jpn. Acad. Ser. B-Phys. Biol. Sci.*, *71*(2), 61-66.
Karato, S. (1998), Seismic Anisotropy in the Deep Mantle, Boundary Layers and the Geometry of Mantle Convection, *Pure and Applied Geophysics*, *151*(2), 565-587, doi:10.1007/s000240050130.
Karato, S., H. Jung, I. Katayama, and P. Skemer (2008), Geodynamic significance of seismic anisotropy of the upper mantle: New insights from laboratory studies, *Annu. Rev. Earth Planet. Sci.*, *36*, 59-95, doi:10.1146/annurev.earth.36.031207.124120.

Karato, S., and D. C. Rubie (1997), Toward an experimental study of deep mantle rheology: A new multianvil sample assembly for deformation studies under high pressures and temperatures, *J. Geophys. Res.-Solid Earth*, *102*(B9), 20111-20122.
Karato, S., D. C. Rubie, and H. Yan (1993), Dislocation Recovery in Olivine under Deep Upper-Mantle Conditions - Implications for Creep and Diffusion, *J. Geophys. Res.-Solid Earth*, *98*(B6), 9761-9768.
Karato, S., and P. Wu (1993), RHEOLOGY OF THE UPPER MANTLE - A SYNTHESIS, *Science*, *260*(5109), 771-778.
Karato, S., S. Zhang, M. E. Zimmerman, M. J. Daines, and D. L. Kohlstedt (1998), Experimental studies of shear deformation of mantle materials: Towards structural geology of the mantle, *Pure and Applied Geophysics*, *151*(2-4), 589-603.
Karato, S. I. (2008a), *Deformation of earth materials*, 463 pp., Cambridge university press, New York.
Karato, S. I. (2008b), Recent progress in the experimental studies on the kinetic properties in minerals, *Physics of the Earth and Planetary Interiors*, *170*(3-4), 152-155, doi:10.1016/j.pepi.2008.07.022.
Karato, S. I., M. Toriumi, and T. Fujii (1980), Dynamic Recrystallization of Olivine Single-Crystals during High-Temperature Creep, *Geophys. Res. Lett.*, *7*(9), 649-652.
Katayama, I., H. Jung, and S.-i. Karato (2004), New type of olivine fabric from deformation experiments at modest water content and low stress, *Geology*, *32*(12), 1045-1048, doi:10.1130/g20805.1.
Katayama, I., and S.-i. Karato (2006), Effect of temperature on the B- to C-type olivine fabric transition and implication for flow pattern in subduction zones, *Physics of the Earth and Planetary Interiors*, *157*(1-2), 33-45.
Katayama, I., and S. I. Karato (2008), Low-temperature, high-stress deformation of olivine under water-saturated conditions, *Physics of the Earth and Planetary Interiors*, *168*(3-4), 125-133, doi:10.1016/j.pepi.2008.05.019.
Kinsland, G. L., and W. A. Bassett (1977), STRENGTH OF MGO AND NACL POLYCRYSTALS TO CONFINING PRESSURES OF 250 KBAR AT 25DEGREESC, *Journal of Applied Physics*, *48*(3), 978-985.
Kohlstedt, D. L. (2006), The role of water in high-temperature rock deformation, *Water in Nominally Anhydrous Minerals*, *62*, 377-396, doi:10.2138/rmg.2006.62.16.
Kohlstedt, D. L., C. Goetze, and W. B. Durham (Eds.) (1976b), *Experimental deformation of single crystal olivine with application to flow in the mantle*, b ed., 35-49 pp., Wiley-Interscience, New York,N.Y.
Kohlstedt, D. L., and S. J. Mackwell (1998), Diffusion of hydrogen and intrinsic point defects in olivine, *Zeitschrift Fur Physikalische Chemie-International Journal of Research in Physical Chemistry & Chemical Physics*, *207*, 147-162.
Kohn, S. C. (2006), Structural Studies of OH in Nominally Anhydrous Minerals Using NMR, *Reviews in Mineralogy and Geochemistry*, *62*(1), 53-66, doi:10.2138/rmg.2006.62.3.
Koizumi, H., H. O. K. Kirchner, and T. Suzuki (1994), NUCLEATION OF TRAPEZOIDAL KINK PAIRS ON A PEIERLS POTENTIAL, *Philos. Mag. A-Phys. Condens. Matter Struct. Defect Mech. Prop.*, *69*(4), 805-820.
Krempl, P., G. Schleinzer, and W. Wallnofer (1997), Gallium phosphate, GaPO4: a new piezoelectric crystal material for high-temperature sensorics, *Sensors and Actuators a-Physical*, *61*(1-3), 361-363.
Libowitzky, E. (1999), Correlation of O-H stretching frequencies and O-H center dot center dot center dot O hydrogen bond lengths in minerals, *Mon. Chem.*, *130*(8), 1047-1059.
Libowitzky, E., and A. Beran (1995), OH defects in forsterite, *Physics and Chemistry of Minerals*, *22*(6), 387-392, doi:10.1007/bf00213336.

Lister, G. S., and B. E. Hobbs (1980), THE SIMULATION OF FABRIC DEVELOPMENT DURING PLASTIC-DEFORMATION AND ITS APPLICATION TO QUARTZITE - THE INFLUENCE OF DEFORMATION HISTORY, *Journal of Structural Geology*, *2*(3), 355-370.

Lister, G. S., and M. S. Paterson (1979), SIMULATION OF FABRIC DEVELOPMENT DURING PLASTIC-DEFORMATION AND ITS APPLICATION TO QUARTZITE - FABRIC TRANSITIONS, *Journal of Structural Geology*, *1*(2), 99-115.

Lister, G. S., M. S. Paterson, and B. E. Hobbs (1978), SIMULATION OF FABRIC DEVELOPMENT IN PLASTIC-DEFORMATION AND ITS APPLICATION TO QUARTZITE - MODEL, *Tectonophysics*, *45*(2-3), 107-158.

Mackwell, S. J., and D. L. Kohlstedt (1990), Diffusion of Hydrogen in Olivine: Implications for Water in the Mantle, *J. Geophys. Res.*, *95*(B4), 5079-5088, doi:10.1029/JB095iB04p05079.

Mainprice, D., G. Barruol, and W. B. Ismail (2000), *Earth's Deep Interior: Mineral Physics and Tomography from the Atomic to the Global Scale* AGU, Washington DC.

Mainprice, D., J. Bascou, P. Cordier, and A. Tommasi (2004), Crystal preferred orientations of garnet: comparison between numerical simulations and electron back-scattered diffraction (EBSD) measurements in naturally deformed eclogites, *Journal of Structural Geology*, *26*(11), 2089-2102.

Mainprice, D., A. Tommasi, H. Couvy, P. Cordier, and D. J. Frost (2005), Pressure sensitivity of olivine slip systems and seismic anisotropy of Earth's upper mantle, *Nature*, *433*(7027), 731-733.

Malherbe, J. B. (1994), SPUTTERING OF COMPOUND SEMICONDUCTOR SURFACES .1. ION-SOLID INTERACTIONS AND SPUTTERING YIELDS, *Critical Reviews in Solid State and Materials Sciences*, *19*(2), 55-127.

Matveev, S., H. S. O'Neill, C. Ballhaus, W. R. Taylor, and D. H. Green (2001), Effect of silica activity on OH-IR spectra of olivine: Implications for low-aSiO(2) mantle metasomatism, *J. Petrol.*, *42*(4), 721-729.

McKenzie, D. (1979), FINITE DEFORMATION DURING FLUID-FLOW, *Geophysical Journal of the Royal Astronomical Society*, *58*(3), 689-715.

Mei, S., and D. L. Kohlstedt (2000), Influence of water on plastic deformation of olivine aggregates 1. Diffusion creep regime, *J. Geophys. Res.-Solid Earth*, *105*(B9), 21457-21469.

Michibayashi, K., T. Ina, and K. Kanagawa (2006), The effect of dynamic recrystallization on olivine fabric and seismic anisotropy: Insight from a ductile shear zone, Oman ophiolite, *Earth and Planetary Science Letters*, *244*(3-4), 695-708.

Montagner, J. P. (1985), Seismic anisotropy of the Pacific Ocean inferred from long-period surface waves dispersion, *Physics of the Earth and Planetary Interiors*, *38*, 28-50.

Montagner, J. P., and B. L. N. Kennett (1996), How to reconcile body-wave and normal-mode reference earth models, *Geophys. J. Int.*, *125*(1), 229-248.

Montesi, L. G. J., and G. Hirth (2003), Grain size evolution and the rheology of ductile shear zones: from laboratory experiments to postseismic creep, *Earth and Planetary Science Letters*, *211*(1-2), 97-110, doi:10.1016/s0012-821x(03)00196-1.

Nabarro, F. (1967), *Theory of Crystal Dislocations* Oxford Univ. Press, Oxford, UK.

Nicolas, A. (1978), STRESS ESTIMATES FROM STRUCTURAL STUDIES IN SOME MANTLE PERIDOTITES, *Philosophical Transactions of the Royal Society of London Series a-Mathematical Physical and Engineering Sciences*, *288*(1350), 49-&.

Nicolas, A., F. Boudier, and A. M. Boullier (1973), MECHANISMS OF FLOW IN NATURALLY AND EXPERIMENTALLY DEFORMED PERIDOTITES, *Am. J. Sci.*, *273*(10), 853-876.

Nishimura, C. E., and D. W. Forsyth (1989), The anisotropic structure of the upper mantle in the Pacific, *Geophys. J.*, *96*, 203-230.

Ohuchi, T., T. Kawazoe, Y. Nishihara, N. Nishiyama, and T. Irifune (2011), High pressure and temperature fabric transitions in olivine and variations in upper mantle seismic anisotropy, *Earth and Planetary Science Letters*, *304*(1-2), 55-63.

Olsen, A., and Birkelan.T (1973), ELECTRON-MICROSCOPE STUDY OF PERIDOTITE XENOLITHS IN KIMBERLITES, *Contributions to Mineralogy and Petrology*, *42*(2), 147-157.

Osugi, J., K. Shimizu, K. Inoue, and K. Yasunami (1964), A COMPACT CUBIC ANVIL HIGH PRESSURE APPARATUS, *Review of Physical Chemistry of Japan*, *34*(1), 1-&.

Phakey, P. P., Dollinge.G, and J. M. Christie (1971), TRANSMISSION ELECTRON MICROSCOPY OF EXPERIMENTALLY DEFORMED OLIVINE CRYSTALS, *Transactions-American Geophysical Union*, *52*(11), 919-&.

Raterron, P., J. Chen, L. Li', D. Weidner, and P. Cordier (2007), Pressure-induced slip-system transition in forsterite: Single-crystal rheological properties at mantle pressure and temperature, *American Mineralogist*, *92*(8-9), 1436-1445, doi:Doi 10.2138/Am.2007.2474.

Revenaugh, J., and T. Jordan (1991), Mantle layering from ScS reverberations 3. The upper mantle, *J. Geophys. Res.*, *96*, 19781-19810.

Ribe, N. M. (1992), ON THE RELATION BETWEEN SEISMIC ANISOTROPY AND FINITE STRAIN, *J. Geophys. Res.-Solid Earth*, *97*(B6), 8737-8747.

Ringwood, A. (1975), *Composition and Structure of the Earth's Mantle*, McGraw-Hill, New York.

Ross, J. V., H. G. Ave Lallemant, and N. L. Carter (1980), Stress dependence of recrystallized-grain and subgrain size in olivine, *Tectonophysics*, *70*(1-2), 39-61.

Schmid, S. (1982), Laboratory experiments on rheology and deformation mechanisms in calcite and their application to studies in the field, edited, pp. 1-62, Mitt. geol. Inst. ETH Univ. Zurich.

Schwarzer, R. A., and H. Weiland (1988), Texture Analysis by the Measurement of Individual Grain Orientations—Electron Microscopical Methods and Application on Dual-Phase Steel, *Textures and Microstructures*, *8-9*, 551-577, doi:10.1155/TSM.8-9.551.

Sharp, T. G., H. Jung, J. D. Fitz Gerald, and S. I. Karato (2004), Dislocation Microstructures and Dissociation in Deformed Olivine Displaying the A-, B- and C-type Fabrics, paper presented at American Geophysical Union.

Shearer, P. M. (1999), Introduction to Seismology, edited.

Sowa, H. (1994), THE CRYSTAL-STRUCTURE OF GAPO4 AT HIGH-PRESSURE, *Zeitschrift Fur Kristallographie*, *209*(12), 954-960.

Stagno, V., Y. Tange, N. Miyajima, C. A. McCammon, T. Irifune, and D. J. Frost (2011), The stability of magnesite in the transition zone and the lower mantle as function of oxygen fugacity, *Geophys. Res. Lett.*, *38*(19), L19309, doi:10.1029/2011gl049560.

Stixrude, L., and C. Lithgow-Bertelloni (2005), Mineralogy and elasticity of the oceanic upper mantle: Origin of the low-velocity zone, *J. Geophys. Res.-Solid Earth*, *110*(B3), 16, doi:10.1029/2004jb002965.

Suzuki, T., H. Koizumi, and H. O. K. Kirchner (1995), TEMPERATURE-DEPENDENCE OF THE PLASTIC-FLOW STRESS OF COVALENT CRYSTALS, *Philos. Mag. A-Phys. Condens. Matter Struct. Defect Mech. Prop.*, *71*(2), 389-397.

Sykes, D., G. R. Rossman, D. R. Veblen, and E. S. Grew (1994), ENHANCED H AND F INCORPORATION IN BORIAN OLIVINE, *American Mineralogist*, *79*(9-10), 904-908.

Tommasi, A., D. Mainprice, G. Canova, and Y. Chastel (2000), Viscoplastic self-consistent and equilibrium-based modeling of olivine lattice preferred orientations: Implications for the upper mantle seismic anisotropy, *J. Geophys. Res.*, *105*(B4), 7893-7908, doi:10.1029/1999jb900411.

Tommasi, A., B. Tikoff, and A. Vauchez (1999), Upper mantle tectonics: three-dimensional deformation, olivine crystallographic fabrics and seismic properties, *Earth and Planetary Science Letters*, *168*(1-2), 173-186.

Toriumi, M., and S. I. Karato (1985), Preferred Orientation Development of Dynamically Recrystallized Olivine during High-Temperature Creep, *Journal of Geology*, *93*(4), 407-417.

Twiss, R. J. (1977), Theory and applicability of a recrystallized grain size paleopiezometer, *Pure and Applied Geophysics*, *115*(1), 227-244, doi:10.1007/bf01637105.

Van der Wal, D., P. Chopra, M. Drury, and J. F. Gerald (1993), Relationships between dynamically recrystallized grain size and deformation conditions in experimentally deformed olivine rocks, *Geophys. Res. Lett.*, *20*(14), 1479-1482, doi:10.1029/93gl01382.

Venables, J. A., and C. J. Harland (1973), Electron back-scattering patternsâ€"A new technique for obtaining crystallographic information in the scanning electron microscope, *Philosophical Magazine*, *27*(5), 1193 - 1200.

Wang, Y. B., W. B. Durham, I. C. Getting, and D. J. Weidner (2003), The deformation-DIA: A new apparatus for high temperature triaxial deformation to pressures up to 15 GPa, *Review of Scientific Instruments*, *74*(6), 3002-3011, doi:10.1063/1.1570948.

Warren, J. M., G. Hirth, and P. B. Kelemen (2008), Evolution of olivine lattice preferred orientation during simple shear in the mantle, *Earth and Planetary Science Letters*, *272*(3-4), 501-512, doi:10.1016/j.epsl.2008.03.063.

Wenk, H. R., and C. N. Tome (1999), Modeling dynamic recrystallization of olivine aggregates deformed in simple shear, *J. Geophys. Res.-Solid Earth*, *104*(B11), 25513-25527.

Yamazaki, D., and S. Karato (2001), High-pressure rotational deformation apparatus to 15 GPa, *Review of Scientific Instruments*, *72*(11), 4207-4211.

Zhang, S. Q., and S. Karato (1995), LATTICE PREFERRED ORIENTATION OF OLIVINE AGGREGATES DEFORMED IN SIMPLE SHEAR, *Nature*, *375*(6534), 774-777.

Zhang, S. Q., S. Karato, J. D. Fitz Gerald, U. H. Faul, and Y. Zhou (2000), Simple shear deformation of olivine aggregates, *Tectonophysics*, *316*(1-2), 133-152.

Zhang, Y., B. E. Hobbs, and M. W. Jessell (1994), The effect of grain-boundary sliding on fabric development in polycrystalline aggregates, *Journal of Structural Geology*, *16*(9), 1315-1325.

Appendix I

Table I: List of deformation experiments performed and their outcome

SN No.	Exp. No.	Condition	Observation	Remark
1	*DD 318*	*$GaPO_4$: 33 bar*	*Low V_{out} , Wire broke*	*Need to redesign assembly*
2	*DD 319*	*Olivine : 100 bars; 8/6mm*	*Heater failure*	*Short circuit*
3	*DD 320*	*Olivine : 100 bars; 8/6mm*	*T/C failure (no current)*	*Shearing of heater*
4	*DD 322*	*Olivine : 100 bars; 8/6mm*	*T/C wire broke + short*	*Shearing of heater*
5	*DD 329*	*$GaPO_4$: 33 bar*	*Noisy data*	*Charge counter broken*
6	*DD 330*	*Olivine : 100 bar; 6/4mm; No thermo-couple*	*Heater failure at the onset of deformation*	
7	*DD 331*	*Olivine : 100 bar; 6/4mm*	*Heater problem*	*Shearing of heater*
8	*DD 332*	*Olivine : 100 bar; 6/4mm*	*Heater problem*	*Shearing of heater*
9	*DD 335*	*Olivine : 110 bar; 6/4mm; Fired pyrophyllite*	*O.K.*	*Type-C slip*
10	*DD 337*	*Olivine: 100 bars; No heating stage & no deformation*	*O.K.*	*Almost no deformation*
11	*DD 341*	*$GaPO_4$: 33 bar*	*0.15 mm T/C wire*	*Low assembly resistance*
12	*DD 342*	*Olivine : 100 bar; 8/6mm; Heating stage 5 min*	*Erratic temperature*	*Heating elements need change*
13	*DD 343*	*Olivine : 100 bar; 8/6mm; Heating stage 5 min*	*Mo-foil with Zirconia instead of Mo-ring; failed*	*Try Pt-foil*
14	*DD 344*	*Olivine : 100 bar; 8/6mm*	*700µ deformation*	*Type-A slip*
15	*DD 345*	*Al_2O_3 : replacement for $GaPO_4$*	*Background check*	*Still some readings; assembly needs change*
16	*DD 348*	*Olivine: 100 bar; 6/4mm; No T/C*	*600µ deformation*	*Sample fell apart during cutting*
17	*DD 349*	*Olivine : 100 bar; 6/4mm*	*Blow-out*	*Anvils intact*
18	*DD 350*	*Olivine : 100 bar; 6/4mm*	*600µ deformation*	*Weak type-C slip system possible*
19	*DD 352*	*Olivine : 110 bar; 6/4mm; Pyrophyllite fired at 1000°C; No T/C*	*Blow-out*	*Anvils intact*
20	*DD 353*	*Olivine : 110 bar; 6/4mm; Pyrophyllite fired at 1000°C; No T/C*	*Blow-out*	*Anvils broke*
21	*DD 354*	*Olivine : 110 bar; 6/4mm;*	*Short circuit*	*T/C working*

		Pyrophyllite fired at 1000°C;		
22	*DD 359*	*$GaPO_4$: 20 bar*	*Almost no noise*	*Not sensitive enough*
23	*DD 360*	*Olivine : 110 bar; 6/4mm; Pyrophyllite fired at 1000°C*	*Test for heating elements*	*Blowout*
24	*DD 361*	*Olivine : 110 bar; 6/4mm; Pyrophyllite fired at 1000°C*	*Pyrophyllite gaskets*	*Need lesser amount of Pyrophyllite gasket*
25	*DD 362*	*Bismuth : Pressure calibration of Pyrophyllite cell*	*Loss of electric contact*	
26	*DD 363*	*Bismuth : Pressure calibration of Pyrophyllite cell*	*O.K.*	*Bi I-II & Bi II-III transitions observed at 17 & 19 bars resp.*
27	*DD 364*	*Manganin: Pressure calibration*	*O.K.*	*Data partially noisy*
28	*DD 365*	*Bismuth : Pressure calibration of Boron-epoxy cell*	*Blowout at 51 bars*	*Bi I-II & Bi II-III transitions observed at 14 & 17 bars resp.*
29	*A 191*	*Hot-pressing olivine at 1 GPa and 1200°C*	*Hot-pressed sample developed cracks*	*Need for slow decompression*
30	*B-199, B-184, B-204, B-206 & B-184*	*Hot-pressing olivine at 1 GPa and 1200°C*	*O.K.*	
31	*DD366*	*4/6 unfired pyrophyllite – 100 bar (5 Gpa)*	*Heater failed*	
32	*DD367*	*Manganin Pressure calibration -- 4/6 fired*		*OK*
33	*DD368*	*5 GPa-1300°C-10-4 s-1*	*Heater failed*	*No deformation*
34	*DD369*	*8GPa-1300°C 10-4 s-1*	*Heater failed-* ***Test for Pyrophyllite Gaskets***	*No deformation*
35	***DD370***	***8GPa-1300°C 10-4 s-1***	***400 bar diff. ram pressure- Test for Re furnace***	***Blow out***
36	***DD372***	***8GPa -1300°C 10-4 s-1***	***Temp. drop – No gaskets***	***failed***
37	***DD373***	***8 GPa -1300°C 10-4 s-1***	***Test for Teflon gaskets***	***OK***
38	*DD374*	*8 GPa Boron Epoxy cube*	*Blowout*	*failed*

39	*DD375*	*8 GPa -1300C 10-4 s-1*	*No deformation Null experiment*	*OK*
40	*DD381*	*3 GPa -1300C 10-4 s-1*		*OK*
41	*DD382*	*3 GPa-1300C 10-4 s-1*		*OK*
42	*DD383*	*8 GPa -1300C 10-4 s-1*		*OK*
43	*DD384*	*8 GPa-1300C 10-4 s-1*		*OK*
44	*DD385*	*CaGeO3 : 8 GPa 1000°C*		*PPV found*
45	*DD387*	*Cs → St : 10 GPa (120bar) 1000°C*		*Cs and St found*
46	*DD 388*	*8 GPa-1300C 10-4 s-1*	*Blowout*	
47	*DD391*	*8 GPa & 1550°C*		
48	*DD 400*	*Coet → Stis. 10 GPa(110 bar) -1000°C*		*Coes. found*
49	*DD402*	*8 GPa 1500°C*		*OK*
50	*DD403*	*5 GPa 1400°C 10-4 s-1*		*OK*
51	*DD404*	*5 GPa-1300C 10-4 s-1*	*Failed furnace*	
52	*DD405*	*8 GPa 1500°C Fine grained olivine*		*OK*
53	*DD406*	*8 GPa 1300°C*		
54	*DD407*	*8 GPa 1400°C 2-Pyroxene thermometry*		*OK*
55	*DD408*	*8 GPa 1300°C*	*500 µ deformation Blow-out*	
56	*DD430*	*3 GPa 1300°C Water-Rich olivine*		*OK*
57	*DD451*	*Qtz -> Coesite (4/6mm fired pyroph.) 24bar-1000°c*		*Qtz found*
58	*DD452*	*Same as DD451 but at 27.5 bar – 1000°C*		*Coesite found*
59	*DD454*	*8 GPa 1500°C 2.5x10-5 s-1 – 600µ deformatiom*	*Sample deformed more than necessary*	

60	*DD454*	*8GPa – 1300°C 2.5x10-5 s-1*		*OK*
61	*DD456*	*8 GPa – 1300°C 5x10-4 s-1 with water*		*OK*
62	*DD457*	*8 GPa -1300°C 2.5x10-5 s-1 with water*	*T/C failed at the start of heating*	*OK*
63	*H3115*	*Hotpressed at 8.5 GPa +1200°C in MA press*	*A-type fabric*	*OK*
64	*DD458*	*5 GPa -1300°C 2.5x10-5*		*OK*
65	*DD459*	*5 GPa 1300°C 5x10-4 s-1*		*OK*
66	*DD460*	*8 GPa – 1500°C 5x10-4 s-1*		*OK*
67	*DD461*	*5 GPa 1300°C 5x10-4 s-1 with water*		*OK*
68	*DD462*	*5 GPa 1300°C 2.5x10-5 s-1 with water*		*OK*
69	*DD463*	*5 GPa 1300°C 2.5x10-5 s-1 with water*		*OK*
70	*DD466*	*5 GPa 1300°C 2.5x10-5 s-1 with water*		*OK*
71	*DD467*	*5 GPA 1300°C 2.5x10-5 s-1 Dry*		*OK*
72	*DD468*	*8 GPa 1500°C 10-4 s-1 with water*		*OK*
73	*DD469*	*8 GPa 1500°C 10-4 s-1 - dry*		*OK*
74	*DD473*	*8 GPa 1500°C 10-4 s-1with water*		*OK*
75	*DD474*	*5 GPa 1300°C 10-4 s-1with water*		*OK*
76	*DD475*	*3GPa 1300°C 2.5x10-5 s-1 - Dry*		*OK*
77	*DD476*	*3 GPa 1300°C 5x10-4 s-1with water*		*OK*
78	*DD482*	*Peridotite 8 GPa-1300°C-5x10-4-wet*	*Many grains fell out during cutting and polishing*	
79	*DD483*	*Peridotite 8 GPa-1300°C-5x10-4*		*OK*
80	*DD495*	*Peridotite 8 GPa-1300°C-2.5x10-5*		*OK*

81	*H3354*	*Olivine hotpressing –dry 11 GPa- 1400°C in MA press*	*A-type fabric*	*OK*
82				

Appendix II

Double kink nucleation model (Matlab code)

Start

Based upon Koizumi et al. 1993; Kink pair nucleation and critical shear stress; Acta Metall. Mater., Vol. 41, No. 12, pp. - 3483-3493

```
clear all;

clc;

tic;
```

Define constants and variables

```
b =[4.76e-10;5.99e-10]; % Burger vectors; a and c vectors

a = b(1,1); % Periodcity of peierls potential; ralated to oxygen anion

        % periodicity

G=76500; % Shear strength of olivine at 8GPa pressure and 1300° C (in Pa)

tau_p1 = 9100; % Peierls stress a-slip(Pa)

tau_p2 = 15600; % Peierls stress c-slip(Pa)

n=0; % to be used while defining potential barrier; See line 24-25
```

```
Q=(2^(n-1))*G*(a^(2-n))/n; % Insure that Tau_p = G at x=a/2
x_max = 1.50;
x_int = 0.0001; % x-axis step size
x = a*(0:x_int:x_max); % range of x
nu = 0.25; % Poisson ratio for olivine
Ro = b(1,1)/20; % Cutoff Radius
e = exp(1); % Exponent of natural log

% Max values
i_max = 12; % Steps for stress axis
j_max = 200; j_int = 0.0005; % j_int times j_max is maximum j - maxmimum h
l_max = 500; l_int = 0.1; % maximum kink width
% Pre-allocate memory for better performance
delP =  zeros(j_max,l_max, 'double');
delE = delP;
delW = delP;
delH = delP;
```

Potential barrier (From Hirth and Lothe 1992)

```
Vpx = (a*b(1,1)*tau_p1)/(2*pi)*(1-cos(2*pi*x/a));
```

Potential barrier from koizumi with alpha included

```
% alpha = (alpha_i-1)*0.001;
% C0=sqrt(2*((((1-alpha)^2+4*alpha^2+(1-alpha)*...
%((1-alpha)^2+8*alpha^2)^(0.5))...
%     /((1-alpha^2)+2*alpha^2+(1-alpha)*...
%((1-alpha)^2+8*alpha^2)^(0.5))^(1.5))));
% beta= (log(1/C0))/log(tau_p1/G);
% gx = 1 - cos(2*pi.*x/a)-(alpha/2).*(1-cos(2*pi.*x/a)).^2;
% Vpx = (C0/(2*pi))*a*b(1,1)*tau_p1*((tau_p1/G)^beta).*gx;
% grad_Vpx(alpha_i,:) = max2((C0)*b(1,1)*tau_p1.*sin(2*pi.*x/a)...
%     .*(1 - alpha*(1-cos(2*pi.*x/a)))/(b(1,1)*tau_p1));
```

Plot potential curve

figure(1); plot(x/a,Vpx); %*plot Vp & gradient of Vp xlabel('\fontsize{12}x/a');*
ylabel('\fontsize{12}V_p/Ga^2'); grid on;

Complete expression for delH = delE + delP - delW;

index-i -> Range of h; index-j -> Range of tau; index-k -> Range of K; index-l -> Range of L

```
w0= G*b(1,1)^2/(2*pi); % A constant to be used later for delH calculation
for i = (1:1:i_max);
   tau = 50*(i);  % Stress range (MPa)
    for l = (1:1:l_max);
        L = b(1,1)*l_int*(l); % range of L as multiples of b
        for j = (1:1:j_max);
        h = (0.9+(j/j_max))*a; % critical height
        % Find equilibrium position x0
        m0 = tau*b(1,1); % tau_p1 = Peierls stress * b
        f = @(x1)(tau_p1*b(1,1)*sin(2*pi*x1/a) - m0); %for x <= a/2;f=
        %slope of Vp
        options = optimset('display','notify','TolX',1e-13,'TolFun',1e-12);
        [x0,fval,exitflag] = fzero(f,a*0.15,options); % look for solution
        % near a*0.15
        x0_index = int16(round2((x0/a),x_int)/x_int);
        if x0_index <= 0
            x0_index = 1;
        else
        end
% delH calculation
D=sqrt(L^2+h^2);
% Change in potential from x0 to x0+h;
x0h_index = x0_index + int16(round2((j/j_max),x_int)/x_int);
delP(j,l) = ... % Change in potential energy from x0 to x0+h
    2*trapz(x(x0_index:x0h_index),Vpx(x0_index:x0h_index))...
    + L*(Vpx(x0h_index)-Vpx(x0_index));
delE(j,l) = ... % Change in the elastic interaction energy
```

```
            w0*((D-L-h)...
            +L*log((2*L)/(L+D))...
            -(1/(1-nu))*(L-D+h*log((h+D)/L)-h*log(h/(e*Ro))));
        delW(j,l) = tau*b(1,1)*h*L; % mechanical work done by stress tau
        delH(j,l) = delE(j,l) + delP(j,l) - delW(j,l); % change in enthalpy
                end
            end
```

Plots

```
        f=figure(1);
        delH_l=(1:1:l_max)*l_int;
        delH_j=0.9+(1:1:j_max)*j_int;
        contourf(delH_l,delH_j,delH,500); %
        tname=sprintf('Plot with stress = %d MPa',tau);
        title(tname);
        xlabel('L (times b)');
        ylabel('h/a');
        set(f,'PaperpositionMode','Auto');
```

Directory for file output

```
        fname=sprintf('%d_sigma',tau);
        fullfname = fullfile(pwd,'kinks','9100',fname);
        print(f,'-dpng',fullfname);
        save(fullfname,'delH');
        saveas(f,fullfname,'fig');
        end
        toc;
End
```

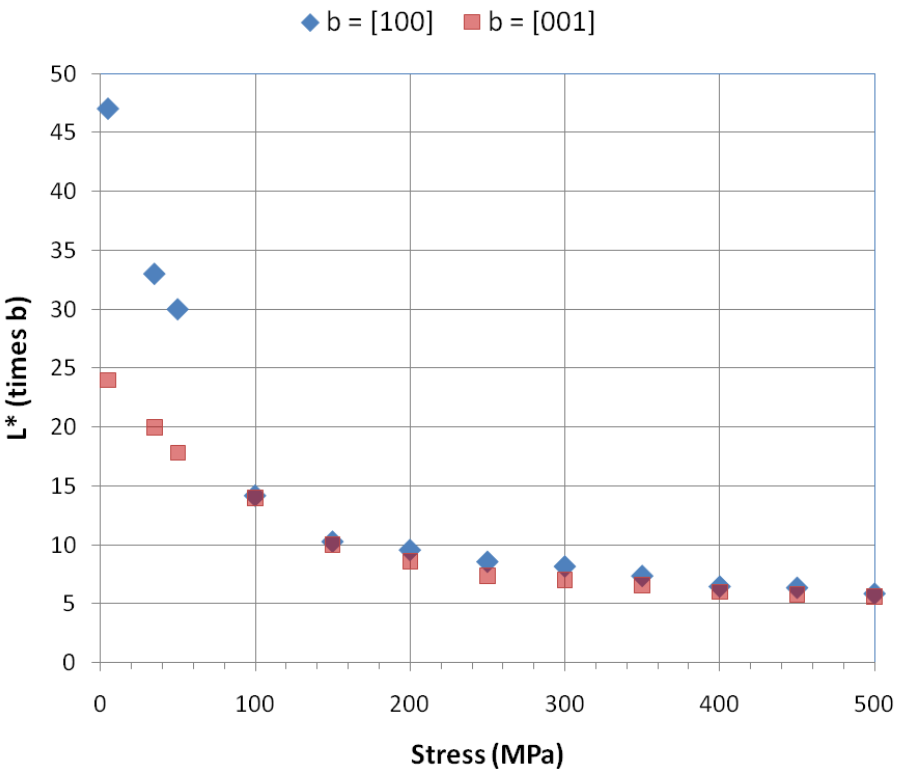

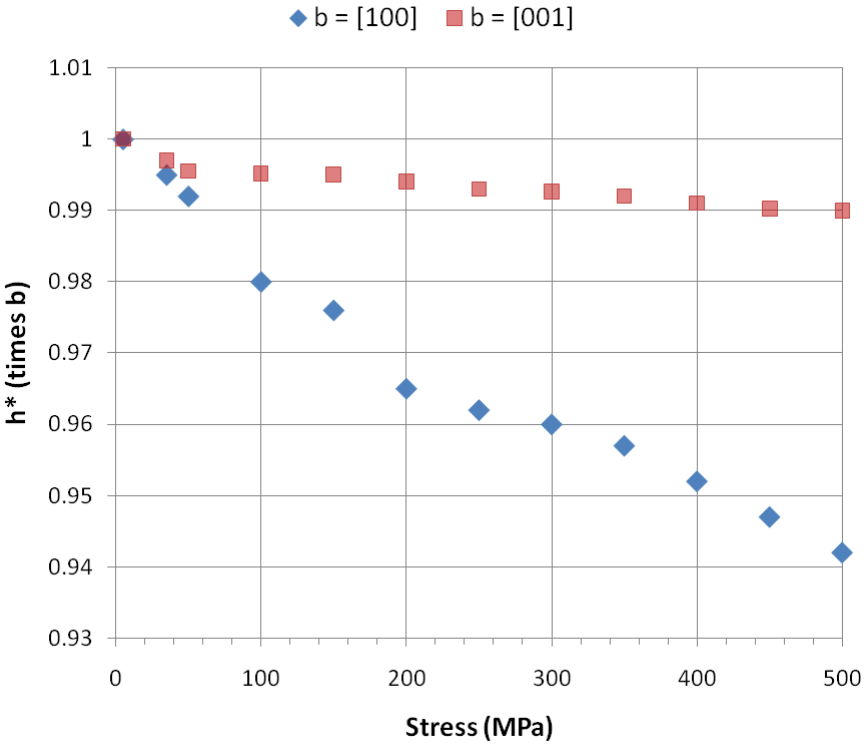

Figure I: Critical kink size for an abrupt kink as a function of stress.

Appendix III

Following figure show the main assembly parts and the assembled setup for a 4/6 mm fired pyrophyllite assembly. This assembly uses a Rhenium heater and Teflon gaskets.

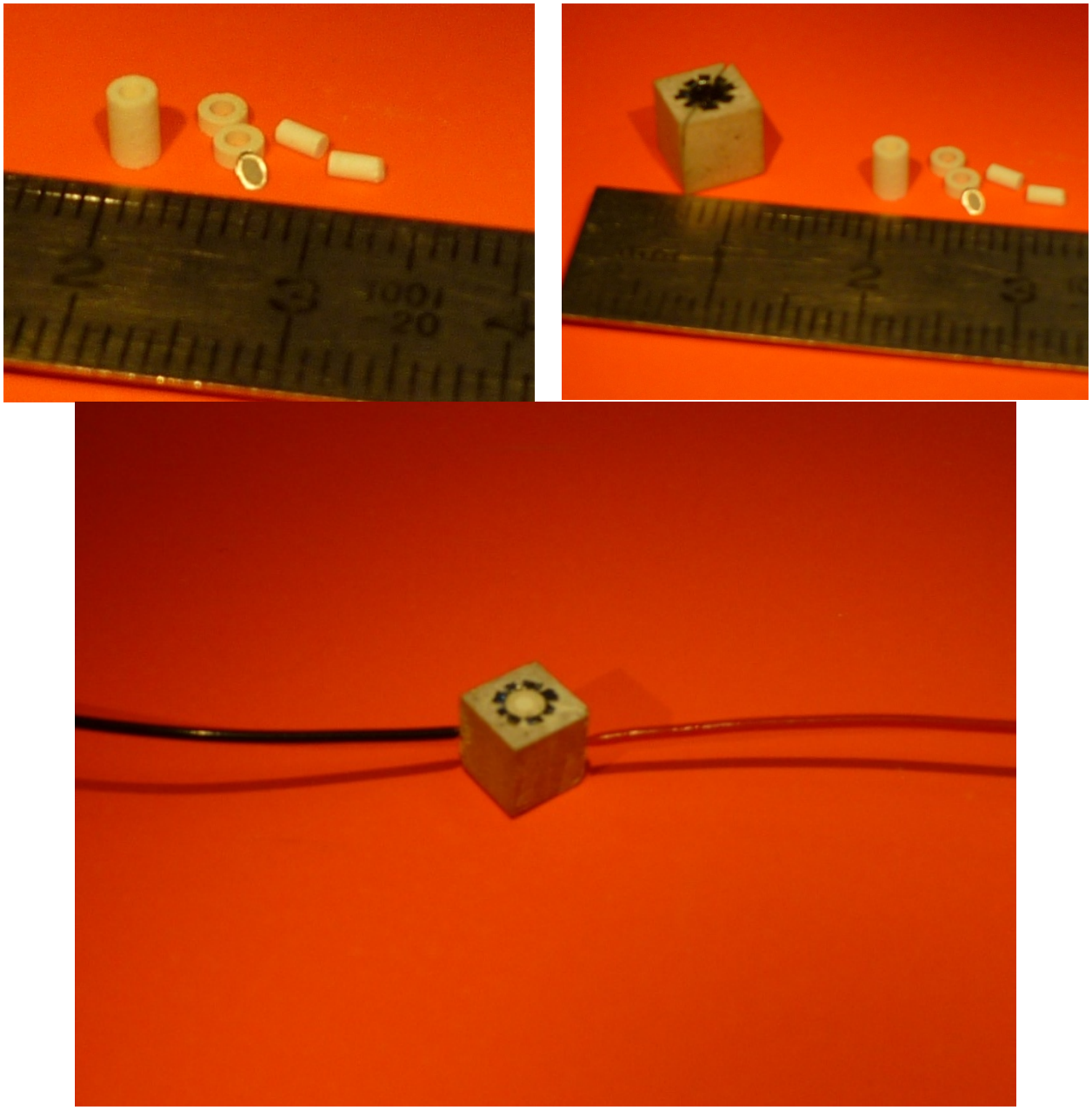

Figure II: Assembly parts before assembly and after assembly. Top figure shows the MgO sleeve, two Zirconia rings and crushable alumina rods. The elliptical shaped sample is jacketed by a Platinum foil. Bottom figure shows all t he parts assembled together.

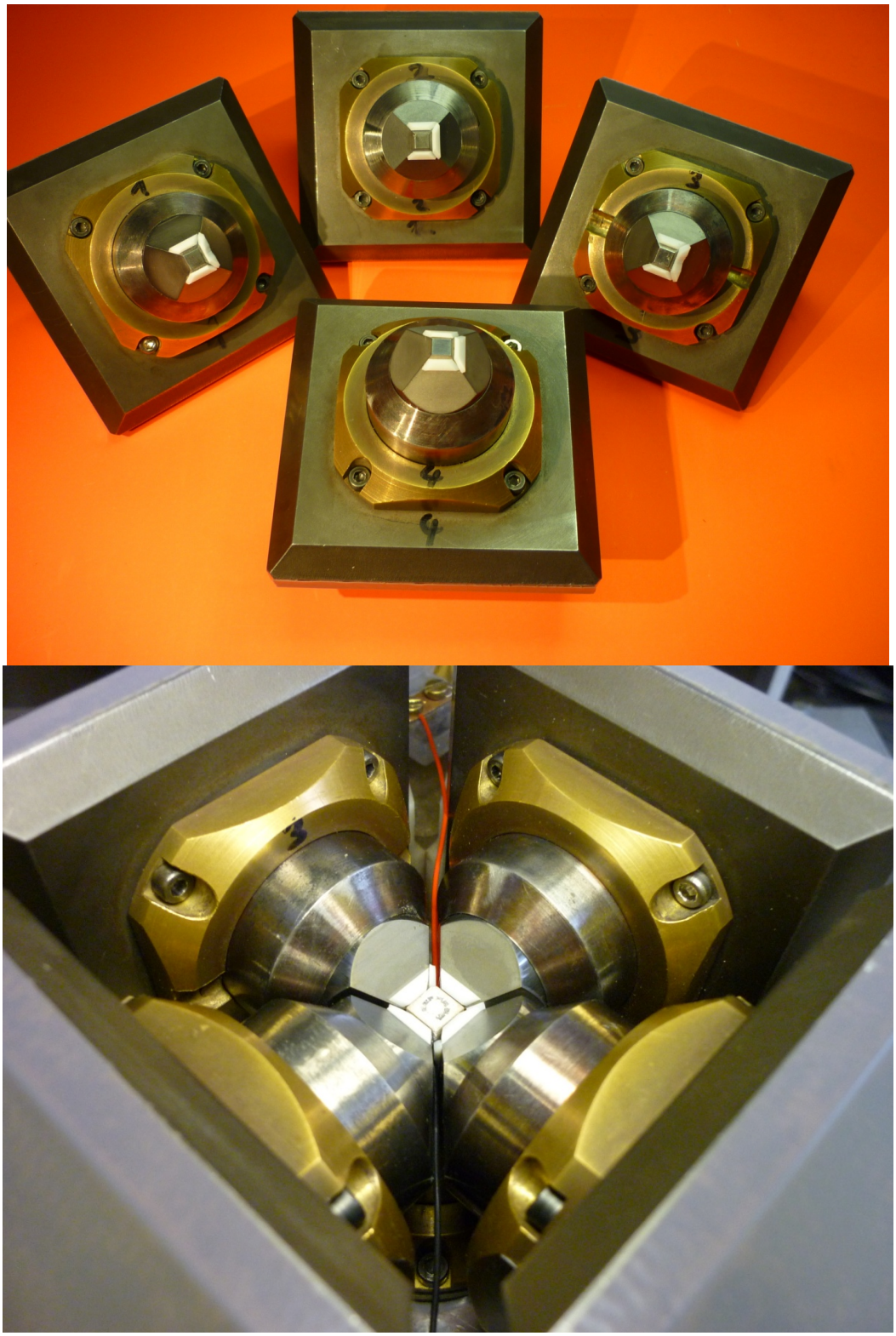

Figure III: Emplacement of Teflon gaskets on the anvils. Top: 12 such gaskets are placed with one for each pair of face of anvils. Bottom: This figure shows how the final setup looks like when placed in D-DIA press.

Appendix IV

Schematics for the 4/6 mm and 6/8 mm assembly

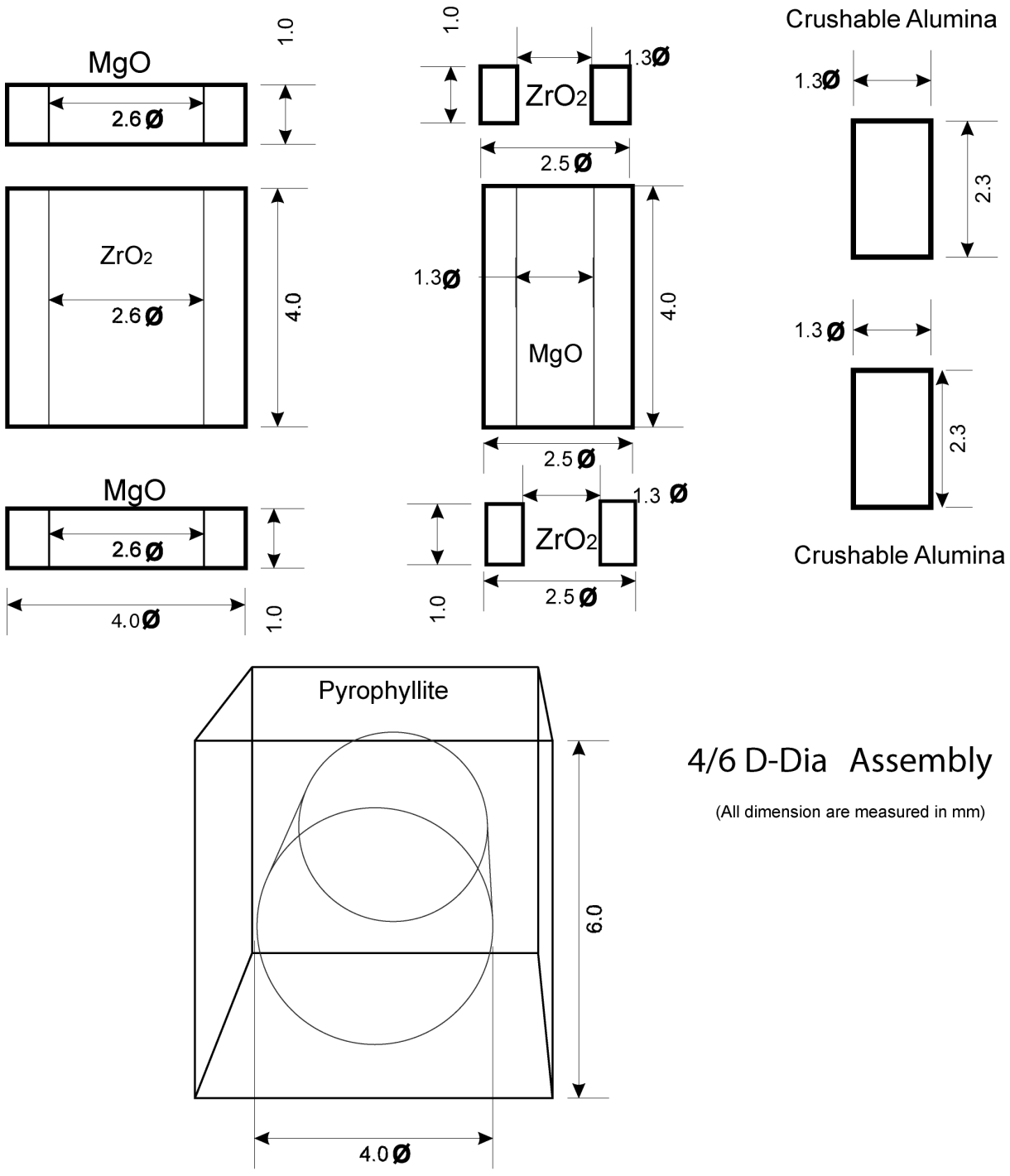

Figure IV: 4/6 mm D-DIA assembly schematic for Rhenium furnace based setup

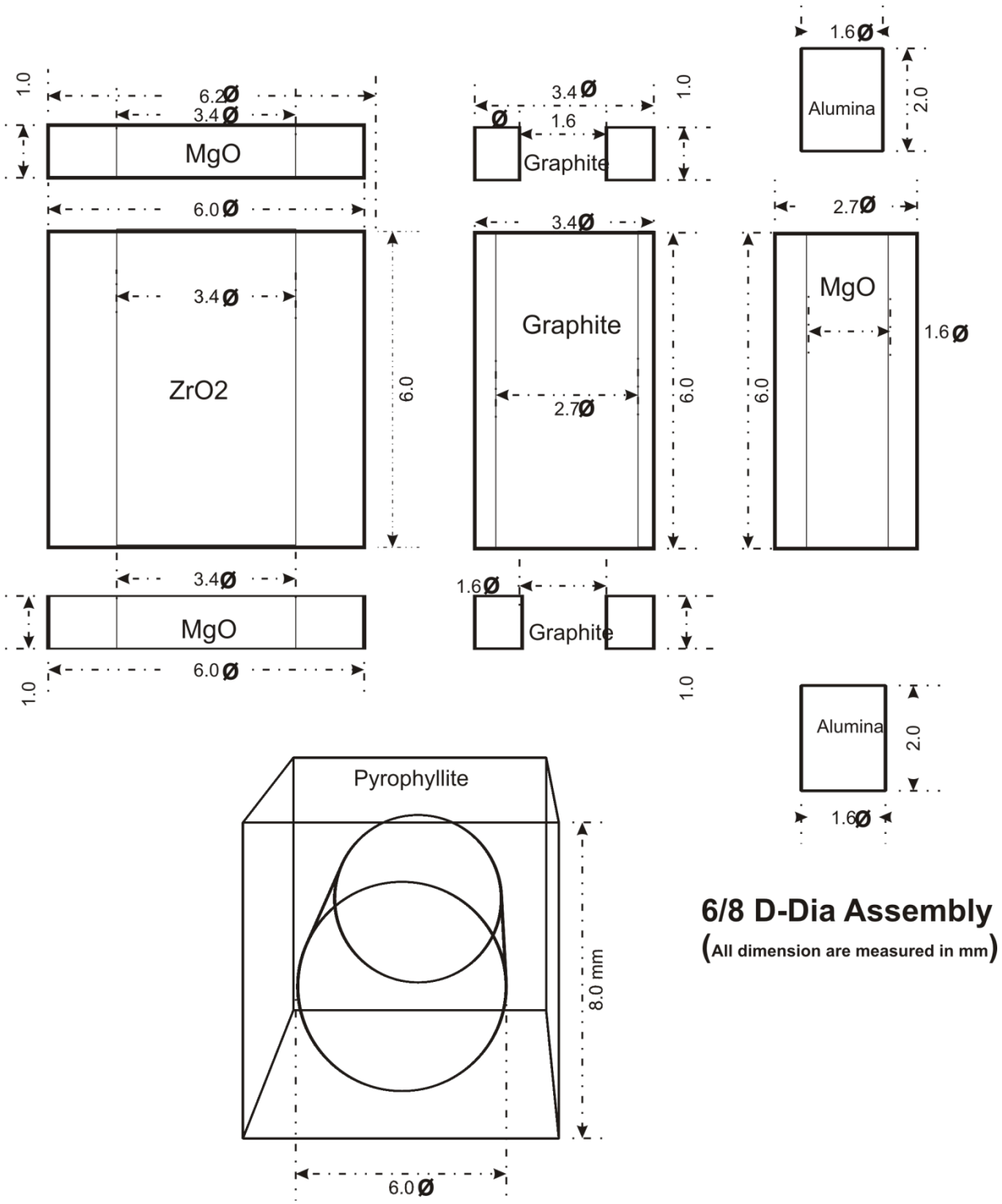

Figure V: 6/8 mm D-DIA assembly schematic for graphite furnace based setup

Erklärung

Hiermit versichere ich, die vorliegende Arbeit selbstständig verfasst und keine anderen als die von mir angegebenen Quellen und Hilfsmittel benutzt zu haben.

Ferner erkläre ich, dass ich weder an der Universität Bayreuth, noch an einer anderen Hochschule versucht habe, eine Dissertation einzureichen, oder mich einer Promotionsprüfung zu unterzeihen.

Sushant Shekhar

Bayreuth, May 2011